TOWARDS MAGNETO-ACOUSTIC OSCILLATORS

A Dissertation

Presented to the Faculty of the Graduate School

of Cornell University

In Partial Fulfillment of the Requirements for the Degree of

Doctor of Philosophy

by

Tanay Arun Gosavi

January 2017

TOWARDS MAGNETO-ACOUSTIC OSCILLATORS

TANAY ARUN GOSAVI, Ph. D.

Cornell University 2017

Spin torque oscillators (STOs) were developed in 2003, and since then, progress has been made in understanding their underlying physics, frequency of operation, frequency tuning range, and functionality. These nanoscale oscillators with their octave-spanning frequency tuning range have been touted for many applications including neuromorphic computing, magnetic field sensing, and microwave signal detection. Since their inception, the output power of spin torque oscillators has been improved by five orders of magnitude. In spite of all these developments, the adoption of spin torque oscillators as an extremely tunable signal source has been hindered due to their large linewidth and frequency stability issues. Solutions such as using spin torque oscillators in a PLL and injection locking of spin torque oscillators has been demonstrated. However, these solutions need an external signal reference for their implementation. Recently, self-locking of spin torque oscillators to their amplified, delayed output signal has been proposed, and initial experiments have demonstrated an encouraging progress in the improvement of the linewidth. Further improving on this concept of self-locking, we propose a system that uses spin torque oscillators in a delay line oscillator with a high quality factor micro-electro-mechanical (MEMS) resonator as the delay element. This spin torque oscillator coupled with a MEMS resonator in a feedback system is presented in this thesis as a magneto-acoustic oscillator.

This dissertation presents all the components needed for realizing the magneto-acoustic oscillator as well as addresses the issues and challenges in its implementation.

To maintain the tuning capability of the magneto-acoustic oscillator, we use high-overtone bulk acoustic resonators (HBARs) as the MEMS resonator, as they have many resonances spread over a large range of frequency. We fabricated and characterized one port, high-overtone bulk acoustic resonators to be used as stress transducers for strain feedback-based magneto-acoustic oscillator. We also developed an analytical model to calculate the stress/strain generated by the HBARs for a given drive voltage. We further performed low temperature characterization of the HBAR resonators, fabricated on different substrate materials, to better understand the dominant loss mechanism that limits its performance as a strain generator. Two port, laterally coupled high-overtone bulk acoustic resonators were fabricated and characterized with measurements indicating quality factors upwards of 20,000 in the 2 to 8 GHz regime. Two port HBARs were demonstrated as a high quality factor, narrow bandwidth filters to be used for current feedback-based magneto-acoustic oscillators that are operational over a large frequency range, with a nominal transmission loss of -25 dB.

We study using strain as the feedback path for implementing a magneto-acoustic oscillator in a macrospin model of a spin torque oscillator. This model incorporates the effect of a uniaxial external AC strain on the spin torque oscillator by considering the effective field generated due to the magnetoelastic property of the free layer magnet. We also calculate the threshold amplitude of strain needed to lock the spin torque oscillator and further calculate the gain required for the HBAR to feedback that strain, when implemented as a magneto-acoustic oscillator. Comparing the gain needed for locking in a current feedback-based magneto-acoustic oscillator and strain feedback-based spin torque oscillator, we find that current feedback based magneto-acoustic oscillator performance is superior.

CoFeGe/CoFe and Terfenol-D as the free layer based spin valves fabricated at HGST with 6% MR and SHE-MTJs with 30% TMR were characterized as spin torque oscillators for implementing the current feedback-based magneto-acoustic oscillators. We demonstrated an open loop current-based magneto-acoustic oscillator, which reduced the linewidth of the spin valve oscillators from 35.4 MHz to 175 kHz with $\Delta f_o/f_o$ ratio as high as 23,657 was measured for in-plane oscillation mode at 4.14 GHz. This is the highest measured $\Delta f_o/f_o$ ratio for any spin valve oscillator in an open loop configuration. Open loop current-based magneto-acoustic oscillator, with the SHE-MTJ, reduced the linewidth of the oscillator from 300 MHz to 280 kHz. This is the smallest reported linewidth for SHE-MTJs.

Upon implementing a closed loop current feedback-based magneto-acoustic oscillator, we observed HBAR oscillations. This was due to the poor isolation from wide bandwidth circulators and because of the high gain needed for locking owing to the low output power of the spin torque oscillators. We propose using a microwave feedback in a magneto-acoustic oscillator that eliminates the implementation problems of the closed loop current feedback-based magneto-acoustic oscillator by changing the domain of feedback signal from electrical to microwave. We simulated different closed loop magneto-acoustic oscillators using strain, current, and microwave feedback in HSPICE to compare their power efficiencies. Simulation results show that the microwave feedback-based magneto-acoustic oscillator is the most promising alternative due to the small gain required in its implementation.

BIOGRAPHICAL SKETCH

Tanay Gosavi was born in Mumbai, India in 1987. He received his Bachelors of Engineering in Electronics Engineering from Sardar Patel Institute of Technology, Mumbai University with a focus on computer architecture and embedded systems in 2009. In August of 2009, he moved to Ithaca, NY to pursue Masters of Engineering in Electrical and Computer Engineering at Cornell University with a focus on RF circuits and received his degree in July 2010. In August 2010, he joined OxideMEMS Lab under the supervision of Prof Sunil Bhave, where he worked on microwave resonators, GPS RF circuits, diamond NV centers, and mechanical logic for low-power correlators. The focus of his thesis has been in the area of spin torque oscillators and coupling them to mechanical resonators to improve their linewidth. His research interests include analog and mixed-signal circuits, MEMS resonators for sensors and timing circuits, optomechanical systems, and spintronics for sensors and memory application.

To my Mamma, Baba and Aaji

ACKNOWLEDGMENTS

I would first like to thank Prof. Sunil Bhave for his guidance and direction throughout my Ph.D. I have him to thank for instilling the knowledge and confidence in me to approach any problem with an open mind, aim high and expect more out of myself. I will always admire and be inspired by his exceptional enthusiasm, farsighted thinking and his ability to motivate his students to do more than their best. I especially thank him for his genuine care and support that he provides his students and I consider it lucky to call him my mentor and friend.

I would also like to thank all members of my graduate committee, Prof. Clifford Pollock, Prof. Gregory Fuchs, and Prof. Daniel Ralph for advice, encouragement, and support they provided me throughout my Ph.D. I am particularly thankful for their willingness to hear me out, sit down to answer my questions and for orienting me in right directions when I felt lost, many times without scheduled appointments. I would especially like to thank Prof Clifford Pollock who has been my committee chair for being a pillar of support in times of crisis. I would also like to thank Prof. Farhan Rana for serving on my MS committee, with whom I had many stimulating discussions regarding my research.

I would like to thank my colleagues of present and past in OxideMEMS Lab with whom I share a strong bond of friendship; Eugene Hwang, Suresh Sridaran, Tiffany Cheng, Laura Fegley, Siddharth Tallur, Ryan Wang, Jonathan Puder, Matthew Storey, Ajay Bhat, Ben Yu, Mert Torunbalci, and Bin Dong. I thoroughly enjoyed the time spent with them, and I look forward to interacting and working with them in future. I particularly want to thank Tiffany and Siddharth who introduced me to CNF and shared valuable insights in fabrication techniques and tricks. I want to acknowledge the mentorship and support from Eugene and Suresh who during my early days as graduate student instilled in me the core tenets of MEMS and a thirst for depth in my

work. I would like to thank Ajay, Matt, and Mert for their support and help with fabricating devices, simulating physics and many insightful discussions regarding my research. I want to thank members of SonicMEMS Lab: Prof. Amit Lal, Serhan Ardanuc, Kwame Amponsah, Sachin Nadig, Po-Cheng Chen, Ved Gund, Jason Hoople, Vinay Kumar, Visrute Pinrod, and Justin Kuo for their friendship, for discussions regarding fabrication, lending me test equipment and fabrication materials.

I want to thank my collaborators and friends in Fuchs research group: Evan MacQuarrie, Nick Jungwirth, Jason Bartell, and Albert Park for discussions on research, measurements and for accepting me as an honorary group member. I especially want to thank Evan with whom I thoroughly enjoyed while working on diamond NV center project. I want to thank members of Ralph Group: Jennifer Grab and Jonathan Gibbons for training me on the projection field setup in CCMR and sharing the setup with me. I want to acknowledge the support of my friends and collaborators from Buhrman research group: Sriharsha Aradhya, Graham Rowlands, Minh Hai Nguyen, and Praveen Gowtham for sharing fabrication know-how, measurement expertise, testing equipment, research insights and guidance through my years at Cornell. I am particularly indebted to Sriharsha and Graham for their mentorship and guidance on the SHE-MTJ fabrication, testing, and measurements.

This thesis would not be possible without the help and support of all the staff members of Cornell Nanoscale Science and Technology Facility (CNF), Nanobiotechnology Center (NBTC) and Cornell Center for Material Research (CCMR). I would specifically like to name Garry Bordonaro for his help with photolithography, Noah Clay for help with the spray coating process flow, Daron Westly for training me helping me with e-beam lithography. I would also like to extend my gratitude to Sue Bulkley, and Daniel Richter for helping me through my Ph.D. with ordering lab equipment, research supplies, and travel reimbursements

paperwork. I would like to thank Scott Coldren with his help on navigating me through the graduate school and department paperwork.

I would like to thank and acknowledge all my friends in Ithaca who made my time in Cornell an enjoyable and memorable experience. I want to thank the members of "Muffandaes" for their love and friendship, for all the crazy coffee and lunch discussions: Mustansir Mukadam, Shantanu Rajwade, Krishna Jayant, Suresh Sridaran, Siddharth Tallur and Adarsh Kowdle. I want to thank my "EmoGroup" friends Chaitanya Joshi, Ayush Dubey, Sachin Nadig, Pooja Gudibanda, Kritika Dusad, Shreyas Honrao, Ajay Bhat, Vaibhavi Vaidya, Amandeep Gupta, and Ritika Jain for the all the board games, political discussions, movie nights. I want to thank Ishita Mukhopadhyay, Mihir Khadilkar, and Amit Vishwas, for always having my back and for being there for me through thick and thin. I want to thank Abhinandan Majumdar, Shreesha Srinath, Ashima Krishna, and Sahas Barve among many others for their friendship and support provided through my time at Cornell.

I want to thank my family for their unfaltering support; my dad for his guidance and encouragement, my mom for her blind and unconditional love and my grandmother for her love and blessings. Special thanks go to Neha Palsokar for her love, support, and encouragement, and being patient with me through the last couple of years of my Ph.D.

TABLE OF CONTENTS

LIST OF FIGURES

LIST OF TABLES

CHAPTER 1

INTRODUCTION

Oscillators or signal sources are ubiquitous in modern day communication systems, sensing systems, and navigation systems. In fact, oscillators are found in almost all physical systems. Very broadly, but aptly, oscillators can be defined by their property to generate an oscillating signal; which means a signal that varies in time with a particular period like a sinusoidal wave. Typical examples of oscillators include lasers, music instruments, clocks and even an atom. What makes oscillators important and so useful is that they are used to count or demarcate time. In digital circuits, oscillators are used to produce the system clock, whose rising or falling edge is used as the basis for triggering or starting Boolean calculations to pace the flow of an algorithm.

In communication systems, oscillators are used to produce a clock, which allocates the use of a communication channel among multiple users for a given period. For higher throughput communication, instead of sharing the channel in the time domain, we share the channel in the frequency domain. This is done by allocating specific frequency bands for communicating between specific users. As modern day bandwidth requirements increase, the spacing between separate communication bands is reduced, while the bandwidth in each band is fully utilized. To facilitate such complex communication systems we use multiple oscillators at different frequencies across multiple bands of communication. A more elegant, cheap and integrated solution to this problem that will enhance the bandwidth of communication is a single oscillator. Such an oscillator will have to function across several bands of frequencies and whose frequency of operation can be picked and chosen according to the needs of communication, which could be mass fabricated and produced cheaply and has a

potential for integrating with CMOS chips. We consider spin torque oscillators due to their small form factor and octave-spanning tuning range to be an ideal candidate.

1.1 *Spin torque oscillators*

Slonczewski [1] and Berger [2] predicted that electron flow in a stack of magnetic materials carries angular momentum from one magnetic layer to another. This angular momentum exerts a torque on the magnetization of the magnetic layer and when the amplitude of the torque is sufficient to overcome the losses in the layer, the magnetization of the layer will oscillate. Shortly after this prediction, Kiselev *et al.* [3] were the first to perform direct measurements of microwave oscillations in nanostructures. These nanostructure devices are broadly called spin torque oscillators (STO). They consist of two conducting magnets; the fixed magnet and the free magnet, which are separated by a spacer (Figure 1.1). The magnetization of the free layer (or magnet) is susceptible to change by the angular momentum of the electrons impinging on it, while the magnetization of fixed magnet is unaffected (or less affected) by the electron moment. Typically, the spacer used in these devices are of two types- conducting non-magnetic metals that have large spin relaxation lengths or insulating oxides like MgO.

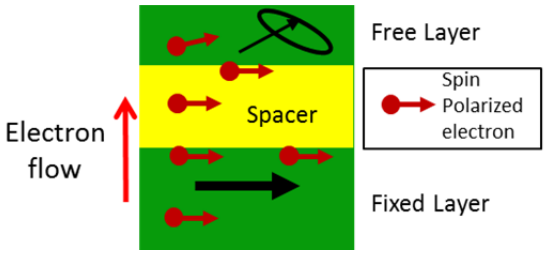

Figure 1.1: The basic structure of a spin torque oscillator shows magnetic layers in green separated by a non-magnetic spacer. Spin-polarized electrons apply a torque on the magnetization of the free layer causing its steady-state precession.

For the electron flow to apply a sufficient amount of torque on a magnet, a significant portion of the electron spins need be oriented along one direction. This orientation of electron spin in an STO is done by passing the electrons through the fixed layer magnet, where due to spin transfer torque, the electrons spins get reoriented along the direction of the magnetization of the fixed layer [4]. We use these spin-polarized electrons to apply torque to the magnetization of the free layer, causing its steady-state precession. Now in a spin torque oscillator, this magnetization precession can be read out electrically as a resistance change by the giant magnetoresistance effect [3] or tunnel magnetoresistance effect [5]. The oscillation of the magnetization in the STO also generates AC dipolar magnetic fields which can be directly recorded as microwave emissions [6], but the power of the microwave signal is much smaller than what could be extracted from the magnetoresistance effect unless it is coupled directly to a microwave resonator [7].

The power of a spin torque oscillator is dependent on the amplitude of resistance change caused by the magnetization precession. The resistance of the spin torque oscillator is given by:

$$R = R_{av} + \frac{\Delta R}{2}\left(\vec{\mathrm{m}}_{fixed}.\vec{\mathrm{m}}_{free}\right) \cong R_{av} + \frac{\Delta R}{2}\cos(\theta_m) \tag{1.1}$$

where R_{av} is the average resistance of the spin torque oscillator, ΔR is the total change in resistance for a device. The instantaneous value of the resistance is determined by the difference in the orientations of the magnetization $\vec{\mathrm{m}}_{fixed}$ of the fixed layer and $\vec{\mathrm{m}}_{free}$ of the free layer. This difference is given by θ_m, which is the relative angle between the two magnetization orientations, the maximum angular difference achieved in oscillations is called as the angle of precession. So the maximum resistance change is determined by the total resistance change possible and the angle

of magnetization precession. The output power for the spin torque oscillation driving a load resistance R_L is given as:

$$P_{out} = \frac{I^2 \Delta R^2 R_L \cos(\theta_m)^2}{8(R_{av} + R_L)} \tag{1.2}$$

where I is the DC bias current applied to the STO to generate the spin-polarized electrons. The frequency of oscillation f_o for the spin torque oscillator having small precession angle is given by the Kittel formula:

$$f_o = \frac{\gamma}{2\pi}[(H_{app} - H_{dip} + H_{an})(H_{app} - H_{dip} + H_{an} + H_{demag}^{eff})]^{1/2} \tag{1.3}$$

where H_{app} is the external applied magnetic field, H_{dip} is the dipole field experienced by the free layer, H_{an} is the in-plane shape based anisotropy field, H_{demag}^{eff} is the effective demagnetization field which depends on the orientation of the magnetization, and material property of the free layer and γ is gyromagnetic ratio of the electron in free layer. The value of the gyromagnetic ratio divided by 2π for the typical materials used in spin torque oscillators is of the order of 28 GHz/T. Thus, a small change in the effective field seen by the free layer can cause a large change in frequency output.

1.1.1 Types of spin torque oscillators

Spin torque oscillators come in a variety of geometries and use different phenomena for their functioning and implementation. On the basis of their geometry, the spin torque oscillators are broadly classified as nanocontact or nanopillar (Figure 1.2)[8]. In nanocontact devices, multiple magnetic layers and spacers are sputtered, and the device is formed out of a narrow contact area for injecting current into the films [9]. Initially, devices with this geometry were implemented by using a

mechanical point contact to the multi-film layer stack (Figure 1.2(a)), but then lithographically defined contacts through insulating layers have been used to build nanocontact based STO (Figure 1.2(b)). In nanocontact devices, only the area of the current generation is limited by the small area of the contact while the magnetic films are continuous over a large area. A different geometry of device patterns the entire stack of magnetic films including the contact and spacer films to nanopillar geometry (Figure 1.2 (c)). In this type of spin torque oscillator, not just the contact but the free and fixed magnetic layers are patterned into circular or elliptical shaped nanomagnets, whose size and dimensions are defined using a combination of e-beam lithography and ion milling. As all the current in nanopillar, geometry flows through entire the device stack, the amplitude of current needed for exciting oscillation is much smaller than the nanocontact geometry. Where a significant portion of the current gets shunted into the

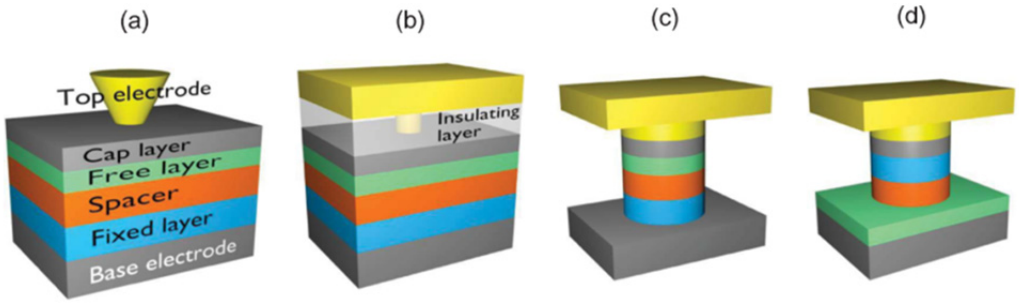

Figure 1.2: Types of spin torque oscillators based on their geometry. (a) Point-contact STO uses a mechanical contact to sputter deposited stack of films forming the STO. (b) Nanocontact STO uses lithographically defined ~10 nm^2 contact to form an electrical connection. (c) Nanopillar geometry where the entire stack of films including the magnetic layers are lithographically patterned to form a vertical nanowire. (d) Hybrid geometry where some of the films are patterned. Adapted from [8].

first magnetic layer. Both these geometries of devices can be combined to form hybrid devices in which one or more films are patterned, while rest of the film stack is not patterned. Typically, the output power of the nanocontact based devices is lower for a similar amplitude of current than the nanopillar devices, because they have smaller magnetoresistance change. However, recently hybrid nanocontact devices with tunneling barriers have been demonstrated with 46% resistance change and a resultant high power oscillation of 2 μW [10]. The nanopillar-based devices typically have larger linewidths compared to the nanocontact devices. This due to their small size, which makes them are more susceptible to thermal fluctuations. The patterning process, used to form the nanopillar geometry, introduces fabrication defects, which results in the formation of non-uniform edge states and results in larger linewidths [11].

The spin torque oscillators use a variety of materials with different magnetic properties in them. By the magnetization orientation, an STO can be classified as in-plane, out-of-plane and hybrid. In-plane devices have the magnetization of the free and fixed layers in the plane of the films and perpendicular to the direction of current flow. These devices typically have low output power, as the angle of precession for in-plane magnetization is small. They also usually need an external bias magnetic field to excite oscillations. Out-of-plane devices have the magnetization of the fixed and free layer out of the plane of the films and along the direction of electron flow. These devices typically have large output power as the angle of precession in these devices can be very large. They also can function in the absence of external magnetic fields [12]. Hybrid orientation devices use a combination of in-plane free/fixed layer with out-of-plane fixed/free layer and even use tilted free layers. These devices, which have been demonstrated with large output powers, operate with low or zero external applied field are more complex to realize and fabricate [13].

Spin torque oscillators can be differentiated based on the physical phenomenon used for their read out. If the spacer material between the fixed and the free layer magnet is non-magnetic metal, the magnetoresistance change is due to the giant magnetoresistance effect. These types of devices are referred to as spin valves and have smaller output power because of the total resistance change, ΔR, is small, typically less than 10%. If the spacer material is made of non-conducting oxide, such that the spin current flow is due to electron tunneling, the magnetoresistance change is due to the tunnel magnetoresistance effect. These types of devices are referred to as magnetic tunnel junctions and are most commonly built using the nanopillar geometry. The output power of MTJ devices is typically much larger than spin valves because, ΔR is large, typically greater than 50% [14]. Another way to differentiate spin torque oscillators is based on the physical phenomenon used to generate spin polarized electrons, which impart the torque to the free layer magnetization causing its steady-state precession. Traditionally and as we described, the spin-polarized electrons are generated by flowing the electric current through the fixed layer magnet, where the spin-transfer effect reorients the electron moment to make it parallel to the fixed layer magnetization. Recently, spin torque oscillators have been demonstrated which use the spin Hall effect for generation of spin current [15]. This method of spin generation, when implemented with the right combination of materials, is shown to be much more energy efficient than the traditional spin transfer method [16].

Spin torque oscillators can be further classified depending upon the modes of excitation- whether they are uniform or non-uniform and localized or non-localized. For the purpose of this thesis, we are interested in uniform precession modes where we can consider the entire magnetization of the free layer to behave in a uniform way and for which a macrospin description holds true. Other forms of modes that have

interesting characteristics are out of the purview of this thesis. More details on them can be found in work by Chen *et al.* [8].

1.1.2 Applications of spin torque oscillators

Due to their small form factor, sensitivity to external magnetic fields, ease of integration with CMOS processing, and their inherent non-linearity spin torque oscillators have been proposed for multiple applications. The primary application that is also the focus of this thesis is the use of spin torque oscillators as wideband tunable and easily integrated signal sources. When compared to other tunable signal sources, STOs are extremely fast devices that can be turned on and off quickly. STOs outperform voltage controlled oscillators (VCO) and dielectric resonator based oscillators (DRO) in their tuning range (Figure 1.3). YIG tunable oscillators (YTO) are the only sources that can match STOs in the frequency tuning range, but these oscillators have a large size and require high power. When comparing the cost of manufacturing, STOs outperform all other devices as they are batch fabricated. STOs require lower power than both DROs and YTOs and their power consumption is comparable to the VCOs. The only area where STOs fall behind compared to other tunable oscillators is their noise performance. STOs have been measured to have phase

Type	Tuning range	Phase noise @100 kHz offset when operating at 10 GHz	Switching speed	Size (inch cube)	Cost	Power consumption*
VCO [240]	Octave	-110 dBc/Hz	1 μs	0.001	Low	Low
YTO [240]	Decade	-120 dBc/Hz	1 ms	1	High	High
DRO [240]	1 %	-120 dBc/Hz	N/A	0.5	Medium	Low
STNO	Multi-octave	~-72 dBc/Hz to ~-55 dBc/Hz @1 MHz offset [118]**, [201], [205], [207]	1 ns	1×10^{-16}	Low	Low

* The power consumption in this case represents only the power consumed by the microwave oscillator.
** Data obtained from a vortex based STNO and extracted from figures.

Figure 1.3: Comparison between spin torque oscillators and other tunable oscillator technologies. Adapted from [8].

noise in the range of -72 dBc/Hz to -55 dBc/Hz at 1 MHz offset from the carrier, which is a very large phase noise when compared to -110 dBc/Hz or less observed at 100 kHz offset for other tunable oscillator technologies.

Spin torque oscillators have been demonstrated as microwave detectors; in this, they use what is called the spin torque diode effect present in MTJ devices. When a microwave frequency is close to the ferromagnetic resonance of one of the magnetic layers, the AC current due to the microwave frequency excites oscillation in the MTJ. The microwave current mixes with the spin torque oscillations to generate a DC voltage signal whose amplitude is proportional to the input power of the microwave signal [17]. STOs as microwave detectors have shown to detect signals as low as 10 nW [18].

Due to their ability to mutually phase lock and show frequency synchronization [19], similar to the behavior of neurons and synapses, spin torque oscillators have been proposed for neuromorphic computing [20]. Spin torque oscillators have also been proposed for non-Boolean associative computing where their oscillating outputs are used as weights in a physical neural network to carry out image recognition, signal detection, or deep learning operations, which are time-consuming to perform using traditional computing approaches [21].

Spin torque devices can leveraging their output frequency dependence on the external magnetic field for large magnetic field detection and have shown a high sensitivity of 180 GHz/T [22]. This technique is different from the traditional use of magnetoresistance for field detection [23] because it is independent of the signal amplitude and signal to noise ratio, but depends on the frequency of oscillation. The sensitivity of the frequency-based detection of magnetic fields is dependent on the accuracy in detecting the oscillation frequency of the spin torque devices and is thus limited by the linewidth of the device for detecting small magnetic field changes.

STOs have an advantage over other traditional field sensors as their nanoscale dimensions results in good addressability in detecting fields from high-density magnetic media like hard disk drives.

Apart from the above-mentioned applications spin torque oscillators have been proposed to be used for AC magnetic field generation during oscillations, random number generation using telegraphic switching and for spin wave generation for applications in the upcoming field of magnonics.

1.1.3 Limitations of spin torque oscillators

Due to the small size of the spin torque oscillators, they are extremely susceptible to temperature fluctuations and thermal noise. In an auto oscillator system like spin torque oscillators the linewidth $\Delta\omega$ at given frequency is given as:

$$\Delta\omega = \Delta\omega_o \frac{\mathrm{k}_B T}{\mathrm{E(p)}} \tag{1.4}$$

where $\Delta\omega_o$ is the intrinsic linewidth of the oscillator, $\mathrm{k}_B T$ is the Boltzmann constant times the temperature T which represents the thermal energy acting on oscillation and $E(p)$ is the energy of the oscillation mode [24]. As the oscillation mode energy in the spin torque oscillators is small, the linewidth is large. Micromagnetic simulations have shown that cooling the spin torque oscillator to cryogenic temperatures can reduce the STO linewidth with temperature, but experimental measurements have found that the linewidth reduction saturates at a temperature of 100 K and further cooling doesn't decrease the STO linewidth further [25]. This means the limitation to spin torque oscillators linewidth due to geometric defects and edge states is significant and determines the limits of reducing the linewidth in a free-running device. This is somewhat verified by the narrow linewidth observed in the nanocontact devices where

the oscillation mode is protected from edge states due to the continuity of the magnetic films compared to the nanopillar geometry based spin torque oscillators. Additional noise is generated due to spatial inhomogeneity during film deposition or growth. This results in non-uniform current injection, which causes spatially varying modes in the nanomagnet of slightly different frequencies leading to an overall broadening of its linewidth. Spin torque oscillators are not just an auto-oscillator but they are non-linear auto-oscillators and hence, their oscillation frequency is correlated with oscillation power. Due to the strong correlation, it has been predicted [26] and observed [27] that the amplitude variations in the spin torque oscillator couple back into frequency fluctuations, adding significantly to the phase noise of the oscillator.

Along with large the linewidth, frequency hopping has also been observed for spin torque oscillators [28]. For spin torque oscillators to be used as signal sources, their oscillation frequency needs to be stable over a large period of time, but mode hopping in spin torque oscillators from one frequency to another results in decoherence of the oscillator frequency. Multiple modes are more commonly observed in nanopillar-based STOs due to the roughness of the edges in fabrication, resulting in separate edge and center mode excitations. When multiple modes are observed the linewidth of the oscillator is usually broadened due to the loss in phase as the STO hops from one mode to another and back. In the nanocontact based spin torque oscillators, mode hopping and frequency jumping is observed at the high drive current, whose onset is observed by linewidth broadening.

The low power of the spin torque oscillator we know already contributes to its poor noise performance, but is also presents a challenge for its adoption as a technology. The typical output power of the spin torque oscillator is in the range of few nanowatts to picowatts. The output power depends upon their readout mechanism and the mode of excitation. The highest peak output power for GMR-based devices is

25.7 nW measured for out of plane oscillations [29] while the highest output power for TMR devices is measured to be 2 μW for a hybrid nanocontact based MTJ device [10]. Device designs for reducing the average resistance are crucial for getting high output power when connecting to low impedance loads. For MTJs type of spin torque oscillators, this means fabricating devices with extremely thin tunnel barriers while having large TMR to allow large current flows. In GMR devices, high output power is achieved by using highly spin-polarized Heusler alloys for magnetic materials which show a large magnetoresistance change.

1.1.4 Injection, mutual and self-locking of spin torque oscillators

Experiments have demonstrated that the broad linewidth and the frequency instability of the spin torque oscillators can be overcome by applying an external signal to the spin torque device [30]. This method of locking the device to an external signal is commonly called as injection locking. When injected by external signal above a threshold of power, dependent on the mode of oscillation, the frequency of the spin torque oscillator locks to the external frequency [31]. In current injection locking experiments, Rippard *et al.* [32] showed that, when locked, the spin torque oscillator linewidth reduces significantly and it takes the noise characteristics of the externally injected signal. Injection locking of the spin torque oscillators has also been observed by applying AC magnetic fields, and they showed similar characteristics as the current injection locking. By injecting an external signal with narrow linewidth and good phase noise performance, we can stabilize the spin torque oscillator and improve its phase noise.

Mutual locking of spin torque oscillators by spin wave coupling has demonstrated similar effects of enhancement in the linewidth as well increase in the output power due to phase matching between the two oscillators [19]. In this experiment, two

nanocontact based spin torque oscillators were fabricated on continuous magnetic films and their combined outputs were measured on a spectrum analyzer. When the oscillation frequencies of the oscillators were tuned to the same frequency, the output observed on the spectrum analyzer showed decreased linewidth at the common oscillation frequency. The output power increased by phase matching of the two oscillators was significantly more than the sum of the powers of the individual oscillators. This is due to the effect of injection locking with phase matching between the individual oscillators, which was indicated by the dependence of the output power on the phase of the individual oscillators, even when they are locked to each other. This method of improving both the linewidth and the oscillation power is very attractive for spin torque oscillators as unlike injection locking it doesn't require an external AC signal. The challenges in extending this system have been in increasing the area of spin wave coupling to couple multiple spin torque oscillators and in fabricating a large number of oscillators close to one another. Even after more than a decade of experimentation, the highest number of oscillators that have been demonstrated to be mutually phase-locked is only five [33]. Additionally, the linewidth improvement in the mutually locked spin torque oscillator, though significant, is limited by the natural linewidth of the individual spin torque devices and its stability susceptible to temperature changes.

A novel method for improving the phase noise and frequency stability in auto-oscillator systems has been proposed by Slavin *et al.* [34]. They observed in simulations that when the output of the auto oscillator, when fed back to the device via filter or a delay line, could substantially reduce the linewidth of the device. This type of locking of an oscillator to its signal is called as self-locking or delayed self-locking. The reduction in linewidth they observed is dependent upon the delay, the amplifier gain, and the oscillator's phase. This theory for a general auto oscillator was extended

for the case of spin torque oscillator having vortex oscillation modes by Khalsa *et al.* [35]. In their numerical simulation, they observed that the linewidth of the oscillator could be decreased by as much as 4 times when the oscillator is injection-locked with some delay to its own input without additional gain. The first experimental measurements of the effect of delayed feedback for a small amplitude of delay showed a reduction in the linewidth by 60% for a delay of 35 ns [36]. This was observed for no additional gain applied in feedback. The linewidth reduction in self-injection locked oscillators can be further enhanced with amplification of the signal before feedback, such that amplitude of the signal is high enough to injection lock the device. Kumar *et al.* recently implemented self-injection locking with amplified signal in presence of delay line [37]. In their experiments, they saw an extremely coherent microwave signal with linewidth less than 200 kHz at 2.5 GHz frequency, compared to an open loop signal where they see linewidth as large as 50 to 100 MHz. The equation of the linewidth, dependent on the loop delay in the self-injection locked auto oscillator system by Kumar *et al.*, was given as:

$$FWHM = \frac{\alpha kT}{4\pi p_o(1-p_o)S}\left(1+\left(\frac{\lambda}{\lambda+p_o\omega_f}\right)^2 v^2(1-p_o)^2\right)\frac{1}{(1+\omega_f\Delta t(1-p_o))^2} \quad (1.5)$$

Where λ is the dynamic damping factor, v denotes dimensionless frequency shift with respect to the amplitude of oscillations given by p_o, α is the Gilbert damping constant, and Δt is the delay of the loop. We can thus see that the linewidth ($FWHM$) of the oscillator is inversely proportional to the amplitude of the oscillation power and the delay in the feedback loop. By increasing the delay in the self-locking loop, we can decrease the linewidth of the oscillator further for a given amplitude of oscillation.

This delayed self-locking of the oscillator using a gain stage is another form of a delay-line oscillator. In various delay-line oscillator systems, a similar inverse dependence of phase noise on the loop delay has been observed, where for a given power level, adding more delay in the feedback improves the phase noise. This has experimentally been observed and implemented in spin-wave delay line oscillators [38] and in optoelectronic oscillators [39]. Even in ring oscillator circuits a decrease in phase noise for a given output power with increasing delay was measured [40]. Delay-line-based self-locking is a useful technique for improving the linewidth and the phase noise of spin torque oscillators. It's more advantageous compared to injection locking because it is independent of an external signal source needed for locking the signal and only relies on the delay and gain for self-locking. Compared to mutual phase locking, the self-locking technique doesn't suffer from complex requirements for fabrication, can be made more resistant to temperature fluctuations and has a potential to scale to multiple spin torque oscillators, if they all are self-locked via a common delay line feedback path.

1.2 *MEMS resonator based locking of spin torque oscillators*

Spin torque oscillators, we learned, are ideal candidates for a variety of application including magnetic field sensing, neuromorphic computing and most prominently for gigahertz frequency tunable oscillators. The biggest challenge they need to overcome for the wide-scale adaptation is to increase their frequency stability and reduce their linewidths, to improve their phase noise performance. The linewidth and frequency stability can be best enhanced by self-locking the spin torque oscillator with a large delay in a feedback system. MEMS resonators, due to their small form factors and large quality factors, can be the ideal devices used to provide long delays at gigahertz frequencies.

MEMS resonators have been used in oscillators as signal sources for communication and timing applications [41]. They have been integrated with CMOS electronics for multiple applications like gyroscopes [42], accelerometers [43], oscillators [44] and filters [45]. The application space for MEMS resonators is large due to their high quality factors, which when used in oscillators, translates to excellent phase noise performance. The high quality factor of the MEMS resonator results in a substantial delay when the resonator is considered as a delay element. The relation between delay and quality factor for a resonator having frequency ω_m is given as:

$$\Delta t = \frac{2 \times \mathrm{Q}}{\omega_{\mathrm{m}}} \tag{1.6}$$

where, Δt is the effective delay due to a resonator with quality factor Q. So, the higher the quality factor of the device, the more is the effective delay it represents. Typical MEMS resonators have been demonstrated with quality factors greater than 1000 at a frequency of 3.4 GHz [46]. The effective delay for such a MEMS resonator is 0.5 μs. This is about 80 times the delay observed in the delay based self-locked spin torque oscillator demonstrated by Kumar *et al.* [37]. Thus, a MEMS resonator when connected in feedback with a self-locked spin torque oscillator can provide a large quantity of delay and will filter the frequency output of the STO, increasing the $\Delta f_o / f_o$ ratio of the closed loop system to reduce the linewidth of the oscillator. In such a system, the high quality factor of the MEMS resonator sets the linewidth of the spin torque oscillator and results in a low phase noise oscillation output (Figure 1.4). We call this hybrid system, combining the magnetic spin torque oscillators and acoustic MEMS resonators, as a magneto-acoustic oscillator.

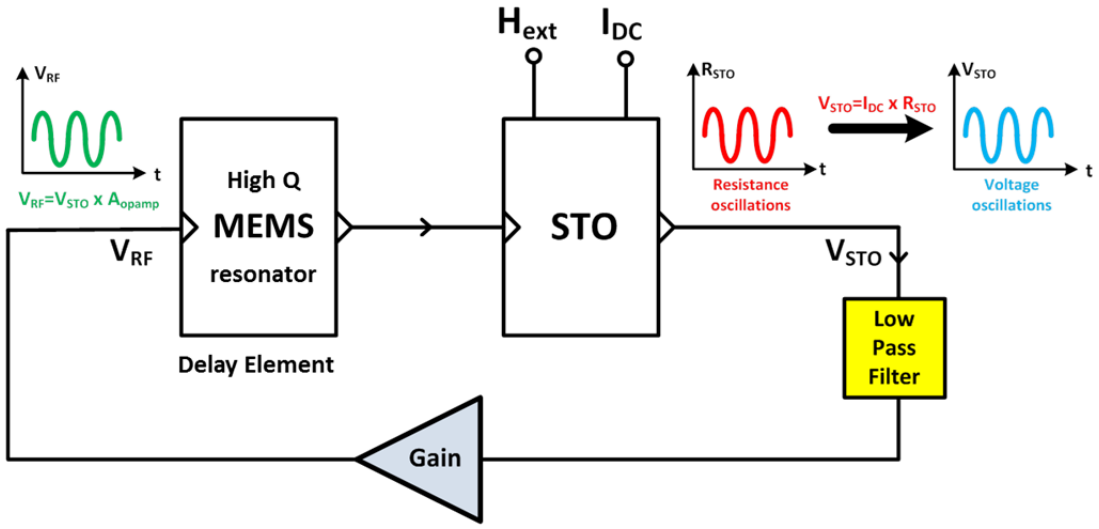

Figure 1.4: Magneto-Acoustic oscillator where self-locking of spin torque oscillator is implemented using high quality factor MEMS as a delay element to improve the linewidth of the oscillator. In a traditional electrical circuit picture, this is represented as a MEMS resonator which filters the output of the spin torque oscillator and feeds it back to injection lock it and thus improves its linewidth.

1.3 *Dissertation outline*

This thesis presents results about the improvement in the linewidth of spin torque oscillators, by coupling them to high quality factor MEMS resonators. Contributions in each of the following chapters towards that goal have been summarized below.

High-overtone bulk acoustic resonators

In Chapter 2, we present work on high-overtone bulk acoustic resonators, which are ideal candidates for the role of MEMS resonators in the magneto-acoustic oscillator, due to their multiple high quality factor resonances across a broad

bandwidth of frequencies. We present work on fabricating, characterizing and analyzing their performance for their role in the building magneto-acoustic oscillator.

Acoustic strain-based locking of spin torque oscillator

In Chapter 3, we discuss using strain as the feedback mechanism for implementing magneto-acoustic oscillator. We show how strain can interact with spin torque oscillator and how this mechanism can be implemented by doing macrospin modeling of a spin torque oscillator in presence of AC strain. We do a realistic estimation of the amplitude of strain needed to see locking in spin torque devices. We also do an estimate of the efficiency of this strain based magneto-acoustic oscillator and compare it to a current based magneto-acoustic oscillator.

Spin valve devices for magneto-acoustic oscillators

In Chapter 4, we characterize and measure spin valve devices made out of CoFeGe/CoFe and Terfenol-D based free layers as spin torque oscillators needed to implement the magneto-acoustic oscillator. We do locking measurements on the spin valve oscillators to characterize the amplitude of a signal necessary to see injection locking for implementing current based magneto-acoustic oscillator. We couple the spin valve oscillator to HBAR in open loop configuration to show a reduction in linewidth and improved noise performance of the spin torque oscillators. We perform measurements on a closed loop current based magneto-acoustic oscillator and discuss the challenges in their successful implementation.

Spin Hall effect-MTJs for switches and magneto-acoustic oscillators

In Chapter 5, we fabricate and characterize spin Hall effect employing magnetic tunnel junctions as a candidate for the spin torque oscillators in magneto-acoustic oscillators. We show an implementation of the SHE-MTJ coupled to HBAR in an open loop configuration that shows promising improvement in linewidth of SHE-MTJ. We also fabricate and characterize the performance of SHE-MTJs as switches and

demonstrate bi-directional high-speed switching at sub10 ns time scale. We further study the effect of scaling SHE electrode compared to the MTJ size and make observations regarding the suitability of SHE-MTJs as MRAM bit cells.

Summary and Future work

In Chapter 6, we discuss issues faced in implementing magneto-acoustic oscillator and summarize significant results achieved in this thesis. We then discuss future directions for implementing a novel microwave feedback based magneto-acoustic oscillator and also propose a new fabrication process flow that will make the strain based magneto-acoustic oscillator implementation much more efficient.

CHAPTER 2

HIGH-OVERTONE BULK ACOUSTIC RESONATORS

2.1 *Introduction*

Film Bulk Acoustic Resonators (FBAR) have become a standard component in cellular systems as filters [47] and are even being employed as gigahertz frequency oscillators used for sensing and timing applications [46]. These devices leverage the recent developments in high quality thin piezoelectric film sputtering for pushing the frequency into the multi-gigahertz frequency range. FBARs have high electromechanical efficiency and high quality factors, which results in large bandwidth and sharp roll off when used as filters. When used as oscillators, this leads to narrow linewidths with excellent phase noise performance [48]. The advantage of FBARs in filter or oscillator comes from their design which suppresses spurious modes and allows for only one single thickness expansion mode over a large bandwidth. For the purpose of our application to make tunable signal sources, we need a resonator that provides FBAR like performance but at several frequencies over a wide bandwidth. Such a resonator, with multiple usable resonant frequencies and high quality factors, was first demonstrated by Lakin *et al.* [49]. High-overtone bulk acoustic resonators (HBARs) consist of a piezoelectric film acting as a transducer to generate a standing wave resonance in a several wavelengths thick substrate (Figure 2.1). In other words, it is an FBAR mounted on a low loss acoustic substrate, where the acoustic substrate acts as a resonant cavity. Lakin *et al.* demonstrated HBARs at 1 to 1.6 GHz frequency range as they were limited in the scaling of thickness and in the quality of the piezoelectric film [49].

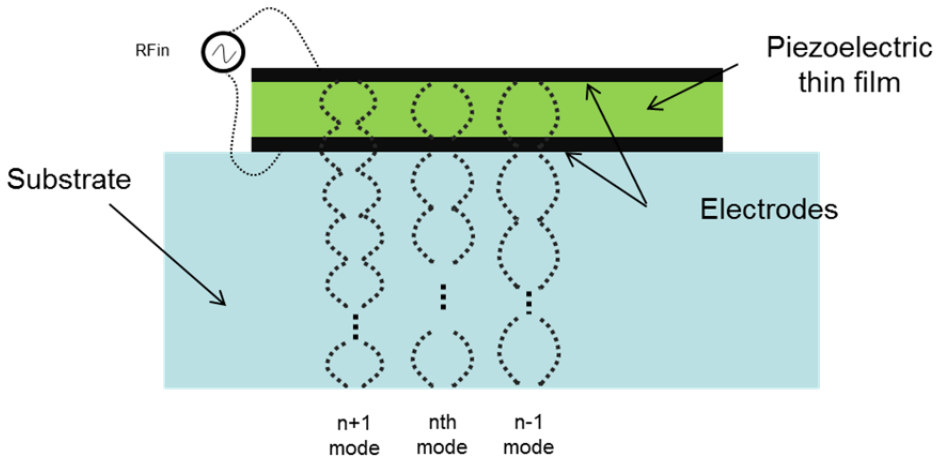

Figure 2.1: Example of an HBAR resonator shows a piezoelectric thin film sandwiched between drive electrodes solidly mounted on a substrate which acts as an acoustic cavity.

The quality factor of HBAR has been demonstrated to be very high, nearing the viscoelastic limit of the substrate [50]. The quality factor depends on the acoustic losses in the substrate and the piezoelectric film, the smoothness of the substrate surface and its flatness. Only a fraction of the mode volume is in the piezoelectric film, while most of the energy is stored in the substrate. Hence, the losses in the substrate dominate the quality factor of the HBAR. Resonances occur at frequencies where the total resonator thickness is a multiple of the half wavelength given by the fundamental mode of the substrate. The spacing between the resonant frequencies Δf is the frequency of the fundamental thickness mode f_o of the substrate given by:

$$\Delta f = f_o = \frac{c_{lsub}}{2t_{sub}} \tag{2.1}$$

where c_{lsub} is the longitudinal wave velocity in the substrate and $t_{sub}$is the thickness of the substrate. The efficiency of driving and picking of resonant modes over a given frequency range is dependent on the resonant frequency of the piezoelectric film which is given by:

$$f_p = \frac{c_{lpiezo}}{2t_{piezo}} \tag{2.2}$$

where c_{tpiezo} is the longitudinal wave velocity in the piezoelectric film and t_{piezo} is the thickness of the piezoelectric film.

In this chapter, we are going to study the HBAR in two different configurations. First, HBAR as a 1-port device, which can be used as a stress generator in a scheme for acoustic strain based locking, is described in Chapter 3. Secondly, HBAR can be used as a 2-port multi-frequency filter which can be utilized for filtering the AC signal generated by spin torque oscillator and for building a current based magneto-acoustic oscillator system, which is described in detail in Chapter 4.

2.2 *1-Port HBAR as a strain generator*

MacQuarrie *et al.* were first to demonstrate acoustically mediated spin-state control of nitrogen-vacancy (NV) centers in diamond using HBAR as a stress generator [51]. In their system, using HBAR, they launched stress waves into the diamond substrate, where these stress waves interacted with the ground state spin triplet of an NV center causing spins to change their state from $m_s = |+1\rangle$ to$|-1\rangle$. They further demonstrated complete, coherent control of the quantum states by driving Rabi oscillations between $|+1\rangle$ to $|-1\rangle$ spin states [52]. In a similar approach, an HBAR can be used to apply AC stress to the free layer of a spin torque oscillator. Using this AC stress, the HBAR can lock the spin torque oscillator at the frequency of

the applied stress. To understand the limits of HBAR as a stress generator in silicon, and compare its performance in high quality acoustic materials like silicon carbide and diamond, we fabricated HBARs on all these substrates and measured quality factor as a function of temperature from 80 K to room temperature at multiple resonant frequencies for each sample. The quality factors measured were then used to estimate the maximum stress generated for a given drive at an anti-node inside the wafer, using a 1D analytical model of an HBAR.

2.2.1 1-port HBAR design and fabrication

2.2.1.1 HBAR simulation in Comsol

To design the HBAR effectively in silicon, we developed a 2D axisymmetric model of HBAR in Comsol FEA solver. The model assumed the quality factor of 2000 for resonant frequencies in a range of 3-4 GHz. This frequency range was picked to match the oscillation frequencies of the CoFeGe/CoFe spin valves shown in Chapter 4. In the model, we used c axis oriented aluminum nitride (AlN) as the piezoelectric material having a thickness of 1.5 μm. AlN piezoelectric film is sandwiched between 200 nm platinum as the bottom electrode and 200 nm aluminum as the top electrode. The size of the simulated devices is 75 μm radius on a 500 μm thick silicon substrate. Using the frequency domain analysis, we were able to extract the admittance spectrum for HBAR (Figure 2.2(a)) showing multiple resonance peaks in the 3-4 GHz frequency range. At the resonant frequency of 3.385 GHz, we simulated the displacement in the HBAR (Figure 2.2(b)), where we see the HBAR mode showing alternate bands of expansion and compression along the depth into the silicon substrate. We were also able to extract the stress generated over the depth into the silicon substrate by the HBAR driven by a 1 V peak signal (Figure 2.3). Stress up to an amplitude of 3.3 MPa can be generated at anti-node for a quality factor of 2000.

The stress is observed to be periodic over the thickness and its period matches the wavelength of the acoustic wave.

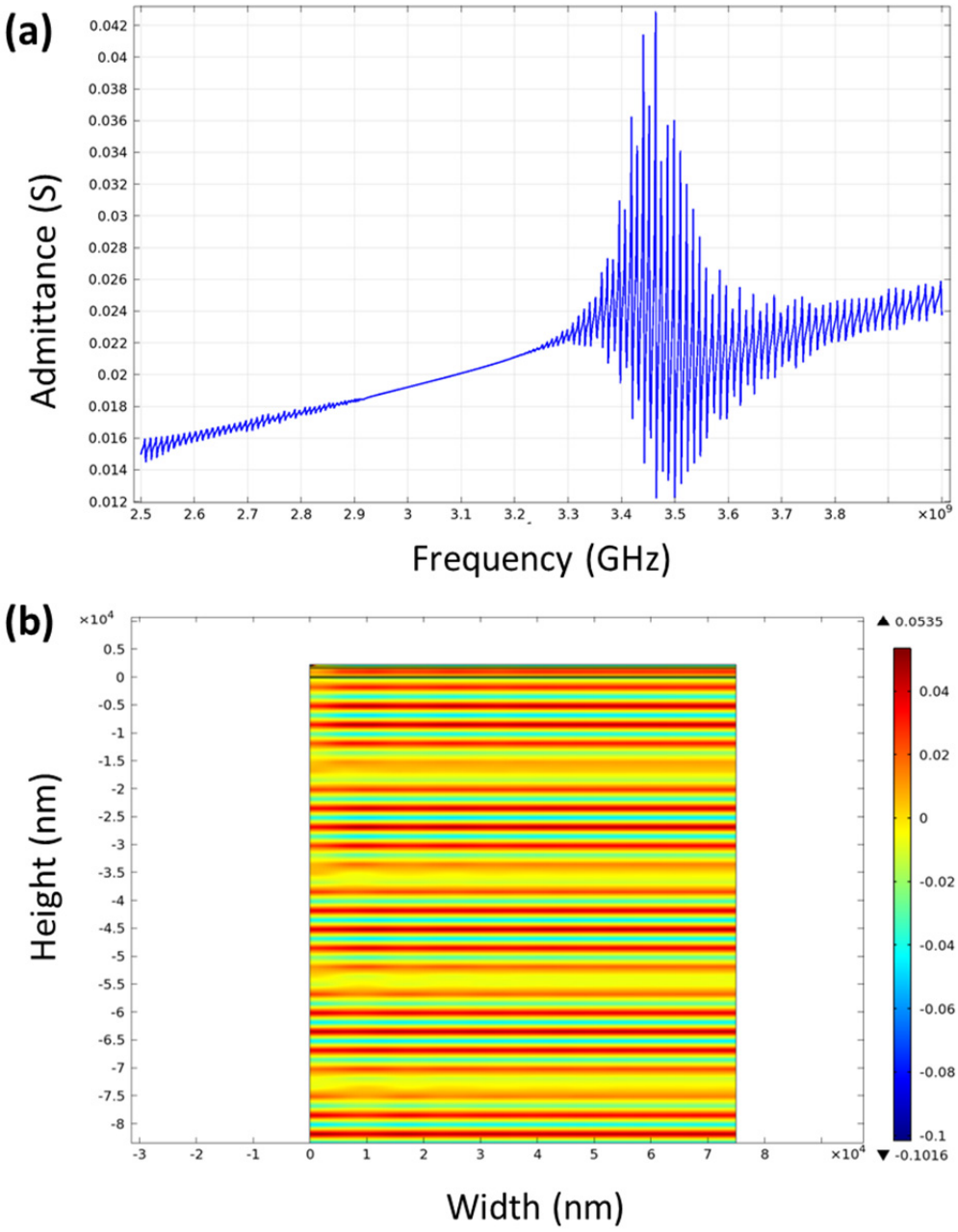

Figure 2.2: Comsol simulation of HBAR with a silicon substrate. (a) Admittance as a function of frequency shows multiple resonances. (b) Displacement over the depth of HBAR shows red areas of expansion and blue-green areas of compression.

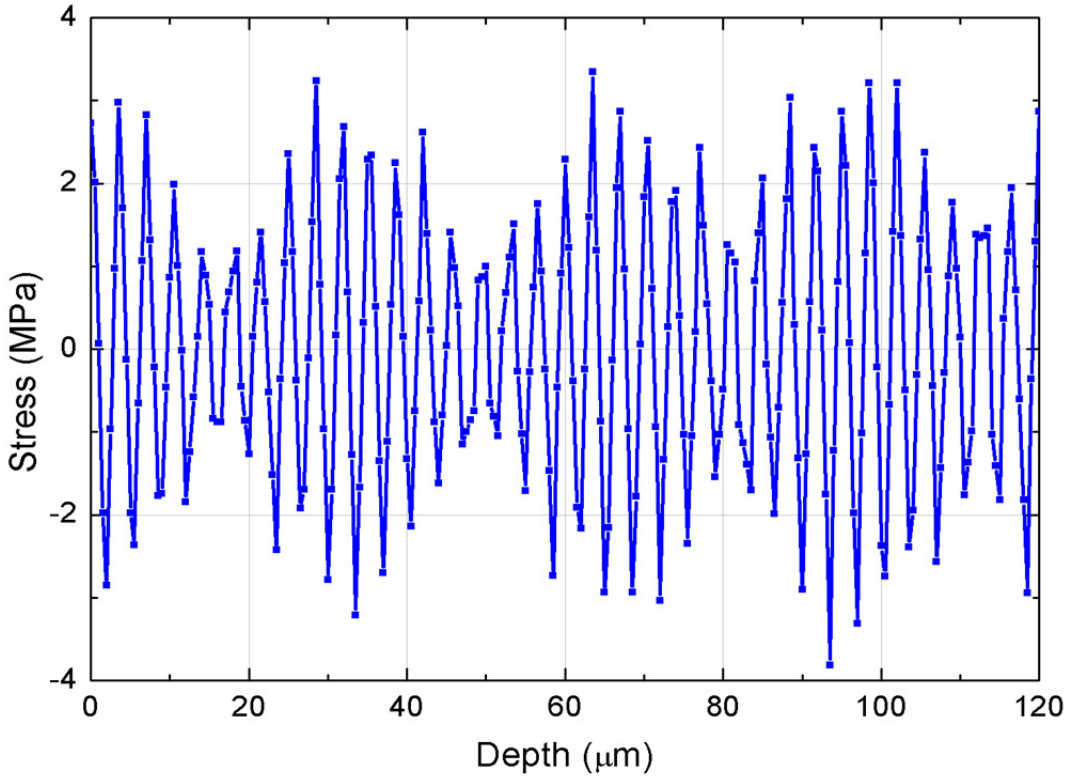

Figure 2.3: Stress generated by HBAR in the silicon substrate due to 1 V drive at 3.385 GHz. We can observe the periodic nature of the stress standing wave into the depth of the substrate.

2.2.1.2 Fabrication of HBAR on Silicon and Silicon Carbide substrate

Silicon and silicon carbide are ubiquitous semiconductor materials that are readily available in wafer sizes. Hence the process flow for both these HBARs is similar. Silicon HBARs were fabricated on 4-inch, 500 μm thick, <100> oriented double side polished (DSP) high resistivity substrates. In fabricating silicon carbide HBARs, we used double side polished 8º of <1120> 3-inch wafers made of a 4H polytype of SiC. Fabrication process flow for HBARs starts with LPCVD deposition of 200 nm thick low-stress silicon nitride the DSP wafers (Figure 2.4 (a)). Silicon nitride ensures there

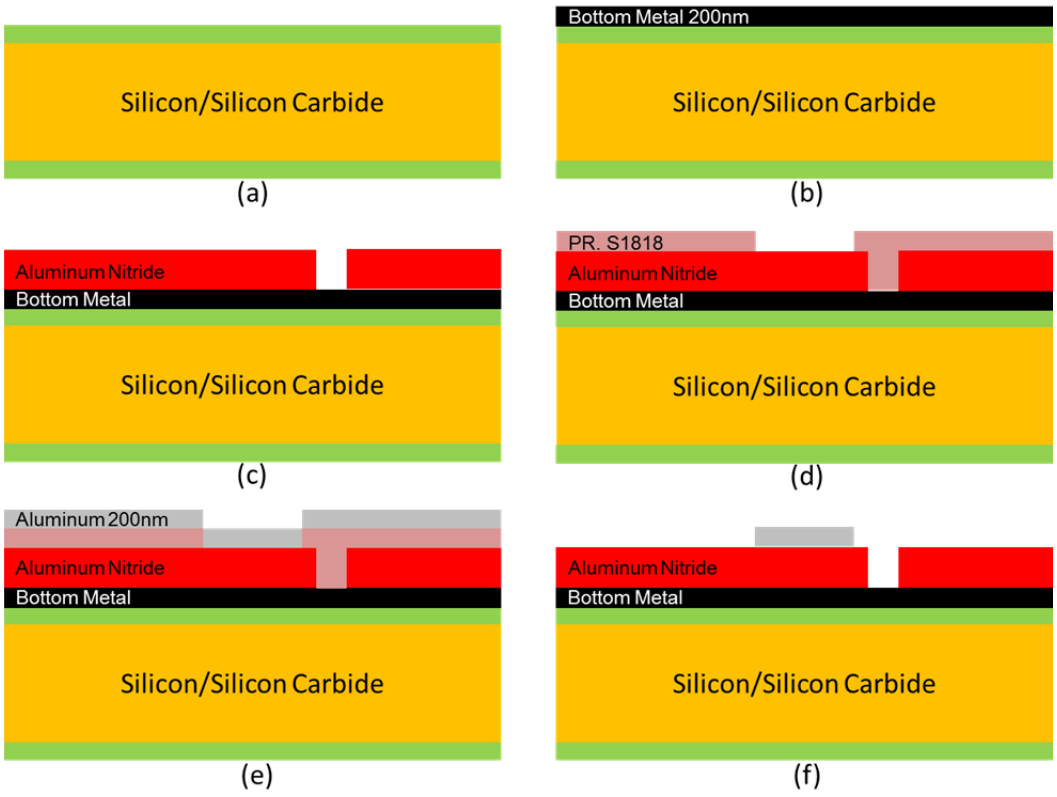

Figure 2.4: Fabrication process flow for silicon and silicon carbide HBAR

is no shorting between the devices on silicon or SiC substrates. This is followed by sputtering 200 nm thick bottom metal (Figure 2.4(b)). Platinum is used as the bottom metal for silicon and molybdenum is used for silicon carbide. We then perform XRD measurements to ensure the bottom metal has <111> lattice orientation. This is needed for the columnar growth of <200> AlN on the bottom metal. 1.5 µm thick AlN is deposited by reactive-ion sputtering at 400ºC (Figure 2.4(c)). Rocking curve measurements are performed to ensure the AlN has good piezoelectric properties. FWHM of 1.5º was measured on the silicon wafer while FWHM of 1.2º was measured on the SiC wafer. AlN is then etched using a photo resist mask in phosphoric acid heated to 160ºC, to open via for making contact to the bottom metal. AlN gets etched

by TMAH, which is a common ingredient in the developers used in photolithography. To avoid using TMAH, we used TMAH free developer like CD-30 which works efficiently with positive photoresist like S1818. An aluminum electrode of 200 nm thickness is e-beam evaporated and is pattered by resist liftoff to form the silicon and SiC HBARs (Figure 2.4(f)). Scanning electron micrograph of a 250 µm radius silicon device shows all the components of the HBAR (Figure 2.5).

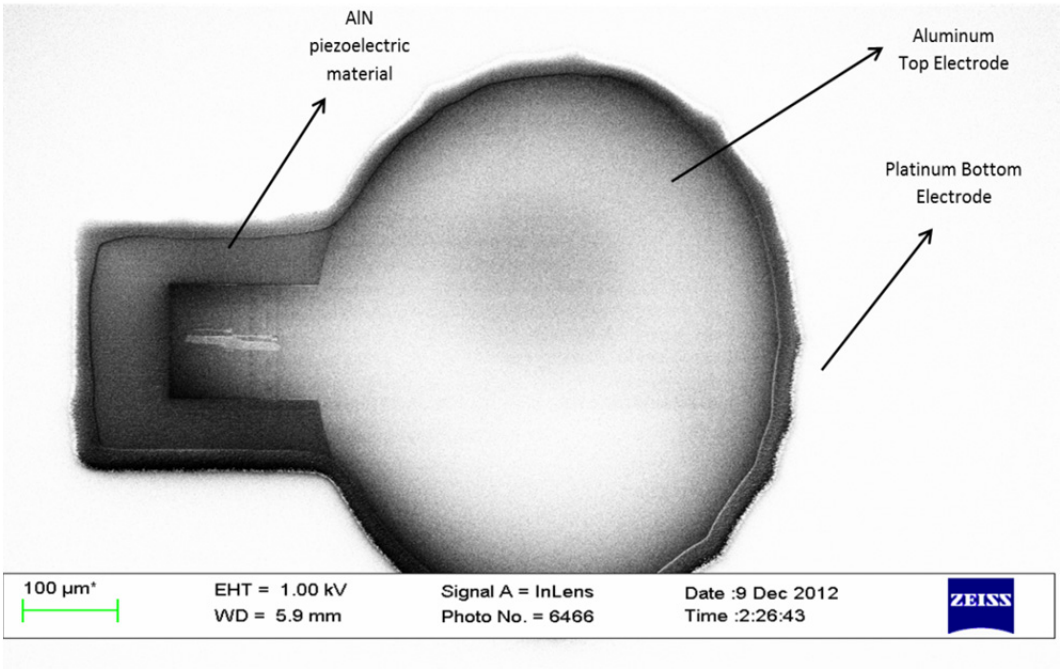

Figure 2.5: Scanning electron micrograph of 250 µm radius HBAR have 1.5 µm thick AlN piezoelectric layer fabricated on 500 µm thick silicon substrate.

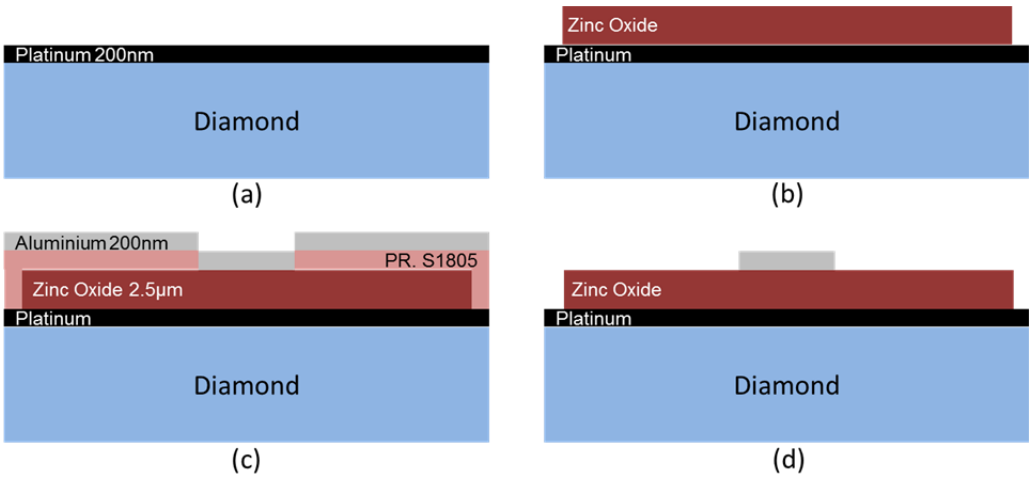

Figure 2.6: Fabrication process flow for diamond HBAR.

2.2.1.3 Fabrication of HBAR on Diamond substrate

The diamond substrate used in making HBARs is a 300 μm thick chip, oriented along the <100> direction. These chips are commercially available, synthetic single crystal type IIA CVD grown diamonds from Element Six Corporation. Because the diamond surface is nonconductive, the bottom platinum electrode can be directly sputtered on the surface without need for a spacer like silicon nitride. The fabrication process flow starts with sputtering 200 nm thick platinum as the bottom metal on the diamond surface (Figure 2.6(a)). We then perform XRD measurements to ensure the platinum is <111> lattice oriented. <111> oriented platinum is needed for the columnar growth of <200> zinc oxide (ZnO) which is used as the piezoelectric material for diamond HBAR. 2.5 μm thick ZnO is then reactive-ion sputtered on the bottom platinum electrode (Figure 2.6(b)). During ZnO deposition, we use a shadow mask on the diamond chip to ensure access to platinum electrode for testing; this helps us avoid an additional ZnO etching step. An S1805 photoresist is spray coated on the diamond chip and is then pattered using contact lithography (Figure 2.6(c)). Spray coating is necessary as the diamond chips are 3 mm × 3 mm in size and face issues

with spinning resist of uniform thickness. An aluminum electrode of 200 nm thickness is e-beam evaporated and then patterned by liftoff to define the top electrode to form the diamond HBAR (Figure 2.6(d)).

2.2.2 Device characterization

1-port HBAR devices are measured with the top electrode being the signal port and the bottom electrode acting as the ground plane. The characterization setup for HBARs consists of a LakeShore vacuum probe station, with the capability to accurately control the temperature of the device under test from 80 K to 295 K and an Agilent N5230A parametric network analyzer (Figure 2.7). During the measurement, cable and probe parasitics were de-embedded from measured signal using calibration substrates. S_{11} measurements performed using the network analyzer, are used to extract device admittance Y_{11} using Equation (2.3) where Zo is 50 Ω. The admittance versus the frequency spectra lets us know accurately the mechanical resonance (series resonance) frequency, which cannot be measured directly from the S_{11} data. Quality factor of resonances of interest are then calculated from the measured spectrum, using the Q circle method developed by Feld *et al*. [53].

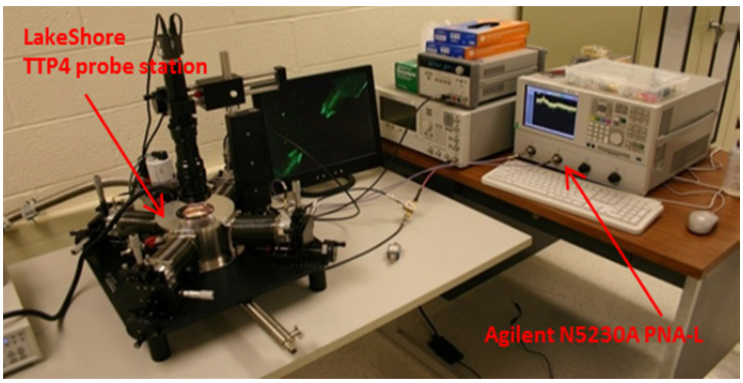

Figure 2.7: Device characterization setup for measuring S_{11} of the HBAR.

$$Y_{11} = \frac{(1 + S_{11})}{Zo \times (1 - S_{11})} \tag{2.3}$$

2.2.2.1 Admittance measurements of Silicon HBAR

Admittance spectrum from 75 µm radius device on silicon substrate measured at room temperature showed resonances over 0.5 GHz to 4 GHz frequency range. With a

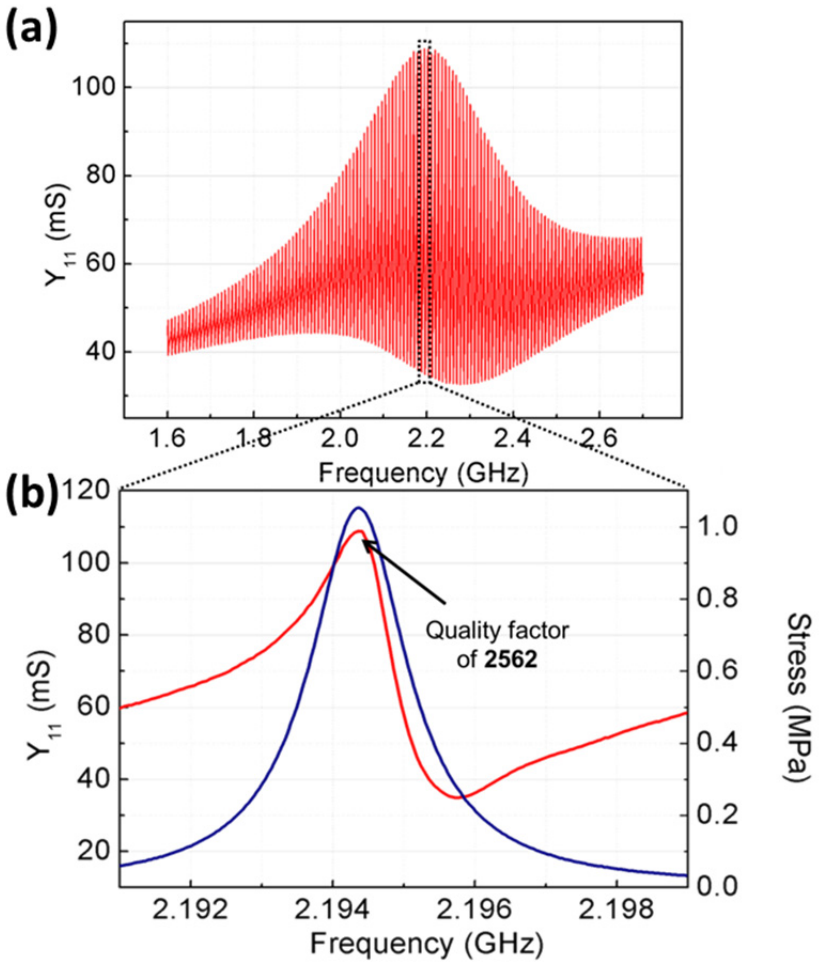

Figure 2.8: (a) Admittance versus frequency of 75 µm radius silicon HBAR. (b) Quality factor 2562 of a single resonance at 2.194 GHz and the associated maximum stress generated due to 1 V peak drive at the resonance frequency.

set of resonances at 2.2 GHz (Figure 2.8(a)) and another set of resonances around 3.4 GHz (Figure 2.9(a)). The quality factor of the 2.194 GHz mechanical mode was measured to be 2562 (Figure 2.8(b)), while that of the 3.38 GHz mode was measured to be 1054 (Figure 2.9(b)). Similar measurements were done on 250 µm radius SiC HBAR and 250 µm radius diamond HBAR to extract their admittance spectra and quality factors. The quality factor multiplied by frequency f-Q product was then calculated for resonances over a range of frequency to compare their performance to Silicon HBAR.

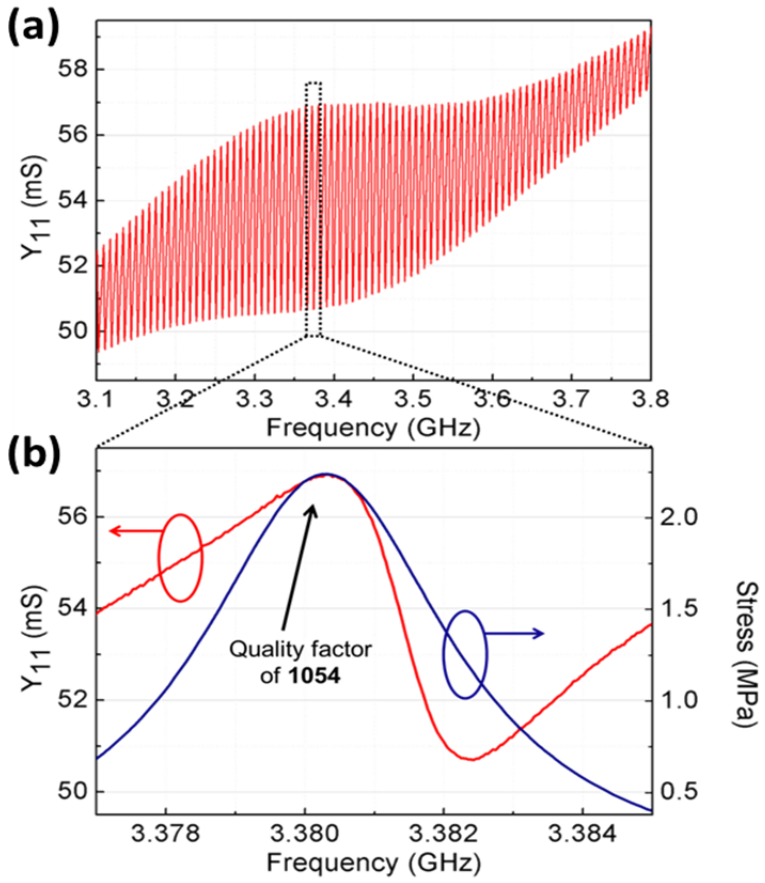

Figure 2.9: (a) Admittance versus frequency of 75 µm radius silicon HBAR. (b) Quality factor 1054 of a single resonance at 3.38 GHz and the associated maximum stress generated due to 1 V peak drive at the resonance frequency.

2.2.2.2 f-Q product measurements from 80 K to room temperature

The LakeShore probe station (Figure 2.7) was used to cool the silicon devices down to 80 K and measurements were performed up to the room temperature of 295 K. Quality factor was measured for different resonances at each temperature step. These measurements were then repeated on SiC and diamond devices. The f-Q products in silicon were studied for 1 GHz, 2.23 GHz, and 3.02 GHz resonance. In SiC, we measured the f-Q product of resonances at 592 MHz, 1.1 GHz, 3.2 GHz and 3.4 GHz. In the diamond HBARs, we measured the f-Q products of resonances at 530 MHz and 1.45 GHz. To compare the f-Q products to the theoretical limits of resonator performance, we benchmark them to the phonon-phonon damping values adopted from Tabrizian *et al.* [54]. There are two major frequency dependent phonon-phonon damping based loss mechanisms: Akheiser and Landau-Rumer. The Akheiser mechanism dominates at low frequencies, and its range is limited to 700 MHz in silicon, where the wavelength of the acoustic mode is larger than the mean free path of the phonons. In this mechanism, the maximum achievable f-Q product is constant for longitudinal waves; so, as the frequency increases the quality factor decreases inversely. The Landau-Rumer mechanism is dominant at high frequencies, where the phonon mean free path is smaller compared to the wavelength of the acoustic mode. In such a scenario, three-phonon interactions are the dominant phonon loss mechanism. Hence, the maximum achievable f-Q product increases linearly with frequency. These regions of dominance by the Akheiser damping or the Landau-Rumer damping are demarcated by frequencies which are dependent on the thermal phonon relaxation lifetimes in the materials.

The f-Q product for silicon was measured to be 2.4×10^{12} Hz at room temperature for 1 GHz resonance, 3.7×10^{12} Hz for the 2.23 GHz and 2.1×10^{12} Hz for the 3.02 GHz resonance (Figure 2.10(a)). These values, though large, are one order of magnitude

smaller than the theoretical limit at room temperature. At 160 K, the f-Q product increased to 5.9×10^{12} Hz for 1 GHz, 5.1×10^{12} Hz for 2.23 GHz and 4.8×10^{12} Hz for the 3.02 GHz mode (Figure 2.10(b)). Cooling silicon HBAR to 80 K, the f-Q product further increased to 1.2×10^{13} Hz for 1 GHz, 1.17×10^{13} Hz for 2.23 GHz and 1.57×10^{13} Hz for 3.02 GHz mode (Figure 2.10(c)). The SiC HBAR had the highest measured f-Q among the three materials at all the resonant frequencies as its theoretical f-Q product is also the highest. Compared to its theoretical limits, the SiC HBAR had f-Q product lower by more than an order of magnitude. The diamond HBAR had the lowest f-Q product among the three materials, with the f-Q product being two orders of magnitude lower than the theoretically predicted limits.

$$Q = T^{-a_T} \tag{2.4}$$

To understand what might be the dominant loss mechanism in these different HBARs, we plot the quality factor as a function of temperature, of one resonance in the Landau-Rumer damping regime for each of the substrates. We observe that the silicon HBAR and SiC HBAR quality factors scale rapidly as the temperature drops, while the quality factors of diamond HBAR quality factor increases very slightly (Figure 2.11). Fitting the quality factor (Q) to temperature (T) using Equation (2.4), where a_T shows the temperature scaling temperament of the HBAR. a_T was calculated to be 1.556 and 1.472 for SiC and silicon HBAR respectively. When a_T is 0, it means that the quality factor doesn't scale with temperature and the dominant loss mechanism is anchor loss, which is temperature independent. Now, with high values for a_T, we can say that in silicon and SiC HBARs anchor loss, which is energy lost to the substrate boundaries, isn't the dominant loss mechanism. In diamond HBAR, the

value of a_T was calculated to be 0.376, implying that anchor loss is much more dominant in the diamond HBAR compared to other materials.

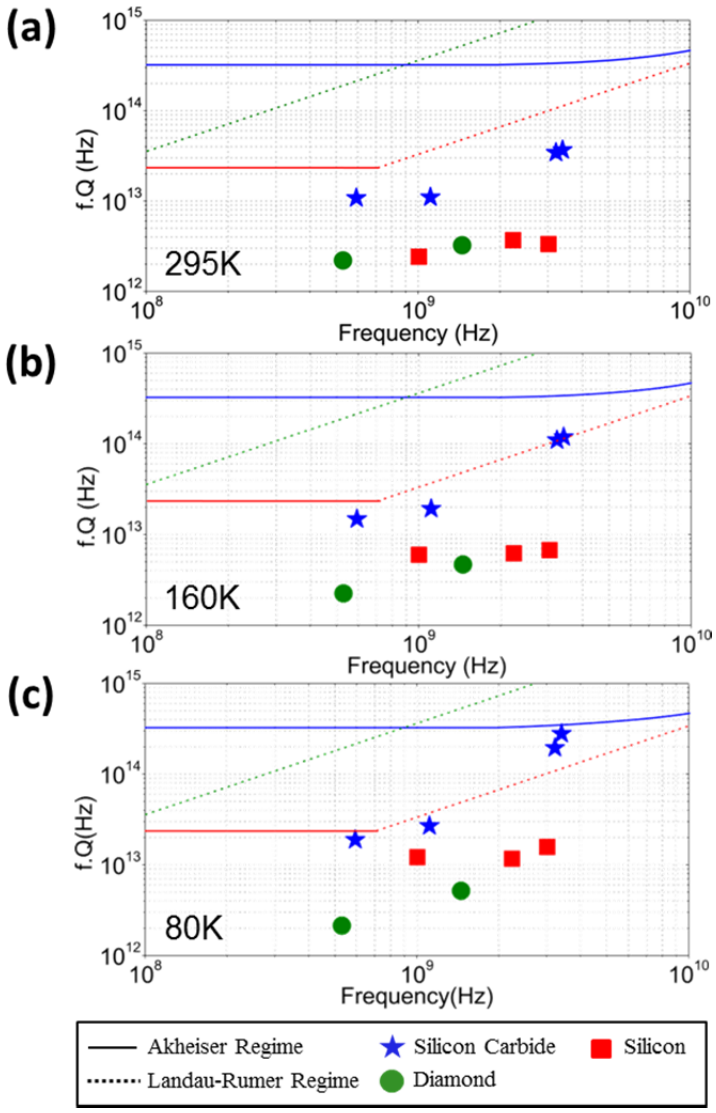

Figure 2.10: f-Q product vs. frequency of HBAR measured at temperatures (a) 295 K, (b) 160 K and (c) 80 K. Data points on the plots represent measured resonances of silicon (red), diamond (green) and SiC (blue) HBARs. The lines on the graph represent the two different phonon-phonon dissipation limited f-Q product calculated for materials at room temperature.

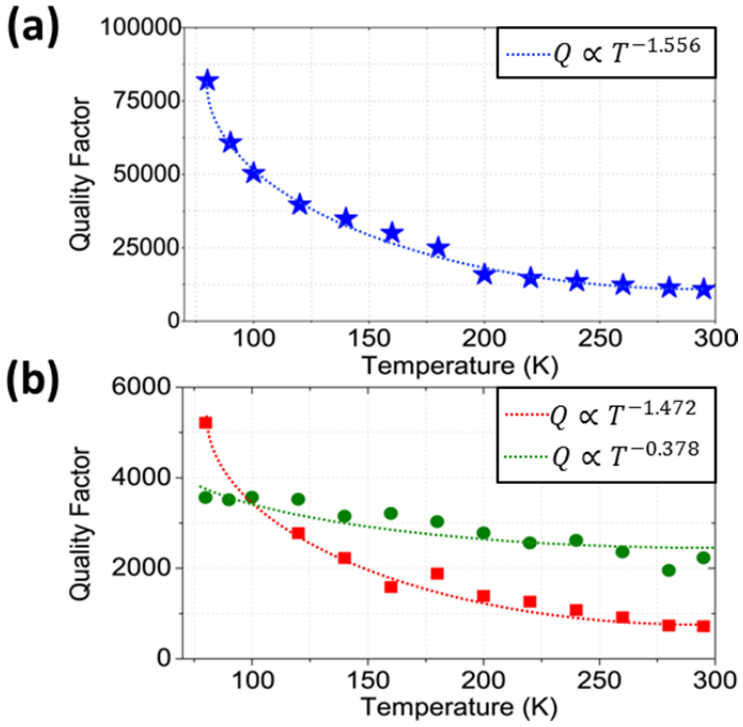

Figure 2.11: Quality Factor vs. Temperature. (a) 3.4 GHz mode of SiC HBAR in blue shows quality factor scaling from 10,800 at 295 K to 82,000 at 80 K. (b) 3.02 GHz mode of the silicon HBAR in red shows quality factor scaling from 720 at 295 K to 5220 at 80 K. 1.45 GHz mode of the diamond HBAR in green shows quality factor scaling from 2232 at 295 K to 3564 at 80 K. The trend lines represent fits to Equation (2.4).

2.2.3 Analytical model for Stress generated by HBAR

Understanding the limits and electrical performance of the HBAR devices, we want to translate these values into the mechanical performance as the 1-port HBAR is meant to be used as stress generator [55, 56]. Mathematically, we can calculate the stress generated in an HBAR into the depth of substrate (Z direction) using a 1D model for a piezoelectric transducer (Figure 2.12).

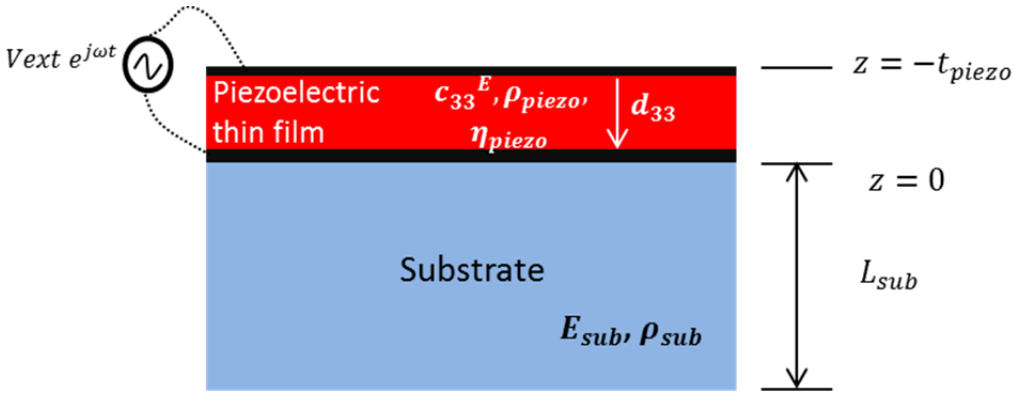

Figure 2.12: Material and dimensional parameters used for analytical model of stress generated by HBAR

Longitudinal stress (T_z) and displacement current (D_z) due to application of an AC voltage of amplitude V_{ext} in Z direction on a piezoelectric film is described by constitutive equations:

$$T_z = c_{33}{}^{E} S_z + e_{33}\, d\emptyset/dz \tag{2.5}$$

$$D_z = \epsilon_{33}{}^{E}\, E_z + e_{33} S_z \tag{2.6}$$

where $\emptyset[z,t]$ is the potential across the piezoelectric layer, S_z the strain in Z direction, E_z is the electric field, c_{33} is the stiffness coefficient, e_{33} is the piezoelectric coefficient and $\epsilon_{33}$is the dielectric permittivity of the piezoelectric layer. The HBAR as a stress transducer can be modeled using the equation of motion given by:

$$\rho \frac{\partial^2 u_z}{\partial t^2} + \eta_{piezo} \frac{\partial u_z}{\partial t} = c_{33}{}^{E}\left(1 + k_{33}{}^{2}\right) \frac{\partial^2 u_z}{\partial z^2} = c_{33}{}^{D} \frac{\partial^2 u_z}{\partial z^2} \tag{2.7}$$

where u_z is the displacement along the Z direction at any point in the resonator. η_{piezo}, which is the damping of this resonator is inversely proportional to the quality factor (Q) of the resonator and is given by:

$$\eta_{piezo} = \rho_{piezo}\omega/Q \tag{2.8}$$

k_{33} which accounts the effect of applied electric potential to the displacement caused by the piezoelectric layer, is given by:

$$k_{33}{}^2 = e_{33}{}^2/\in_{piezo} c_{33}{}^E \tag{2.9}$$

We assume quasistatic condition and that there are no free carriers in the piezoelectric film, by applying conditions :

$$\nabla \cdot D = 0 \tag{2.10}$$

$$E_z = -\nabla \cdot \emptyset[z,t] \tag{2.11}$$

to displacement current (Equation (2.6)) gives us as a second order differential equation relating the potential $\emptyset[z,t]$ to the local displacement u_z:

$$\frac{\partial^2 \emptyset}{\partial z^2} = \frac{e_{33}}{\in_{piezo}} \frac{\partial^2 u_z}{\partial z^2} \tag{2.12}$$

We guess the solution to this differential equation is of the form:

$$\emptyset[z,t] = \left\{\frac{e_{33}}{\in_{piezo}} u_1[z] + A1\ z + A2\right\} e^{jwt} \tag{2.13}$$

where $A1$ and $A2$ are constants and $u_1[z]$ is the displacement in the piezoelectric layer. For resonant solutions, we can further assume that the displacements in the piezoelectric layer $u_1[z]$ and the substrate $u_2[z]$ are of the in form of standing waves and are described as:

$$u_1[z] = C1\sin(\gamma_{piezo}\ z) + C2\cos(\gamma_{piezo}\ z) \tag{2.14}$$

$$u_2[z] = C3\sin(\gamma_{Sub}\ z) + C4\cos(\gamma_{Sub}\ z) \tag{2.15}$$

Where $C1$, $C2$, $C3$ and $C4$ are constants and γ is the wave number in the piezoelectric layer and substrate is given by:

$$\gamma = \sqrt{(\rho\omega^2 - i\omega\eta/E)} \tag{2.16}$$

Substituting the solutions to the differential equation in Equation (2.5), we can calculate the stress generated in the piezoelectric layer (T_1) and in the substrate (T_2) as:

$$T_1[z] = {c_{33}}^D\ {u'}_1[z] + A1\ e_{33} \tag{2.17}$$

$$T_2[z] = E_{sub}\ {u'}_2[z] \tag{2.18}$$

We have six constants $A1$, $A2$, $C1$, $C2$, $C3$ and $C4$ which when plugged into Equation (2.17) and Equation (2.18) give us a value for stress generated at a particular depth of the resonator for a given frequency, quality factor and applied voltage. These constants represent complex relations between the material properties, inputs to the resonator and its performance. To calculate the closed form values, we apply six boundary conditions to the resonator. Two of the boundary conditions are given by the free surfaces at the top of the piezoelectric and the bottom of the substrate, where the stress T_1 and T_2 go to zero. Then we have continuity conditions at the interface of the piezoelectric transducer and the substrate stating that stress and displacement are continuous across the interface. This implies that the stress T_1 in the piezoelectric layer and T_2 in the substrate have the same value at the interface. The continuity condition also applies to the displacement u_1 in the piezoelectric layer and u_2 in the substrate being equal at the interface. Lastly, we have two more boundary conditions due to the known input drive signal. We know that the potential at the top electrode is the drive signal V_{ext} and that the potential at the ground plane goes to 0. Applying the boundary conditions, we get solutions to all the assumed constants, whose values are shown in Chapter 7.1.

We get some key insights from the analytical model, observing the effect of drive signal, quality factor and material of the HBAR on the maximum stress that can be generated. We observe that the stress is proportional to the amplitude of the drive signal and the stiffness of the substrate and scales linearly with it even to large values. While with quality factor, we observe that though initially at low quality factors the stress increases proportionally with the quality factor, it soon begins to saturate as quality factors becomes arbitrarily large. This is non-intuitive as a key resonator principle states that the displacement (thus strain and stress by relation) scales as a

multiple of the quality factor. This effect was also verified by doing simulations in Comsol, where we observed stagnation in the amplitude of stress as the quality factor was increased to large values (Figure 2.13). Plugging in the material properties, geometric sizes and the measured quality factors in the analytical model, we calculated the maximum stress generated for various substrates as shown in Table 2.1. We observe that the silicon HBAR at 3.02 GHz with a quality factor of 720 can generate 2.20 MPa of stress. When the quality factor increases to 5220, the amplitude of stress produced increases to 2.90 MPa.

Table 2.1: Stress generated by HBAR for a 1 V drive

HBAR Material	Stress at 295 K	Stress at 80 K
Silicon -3.02 GHz	2.20 MPa	2.90 MPa
Diamond -1.45 GHz	1.43 MPa	1.51 MPa
Silicon Carbide -3.40 GHz	4.05 MPa	6.15 MPa

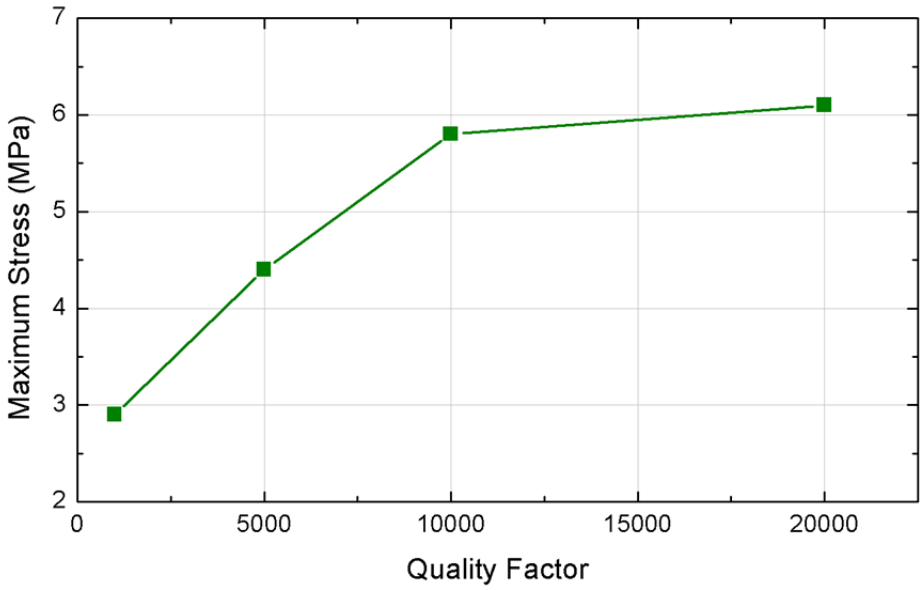

Figure 2.13: Maximum stress generated versus quality factor extracted from simulation of 1-Port HBAR in Comsol.

2.3 *2-Port HBAR as a multi frequency filter*

HBARs, we showed in the previous section have capability to provide very high quality factor resonances at gigahertz frequencies. HBARs can thus have potential to be utlized as filters or as resonant elements for frequency generation in gigahertz oscillators, when mutiple devices are connected in a network. A more direct approach to use HBAR as resonant element in electric circuits demands a two port configuration. Recently, laterally coupled HBAR have been shown as two port resonant elements, allowing them to be diretly used as series filters in microwave frequency circuits [57]. The challenge of these devices have been scaling them to high gigahertz frequencies range while having low transmission loss. Reinhardt *et al*. in [58] showed that frequency of operation can be extended to 2-5 GHz range by using two HBARs made of thin film piezoelectric AlN on saphhire, placed close to each other. Sapphire is used for having low acosutic losses and enhancing the mechanical coupling between the two HBAR. In this configuration, one HBAR acts as input port while the other acts as output port. Electrical signal from the input port is mechanically coupled through the substrate via the HBAR resonance modes to the electrical pickoff of the output port. These devices show low transmission losses in the range of -15 to -25 dB at 4-5 GHz frequencies. Reinhardt *et al.* demonstrated that the magnitude of transmission loss is dependent on the spacing between the two laterally coupled ports. As the gap between the ports increases, the mechanical coupling between the two resonant elements decreases and the transmission loss increases. Transmission loss is also dependent on the acousitc material, with high quality acoustic materials like sapphire having lower losses as compared to silicon.

2.3.1 Laterally coupled HBAR design and fabrication

2.3.1.1 Comsol simulation of laterally coupled HBAR

To design the laterally coupled HBAR effectively, we developed a 2D axisymmetric model of the device in Comsol FEA solver. In the model, we have two 1-port HBAR devices separated by 5 μm gap placed on a common sapphire substrate. The model assumed the quality factor of 3000 for resonant frequencies in the range of 4-8 GHz, which is typical for sapphire having an f-Q product of 1×10^{14} Hz. This frequency range was picked to match the oscillation frequencies of the CoFeGe/CoFe spin valves discussed in Chapter 4. In the model, we used c axis oriented AlN as the piezoelectric material of 600 nm thickness. AlN piezoelectric film is sandwiched between 100 nm platinum as the bottom electrode and 100 nm thick aluminum as the top electrode. The size of the simulated devices is 25 μm radius for the input port and 15 um radius ring for the output port on a 500 μm thick sapphire substrate. Using the frequency domain analysis, we were able to extract the admittance spectrum for HBAR (Figure 2.14(a)) showing multiple resonance peaks in the 4-8 GHz frequency range. At one of the resonant frequency of 5.21 GHz, we simulated the displacement in the HBAR (Figure 2.14(b)), where we see the alternate bands of high expansion and compression in the areas underneath the input port electrode on the left side through the depth of the sapphire substrate. We also notice the weaker displacement amplitudes from underneath the gap between two electrodes and under the output port electrode on the right side. We were able to extract the electrical signal transmission from port one to port two shown by S_{21} versus frequency spectra (Figure 2.15), where we observe multiple resonance peaks over entire frequency range. The peaks are spaced by uniform gap, which is given by Δf as shown in Equation (2.1). The

simulated transmission losses for laterally coupled HBAR are about -20 dB to -40 dB range.

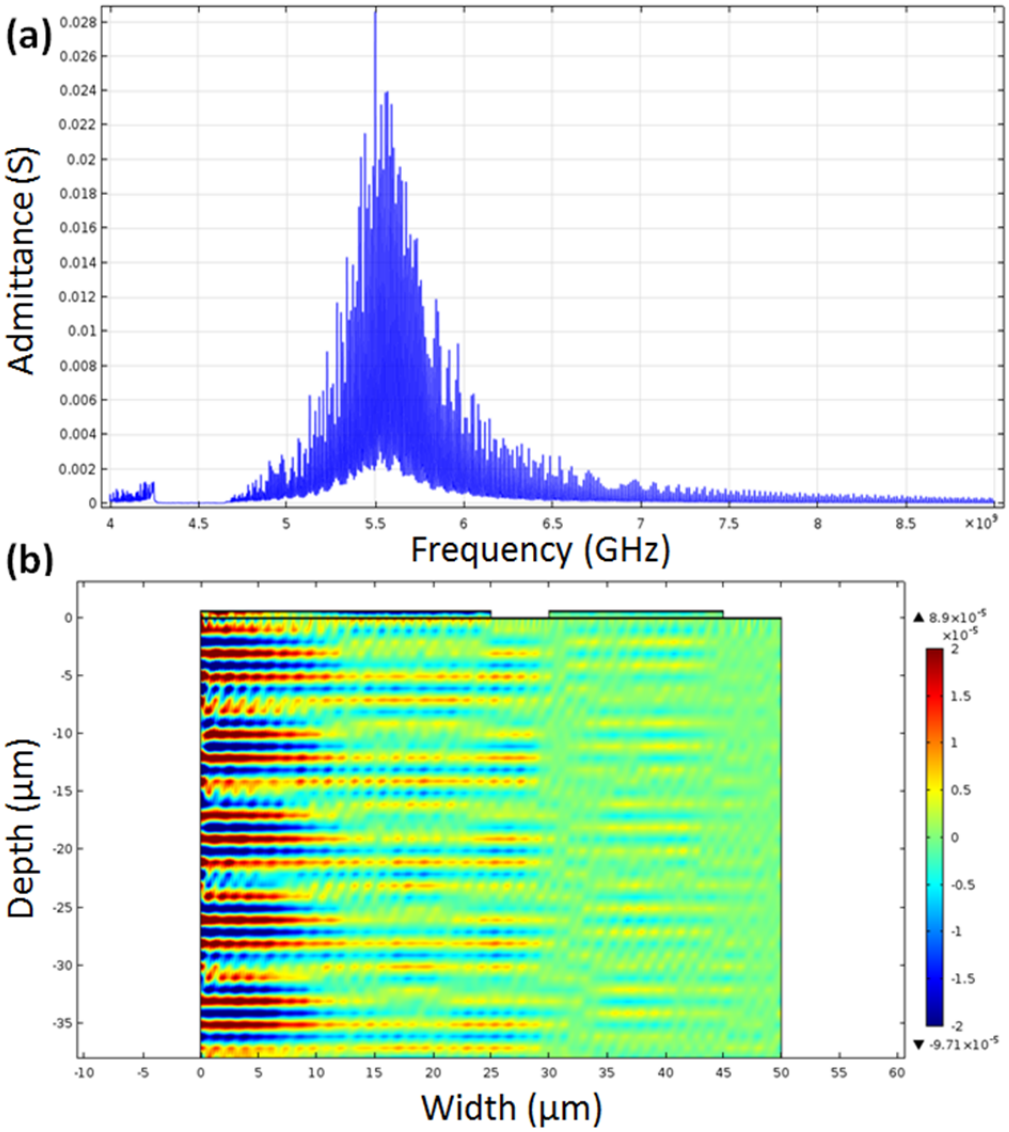

Figure 2.14: Laterally coupled HBAR on sapphire substrate simulated in Comsol. (a) Admittance in Siemens as a function of frequency in GHz shows multiple resonances. (b) Displacement in nanometers over the depth of HBAR shows red areas of expansion and blue area of compression as mechanical energy is coupled from input port on the right to output port on the left.

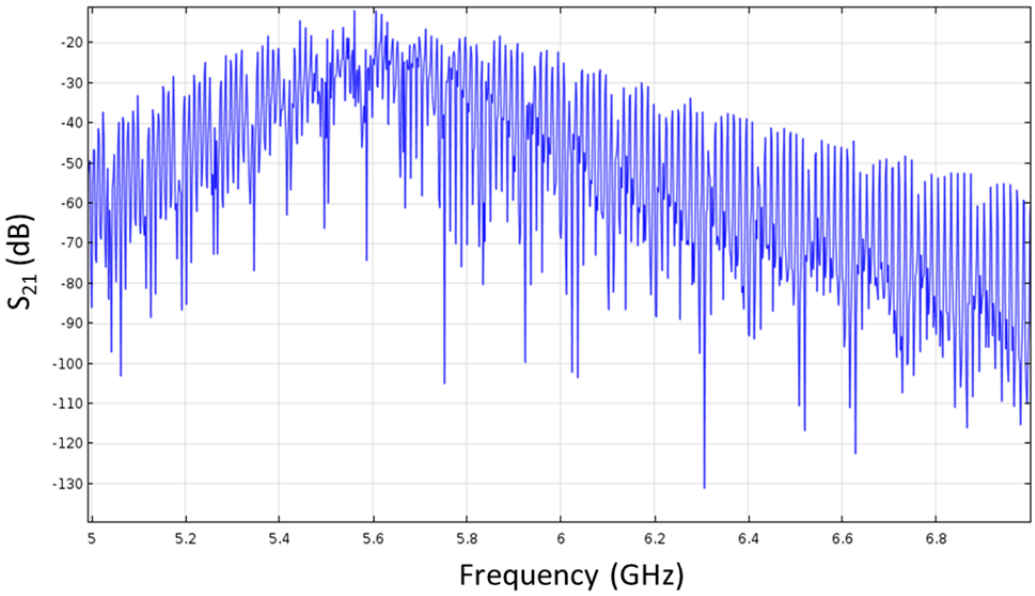

Figure 2.15: S_{21} versus frequency extracted from Comsol simulation of laterally coupled HBAR on a sapphire substrate. Multiple resonances spaced by frequency Δf are observed over the frequency range of 5 GHz to 7 GHz with transmission losses in the range of -20 dB to -40 dB.

2.3.1.2 Fabrication of laterally coupled HBAR

C-plane (0001) oriented sapphire wafers were used for fabricating laterally coupled HBARs. We preferred wafers of 300 µm thickness to have a frequency spacing of 20 MHz between resonances due to lack of availability, we used 650 µm thick, double side polished 4-inch sapphire substrate. Fabrication process flow for HBARs starts with photolithography for patterning the bottom metal (Figure 2.16(a)). We use a resist mask to pattern platinum bottom metal of thickness 200 nm via liftoff. The bottom metal is patterned to remove it from underneath the aluminum electrodes. This helps in reducing the capacitance of the device, which becomes a significant factor at high frequencies (Figure 2.16(b)). We then perform XRD measurements to ensure the bottom metal has <111> lattice orientation. This is needed for the c axis

oriented growth of <200> AlN on the bottom metal. A 600 nm thick AlN layer is deposited by reactive-ion sputtering at 400ºC (Figure 2.16(c)). Rocking curve measurements are performed to ensure that the AlN has good piezoelectric properties; FWHM of 1.85º was measured for <200> peak of the AlN deposited on the sapphire wafer. The AlN layer is then etched using a photoresist mask in phosphoric acid heated to 160ºC to open via for connecting to the bottom metal. AlN gets etched by TMAH, which is a common ingredient in the developers used in photolithography. To avoid using TMAH, we used TMAH free developer like CD-30, which works efficiently with positive photoresist like S1818. An aluminum electrode of thickness 100 nm is e-beam evaporated and is patterned by resist liftoff to form laterally couple two-port HBAR (Figure 2.16(f)). Microscope image of a 50 µm radius input port device which is laterally spaced by 5 µm from the output port shows all the components of the HBAR (Figure 2.17).

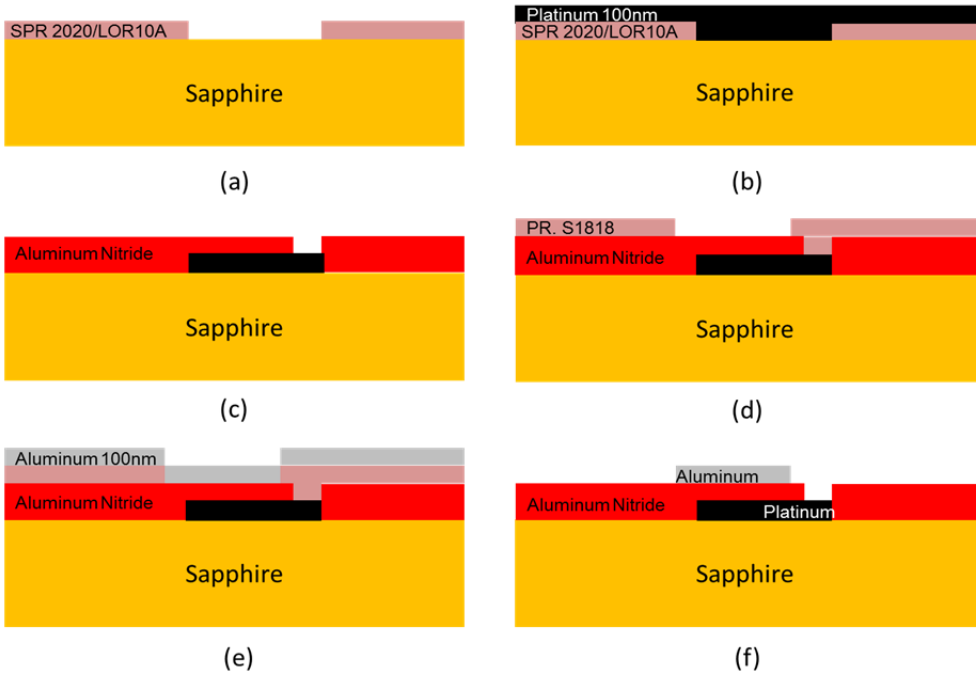

Figure 2.16: Fabrication process flow for laterally coupled HBAR on sapphire.

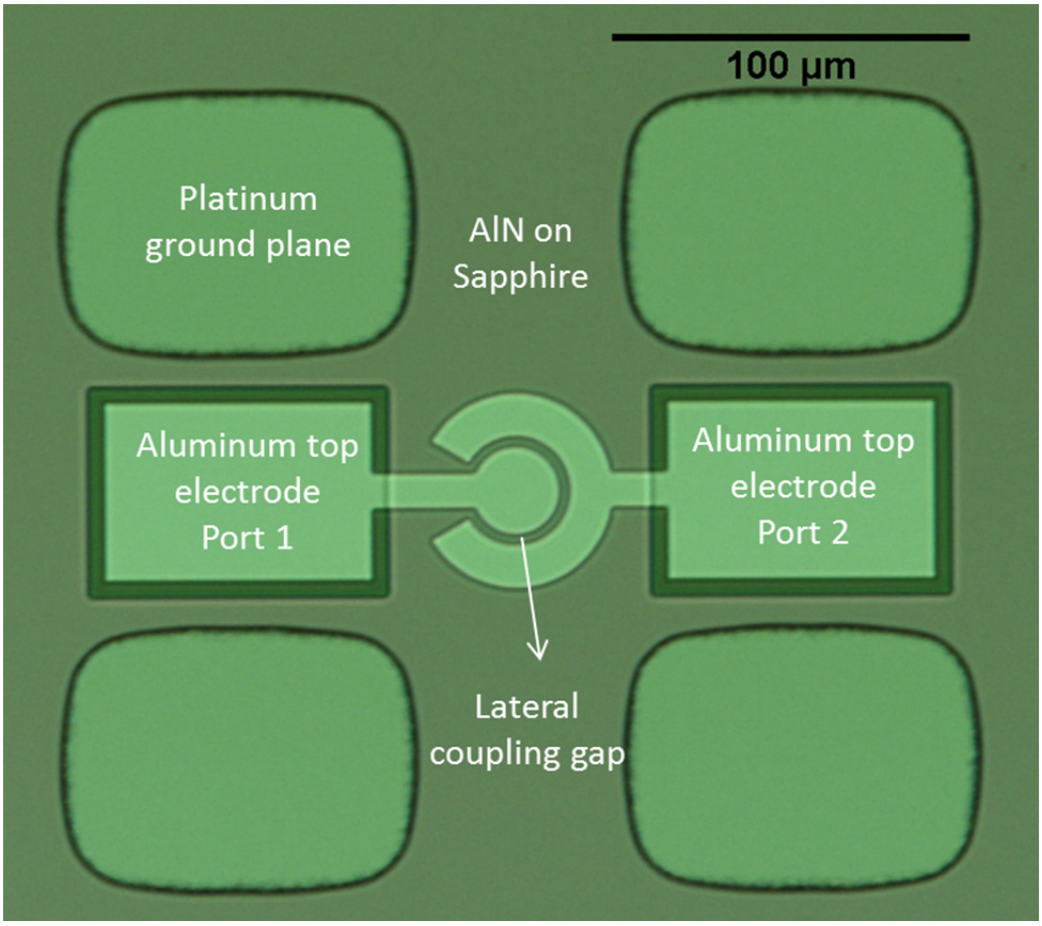

Figure 2.17: Microscope image of laterally coupled HBAR fabricated on a sapphire substrate. The input port called Port 1 has a radius of 50 µm, is spaced from output port called Port 2 by a 5 µm gap. The dark area around and underneath the aluminum top electrode is where the platinum removed by lifting off photoresist for reducing the pad capacitance.

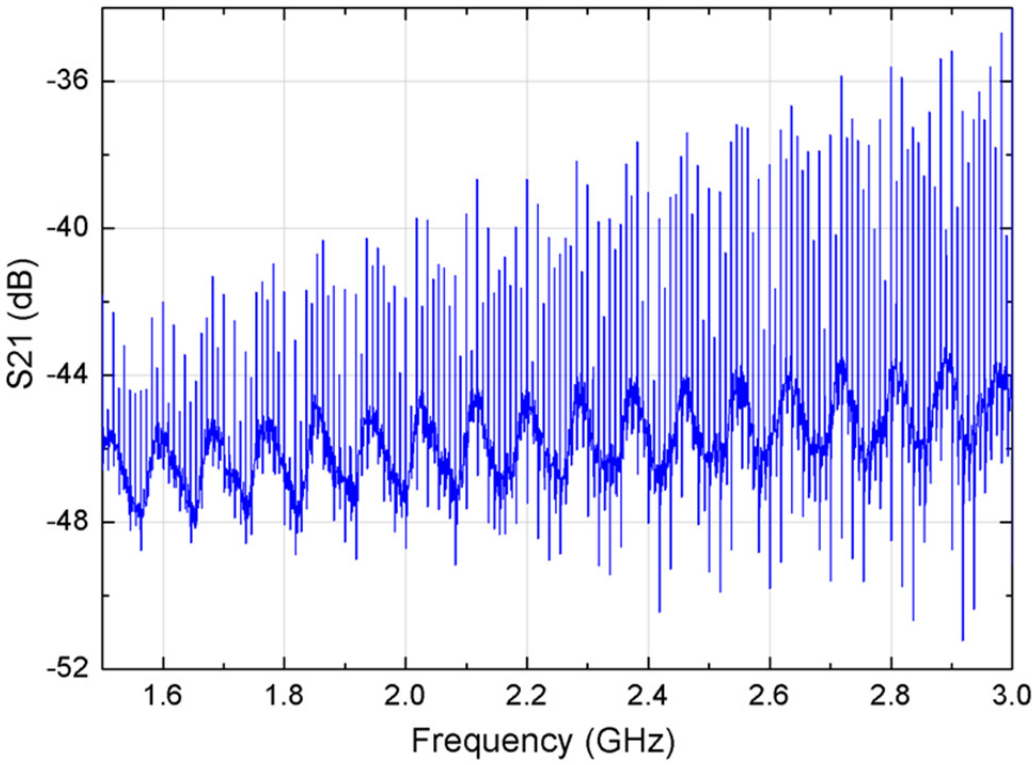

Figure 2.18: S_{21} versus frequency from 1.5 GHz to 3 GHz shows multiple resonances with transmission loss ranging from -44 dB to -34 dB.

2.3.2 Device characterization

The characterization setup for laterally coupled HBARs is similar to the one described for 1-Port HBAR in Chapter 2.2.2. It consists of probe station for probing the device under a microscope and an Agilent N5230A parametric network analyzer. In these measurements, we use two ports of the network analyzer to measure the S_{21} transmission response of the HBAR. Cable and probe parasitics were not de-embedded to get a realistic performance of the device when it is meant to be used as inline filter in Chapter 4 and Chapter 5. The S_{21} versus the frequency was plotted over 1.5 GHz to 6 GHz frequency range shows the device performance. At low frequencies, the transmission loss at resonance peaks ranges from -42 dB to –34 dB (Figure 2.18).

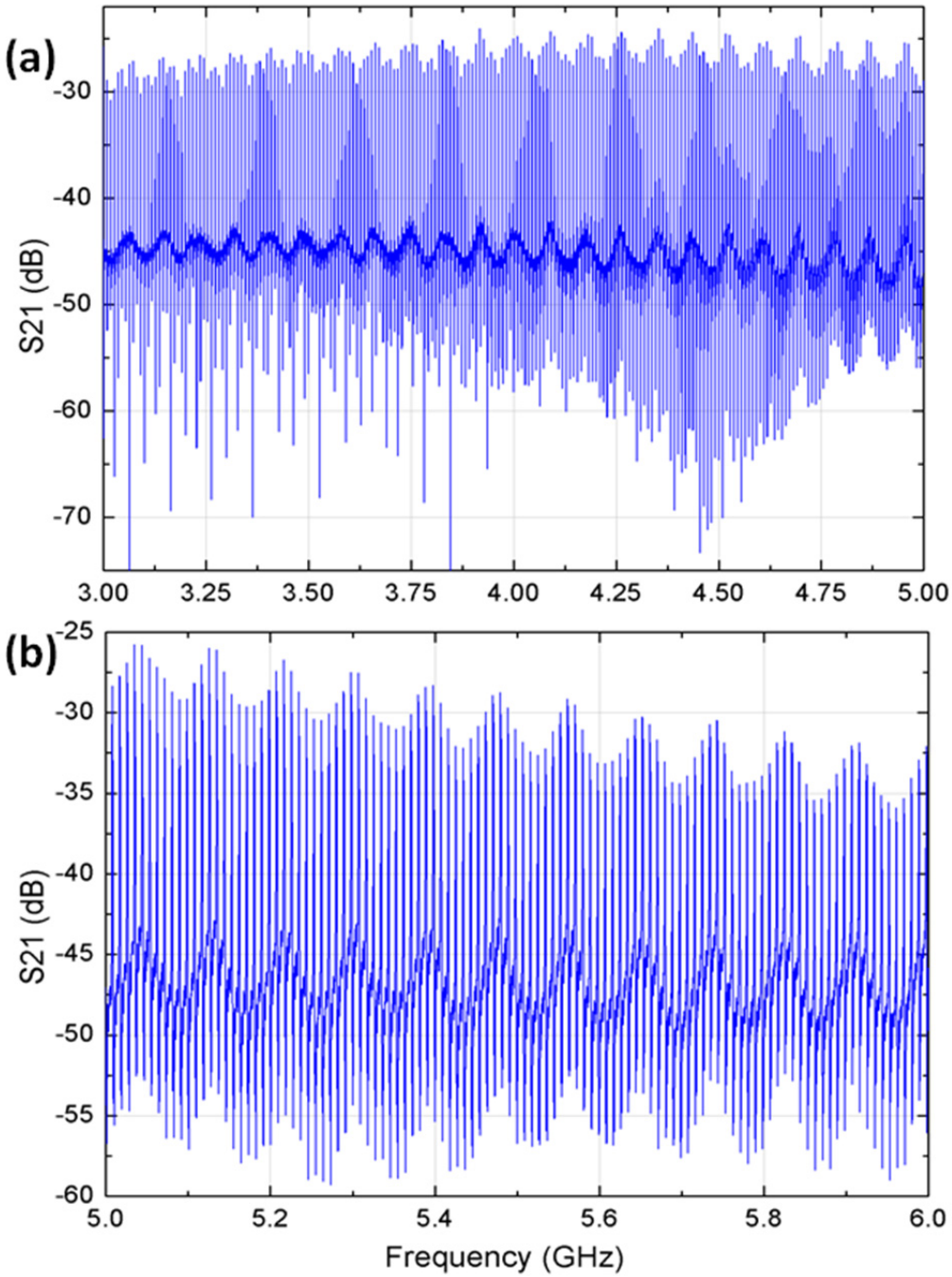

Figure 2.19: S_{21} versus frequency (a) 3 GHz to 5 GHz frequency ranges and (b) 5 GHz to 6 GHz frequency ranges show multiple high quality factor resonances.

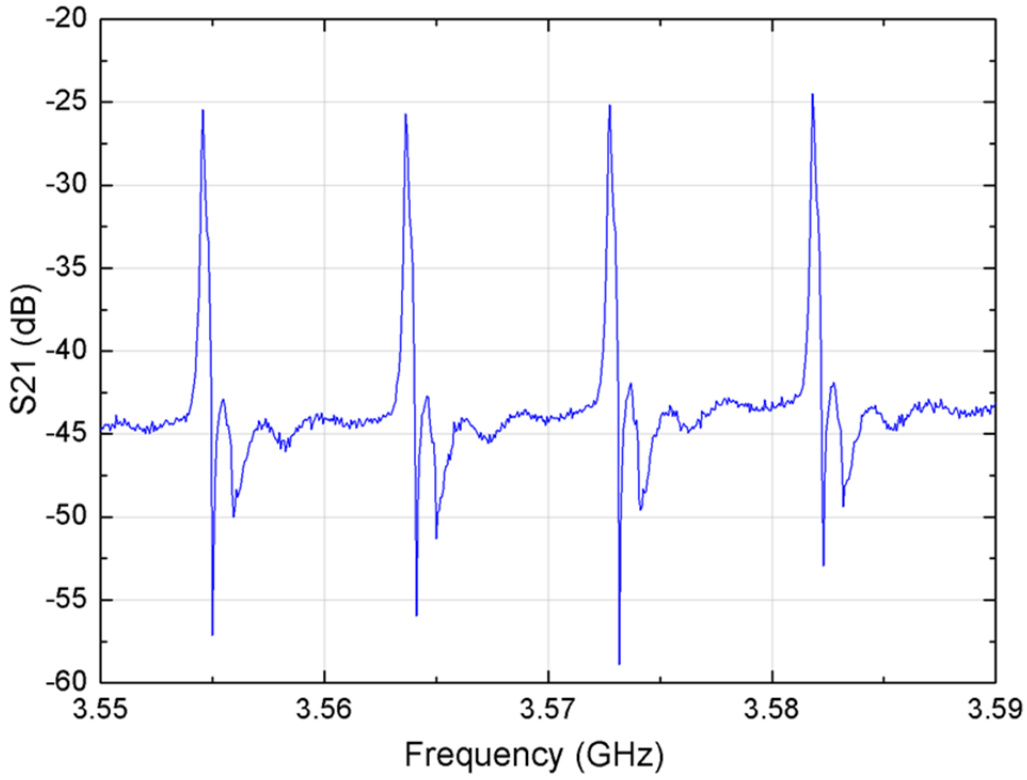

Figure 2.20: S_{21} versus frequency plot shows the spacing of 9.2 MHz between resonances at 3.57 GHz.

At higher frequency range between 3 GHz to 6 GHz, there is a better matching between the piezoelectric pickoff and the mechanical resonances; hence, the transmission losses reduce to -25 dB (Figure 2.19). The resonances are periodic in nature, as simulated and the period is roughly 9.1 MHz (Figure 2.20). This frequency spacing is smaller than what we intended and is due to lack of availability of thinner sapphire substrate. Table 2.2 shows the measured quality factor from the Q circle for different resonances. The f-Q product for the 6 GHz resonance was measured to be 1.49×10^{14} Hz is the highest f-Q product reported up to date for a sapphire resonator.

Table 2.2 Quality factors and f-Q products of laterally coupled HBAR

Frequency (GHz)	Quality Factor	f-Q product (Hz)
2.265	7575	1.71×10^{13}
3.036	33551	1.01×10^{14}
3.982	22753	9.06×10^{13}
4.581	23737	1.09×10^{14}
4.981	22136	1.10×10^{14}
5.044	20177	1.02×10^{14}
6.034	24675	1.49×10^{14}
6.969	20805	1.45×10^{14}

2.4 *Conclusion and future directions*

In this chapter, we have demonstrated microelectromechanical components which will be coupled to spin torque oscillators to form the magneto-acoustic oscillator. We described two types of these components. One for mechanical stress/strain wave based coupling to spin torque oscillator and second, for electrical filtering based coupling to the spin torque oscillator.

1-Port HBAR devices, which form the mechanical coupling components, were simulated, fabricated and measured. These silicon-based devices, when benchmarked against diamond and silicon carbide based devices, outperformed the diamond in their quality factor and the amplitude of stress that can be generated. We show that silicon HBARs can generate 2.2 MPa of stress for 1 V drive amplitude. We also studied the loss mechanisms in these devices and concluded that though partially limited by anchor loss, the devices have good resonator performance. Solving the general

equation of motion for the specific case of the HBAR, we were able to develop an analytical model for HBAR that lets us estimate the amplitude of stress/strain generated by an HBAR for a given resonant frequency and quality factor of a mode.

Laterally coupled HBAR are relatively new devices that allow us to use HBAR directly as high quality factor, multi frequency gigahertz inline filters. 2-Port HBARs that were fabricated on the sapphire substrate show sharp resonances over a wide range of frequencies, from 1.5 GHz all the way up to 8 GHz. By keeping the spacing between the two ports small, we were able to get transmission loss as low as -25 dB over a wide range of frequencies. The quality factors for the laterally coupled HBARs are extremely high hence the filter bandwidth at all the resonance frequencies is narrow and will result in sharp output oscillations. We measured record breaking f-Q product of 1.49×10^{14} Hz at 6 GHz, which shows that these HBARs potentially can be used with high success as resonant components in oscillator loops.

CHAPTER 3

ACOUSTIC STRAIN-BASED LOCKING OF SPIN TORQUE OSCILLATOR

3.1 *Introduction*

As discussed in Chapter 1.1 spin torque oscillators (STOs) are nanoscale, gigahertz frequency, and self-oscillating magnetic devices. STOs are advantageous due to their tiny form factor and large tuning range. However, they suffer from low output power and large linewidths that limit their practical use. To address these issues, locking multiple STOs to a common external reference oscillator has been proposed and injection locking to a microwave current source has been demonstrated [30]. Injection locking STO has shown to improve the output power and reduced the linewidth. Tamaru *et al.* [59] recently demonstrated a spin torque oscillator with a linewidth of 1 Hz. This was accomplished by using, STO as a voltage controlled oscillator in a high-speed phase locked loop circuit. Both these schemes are limited in their application because they need high quality external references to work. Moreover, when STOs are used in these schemes, they lose their frequency tunability. Additionally, there are further challenges to scaling injection locking to lock multiple devices due to impedance mismatch and phase delays between STOs [60, 61].

In this chapter, we discuss a new scheme to overcome the challenges faced by an injection locking system. We demonstrate locking of STOs by using an AC high frequency strain generated by 1-port HBAR devices, as discussed in Chapter 2.2. In acoustic strain locking of STO, an external reference source is not required. The signal from the STO can be amplified and used to drive the HBAR to generate AC strain. The HBAR then filters the broad linewidth AC signal from the STO to transduce AC strain at its resonance frequencies. When the AC strain is applied to free layer of the

STO, due to inverse magnetostriction effect, it generates an effective AC magnetic field [62]. The generated AC magnetic field acts as a locking signal for the STO, narrowing its linewidth and increasing its output power. Acoustic locking can be scaled to a large number of STOs. Multiple closely spaced STOs can be locked by a single HBAR, to generate a narrow linewidth output.

We present a realistic macrospin mathematical model for a spin torque oscillator that incorporates the effect of AC strain acting on its magnetostrictive free layer. We demonstrate that we can use the AC strain to lock a spin torque oscillator by observing the Fourier transform of the STO output. Using the analytical model for the HBAR discussed in Chapter 2.2.3, we estimate the voltage drive for a given quality factor of a HBAR that is needed to acoustically lock the spin torque oscillator.

3.2 *Macrospin model of STO with magnetostrictive free layer*

3.2.1 Landau-Lifshitz-Gilbert-Slonczewski (LLGS) equation

Magnetization dynamics of the free layer of a spin torque oscillator are modelled using the LLGS equation given by:

$$\frac{d\hat{m}}{dt} = -\gamma\hat{m} \times \overrightarrow{H_{eff}} + \alpha\hat{m} \times \frac{d\hat{m}}{dt} + \frac{\gamma\hbar J\eta}{2edM_s}\hat{m} \times (\hat{m} \times \hat{ep}) \tag{3.1}$$

where, $\hat{m}$ is a unit vector given by:

$$\hat{m} = \vec{M}/M_s \tag{3.2}$$

is the magnetization $\vec{M}$of the free layer, and where M_s is the saturation magnetization [4]. The first term on the right side of Equation (3.1) describes the precession of the magnetization $\hat{m}$ around the effective magnetic field $\overrightarrow{H_{eff}}$, where γ is the

gyromagnetic ratio of the electron in free layer of the STO (Figure 3.1). The second term on the right side of Equation (3.1) is the damping term, where α is the phenomenological Gilbert damping constant. The damping term relaxes the magnetization $\hat{m}$ along magnetic field $\overrightarrow{H_{eff}}$. The value of Gilbert damping constant is material dependent and has an origin in magnon-magnon and magnon-phonon scattering [4]. The third term on the right side of Equation (3.1) represents the in-plane spin torque term, where J is the current density, ħ is the reduced plank constant, η is the spin polarization efficiency, e is the charge of an electron, and d is the thickness of the free layer. Here $\widehat{ep}$ is the spin polarizer vector which is along the direction of the polarizer or the fixed layer magnet in an STO. $\widehat{ep}$ in Equation (3.1) is used to represent the direction of the spin-polarized electrons that are applying a torque to the magnetization of the free layer. In addition to the in-plane spin transfer torque, there is an out-of-plane (OOP) torque, whose amplitude can be as much as 40% of in-plane torque for MTJs based STOs. The OOP torque acts along or against the externally applied field and its effect can be absorbed in $\overrightarrow{H_{eff}}$ [20].

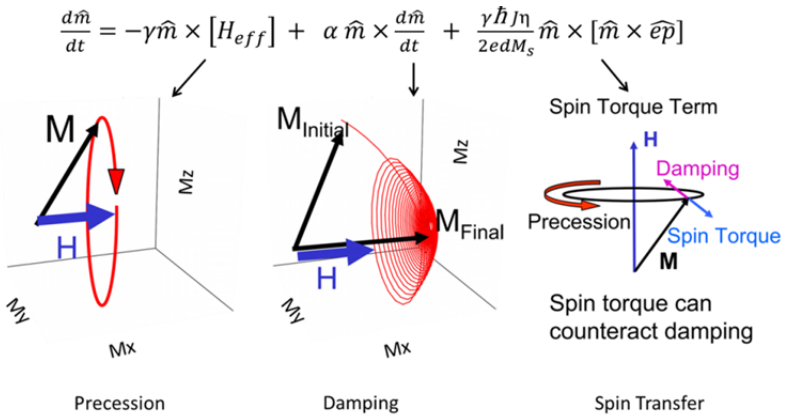

Figure 3.1: Illustration of LLGS equation. Adopted from [63].

The amplitude and the sign of the current density J have direct control over the spin transfer torque amplitude and direction. By increasing the magnitude of the bias

current, the spin torque can overcome the damping in the free layer. This results in steady state precession of magnetization. The total effective magnetic field $\overrightarrow{H_{eff}}$ for the free layer magnet is the derivative of its total energy $\overrightarrow{E_{eff}}$ with respect to its magnetization $\hat{m}$ given by:

$$\overrightarrow{H_{eff}} = d\overrightarrow{E_{eff}}/d\hat{m} \tag{3.1}$$

The components of $\overrightarrow{H_{eff}}$ are derived from constituent energy terms of the magnet are given as:

$$\overrightarrow{H_{eff}} = \overrightarrow{H_{ap}} + H_{an}\hat{n}(\hat{n}.\hat{m}) + H_d\hat{d}(\hat{d}.\hat{m}) + \overrightarrow{H_T} \tag{3.2}$$

$\overrightarrow{H_{ap}}$ is the external applied magnetic field which is used as a bias field to get oscillations. By varying $\overrightarrow{H_{ap}}$ the frequency of oscillation of the STO can be changed. H_{an} and H_d are the anisotropy and demagnetization fields whose amplitude and directions $\hat{n}$ and $\hat{d}$ respectively are dependent on the shape of the magnet [64]. The size and the shape of the free layer magnet also determine the initial direction of the magnetization $\hat{m}$. In the simulation, the direction of magnetization is given in polar coordinates with the azimuthal angle φ and polar angle θ.

3.2.1.1 Thermal Noise in LLGS

The effect of non-zero temperature T and corresponding thermal noise in dynamics of magnetization is accounted via term $\overrightarrow{H_T}$ in Equation (3.4). $\overrightarrow{H_T}$ is a Gaussian-distributed Langevin term with random direction whose RMS amplitude was calculated using fluctuation-dissipation theorem is given by:

$$H_T^{RMS} = \sqrt{2\alpha k_B T/\gamma M_s V \Delta t} \tag{3.3}$$

where Δt is the simulation step size, V is the volume of the free layer magnet and k_B is the Boltzmann constant [65]. Additionally, to incorporate the effect of thermal noise in the model we assume that the starting azimuthal angle φ_0 and polar angle θ_0 of the magnetization have random fluctuations around them. The RMS amplitudes of these thermal fluctuations calculated using equipartition theorem is given by:

$$\varphi_0^{RMS} = \sqrt{k_B T/H_{an} M_s V} \tag{3.6}$$

$$\theta_0^{RMS} = \sqrt{k_B T/H_d M_s V} \tag{3.7}$$

3.2.1.2 Magnetoelastic strain-based locking term

The effect of out-of-plane strain applied by the HBAR on the free layer magnet can be incorporated in the magnetization dynamics as an effective out-of-plane uniaxial shape-anisotropy term H_{st} that has a directional component given by the direction of the strain as $\hat{t}$. The amplitude of H_{st} is given by:

$$H_{st} = 2B_{eff} S/M_s \tag{3.8}$$

where B_{eff} is the magneto-elastic coupling coefficient. The value of which is dependent on the material of the free layer magnet. The amplitude of H_{st} is proportional to S which is the magnitude of the AC strain along direction $\hat{t}$ acting on the free layer of STO. Thus the effect of strain is incorporated in the LLGS equation

by adding the uniaxial shape-anisotropy term to Equation (3.4). The resultant total magnetic field $\overrightarrow{H_{eff}}$ is given by:

$$\overrightarrow{H_{eff}} = \overrightarrow{H_{ap}} + H_{an}\hat{n}(\hat{n}.\hat{m}) + H_d\hat{d}(\hat{d}.\hat{m}) + \overrightarrow{H_T} + H_{st}\hat{t}(\hat{t}.\hat{m}) \tag{3.9}$$

3.2.2 Simulation parameters

In our STO simulation, we use an MTJ with CoFeB for both free and fixed layers. An MgO tunnel barrier separates these layers. The size of the free layer and its associated magnetic and material properties are shown in Table 3.1 have been adopted from work by Liu *et al.* [15]. We used the value for B_{eff} of a 1.5 nm thin CoFeB film from Gowtham et al. [66]. DC bias currents values and the $\overrightarrow{H_{ap}}$ values are also shown in Table 3.1. For our simulation model with the chosen elliptical shape and size of the free layer the shape H_{an} is along the long axis of the magnet in X direction and H_d, which keeps the in-plane magnet from pointing out-of-plane, is along the Z direction (Figure 3.2).

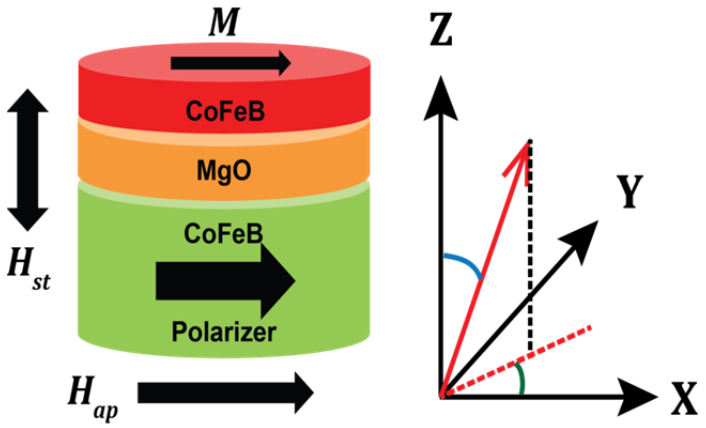

Figure 3.2: Directions of free layer magnetization, applied magnetic field, strain generated uniaxial anisotropy field H_{st}, polarizer $\widehat{ep}$, and the coordinate system used in the simulations.

The initial direction of magnetization $\hat{m}$ is assumed to be along the $+X$ axis. Externally applied bias field $\overrightarrow{H_{ap}}$ of amplitude 300 Oe is along the easy axis of the magnet in the $+X$ direction. The HBAR will generate strain in the Z direction which is the out-of-plane direction for the magnet. Thus the magneto-elastic field due to strain H_{st} will be along the Z direction. The direction of the spin-polarized current due to the polarizer layer $\hat{ep}$ is chosen along the $+X$ direction. In the simulation, we use step time (Δt) of 10 ps, with a total simulation time of 1 μs. This results in a resolution of 2 MHz in the frequency spectrum. Simulations were first done without the AC strain S to extract the original spectra of the STO and then repeated with strain field applied at the fundamental oscillation frequency. After first 30 ns, the strain field is turned on which is sufficient time for magnetization to settle into steady-state precession.

Table 3.1 Simulation parameters for macrospin model of STO incorporating effect of AC strain

Property	Value
Free layer size	$170\ nm\ \times\ 100\ nm\ \times\ 1.5\ nm$
M_s	$1100\ \mathrm{erg}/cm^3$
H_{an}	$219\ Oe$
H_d	$13000\ Oe$
α	0.01
B_{eff}	$-7 \times 10^7 \mathrm{emu}/cm^3$
η	0.3
H_{ap}	$300\ Oe$
Current Range	$1.8 - 13$ mA

3.2.3 Simulation results

As we changed the applied bias current from 1.8 mA to 13 mA, the frequency of the simulated STO changes from 3 GHz to 11 GHz. The frequency changes because of the amplitude of the spin torque, dependent on the applied bias current, changes the trajectory of the magnetization precession. For an MTJ based STO, the maximum applicable current is usually limited to low milliamps due to the tunneling barrier. However, we consider all these modes to demonstrate, that irrespective of the mode shape, acoustic locking of the mode is feasible. There are two main types of modes observed in the spin torque oscillators that have different behaviors with applied bias current. The first mode is the in-plane mode (Figure 3.4(a)), where the oscillation frequency decreases with the increasing bias current. Second is the out-of-plane mode for which the oscillation frequency increases with the bias current (Figure 3.4(b)). As the STO transitions from in-plane mode to the out-of-plane mode, it goes through a region where the mode has the clam-like shape (Figure 3.4(c)). This clam-shaped mode is considered as a subset of the in-plane mode as it follows the same frequency-current relationship. In this mode, the magnetization tilts slightly out-of-plane in both the $+Z$ and $-Z$ directions.

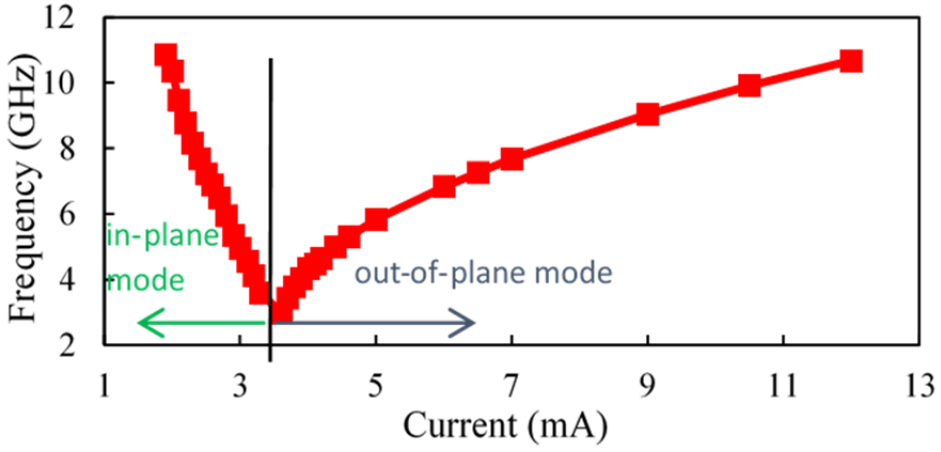

Figure 3.3: (a) STO oscillation frequency mode as a function of bias DC current.

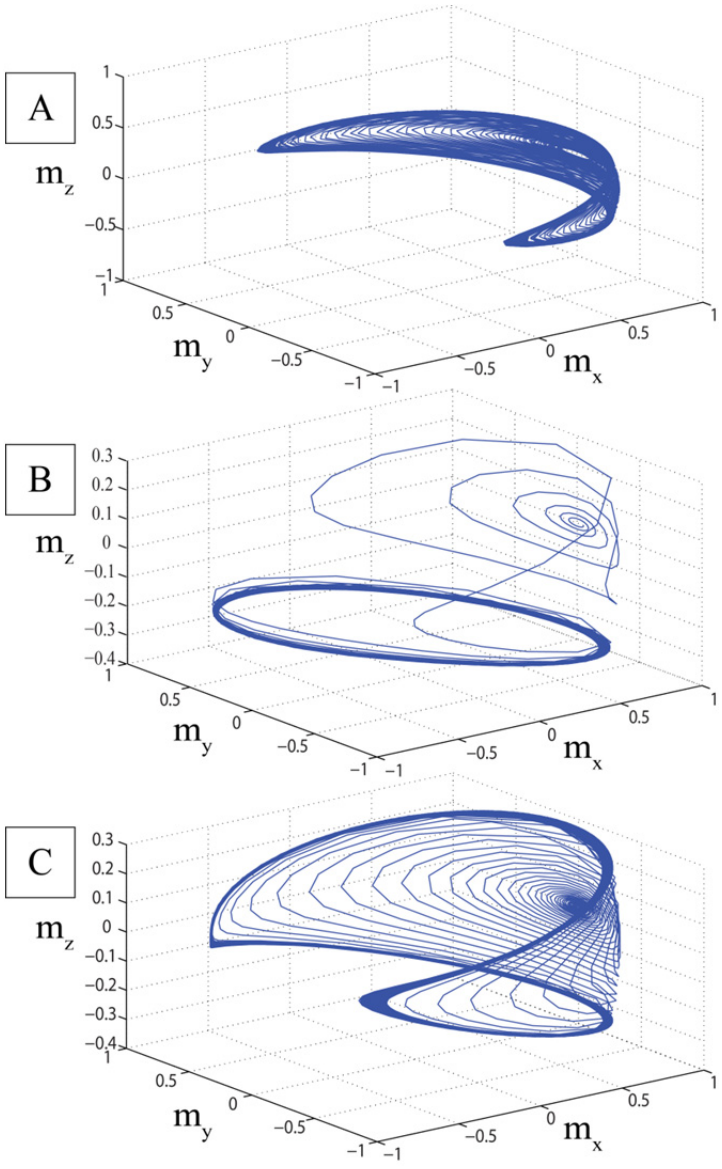

Figure 3.4: Magnetization of the free layer in different oscillation modes. (a) In-plane mode of oscillation with the frequency of 9.445 GHz observed at a bias current of 2.1 mA. (b) Out-of-plane mode of oscillation with frequency 7.685 GHz observed at a bias current of 7 mA. (c) Clam-shaped mode of oscillation with frequency 5.766 GHz observed at a bias current of 2.85 mA.

3.2.3.1 Effect of AC strain on simulation results

Effect of the applied AC strain induced locking of the STO is studied by taking the Fourier transform of the AC output voltage of the STO. The amplitude of the output voltage depends on a fractional change in the output resistance of the STO due to magnetization precession. The magnitude of the resistance change is dependent on the maximum change in the MTJ impedance. This occurs when the device switches from parallel state to antiparallel state and the precession angle of the magnetization around the polarizer. For the fast Fourier transform of the output signal, we consider the oscillation data only after initial 60 ns. This is sufficient amount of time for magnetization to settle into steady state precession and for it to respond to the locking AC strain S. From our results we observe that AC strain can be used to successfully lock all three different oscillation modes of STO (Figure 3.5). The relative amplitude of the STO oscillation in the absence of the locking signal across different oscillation modes is reflective of the actual amplitude measured in different experiments [3, 9, 67]. Specifically, the output power of STO increases from in-plane mode (Figure 3.5(a)) to out-of-plane mode (Figure 3.5(b)), with the clam-shaped mode of oscillation (Figure 3.5(c)) having intermediate output power. In the FFT spectrum of STO with AC strain, we observed increased output power. We also observe, the linewidth of the oscillation narrowing around the frequency of the applied AC strain along with the suppression of spurious modes. This change in the output is indicative of the locking of the STO across various modes by the AC strain (S) that can be generated by the HBAR.

The amplitude of the AC strain needed to lock STOs in the different modes of oscillations is shown in Table 3.2. Out-of-plane mode needed 21 ppm of AC strain, while in-plane mode required 107 ppm. The huge difference in amplitude of strain S is due to the magnetoelastic locking field H_{st}, with direction $\hat{t}$, coupling into the $\overrightarrow{H_{eff}}$

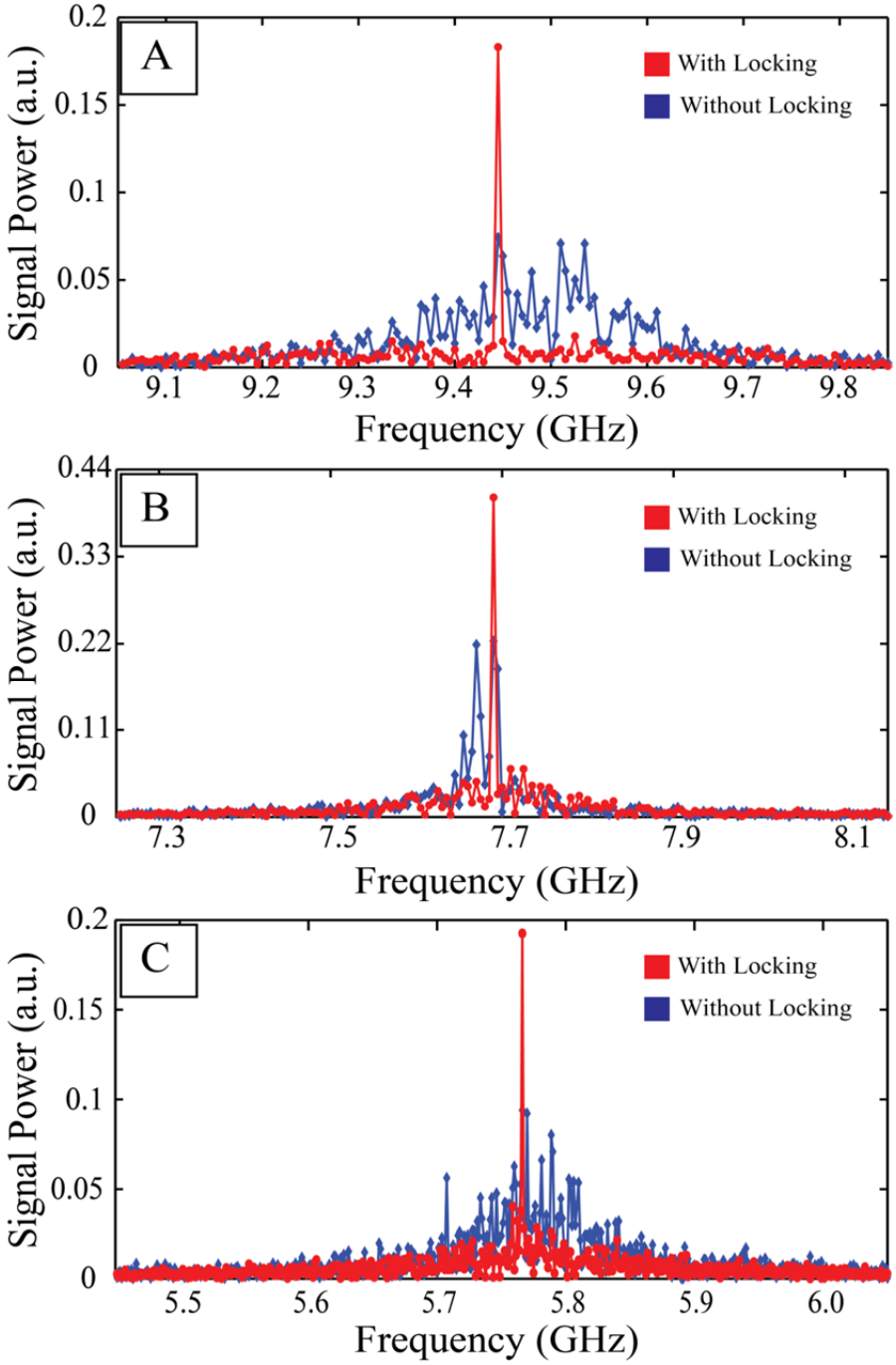

Figure 3.5 FFT spectrum of the STO with locking AC strain *S* in red and without locking strain in blue for the (a) in-plane mode, (b) out-of-plane mode and (c) clam-shaped mode of oscillation.

Table 3.2 Strain amplitude and drive voltages needed for locking

Oscillation Mode	Locking AC Strain S (ppm)	HBAR Drive (V)
In-Plane	107	4.9
Clam-Shaped	33	2.2
Out-of-Plane	21	1.4

as a dot product with magnetization $\hat{m}$ as shown in Equation (3.9). For the *Z*-directional strain used in our simulations, the amplitude of H_{st} is weighted by the *Z* component of $\hat{m}$. In the in-plane mode of oscillation, the magnetization precession is mostly along the *X*-*Y* plane with a tiny *Z* component, so the locking field amplitude is greatly reduced when it is coupled into the LLGS equation. Hence, a larger magnitude of AC strain is required for locking in-plane mode compared to the out-of-plane or clam-shaped modes. Table 3.2 also shows the voltage drive needed by an AlN HBAR with a silicon substrate, to generate the locking strain amplitude at the frequency of the STO oscillation. The drive voltage values were calculated using the analytical model for HBAR described in Chapter 2.2.3. We assumed a quality factor of 1000 and the AlN film thickness of half the wavelength, to get efficient drive and pickoff [68]. H_{st} due to the *Z*-directional strain acts a small AC signal on top of the constant DC *Z*-directional demagnetization field H_d of amplitude 13000 Oe. Hence, we need a significant amount of strain to lock the STO. The magnitude of *Z*-directional strain needed to lock an STO scales proportionally with the demagnetization field.

3.2.3.2 Locking range of AC strain

HBARs have resonances at fixed frequencies and are spaced by a fixed frequency gap which is described in detail in Chapter 2.2.1. This makes HBAR ideal for locking

tunable oscillators like STO, as we can hop from one resonance to other as the oscillation frequency changes. If the HBAR resonance is offset from the oscillation frequency of STO, we can still pull the signal to the nearest resonance frequency by applying higher amplitude of strain. The pulling/locking range of acoustic strain locking was studied by repeating the locking simulation in which the strain is applied by an offset frequency Δf_{Lock} to the oscillation frequency. The locking range of AC strain(S) for the clam-shaped mode of oscillation with frequency 5.766 GHz was calculated from multiple simulations (Figure 3.6). We observe that the locking range is linear over an offset frequency range of +/− 105 MHz for 110 ppm amplitude of AC strain.

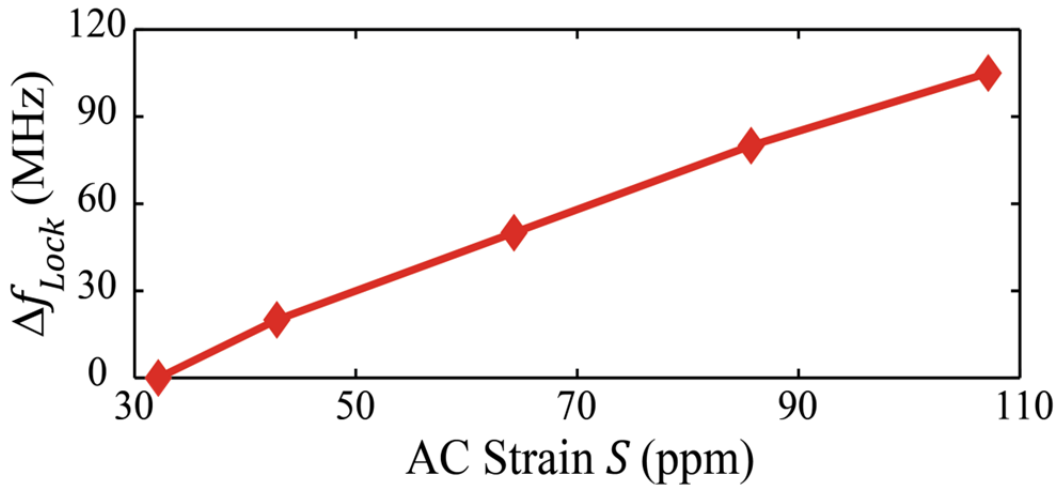

Figure 3.6: Frequency offset from the STO output frequency versus amplitude of AC strain S needed to lock the STO calculated from simulations for the clam-shaped mode of oscillation at 5.766 GHz.

The limit of the locking range, observed as a saturation of the offset frequency, was not seen in our simulations, because we limited our simulations to maximum strain amplitude of 110 ppm, which is very tough to achieve using HBAR. An HBAR

which typically has resonances spaced by 10 MHz can easily be easily used to pull and lock an STO oscillation frequency within its range.

3.3 *Challenges in acoustic strain locking of spin torque oscillators*

The model for acoustic locking an STO using AC strain generated from an HBAR shows that, with a strong drive signal applied to the HBAR, we can lock the STO output oscillation to the closest HBAR resonance. However, implementing such a system isn't straightforward. Apart from the challenges in the complex fabrication process, which would involve a double side fabrication with STO on one side and HBAR fabricated on another side, main challenge comes from accurately positioning the free layer magnet in the STO at the acoustic standing wave antinode, for efficiently driving the STO. To study this in detail, we plot the position of the of the standing wave antinode, where the strain is maximum, from the surface edge at different frequencies in silicon HBAR (Figure 3.7). This position corresponds to the quarter wavelength of the HBAR mode, as the strain at the surface is zero. At 2 GHz, the strain maxima is located at 1.2 μm into the substrate while at 8 GHz, the strain is maximum at 300 nm into the substrate. This becomes more challenging considering that typically the STO material stack, including the contact leads, is about 100 nm thick, with the free layer being only 80 nm from the surface. Thus, there is an inherent position mismatch with the size of STO being small compared the acoustic wavelength at gigahertz frequencies.

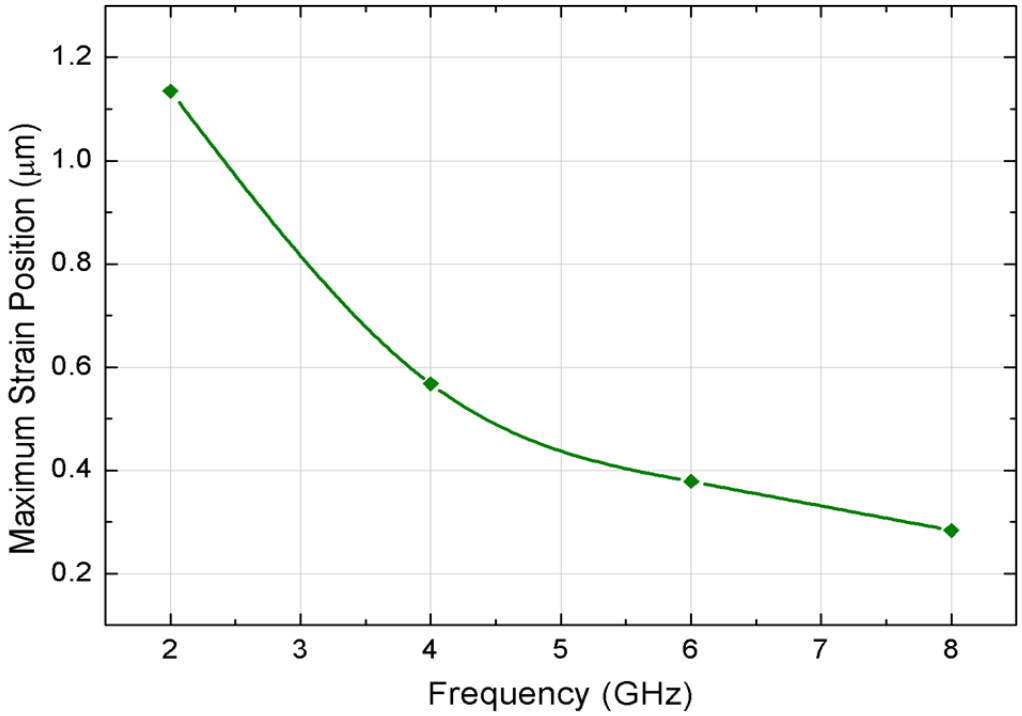

Figure 3.7: Maximum strain position from the surface edge as a function of frequency.

Position mismatch can be remedied by having thicker leads to make contacts to the STO. A better solution that ensures the quality factor of HBAR is unaffected by the STO fabricated on the backside of the substrate. Is to add a capping layer made of a high quality acoustic material (high f-Q product) like silicon dioxide or silicon nitride on top the MTJ, to position the free layer accurate at a strain maxima. This solution, though elegant, only works over a short frequency range. If we modulate the oscillation frequency of the STO changes from 4 GHz to 6 GHz, the corresponding change in the wavelength of the acoustic mode, causes the strain maxima position shift 200 nm, from 0.6 μm to 0.4 μm (Figure 3.7). This change in the maxima position is larger at low frequencies. For a frequency change from 4 GHz to 2 GHz, typically observed for devices shown in Chapter 4, the strain maxima shifts by 500 nm (Figure

3.7). This shift in the strain maxima is 5 times the size of a typical STO. A solution to this problem is to choose the capping layer thickness optimally to position the free layer magnet half way between the strain maxima positions, given by its frequency tuning range. This allows for best strain coupling in the center of the frequency range. The efficiency lost in strain coupling at both the ends of the frequency tuning range, has to be recovered by driving the HBAR with a larger voltage.

3.3.1 Acoustic strain injection locking versus current injection locking

It is important to compare the system efficiency in terms of power and signal amplification needed between acoustic AC strain-based injection locking and AC current/voltage-based injection locking. Drive voltages required for strain locking for different modes ranges from 1.4 V to 4.9 V are shown in Table 3.2. For building a strain based locking system in feedback with HBAR, we would need to amplify the output from the STO and feed it back to drive the HBAR strain signal (Figure 3.8).

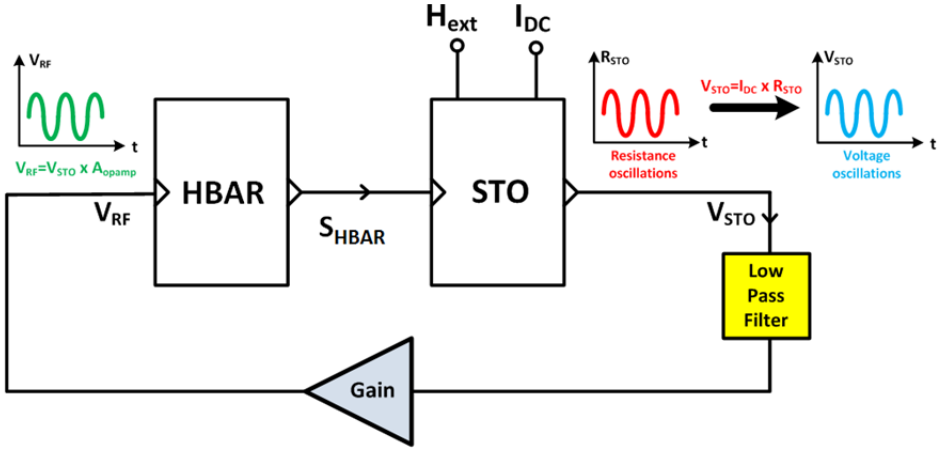

Figure 3.8: Acoustic strain based magneto-acoustic oscillator. The output from the STO is amplified and feedback via HBAR as strain S_{HBAR} to lock the STO. Low pass filter shows that only the fundamental mode is feedback without higher harmonics.

Typical output powers for the SHE-MTJs oscillators, as discussed in Chapter 5, are 20 pW. So the output voltage measured for a 50 Ω load is 31.6 μV. Assuming that HBAR input impedance is matched to the output of the amplifiers we would need about 97 dB of power gain to drive voltage of 2.2 V for HBAR to generate enough strain for locking the STO. To compare, the power needed for current-based injection locking to strain-based locking of the STO, we did macrospin simulations of STO with an AC current injected into the device. All the simulation parameters for the two systems were identical so that the results could be compared directly. The simulation was done for the clam shaped mode of oscillation with frequency 5.766 GHz observed for a DC bias current of 2.85 mA. In the macrospin model, the AC current of 50 μA applied after 30 ns into the simulation through current density term J shown in Equation (3.1) was able to lock the oscillator (Figure 3.9). Considering the impedance of the SHE-MTJ is 5 kΩ the locking signal power is 12.5 μW. The amplification gain needed if the STO output was feedback to lock itself is 68 dB, which is 39 dB less than the power needed to use AC strain to lock the STO.

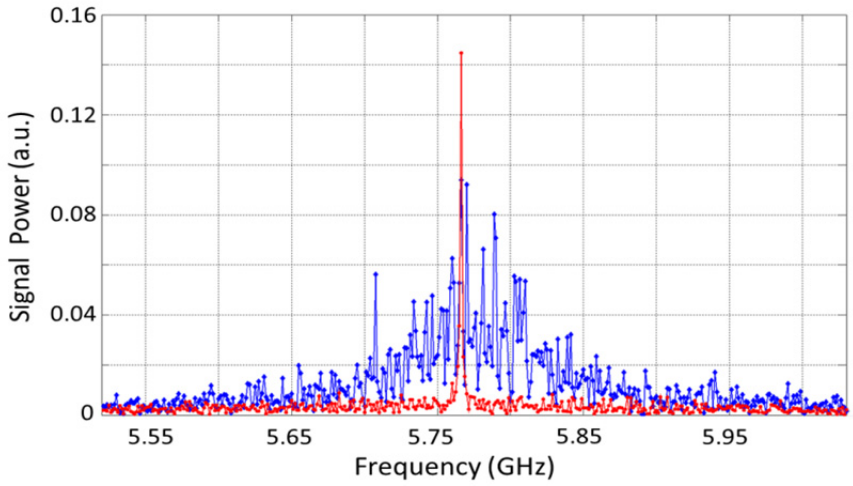

Figure 3.9: FFT spectrum of the STO with locking AC current of 50 μA in red and without locking current in blue for a clam shaped mode of oscillation.

We can, therefore, implement AC current-based locking system, where the output power of the STO is amplified and filtered by a laterally coupled HBAR and feedback to the STO as a filtered AC current (Figure 3.10). This AC current then locks the STO, resulting in a narrow linewidth signal. Considering even -20 dB transmission loss in laterally coupled HBAR the current-based magneto-acoustic oscillator is still more efficient than the strain-based magneto-acoustic oscillator. The current-based magneto-acoustic oscillator also works efficiently across the entire frequency range of operation of both the STO and the HBAR. This is unlike the strain-based version, where more gain is needed if the free layer magnet is offset from the strain maxima position. The current-based magneto-acoustic oscillator greatly simplifies the fabrication process involved in implementing the system, as the devices are fabricated on two separate wafers.

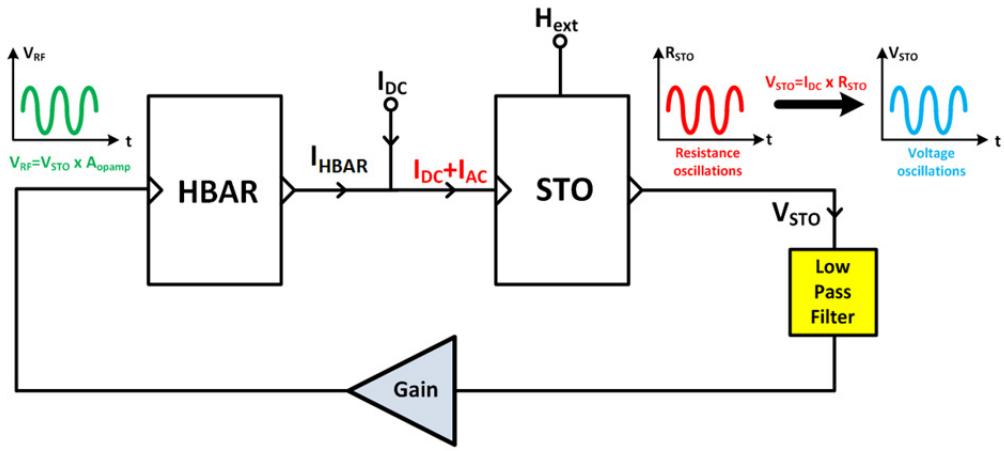

Figure 3.10: Current based magneto-acoustic oscillator. The output from the STO is amplified and feedback via HBAR as AC current I_{HBAR} to lock the STO. Low pass filter shows that only the fundamental mode is feedback without higher harmonics.

3.4 *Conclusion and future directions*

In this chapter, we have presented a novel scheme which uses AC strain generated by a high-overtone bulk acoustic resonator to injection lock the spin torque oscillator. We developed a realistic macrospin model of STO using an LLGS equation that incorporates the effect of strain acting on the free layer of a magnet by using a magnetoelastic coupling term. The macrospin model accounts for the effect of thermal noise and shows enhancement in linewidth when subjected to AC locking strain. We have demonstrated locking for various oscillation modes of STO. We observed that the out-of-plane strain generated by the HBAR is more suited for locking the clam-shaped mode or the out-of-plane mode. Using the analytical model for HBAR as a strain generator from Chapter 2.2.3, we calculated the amplitude of drive voltages needed for locking the different modes of the STO. We did simulations to study the locking range of AC strained-based locking and observed that the locking range increases linearly with the amplitude of AC strain.

Acoustic strain-based locking, though interesting, has some critical challenges for implementation. One significant problem is the positioning of the STO at a correct depth using a capping layer for getting efficient strain transduction. However, such a scheme is still limited to narrow frequency of operation. This is particularly true at low gigahertz frequencies, where the strain maxima position shifts rapidly with the frequency of operation. This problem can be fixed by driving the device harder, which makes the AC strain based locking less efficient. We also compared the AC strain-based locking to the AC current-based locking with respect to their efficiencies. This was done to develop a closed loop system, where STO output is amplified and is fed back as strain or current to lock the STO. In such systems, we observed that the AC current based locking is superior as it requires lesser gain to lock the STO.

Furthermore, unlike the strain-based version, the AC current feedback-based magneto-acoustic oscillator works equally efficiently across a larger range of bandwidth. It is also much easier to design, fabricate, and implement.

In the future, AC strain based locking can be implemented efficiently by using a thin film FBAR device. This device can generate AC strain much more effectively than the HBAR. While such a device is more efficient as strain transducer, it will be limited in the number of mechanical modes it can drive to make a tunable magneto-acoustic oscillator.

CHAPTER 4

SPIN VALVE DEVICES FOR MAGNETO-ACOUSTIC OSCILLATORS

4.1 *Introduction*

Spin valve devices, in their basic form, consist of two conducting ferromagnets that are separated by a non-magnetic metallic spacer. The resistance of spin valve device depends upon the relative alignment of magnetization of the two magnetic layers. The term "spin valve" was coined by Dieny *et al.* [69] describing an all metallic device, which allows the flow of spin current when the moments of the magnetic layers are parallel and blocks the spin current when the layer magnetizations are antiparallel. This spin current transmission, which changes the resistance of the spin valve, based on the relative direction of the magnetization is called the giant magnetoresistance effect (GMR). GMR originally was discovered in structures that had the current flow in the plane (CIP) of the magnetic layers [70]. The same principle applies to spin valve devices, which have current flow perpendicular to the plane (CPP) of the magnetic layers. In fact, in CPP devices the resistance change due to GMR is much more prominent, and it allows for large spin-polarized current flow [71]. This large current flow is necessary to use spin-transfer effects for switching or oscillating the device impedance from high impedance to low impedance and vice versa [4].

To understand the physics behind GMR, we look at the typical band structure for a transition metal based upon the sd model proposed by Mott *et al.* [72] (Figure 4.1(a)). In the model, we assume that transition metals consist of partially filled d shells, which provide most of the spin polarization, as exchange interaction promotes alignment of electron spins in them. Unlike the s electrons, most of the d shell electrons are below the Fermi level and have larger effective masses with low

velocities, so they do not contribute to current flow. Electrons with magnetic moments parallel to the magnetization direction are called the majority electrons, while electrons with magnetic moments antiparallel to magnetization are called minority electrons. Since the minority d band is at the Fermi surface, there are many more minority spins than majority spins (majority d band is below Fermi surface) at the Fermi surface. Most of the electron scattering preserves spin direction, majority electrons scatter into other majority states and similarly, minority electrons scatter into other minority states. As there are a larger number of minority states at the Fermi level (Figure 4.1 (b)), there is more scattering for minority spin electrons as compared to majority spin electrons. This called as sd scattering. Most of the current is anyway due to s electrons, the dominant part of the current is composed of flow of majority s electrons, as the minority s electrons having a shorter mean free path scatter more.

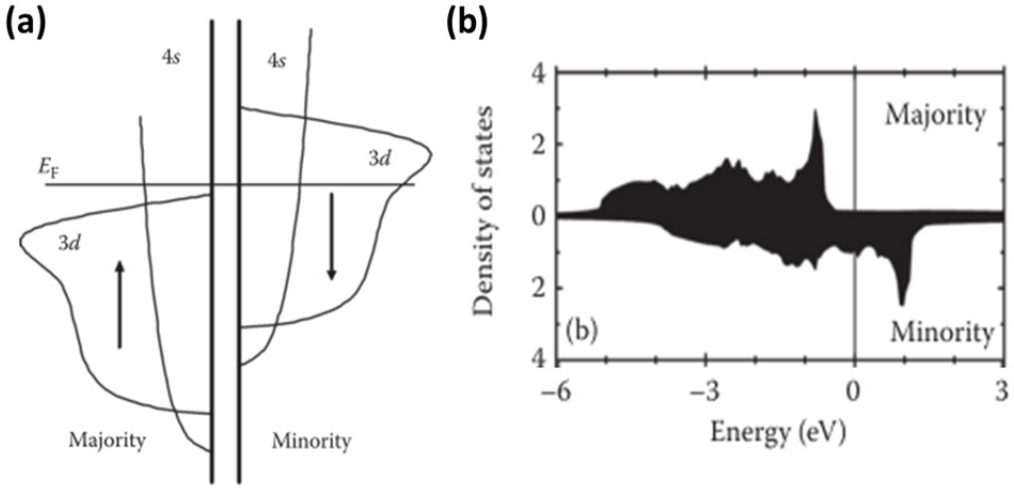

Figure 4.1: (a) Schematic density of states for a transition metal. (b) Calculated density of states for the majority and minority electrons in FCC Co. Adopted from [73].

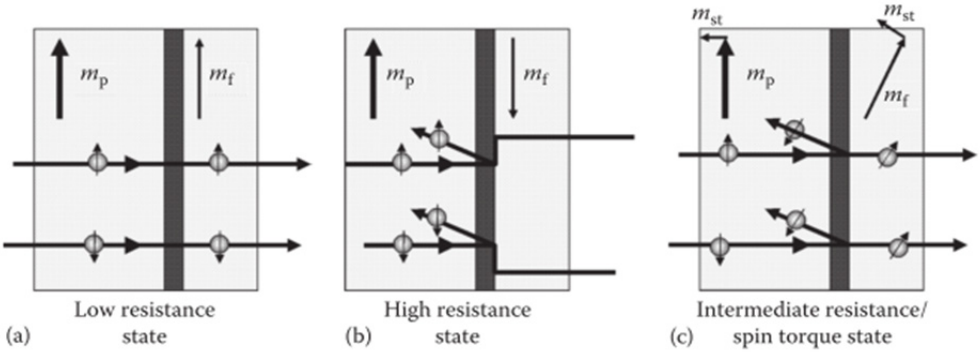

Figure 4.2: (a) Magnetic layers in a parallel state where electron pass through the interface with no or minimal scattering as they maintain their spin states. (b) Magnetic layers in an antiparallel state where there is high scattering due to a state change from the majority to minority electrons and vice versa. (c) Magnetic layer layers in an intermediate state where there is spin torque, m_{st}, applied to the magnetization of both the layers. Here the conduction electrons rotate their polarizations and in this process apply a torque to the magnetization of the layer. Adopted from [25].

To understand how the spin dependent scattering causes a resistance change in spin valves that is dependent on the relative directions of the magnetizations, we consider the interface between two magnets. These magnets have independent magnetizations, m_p and m_f for the polarizer (fixed) layer and the free layer respectively (Figure 4.2) [25]. The electron scattering, when the magnetization orientations are parallel is small because the spin states of electrons are preserved as they flow from one layer to another. The current flow in a parallel configuration is dominated by majority electrons resulting in a low resistance state (Figure 4.2(a)). The electrons are scattered strongly from the interface of the magnets and in the bulk when their spin state changes as they flow from one layer to another. This happens

when the magnetization orientations are antiparallel. Increased scattering of electrons leads to higher resistance because the current flow is in the antiparallel state is dominated by minority electrons (Figure 4.2(b)). In case of partial non-alignment (Figure 4.2(c)) where, θ_m is the angle between the magnetization of free layer and polarizer, the device resistance R is given by:

$$R = R_{av} - \frac{\Delta R}{2}\cos(\theta_m) \tag{4.1}$$

where, R_{av} is the average resistance of the device given by:

$$R_{av} = \frac{R_{ap} + R_p}{2} \tag{4.2}$$

R_{ap} and R_p are the resistance antiparallel and parallel state respectively. ΔR is the difference in the impedance of the two states is given by:

$$\Delta R = R_{ap} - R_p \tag{4.3}$$

In spin valve devices, we use a thin metallic spacer between the two magnetic layers. This spacer is needed because due to the exchange coupling at the interface of two magnetic layers, it is impossible to get a sharp change in magnetization. The most commonly used spacer is copper; it has a large spin-flip relaxation length at room temperature (~100 nm) and it can match the states of the conducting electrons from transition metals magnets, resulting in low unwanted scattering. The thickness of the spacer is kept smaller than the spin flip relaxation length to avoid unintentional scattering and to observe a large change in the magnetoresistance as the state changes

from parallel to antiparallel and vice versa. Typically spin valves have low magnetoresistance ratio (MR) of 2-10% which is calculated as:

$$MR = {}^{\Delta R}/_{R_p} \tag{4.4}$$

with small resistance area products in the range of 10^{-2} Ωμm^2 with cross-sectional areas, less than 250 nm diameter to ensure that spin transfer torque effect dominates over the Oersted fields produced due to current flow through the device.

In this chapter, we first study spin valves of nanopillar geometry with the free layer made of CoFe/CoFeGe bilayer. These devices fabricated in collaboration with Dr. Patrick Braganca of HGST will be used as a model STO for building current-based magneto-acoustic oscillator we described in Chapter 3.3.1. This implementation of STO is preferable to SHE-STO because their device impedance is smaller by two orders of magnitude, so higher locking current can be applied at lower input power, making this system much more efficient to implement and experiment on.

In this chapter, we also investigate nanopillar spin valves with TbDyFe (Terfenol-D) free layer. TbDyFe is highly magnetostrictive material and has recently gathered interest for designing low power strain-based switching of magnetic random access memory [74, 75]. TbDyFe, though investigated independently as a magnetic material, hasn't been used in a spin valve or MTJ configuration. These spin valve devices, which have Terfenol-D as the free layer were also fabricated in collaboration with Dr. Patrick Braganca, HGST, are completely identical to the CoFe/CoFeGe free layer devices in the structure and hence provides us an opportunity to benchmark their performance.

4.2 *CoFe/CoFeGe spin valve device*

CoFe/CoFeGe magnet used as the free layer of a spin valve has shown to have high MR of 6% [76]. These devices use a pinned fixed layer, which is implemented by pinning the reference layer magnet to synthetic antiferromagnet (SAF) using exchange interaction by sputter depositing films in the presence of a bias magnetic field or by annealing them with a bias magnetic field. The overall device stack comprises of IrMn /CoFe /Ru /CoFeGe (30 Å) /CoFe (5 Å) /Cu (40Å) /CoFe (5 Å) / CoFeGe (20 Å). In the device, IrMn acts as the pinning antiferromagnet, the first CoFe layer, which is pinned to the antiferromagnet, is then anti-parallel coupled due to the thin Ru spacer to the CoFeGe/CoFe layer. CoFeGe (30Å)/CoFe (5Å) is the reference layer of fixed magnet. CoFe (5Å)/CoFeGe (20Å) is the free layer magnet which is separated from reference layer using a 40 Å thick Cu spacer. The thickness dimension of the SAF layers, the materials used in the seed and capping layers and the fabrication process flow are proprietary information will not be disclosed. The spin valve tested as our reference oscillator is a circular device with 50 nm radius. We used circular devices as these are ideal for measuring oscillation without an external bias magnetic field, making them attractive to implement them in complex standalone circuits.

To implement current based magneto-acoustic oscillator, we first characterize the standalone device performance. The device response to DC magnetic field was measured to calculate its magnetoresistance MR. AC characterization of the device was done by driving it at fixed bias current to observe spin torque generated oscillations. Magnetic field bias dependence of spin valve oscillation frequency was measured by driving the spin valve oscillation at a fixed bias current and sweeping the bias magnetic field. Similarly, DC current bias dependent frequency tuning of the spin valve oscillation frequency was measured at a fixed bias magnetic field. To understand

injection locking of spin valve devices, we measured the device AC response when it's driven by an external AC signal of varying powers at its oscillation frequency. From these measurements, we were able to extract the locking range of the device as a function of locking signal power and were able to calculate the threshold power needed to see locking.

4.2.1 DC Measurements of CoFeGe/CoFe spin valves

4.2.1.1 Resistance versus magnetic field

We measured the resistance of the spin valve device using a lock-in amplifier in a voltage divider configuration as the externally applied bias magnetic field $H_{Applied}$ was swept from -2000 Oe to 2000 Oe and back (Figure 4.3(a)). The direction of $H_{Applied}$ is parallel to the direction of the magnetization of pinned reference layer. At 0 Oe $H_{Applied}$, we measured the device impedance to be 28.58 Ω (Figure 4.3(b)). When the bias field is increased, the device impedance reduces smoothly as the magnetizations of the reference layer and the free layer are aligned. As the $H_{Applied}$ is swept back, resistance measurements don't show any hysteresis. The device doesn't have any in-plane shape anisotropy field due to the circular shape; hence, we don't observe abrupt switching from the antiparallel state to parallel state. At 2000 Oe and -2000 Oe $H_{Applied}$ the device resistance is about the equal to about 26.98 Ω. We consider this the resistance of the parallel state. The ΔR for the device was calculated using Equation (4.3) to be 1.6 Ω and device magnetoresistance MR was calculated using Equation (4.4) to be 5.93%. This is in the range of MR measured on devices with elliptical geometry, fabricated on the same wafer, where magnetic field switching was observed. The change in resistance area product with magnetic field was 12.5 mΩμm^2.

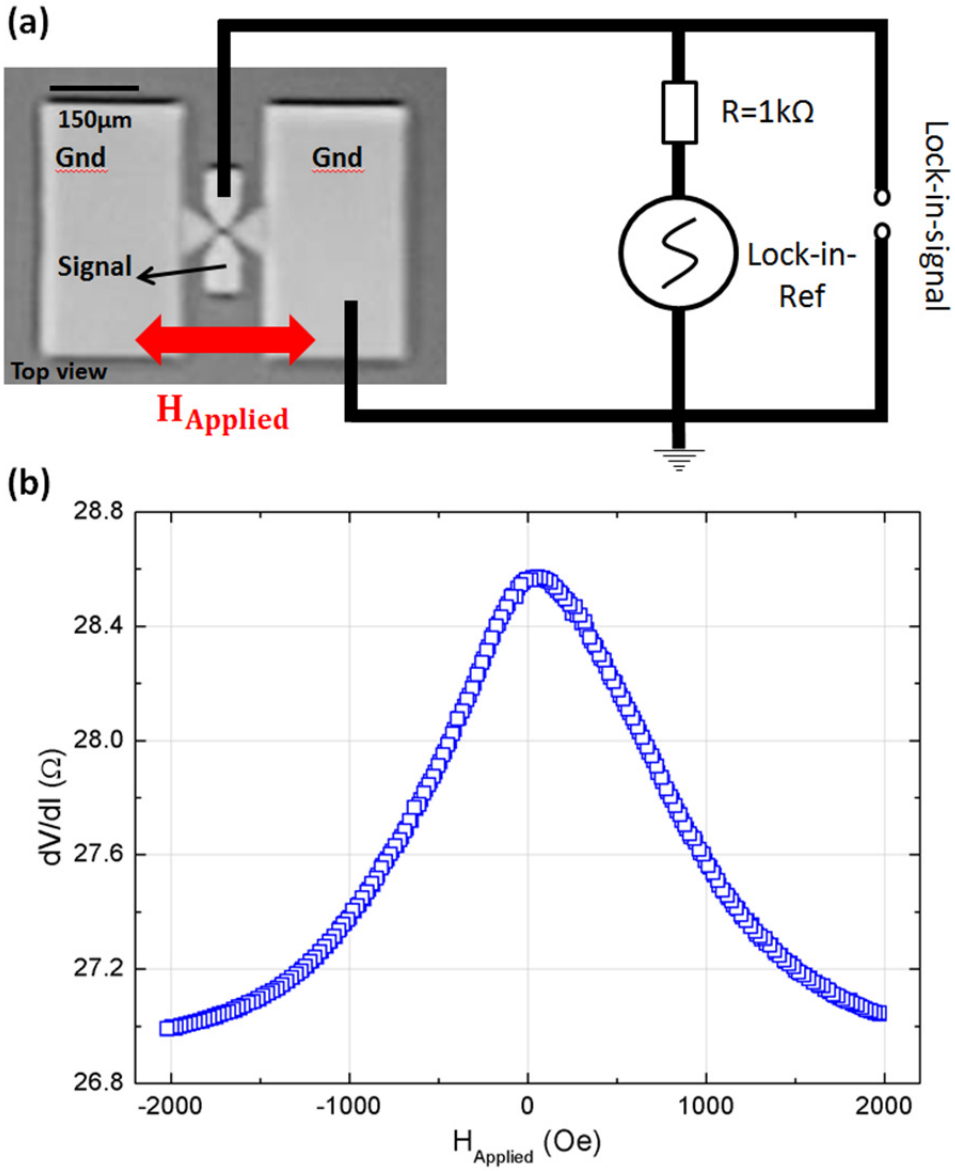

Figure 4.3: Resistance versus magnetic field measurements. (a) Measurement setup uses lock-in amplifier in a voltage divider configuration, with a reference 1 kΩ resistor, to measure the spin valve resistance as the magnetic field applied parallel to the direction of the polarizer is swept. (b) The plot of device resistance versus magnetic field showing an *MR* of 5.93% with a Δ*R* of 1.6 Ω.

4.2.1.2 Resistance versus DC bias current

Spin valve device resistance was measured using a lock-in amplifier in a voltage divider configuration as the bias DC current I_{Bias}, applied using a Keithley 2400 sourcemeter was swept from -1.5 mA to 1.5 mA and back (Figure 4.4(a)). The measurement was performed without applying any bias magnetic field. At 0 mA of I_{Bias}, we measured the device impedance to be 28.41 Ω (Figure 4.3(b)). When the bias current is increased, we observed the device impedance reduce smoothly as the spin torque from the spin-polarized electrons aligns the magnetizations of the free layer to the reference layer. With the positive current sweep, we measured the device resistance of 27.78 Ω at 1.5 mA of bias current. On the negative side, we observed a rapid change in resistance from 28.41 Ω to 27.23 Ω as the current is swept from 0 mA to -0.4 mA. Further decreasing the current we observe the device impedance increases to 27.65 Ω and remains constant till I_{Bias} of -1.5 mA. The overall change in resistance of the device, including the offshoot in the current sweep around -0.3 mA, is 1.16 Ω. Because the device is circular, it does not show any hysteresis usually observed for devices with shape anisotropy and the resistance value at a given bias current remains constant. The rapid change in the resistance measured only for negative I_{Bias}, though interesting, was not investigated further because the interest of this work has been to study the oscillation dynamics of the spin valves. This measurement shows that spin transfer torque can change the resistance of the device. This is a necessary measurement to ensure that the spin valve device will show magnetization dynamics resulting in oscillations when biased at an appropriate bias current and magnetic field. The change in resistance also tells us that as the amplitude of spin torque changes, the oscillation mode shape and hence the frequency of oscillation will change with the bias current.

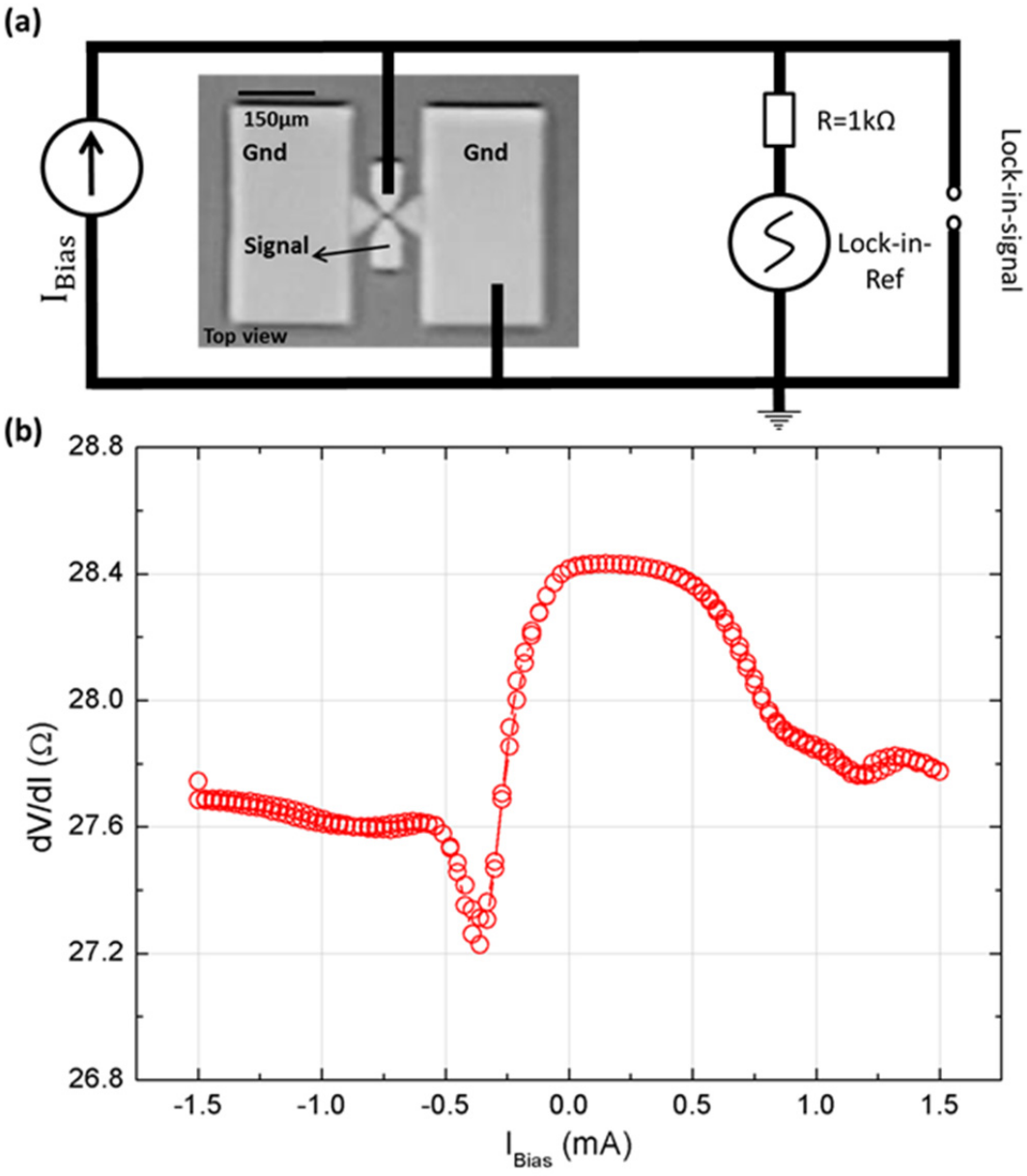

Figure 4.4: Resistance versus DC bias current measurements. (a) Measurement setup uses lock-in amplifier in a voltage divider configuration, with a reference 1 kΩ resistor, to measure the spin valve resistance as a DC bias current is applied using a Keithley 2400 sourcemeter is swept from -1.5 mA to 1.5 mA and back. (b) The plot of device resistance versus DC bias showing a total ΔR of 1.16 Ω.

4.2.2 High-frequency measurements of CoFeGe/CoFe spin valves

Spin valve devices were biased with a nominal magnetic field $H_{Applied}$ of 25 Oe in a direction parallel to the polarizer/fixed layer magnetization. Using a bias tee and Keithley 2400 sourcemeter an I_{Bias} was applied to the device. The output of the capacitor (RF) end of the bias tee was connected to the spectrum analyzer (Figure 4.5(a)). The spectrum analyzer is set for a 1 MHz resolution bandwidth and 6 kHz video bandwidth, selected to keep the noise floor as low as possible. All our measurements were carried out with using 30 data averages to ensure low noise. I_{Bias} was slowly increased to measure oscillation of the spin valves (Figure 4.5(a)). We measured oscillation with the fundamental mode at 3.6 GHz with a peak power of -94.5 dBm for an I_{Bias} of 330 μA (Figure 4.5(b)). The total power of the fundamental mode is measured 32.5 pW. The linewidth of the fundamental mode is 36.6 MHz, so the $\Delta f_o/f_o$ ratio of the oscillation mode is 98.36. The second harmonic at 7.2 GHz has a linewidth of 120 MHz, and total power is 36 pW.

By changing the bias current, we can change the amplitude of spin torque acting on the free layer magnetization. This modifies the mode shape of the magnetization precession and changes the output power and frequency of the spin valve. We observed the oscillation frequency of the spin valve decreases with the increased bias current (Figure 4.6(a)). As the fundamental mode frequency changes, the second harmonic frequency also changes with it. The change in the oscillation frequency for a 160 μA change in I_{Bias} from 260 μA to 420 μA was 230 MHz (Figure 4.6(b)). This tuning range of 6.3% for just 160 μA change in current is impressive compared to traditional MEMS oscillators, where frequency tuning is usually in the ppm range. Driving the spin valves at constant I_{Bias} of 430 μA, as the bias magnetic field $H_{Applied}$ was changed from 0 Oe to 80 Oe, we observed the frequency of oscillations reduce from 3.485 GHz to 3.41 GHz (Figure 4.7).

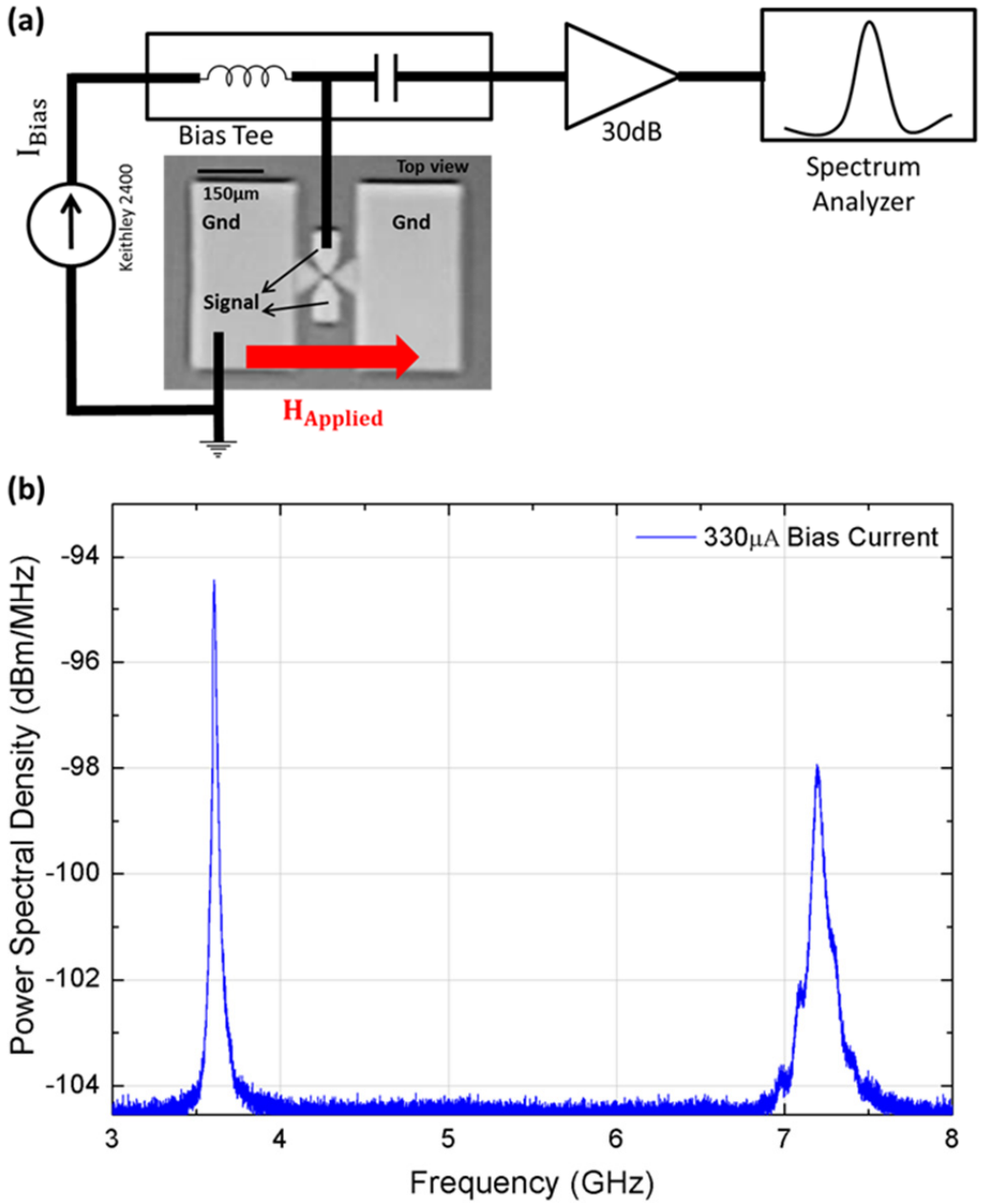

Figure 4.5: High-frequency measurements of spin valve devices. (a) Measurement setup uses bias tee to apply DC bias current to spin valve devices, at a given bias magnetic field, the RF output of the devices is measured on the spectrum analyzer. (b) RF output of a spin valve device measured at I_{Bias} of 330 μA for an $H_{Applied}$ of 25 Oe.

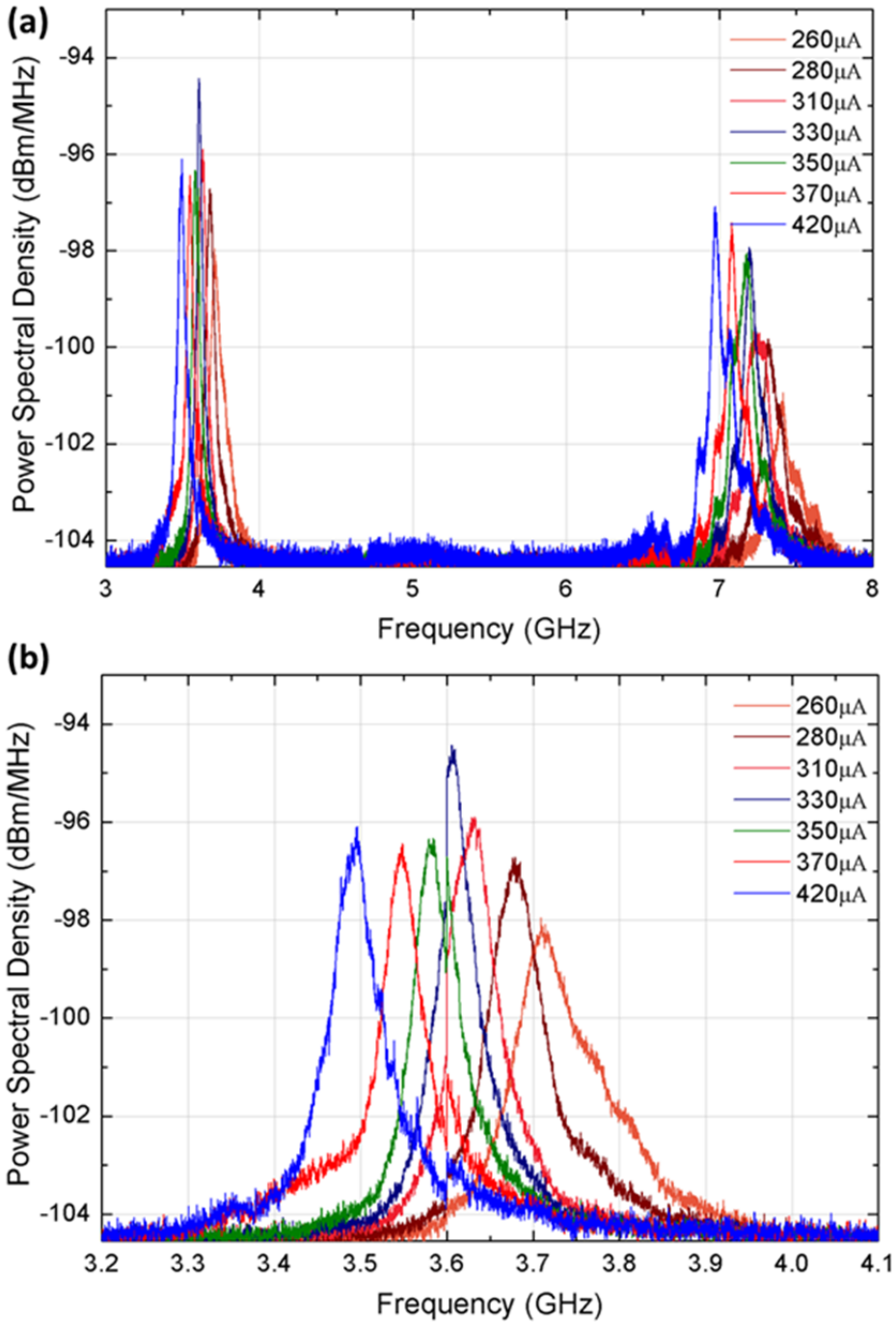

Figure 4.6: Tuning of spin valve oscillation frequency with DC bias current. (a) The plot shows the tuning of the fundamental frequency and the second harmonic with the bias current. (b) The plot shows frequency tuning of the fundamental mode, a 160 μA increase in bias current reduces the oscillation frequency by 230 MHz.

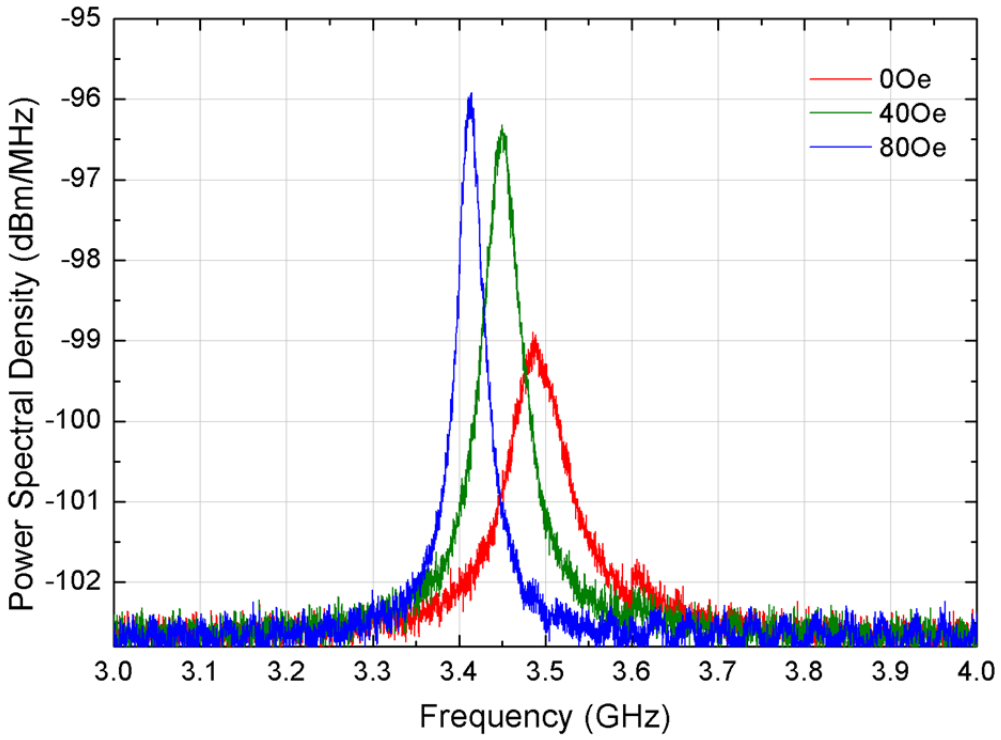

Figure 4.7: Tuning of spin valve oscillation frequency with applied bias magnetic field for I_{Bias} of 430 μA. The frequency of oscillation reduces from 3.485 GHz to 3.41 GHz. Frequency reduction with increasing bias field implies that the bias field counters the demagnetization field of the spin valve thereby reducing the overall magnetic field experienced by the CoFeGe/CoFe free layer.

4.2.3 Locking to external reference signal

Current-based magneto-acoustic oscillator, described in Chapter 3.3.1, will inject amplified and high quality factor filtered spin valve oscillation output back into spin torque device. In an open loop configuration, this system behaves similarly to a spin valve device injected with an AC signal at the frequency of oscillation. Rippard *et al.* observed that injection locking works only above a certain amplitude of power is injected in a spin valve device [32, 63]. To understand the response of CoFeGe/CoFe

based spin valve oscillator to the injected AC power and to measure the threshold power needed for injection locking, we performed injection locking measurements on the spin valve devices (Figure 4.8).

Spin valve devices were first driven by a bias DC current 890 μA at a 0 Oe applied bias field to get steady state oscillation at 3.125 GHz (Figure 4.9(a)). Then, using a circulator, AC signal from a signal generator was injected in the spin valve device and its power was increased from -120 dBm to see the onset of locking. We observed that when the AC signal power was increased up to -25 dBm the device locked to the injected input. The locking was observed as the device linewidth completely vanished from the spectrum and only the reflected signal from the signal generator was observed (Figure 4.9(c)). We also noted an increase in the DC voltage measured by the Keithley 2400 sourcemeter which was used for applying bias current. This is because the input AC injection power from the signal source mixes with the locked spin valve oscillation output to generate a rectified DC signal.

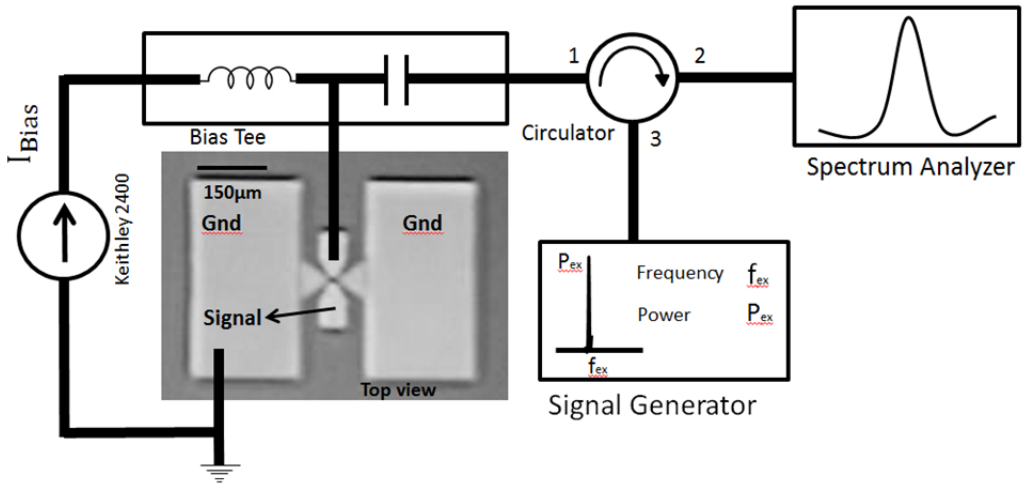

Figure 4.8: Experimental setup used for performing injection locking measurements on spin valve devices. The circulator is used to isolate the signal generator output from the spectrum analyzer input.

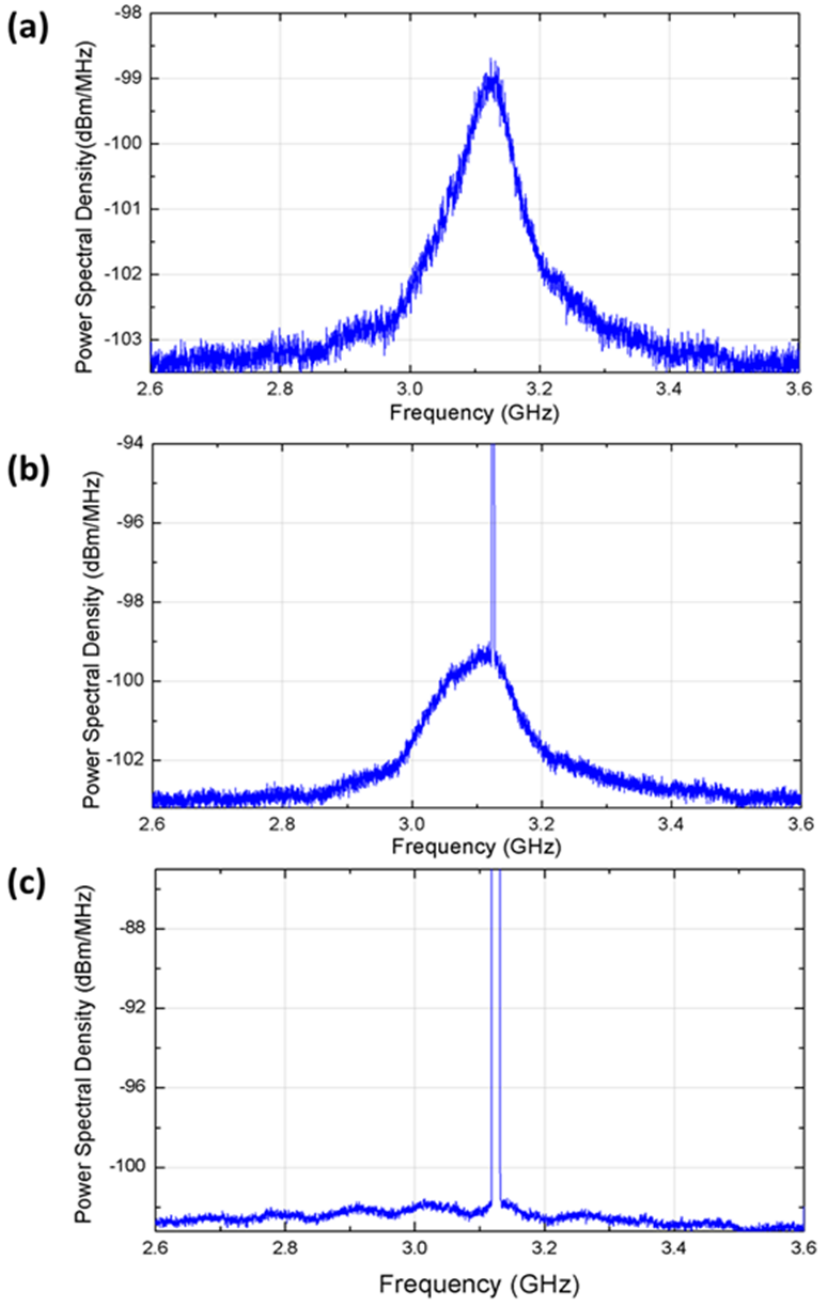

Figure 4.9: Frequency spectrum of the spin valve biased with 890 μA of DC current measured at different stages of injection locking. (a) Spectrum measured without AC injection signal shows oscillation peak at 3.125 GHz. (b) Spectrum measured with AC injection signal of power -30 dBm injected at 3.125 GHz. (c) Frequency spectrum measured with AC injection signal of power -25 dBm.

Locking range of the spin valve devices was measured by applying a fixed AC injection power of -25 dB and then sweeping the bias current. Once the locking range bandwidth for given power was measured, the injected power was increased by the step of 1 dBm, and the measurement was repeated. At AC injection power of -20 dBm for a current change from 700 μA to 1.07 mA the spin valve remains locked to the injected oscillation frequency of 3.125 GHz (Figure 4.10). When the spectrum was measured for the same current range with the AC injection signal power of -120 dBm, we observed the frequency of the oscillator change from 3.17 GHz to 3.07 GHz.

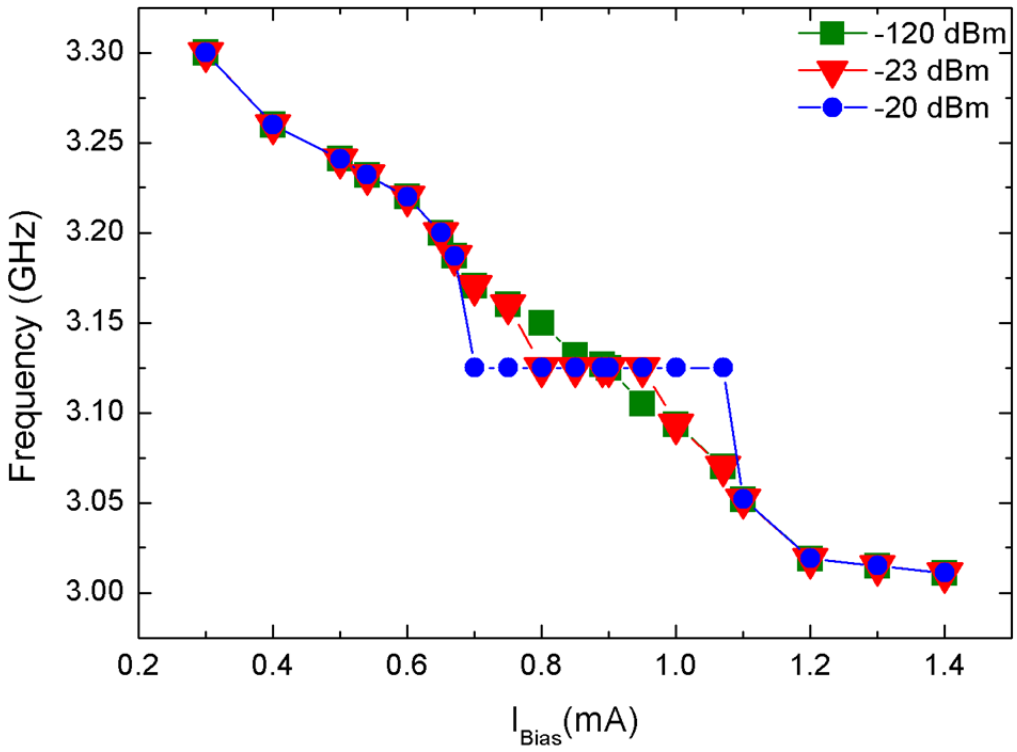

Figure 4.10: Spin valve oscillation frequency measured at different injection power levels as the bias current is swept from 1.4 mA to 0.3 mA.

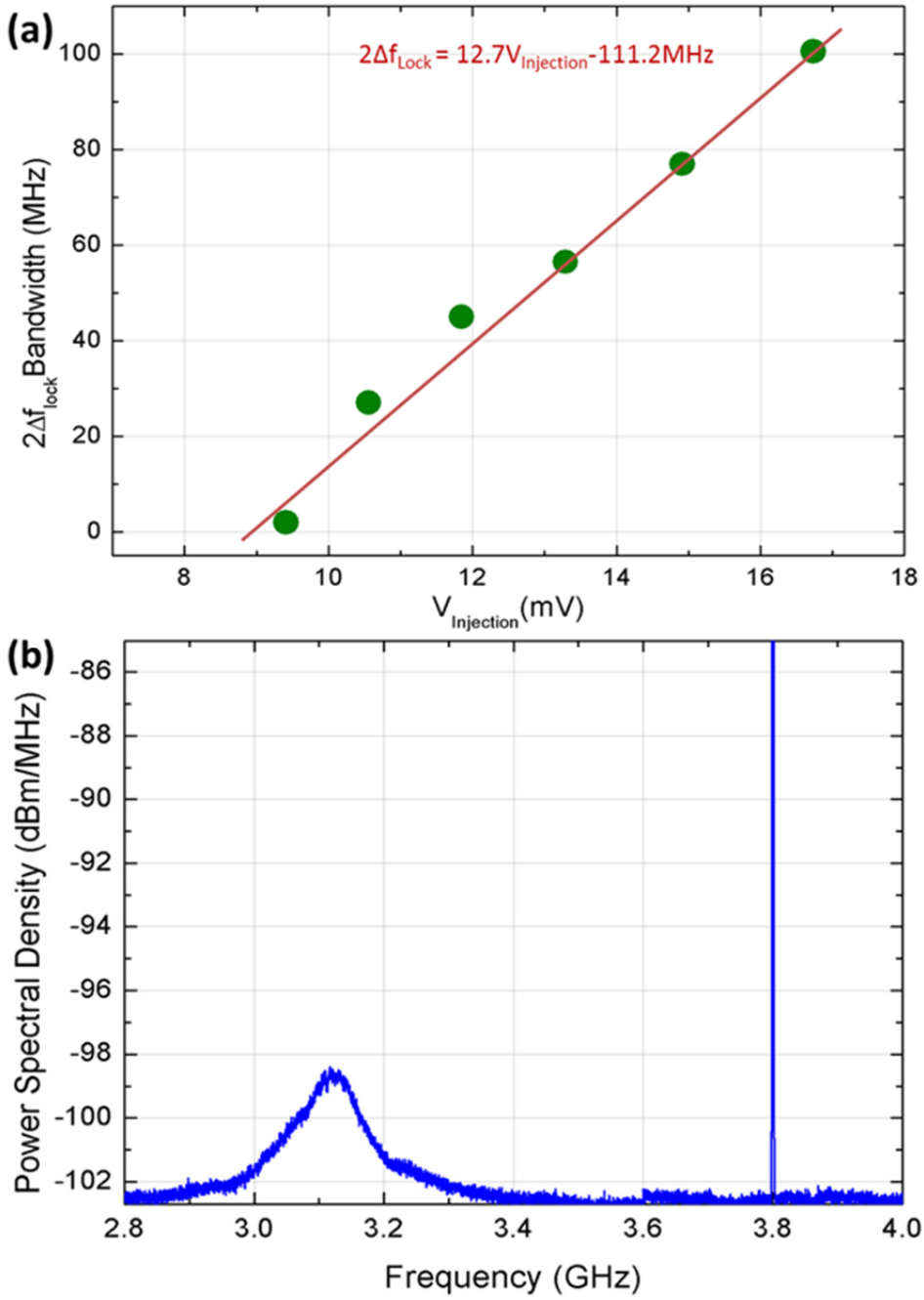

Figure 4.11:(a) Locking range measured for a given injection voltage shows linear relation up to 100.5 MHz. (b) High power AC signal (-10 dBm) injected at a frequency out of the pulling range of the oscillators shows free running oscillator spectrum, indicating a practical limit to locking range of the spin valve device.

Extracting the injection voltage from the injection power and plotting it as the function of the locked bandwidth, we observed a linear dependence of the locking BW to the injection voltage (Figure 4.11(a)). At injection voltage of 16.7 mV corresponding to -20 dBm input power, we measured a locking bandwidth of 100.5 MHz. We need a much higher amplitude of injection voltage (and power) to lock our spin valve devices compared to the measurements done by Rippard *et al.* [30]. This higher threshold for locking is attributed to the fact that oscillation modes of our spin valve devices are in-plane. In-plane modes are not as conducive to lock, to injected current at the fundamental oscillation frequency, as the out-of-plane modes in case of Rippard *et al.* [31]. When the signal is applied far from the oscillation frequency, it was observed that even at higher input signal power level of -10 dBm the signal is unable to pull the oscillation frequency of the spin valve. This shows that there are limits associated with the pulling range for injection locking the spin valve. These limits are dependent on the ability of the drive signal to break the symmetry of the oscillation mode or may be due to the absence of possible magnetization precession trajectory at the frequency of the applied AC input signal.

4.3 ***Terfenol-D spin valves devices***

We measured spin valves with Terfenol-D magnet as the free-layer to benchmark their performance. Terfenol-D has shown to have a large magnetostriction coefficient measured to be as high as 670 ppm, which when compared to typical magnetic materials (0.5-60 ppm) is of interest for building hybrid magnetostrictive stress controlled devices [74, 77]. Terfenol-D can be ideal for implementation of the strain-based magneto-acoustic oscillator, where the strain coupling from an HBAR to the Terfenol-D based free layer will be 20 times that of CoFeB free layer that we simulated in Chapter 3. The Terfenol-D spin valve device stack comprised of IrMn

/CoFe /Ru / CoFeGe (30 Å)/CoFe (5 Å)/Cu (40 Å) /TbDyFe. In the device, IrMn acts as the pinning antiferromagnet. The first CoFe layer which is pinned to the antiferromagnet is then antiparallel coupled due to the thin Ru spacer to the CoFeGe/CoFe layer. CoFeGe (30Å)/CoFe (5Å) is the reference layer of fixed magnet. TbDyFe is the free layer magnet which is separated from reference layers using a 40 Å thick Cu spacer. The thickness dimension of the SAF layers, the TbDyFe free layer, the materials used in the seed and capping layers and the fabrication process flow are proprietary information so are not disclosed. To benchmark the device performance, we tested a 50 nm radius circular, same as the CoFeGe/CoFe, spin valve.

4.3.1 DC Measurements of Terfenol-D spin valves

4.3.1.1 Resistance versus magnetic field

Terfenol-D Spin valve device resistance was measured using a lock-in amplifier in a voltage divider configuration as the externally applied bias magnetic field $H_{Applied}$ was swept from -1500 Oe to 1500 Oe and back (Figure 4.12(a)). The direction of $H_{Applied}$ is parallel to the direction of magnetization of the pinned reference layer. At 0 Oe $H_{Applied}$, we measured the device impedance to be 19.18 Ω, about 10 Ω less than the CoFeGe/CoFe devices of the same size (Figure 4.12(b)). When the bias field is increased, the device impedance reduces smoothly as the magnetizations of the reference layer and the free layer are aligned. As the $H_{Applied}$ is swept back, resistance measurements don't show any hysteresis. The device being circular in shape it doesn't have an in-plane shape anisotropy field. As a result, we don't observe abrupt switching from the antiparallel state to parallel state. At 1500 Oe $H_{Applied}$ the device resistance is about the equal to about 18.21 Ω. We consider this the resistance of the parallel state. The ΔR for the device was calculated using Equation (4.3) to be 0.98 Ω and device magnetoresistance MR was calculated using Equation (4.4) to be 5.36%. This value of

MR is smaller than the CoFeGe/CoFe devices but is on the higher side compared to typical spin valve devices. The change in resistance area product with magnetic field was 7.696 mΩμm^2.

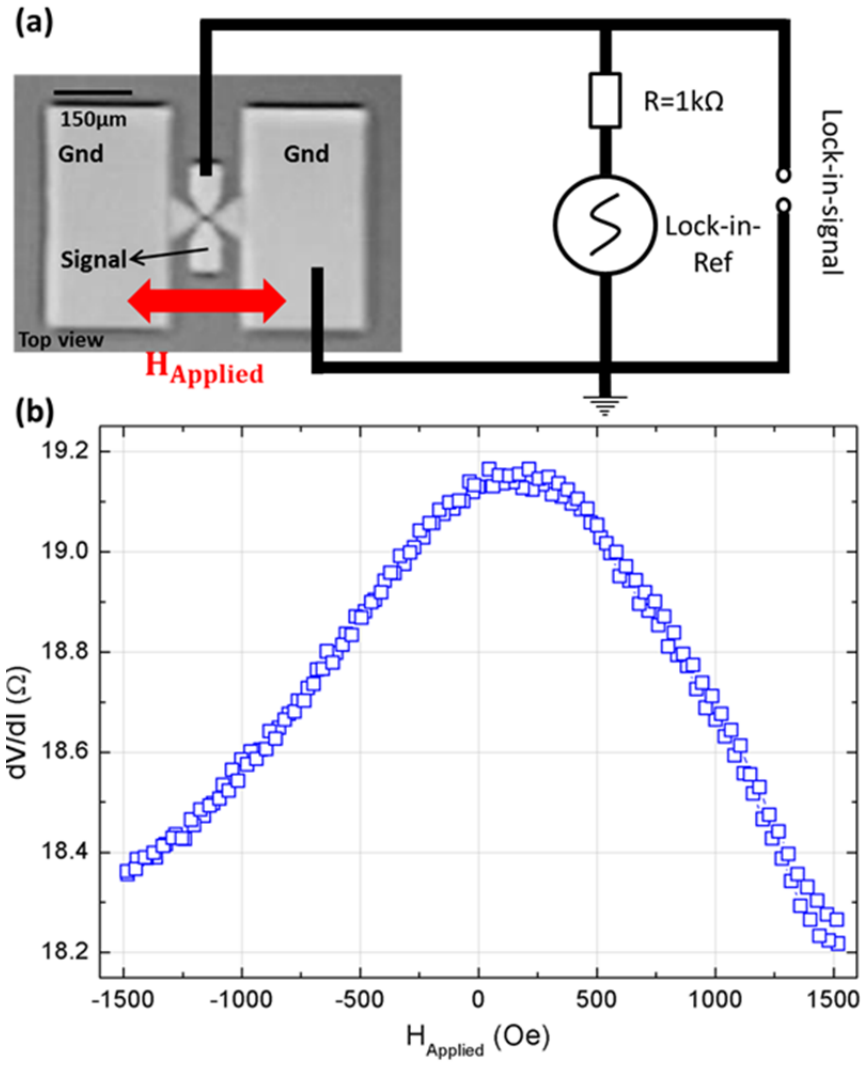

Figure 4.12: Resistance versus magnetic field measurements. (a) Measurement setup uses lock-in amplifier in a voltage divider configuration, with a reference 1 kΩ resistor, to measure the spin valve resistance as the magnetic field applied parallel to the direction of the polarizer is swept. (b) The plot of device resistance versus magnetic field showing an *MR* of 5.36% with a Δ*R* of 0.98 Ω.

4.3.1.2 Resistance versus DC bias current

Terfenol-D spin valve device resistance was measured using a lock-in amplifier in a voltage divider configuration, as the bias DC current I_{Bias} applied using a Keithley 2400 sourcemeter was swept from -1.5 mA to 1.5 mA and back (Figure 4.13(a)). The measurement was performed without applying any bias magnetic field. At 0 mA of I_{Bias}, we measured the device impedance to be 19.13 Ω (Figure 4.13(b)). When the bias current is increased, we observed the device impedance reduce smoothly as the spin torque from the polarized electrons aligns the magnetization of the free layer to the reference layer. With the negative current sweep, we measured the device resistance of 18.72 Ω at 1.5 mA of bias current. On the positive side, we observed a rapid change in resistance from 19.13 Ω to 18.38 Ω as the current is swept from 0 mA to 1 mA. As the current is further increased the device impedance increases to 18.45 Ω and remains constant till I_{Bias} of -1.5 mA. The overall change in resistance of the device, including the offshoot in the current sweep around 1 mA, is 0.75 Ω. This impedance change, though smaller than the CoFeGe/CoFe devices, is comparable to their change of 1.16 Ω. The rapid change is the resistance change observed only for the positive I_{Bias} was similar to one observed in CoFeGe/CoFe devices. This measurement confirms that spin transfer torque can change the resistance of the Terfenol-D spin valve. It is a necessary measurement to ensure that the spin valve device will show magnetization dynamics resulting in oscillations when biased at an appropriate bias current and magnetic field. The change in resistance also tells us that as the amplitude of spin torque changes, the oscillation mode shape and hence the frequency of oscillation will change with the bias current.

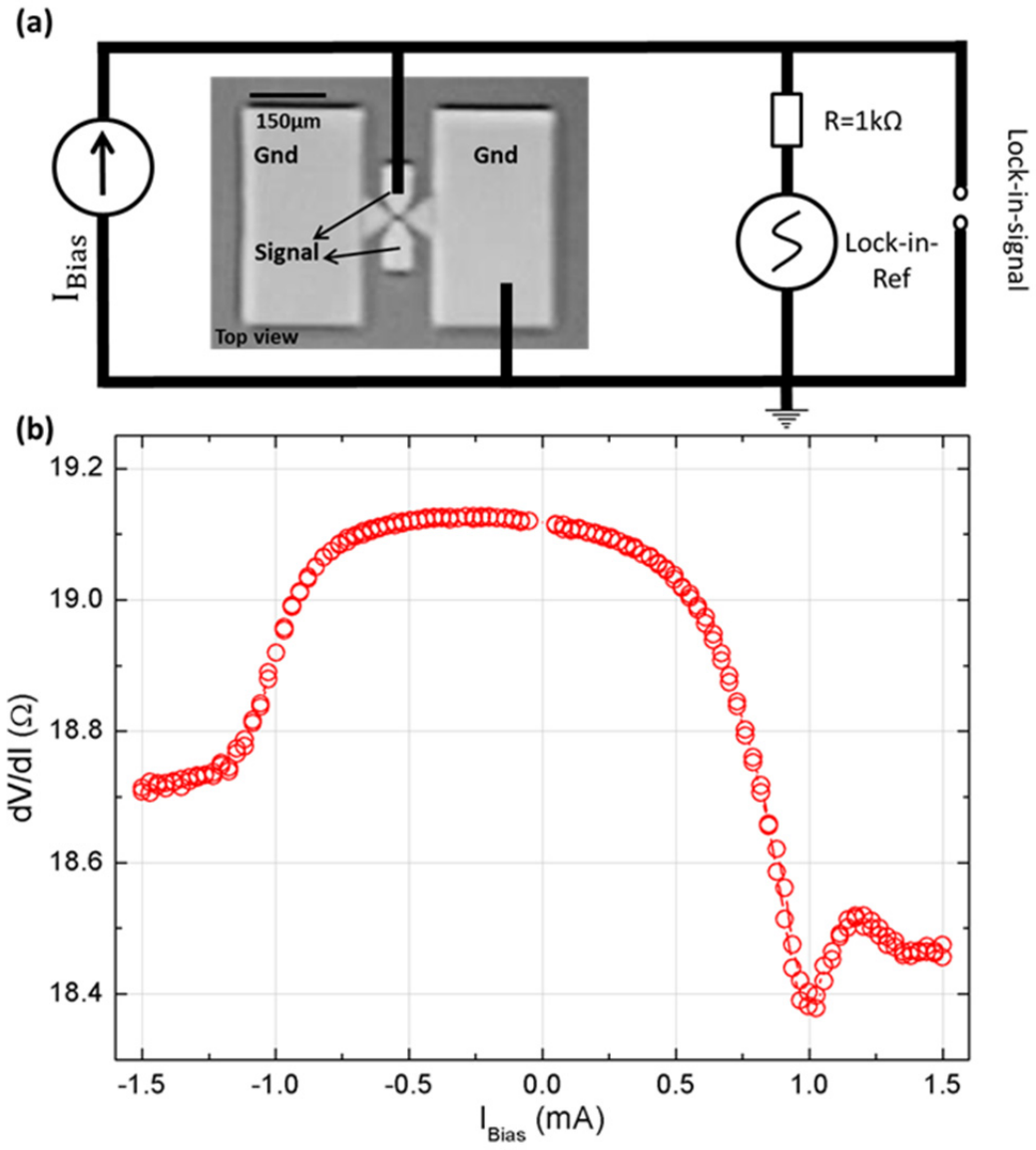

Figure 4.13: Resistance versus DC bias current measurements. (a) Measurement setup uses lock-in amplifier in a voltage divider configuration, with a reference 1 k Ω resistor, to measure the spin valve resistance as a DC bias magnetic field is applied using a Keithley 2400 sourcemeter is swept from -1.5 mA to 1.5 mA and back. (b) The plot of device resistance versus DC bias showing a total ΔR of 0.75 Ω.

4.3.2 High-frequency measurements of Terfenol-D spin valves

We biased Terfenol-D spin valve devices with a nominal magnetic field, $H_{Applied}$, of 0 Oe in a direction parallel to the polarizer/fixed layer magnetization. Using a bias tee and Keithley 2400 sourcemeter an I_{Bias} was applied to the device. The output of the capacitor (RF) end of the bias tee was connected to the spectrum analyzer (Figure 4.14(a)). The Spectrum analyzer is set for a 1 MHz resolution bandwidth and 6 kHz video bandwidth, selected to keep the noise floor as low as possible. All our measurements were carried out with using 30 data averages to ensure low noise. I_{Bias} was slowly increased to measure oscillation of the spin valves (Figure 4.14(a)). We measured oscillation with the fundamental mode at 3.9 GHz with a peak power of -88.5 dBm for an I_{Bias} of 500 μA (Figure 4.14(b)). The total power of the fundamental mode is measured to be 176.5 pW. The linewidth of the fundamental mode is 51.5 MHz, so the $\Delta f_o/f_o$ ratio of the oscillation mode is 75.73. The second harmonic at 7.8 GHz has a linewidth of 125 MHz, and total power is 93 pW.

We observed the oscillation frequency of the spin valve decreases with the increased bias current (Figure 4.15(a)). This implies that the mode of oscillation is in-plane. The change in the oscillation frequency for a 300 μA change in I_{Bias} from 400 μA to 500 μA was 375 MHz. This tuning range of 9.8% with 1.25 MHz/μA rate is comparable to 1.4375 MHz/μA rate observed for CoFeGe/CoFe spin valves. Driving the spin valves at constant I_{Bias} of 450 μA as the bias magnetic field $H_{Applied}$ was changed from -50 Oe to 250 Oe, we observed the frequency of oscillations reduce from 4.05 GHz to 3.25 GHz (Figure 4.15(b)). The frequency tunes with $H_{Applied}$ at a rate of 2.66 MHz/Oe compared to 0.9375 MHz/Oe observed for the CoFeGe/CoFe devices. The oscillation frequency decreasing the increasing external magnetic field implies that the $H_{Applied}$ counters the demagnetization field and reduces the overall magnetic field Terfenol-D free layer experiences.

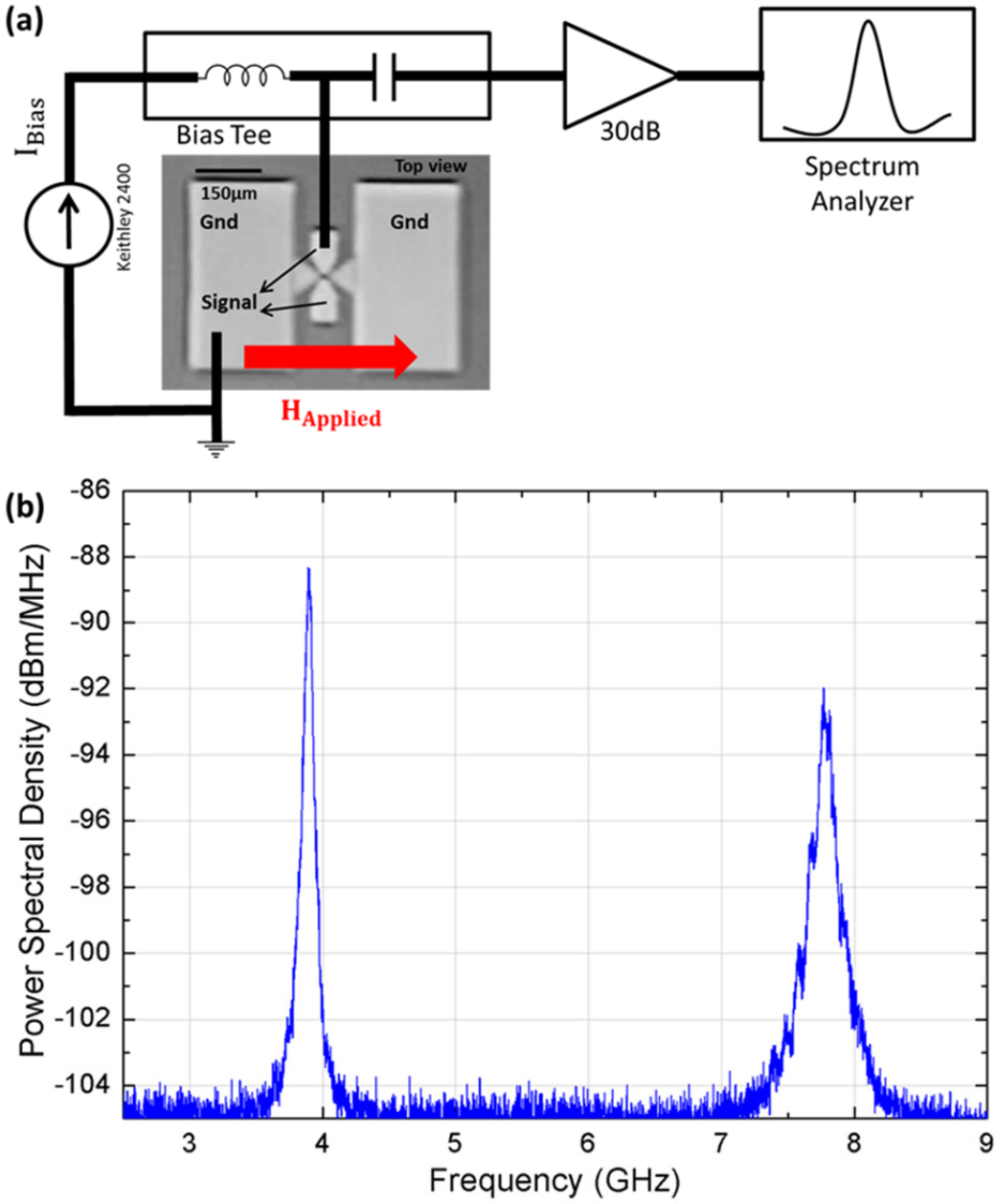

Figure 4.14: High-frequency measurements of Terfenol-D spin valve devices. (a) Measurement setup uses bias tee to apply DC bias current to spin valve devices, at a given bias magnetic field, the RF output of the devices is measured on the spectrum analyzer. (b) RF output of a spin valve device measured at I_{Bias} of 500 μA without any bias magnetic field.

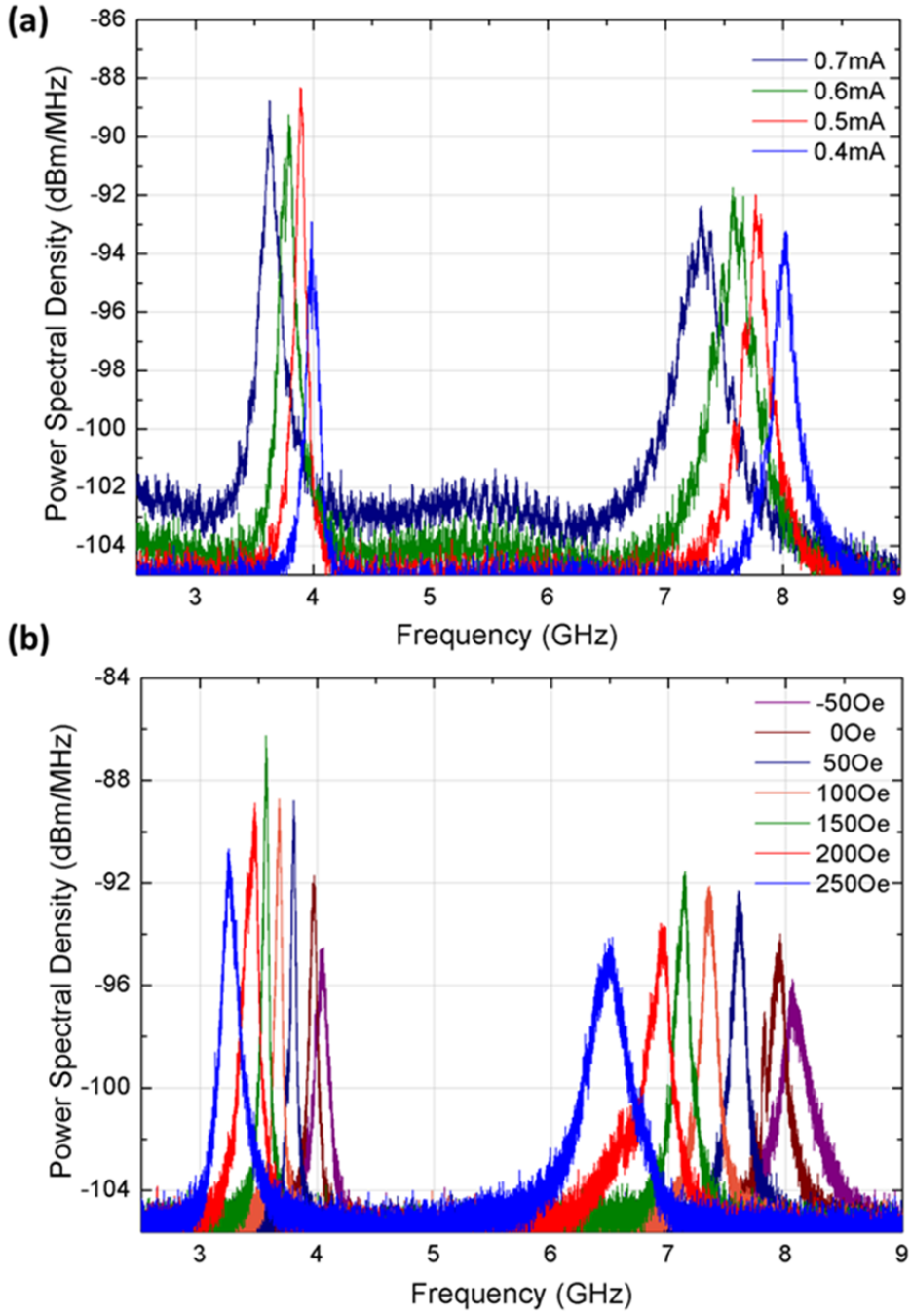

Figure 4.15: Tuning of spin valve oscillation frequency. (a) The plot shows the tuning of the fundamental frequency and the second harmonic with the bias current. (b) The plot shows frequency tuning of the fundamental mode and second harmonic with applied bias magnetic field for a device with a bias current of 450 μA.

4.3.3 Comparison to CoFeGe/CoFe spin valve devices

Terfenol-D spin valves measured here, performed remarkably similar to the CoFeGe/CoFe spin valves in DC characterization. They had comparable magnetoresistance to each other and the ΔR of both the devices was also similar. The biggest difference, we observed from the DC measurements was in the resistance of the device. This difference can either be attributed to the thicker CoFeGe/CoFe free layer or due to lower conductivity of CoFeGe layers used in the free layer.

In AC characterization, the overall behavior of the Terfenol-D spin valves was similar to that of CoFeGe/CoFe devices. The Terfenol-D device was two times more tunable with the magnetic field than the CoFeGe/CoFe spin valves, though their rate of tuning for bias current was comparable. This may because the demagnetization field for Terfenol-D devices was smaller than the CoFeGe/CoFe devices and hence, their dependence on the external field is higher.

We believe the damping of both Terfenol-D and CoFeGe/CoFe layers are also comparable or at least are in order of magnitude of each other due to the similarity of their magnetization dynamics. This observation is in contrast to some of the high values of Gilbert damping reported in the literature for similar films [78]. Since we are not aware of the exact doping of the alloy contents or the deposition method we are unable to make a direct comparison. Some of the similarities in measurements even with higher damping for Terfenol-D can be explained away due to smaller saturation magnetization (M_s) of 600 emu/cm^3 compared to 800-1200 emu/cm^3 for CoFeGe/CoFe devices, which depends on the doping percentage of germanium. Further investigation is required to comment with certainty about the damping of the Terfenol-D layer in the spin valves compared to CoFeGe/CoFe even though functionally as oscillators their behavior is rather similar.

4.4 *Current based magneto-acoustic oscillator using spin valves*

4.4.1 Open loop current based magneto-acoustic oscillator

Laterally coupled HBAR devices described in Chapter 2.3.2 are ideal to be used as multi-frequency high quality factor filters which are operational over a frequency range of 1.5-7 GHz. We aim to use these filters in a feedback configuration with the CoFeGe/CoFe spin valve to build a current-based magneto-acoustic oscillator. The oscillation output from the spin valve will be first amplified and then filtered by the HBAR resonator. Due to the narrow passband of the HBAR filter, most of the spin valve linewidth is rejected, and only the signal in the pass band is allowed to pass unfiltered, thereby generating a narrow linewidth signal of much higher $\Delta f_o/f_o$ ratio than STO oscillation linewidth. This signal when amplified and used to injection lock the spin valve, like an external AC drive, described earlier in Chapter 4.2.3, will reduce the linewidth of the STO to that of the injection locking signal. The linewidth of the spin valve which we measured to be around 36 MHz at 3.6 GHz will then reduce the bandwidth of the passband of the HBAR resonance at that frequency, thus enhancing the overall $\Delta f_o/f_o$ ratio of the spin valve oscillator.

Towards the goal of building the above described closed-loop feedback system, we perform open loop measurements of the current-based magneto-acoustic oscillator. Where the oscillation signal from bias current driven spin valve device is first amplified and then filtered by a laterally coupled HBAR is measured on a spectrum analyzer (Figure 4.16(a)). The initial amplification of the signal is necessary as HBARs have a transmission loss of -25 dB, which without amplification would cause the oscillation signal to drop below the noise floor of the spectrum analyzer. The output from the standalone spin valve driven by I_{Bias} was directly measured, without filtering, for comparing it to the filtered HBAR output.

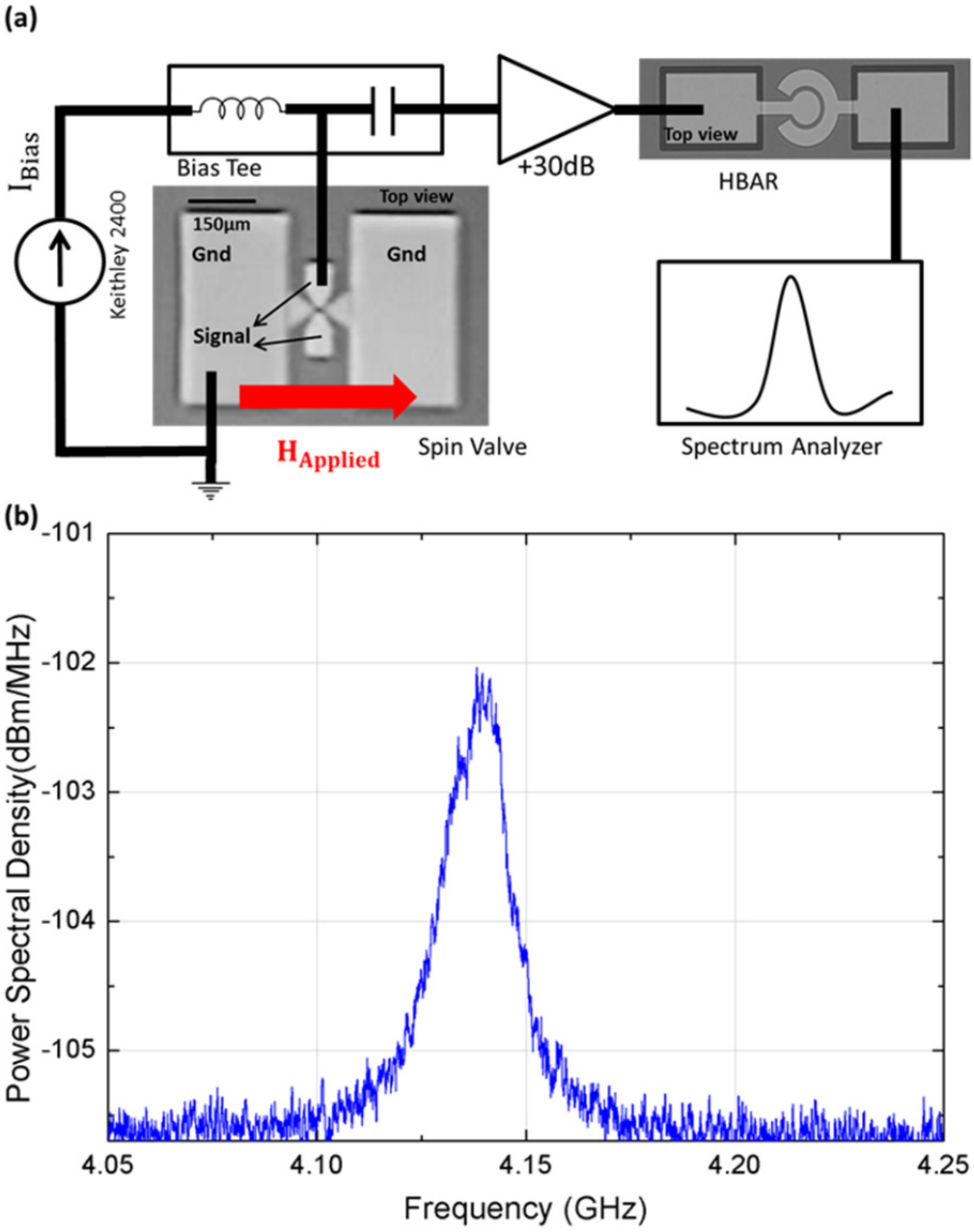

Figure 4.16: (a) Experimental setup for open loop measurements. Oscillation signal from the spin valve is amplified and the filtered by HBAR and measured on the spectrum analyzer. (b) Oscillation of a 50 nm radius CoFeGe/CoFe spin valve device measured for 370 μA of bias current had a linewidth of 35.4 MHz and $\Delta f_o/f_o$ ratio of 116.9.

4.4.2 Results for open loop current based magneto-acoustic oscillator

The standalone CoFeGe/CoFe spin valve device oscillates at 4.14 GHz for an I_{Bias} of 370 μA with $H_{Applied}$ of 0 Oe (Figure 4.16(b)). The oscillation measured had a linewidth of 35.4 MHz for a $\Delta f_o/f_o$ ratio of 116.9. For this measurement, the device was measured directly without any amplification by connecting the RF end of the bias tee directly to the spectrum analyzer. The peak output power of the device was measured to -102 dBm about 4 dB above the noise floor of our measurement. The total power of this mode was calculated to be 4.5 pW. The device was then connected to the HBAR filter via a 30 dB broadband amplifier for doing open loop measurements. The transmission response of the HBAR was measured for the bandwidth of interest using a network analyzer (Figure 4.17(a)).

The output of the HBAR measured was plotted on top of the previously measured oscillation spectrum of the spin valve (Figure 4.17(b)). We observed a sharp signal peak in the center of the spectrum that corresponds to the oscillation peak of the spin valve device. The oscillation frequency was selected to ensure that the HBAR filter transmission peak coincides with the oscillation peak to get the best response from the filtering system. This frequency centering was easy to achieve as the HBAR has resonances spaced by Δf of 9.1 MHz. The linewidth of the filtered spin valve was measured to be 175 kHz, which corresponds to a $\Delta f_o/f_o$ ratio of 23,657. This is the highest reported $\Delta f_o/f_o$ ratio for an open loop spin valve in an in-plane mode of oscillation [37]. The measured linewidth depends on the quality factor of HBAR at the frequency of STO oscillation. A closed loop system with the HBAR in feedback will further reduce the linewidth to get a record breaking $\Delta f_o/f_o$ ratio. The peak output power of the device was observed to be -98 dBm this increase in power by 4 dB from the unfiltered spin valve device is due to the 30 dB gain of the amplifier followed by a transmission loss of -26 dB from the HBAR. We also observe sideband like peaks

around the large central peak of the oscillator output. These arise from the nearest HBAR resonances, which are spaced from the central resonance by Δf of only

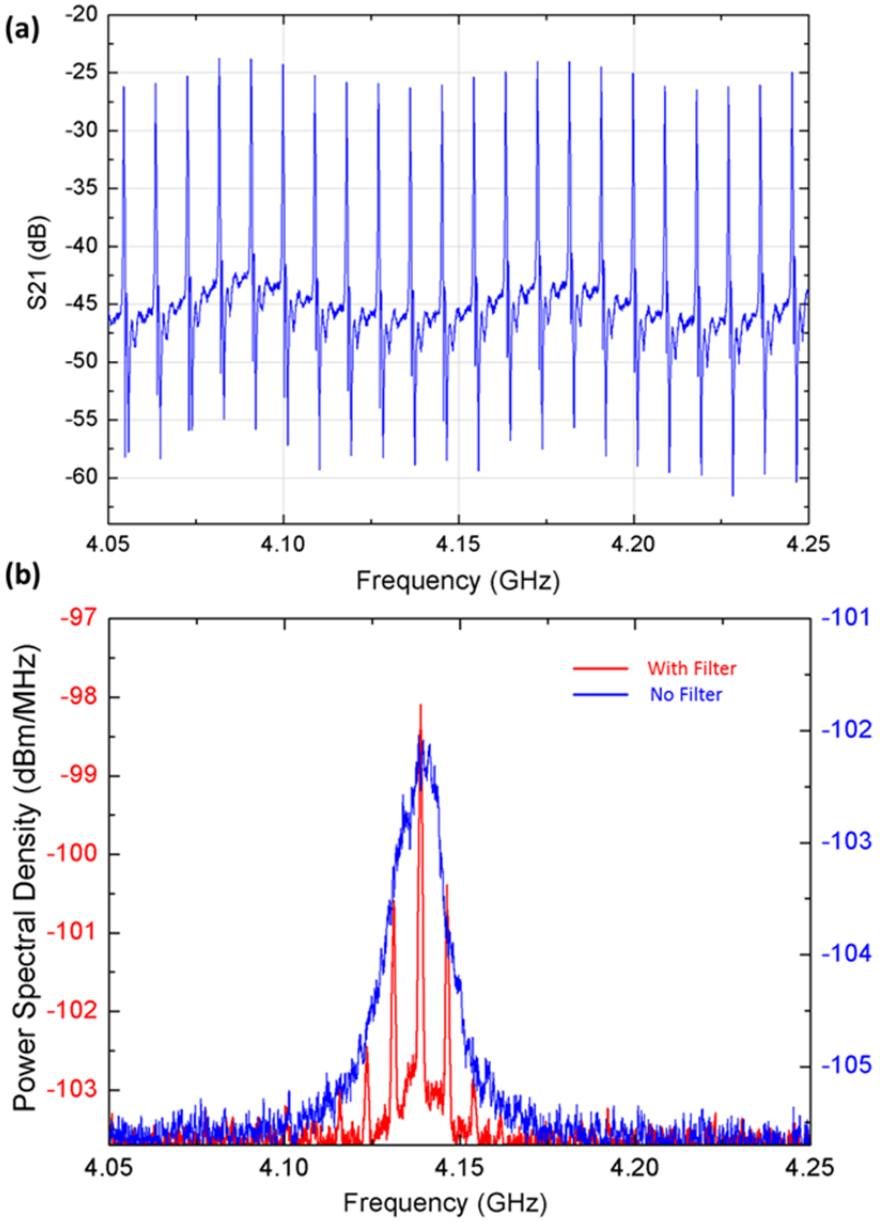

Figure 4.17: (a) Plot shows transmission spectrum of the laterally coupled HBAR used for filtering the spin valve oscillations. (b) The plot shows the frequency spectrum of the spin valve oscillator measured after HBAR filtering shown in red and the frequency spectrum of the oscillator without HBAR filtering for comparison.

9.1 MHz and hence lie in the large linewidth (36.6 MHz) of the spin valve device. For a smaller linewidth STO, less than 9.1 MHz, the output of the HBAR would only show the large single oscillation peak. This problem can also be fixed by using a thinner substrate for laterally coupled HBAR filter. For a substrate of thickness 300 μm the spacing between two HBAR resonances will be 20 MHz allowing for effective operation with an STO having linewidth less than 20 MHz.

4.4.2.1 Tuning of the open loop current based magneto-acoustic oscillator

I_{Bias} or the $H_{Applied}$ can be used to tune the oscillation frequency of the spin valve. As the oscillation frequency of the spin valve changes, the oscillation mode traverses across the multi-frequency filter comb of HBAR resonances (Figure 4.18). The oscillation signal gets shaped by the HBAR transmission spectrum. The best response

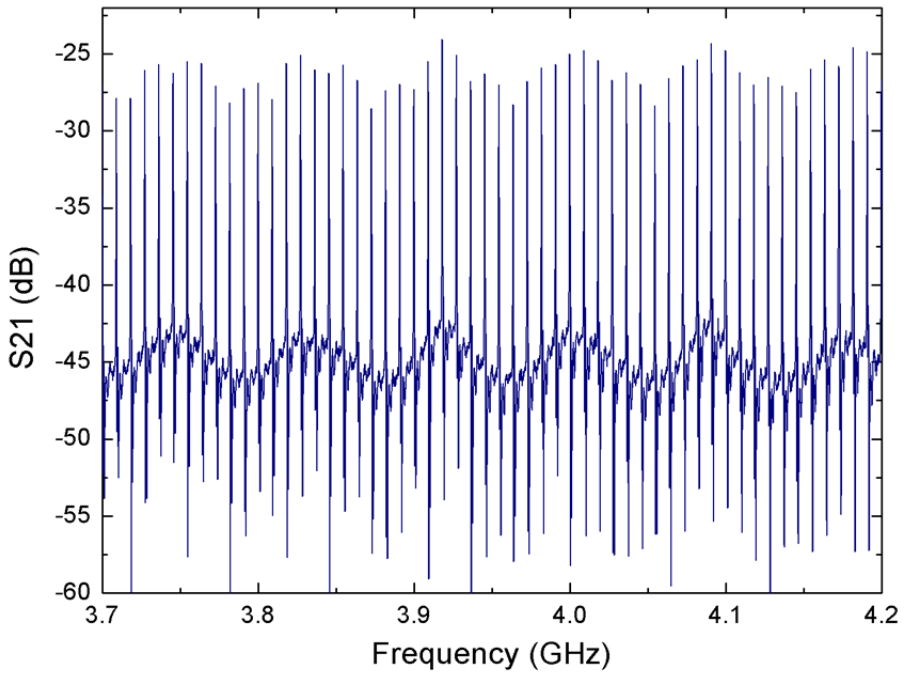

Figure 4.18: HBAR transmission spectrum for the frequency range of 3.7 GHz to 4.2 GHz shapes the oscillation output of the spin valve.

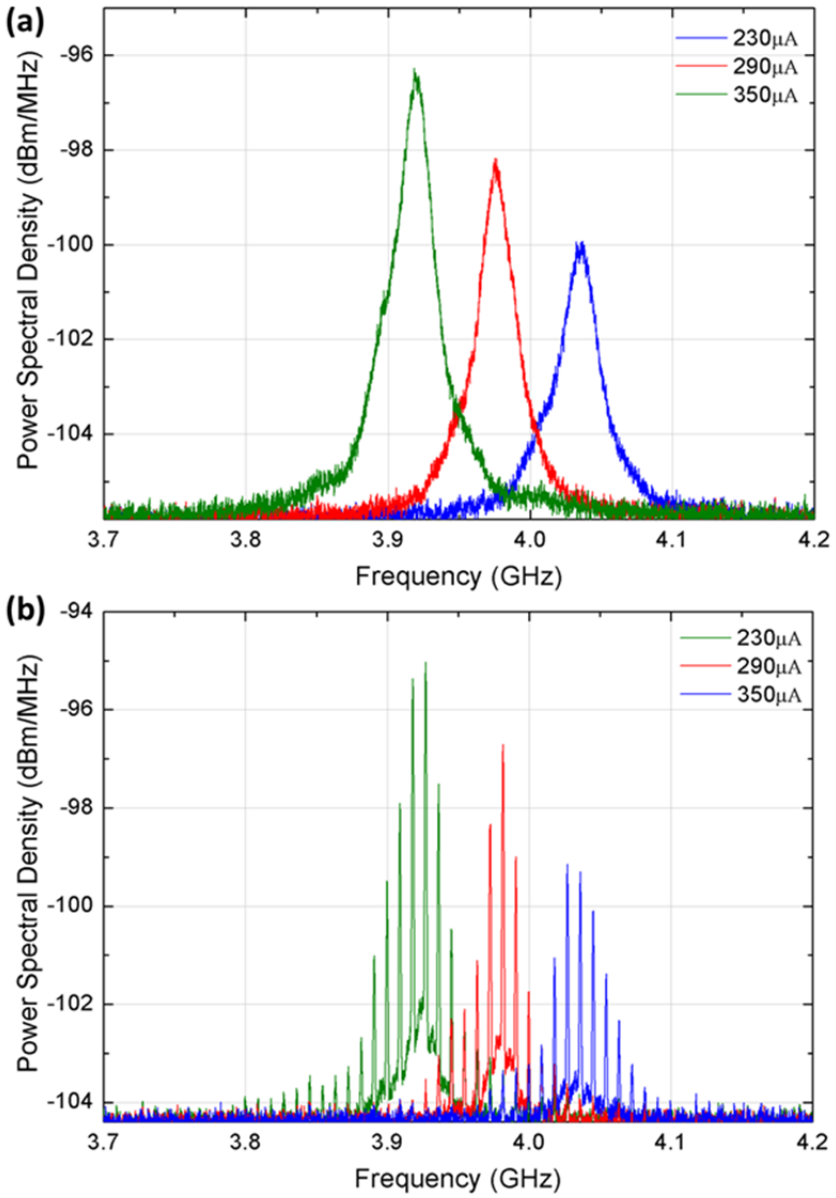

Figure 4.19: Frequency tuning of spin valve oscillator in the presence of in line HBAR filter. (a) The frequency spectrum of a spin valve oscillator shows oscillations frequency decrease as I_{Bias} is swept from 230 μA to 350 μA. (b) The frequency spectrum of the spin valve oscillator after the HBAR filters it shows about 195 times reduction in linewidth of central oscillations frequency as the frequency of the spin valve is tuned with I_{Bias}.

is when the oscillation peak corresponds to HBAR resonance frequency. By changing the I_{Bias} from 230 μA to 350 μA, the oscillation frequency of the spin valve was tuned from 4.036 GHz to 3.92 GHz (Figure 4.19(a)). The output of the spin valve device showed a reduction in linewidth from 35.2 MHz to 180 kHz for I_{Bias} of 230 μA. This corresponds to a 195x improvement in the $\Delta f_o/f_o$ ratio (Figure 4.19(b)). Similar improvement was measured for the lower frequency oscillation, measured for I_{Bias} of 350 μA, whose linewidth of 24.5 MHz is reduced to 178 kHz. Thus, the frequency tuning capability of the spin valve is unhindered by the HBAR filter. We have measured similar filtering and $\Delta f_o/f_o$ ratio enhancement of the spin valve oscillator across the frequency spectrum of HBAR from 2.5 GHz all the way up to 6 GHz.

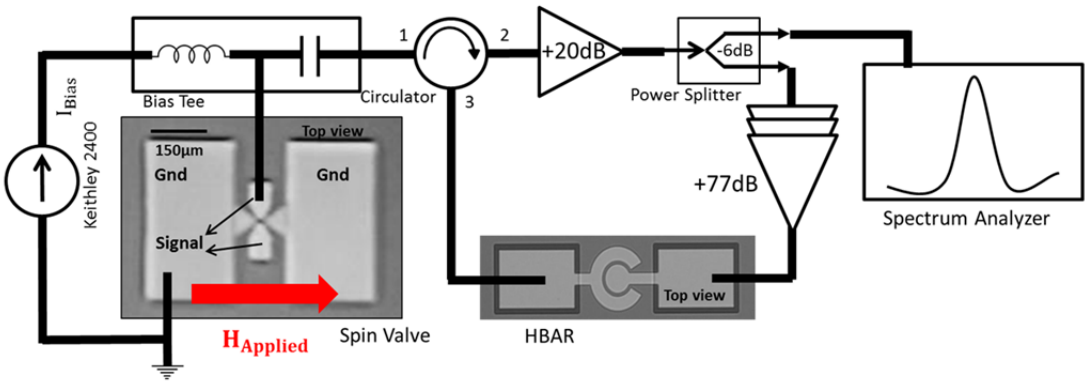

Figure 4.20: Experimental setup used for measuring the closed loop response of current based magneto-acoustic oscillator.

4.4.3 Closed loop current based magneto-acoustic oscillator

Locking experiments on the spin valve showed that the threshold power for current locking of the spin valves for its fundamental mode of operation was around -25 dBm. With the HBAR device having -25 dB transmission loss, the overall gain needed for a spin valve device of an output power of -90 dBm for injection locking itself is around

90 dB. We used four broadband amplifiers in a signal chain with gains of 20 dB, 25 dB, 27 dB and 25 dB each to get a net gain of 97 dB to amplify the spin valve output. The signal from the amplifiers was then filtered by HBAR for reducing the linewidth of the spin valve oscillator. The arrangement of the amplifiers was chosen to be in the increasing order of the noise figure to ensure that closed loop system will have the best optimal noise performance. The output of the first amplifier is split using a broadband power divider and is connected to the spectrum analyzer to measure the closed loop response. This reduces the loop gain by 6 dB, but the amplifier chain, has enough gain to amplify injected power to -24 dBm. The output of the HBAR is then connected back to the spin valve via a circulator (Figure 4.20). The arrangement of the signal chain, with the filter in the middle of the amplifier chain was also tried, but the results obtained for the system remain the same. When the loop is connected, and the amplifiers in the feedback path are off, the spectrum analyzer shows the amplified output of the spin valve output at 3.43 GHz (Figure 4.21(a)). When the amplifiers in the feedback path are turned on, we observe a very sharp peak on the spectrum analyzer having a power of -40 dBm at 3.563 GHz (Figure 4.21(b)). Changing the bias current drive of the spin valve device doesn't affect the sharp signal. Even when the current drive to the spin valve is turned off the signal remains unchanged. This shows that the measured close loop response was the oscillation signal of the HBAR, rather than the locked spin valve device.

Low isolation of only -14 dB of the circulator results in the amplified HBAR output to feedback and thus oscillates the HBAR. HBAR has multiple resonances, so only for the resonant frequency at which the Barkhausen criterion is met goes into oscillation. We believe the limiting factor for the oscillation is phase matching rather than the loop gain. The loop gain necessary for the HBAR oscillation is approximately

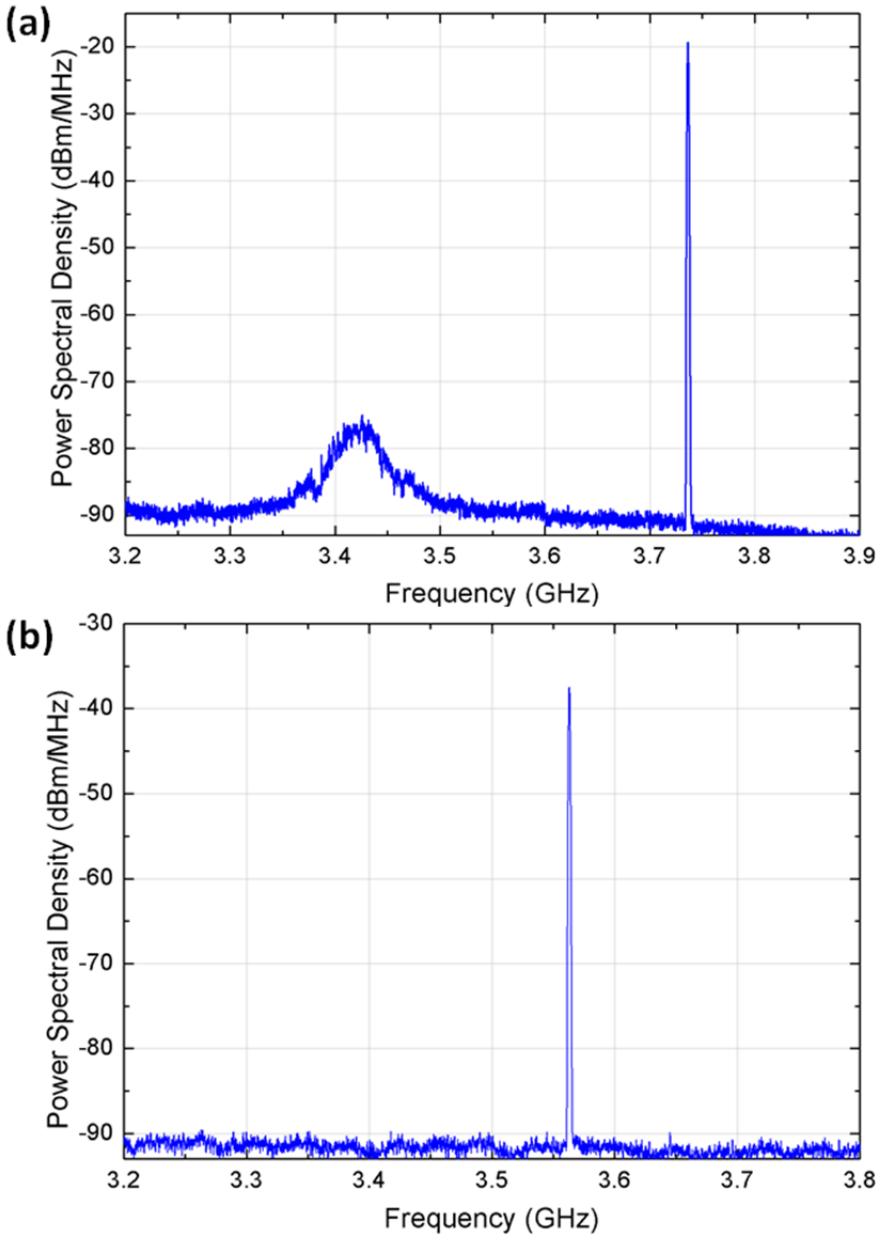

Figure 4.21: Frequency spectrum of the output of closed loop current based magneto-acoustic oscillator. (a) Plot shows the amplified output of the spin valve oscillator, measured at I_{Bias} of 430 μA, when the feedback amplifiers are turned off. (b) Plot shows the HBAR oscillator output that locks the spin valve device when the feedback amplifiers are turned on.

45 dB, which includes the -25 dB transmission loss of the HBAR device, the -14 dB isolation of the circulator, and the -6 dB loss from the power divider. Repeating the closed measurements with a lower number of amplifiers such that the loop gain is less than 45 dB, the closed loop output shows a free running spin valve oscillator response. This is because the output power of -60 dB is not enough to injection lock the spin valve oscillator. To get closed loop current locking of the spin valve devices, we calculate the isolation needed in the circulator is 66 dB so that the spin valve device can be injection locked by the filtered HBAR response. Such circulators, with a wideband operation, aren't commercially available. Lack of which limits the realization of the closed loop current-based magneto-acoustic oscillator. The constraints on the isolation performance of the circulator are exacerbated by the low output power of the spin valve devices. For a higher output power device, with signal output in 10-100 nW power level, would require 40 dB to 50 dB lesser gain for injection locking. This reduces the needed circulator isolation to a range of 20 dB to 30 dB. Such circulators with moderate isolation range are commercially available.

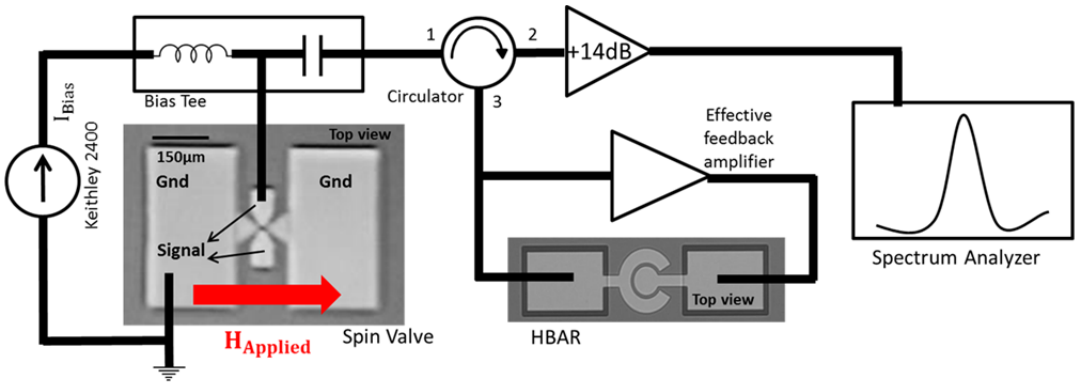

Figure 4.22: Effective experimental setup of closed loop magneto-acoustic oscillator shows an HBAR oscillator injection locking a spin valve oscillator when the feedback gain is more than 51 dB.

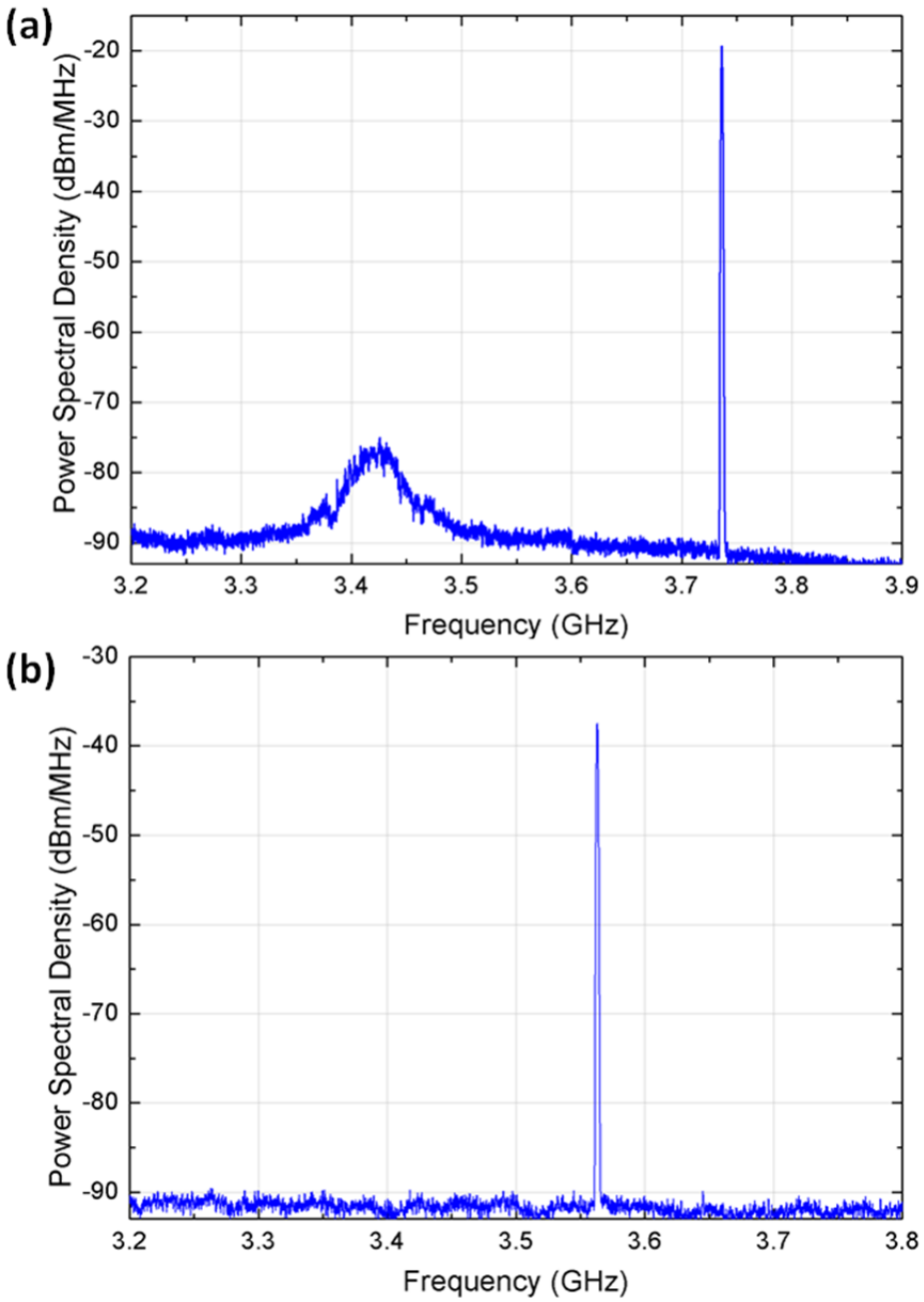

Figure 4.23: Frequency spectrum of the spin valve while being injection locked by the HBAR oscillator. (a) The plot shows the HBAR oscillator output at 3.74 GHz is unable to injection lock the 3.43 GHz spin valve oscillation measured at I_{Bias} of 430 μA. (b) Plot shows the new HBAR oscillation at 3.56 GHz injection locks the spin valve oscillator.

4.4.3.1 HBAR oscillator induced injection locking of CoFeGe/CoFe devices

The closed loop measurements of the current based magneto-acoustic oscillator because of the poor isolation of circulator and due to the low output power of the available spin valve devices result in oscillation of the HBAR resonator. The oscillation frequency of the HBAR, due to its multiple resonances, is set randomly by the combination of amplifiers used in the feedback system. By picking and choosing a different set of amplifiers, we get to set the oscillation frequency coarsely. Since the output of the HBAR is connected to the input of the spin valve in the closed loop configuration the HBAR oscillator output is injected into the spin valve device (Figure 4.20). Thus the closed-loop current-based magneto-acoustic oscillator system can be envisioned as an HBAR oscillator injection locking a spin valve device (Figure 4.22).

In the HBAR injection locking of the spin valve device, we observe that when the HBAR oscillation output frequency is far from the spin valve oscillation frequency, both the spin valve oscillation and the HBAR oscillation can be measured simultaneously (Figure 4.23(a)). This is similar to the result observed for injection locking, when the AC signal from the signal generator is injected out of the pulling range of the spin valve device (Figure 4.11(b)). By changing the combination of amplifiers available to us, we change the oscillation frequency of the HBAR to bring it closer to the spin valve oscillation frequency. We then observe that the spin valve oscillation vanishes from the spectrum as the spin valve gets locked to the HBAR oscillation (Figure 4.23(b)). Repeating similar measurements for a different spin valve device having an oscillation frequency of 5.05 GHz (Figure 4.24), we were able to verify that the closed-loop current-based magneto-acoustic oscillator behaves as HBAR oscillator injection locking a spin valve device. Such a system will benefit from the extremely narrow linewidth of the HBAR oscillator, but due to lack of direct

control over the frequency of the HBAR oscillator, the system won't be tunable in frequency.

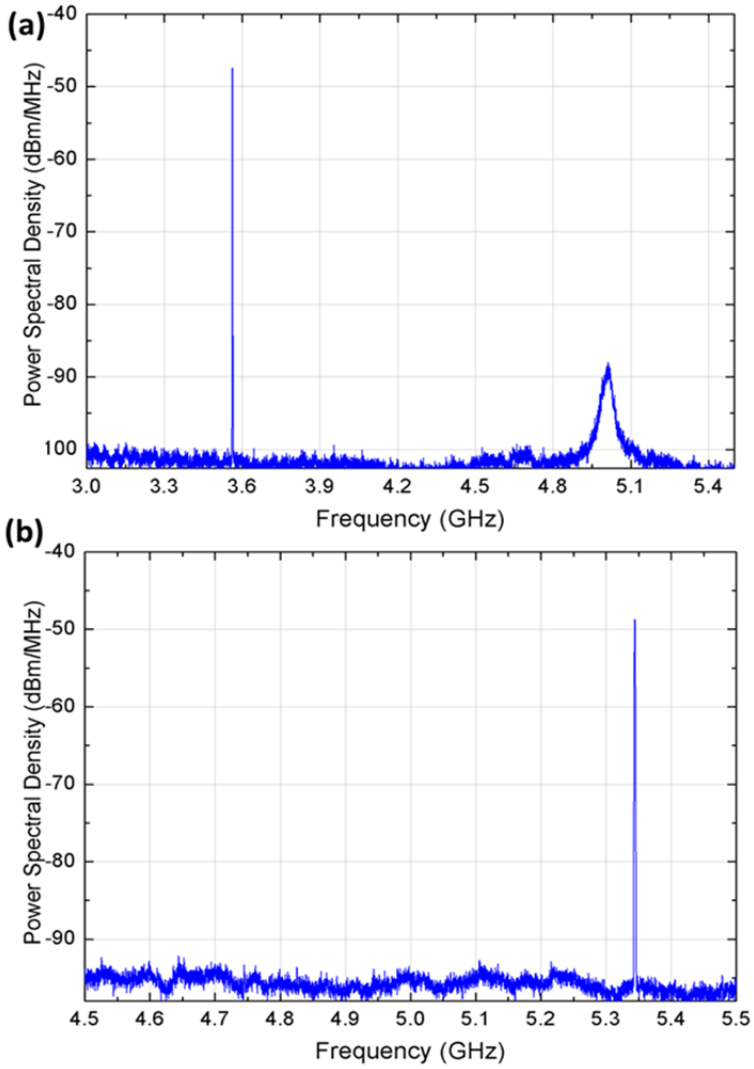

Figure 4.24: Frequency spectrum of the spin valve while being injection locked by the HBAR oscillator. (a) The plot shows the HBAR oscillator output at 3.58 GHz is unable to injection lock the 5.05 GHz spin valve oscillation measured at I_{Bias} of 400 μA. (b) The plot shows the new HBAR oscillation at 5.34 GHz injection locks the spin valve oscillator.

4.5 *Conclusion and future directions*

In this chapter, we introduced spin valve devices and described how the spin-dependent scattering of the s band electrons results in magnetoresistance. The resistance of the spin valves is low when majority electrons dominate the current flow because of the magnetizations being parallel to each other. The resistance of the device is high when the scattering at the interface is high because of the antiparallel orientation of magnetizations. Resistance versus magnetic field measurements showed a high MR of 5.93% for CoFeGe/CoFe spin valves. Resistance versus bias current measurements showed that the resistance, and thus the direction of magnetization of the free layer of the spin valve devices, could be controlled by applying spin transfer torque. AC measurements on spin valves measured in-plane oscillation mode had $\Delta f_o/f_o$ ratio of 98.63 at 3.6 GHz with a total power of 32 pW. The oscillation frequency of the spin valve was then tuned with both a bias current and an applied magnetic field to study the tunability of the device. Injection locking measurements showed a threshold power of -25 dBm is needed for implementing current-based magneto-acoustic oscillator.

Spin valves devices with TbDyFe (Terfenol-D) as a free layer were measured and characterized. DC measurements on these spin valves revealed that they have comparable MR of 5.36%. AC measurements on Terfenol-D spin valves showed magnetization dynamics that are similar to that of spin valve device with an increased susceptibility to magnetic field tuning. We were not able to comment about the damping of the Terfenol-D devices with high certainty without further measurements. We do make an observation that due to the comparable spin dynamics of Terfenol-D and CoFeGe/CoFe spin valve devices the damping for Terfenol-D devices should be within an order of magnitude of the CoFeGe/CoFe devices.

We measured open loop current-based magneto-acoustic oscillator, where the output from the spin valve is amplified and then filtered by the high quality factor laterally coupled HBAR devices. This system has shown to significantly enhance the linewidth of the spin valve oscillators with $\Delta f_o/f_o$ ratio as high as 23,657 measured for in-plane oscillation mode at 4.14 GHz. This enhancement in linewidth is due to the narrow bandwidth of the HBAR filtering the spin valve oscillator. The small spacing of 9.1 MHz of the HBAR results in sideband like peaks when the linewidth of the oscillator is bigger than 9.1 MHz. Laterally coupled HBAR on thinner substrates are necessary for more efficient filtering of the CoFeGe/CoFe spin valves. The open loop system has a large bandwidth of operation over the entire HBAR spectrum of 2 GHz to 6 GHz and thus, is an easy way of getting narrow linewidth tunable oscillator.

Lastly, we implemented a self-locking closed loop current based magneto-acoustic oscillator. Due to the low output power of the free running spin valve oscillators, it was necessary to amplify the signal by at least 90 dB to get current-based injection locking. But due to the low isolation of the circulator and high loop gain the laterally coupled HBAR is driven into oscillations instead. Attempts at closing the loop with less gain, to avoid HBAR oscillation, were unable to injection lock the spin valve oscillator. We deduced that the solution to this problem could be solved in two ways. The first way is to use an extremely high isolation circulator with approximately 60 dB isolation for implementing the injection locking of low power spin valve oscillator. The second way is to use spin valve devices with 4 orders of magnitude higher output power, which will need a moderate isolation of -20 to -30 dB from the circulator. Using the HBAR oscillator, we were able to injection lock the spin valve oscillator at multiple frequencies to get extremely narrow linewidth output. But since there is no control over the oscillation frequency of the HBAR, this method of

improving the spin valve oscillator linewidth is of little application. The spectrum of the HBAR oscillator and its measured phase noise are shown in Chapter 7.2.

In the future, we would like to increase the spacing between the adjacent resonances of the HBAR filter by fabricating devices on a thinner substrate. Transmission loss of laterally coupled HBARs could be further improved by reducing the gap between the electrodes. Both these steps will make the open loop current based magneto-acoustic oscillator an extremely efficient, easily implementable, and a full octave tunable narrow linewidth oscillator. We also would like to implement a closed loop current-based magneto-acoustic oscillator, using a higher output power STO that could potentially be injection locked at lower injection voltage and hence could be implemented with a commercially available circulator.

CHAPTER 5

SPIN HALL EFFECT – MTJ FOR SWITCHES AND MAGNETO-ACOUSTIC OSCILLATORS

5.1 *Introduction*

In a magnetic tunnel junction (MTJ), we have two ferromagnetic layers separated by tunneling barrier. As we discussed in Chapter 4.1, the current in the ferromagnetic material consists of both majority and minority electrons. Electrons with magnetic moments parallel to the magnetization direction are called the majority electron, while electrons with magnetic moments antiparallel to magnetization are called minority electrons. In a tunneling process, where an electron spin is conserved, the tunneling resistance depends on whether the magnetizations of the two ferromagnets are parallel (P) or antiparallel (AP).

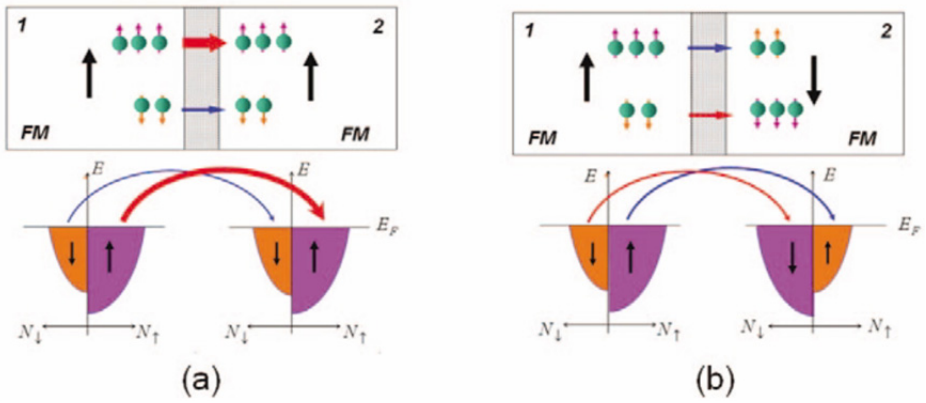

Figure 5.1: Schematic of TMR effect in MTJ shows that the spin of the electrons is preserved during tunneling which leads to two different tunneling situations. (a) Parallel state, where majority and minority carriers tunnel into their sub-bands in the two ferromagnets and (b) antiparallel state, where the majority and minority carriers sub-bands are opposite in the two ferromagnets. Adopted from [79].

Tunneling conductance depends on magnetization due to the difference in the density of states at the Fermi level of the majority and minority electrons. Because the tunneling process preserves spin, the majority, and the minority electrons can only tunnel into their individual sub-bands [79]. If the magnetizations of the ferromagnets across the tunneling barrier are aligned, the numbers of available states for tunneling majority and minority electrons are large as they tunnel into their individual sub-bands. On the other hand, if the magnetizations of the two ferromagnets are antiparallel, then the majority electrons for the first ferromagnet will have to tunnel into the minority sub-band of the second ferromagnet and vice versa (Figure 5.1). As there is a difference in the number of states available for the majority and minority electrons, this creates a difference in resistance for the P and AP state of the magnetizations of the two ferromagnets. Tunneling dependent magnetoresistance (TMR), defined as the ratio of the resistance change, is given by the equation:

$$TMR = \frac{R_{AP} - R_P}{R_P} \tag{5.1}$$

where R_{AP} is the resistance of the AP state, while R_P is the resistance of the P state of the magnetization. Julliere *et al* .[80] extended this definition to:

$$TMR = \frac{2P_1P_2}{1 - P_1P_2} \tag{5.2}$$

where $P_1$and P_2 are the polarization factors for the two ferromagnets respectively, are dependent on the density of states of the majority and minority electrons in the two ferromagnets. Butler *et al.* [81] predicted extremely high TMR ratios for Fe/MgO/Fe MTJs, where they suggested crystalline MgO with (001) orientation will enhance the

lattice matching with the (001) plane of the BCC Fe. This will improve the TMR because of the spin dependent matching of the evanescent states within the tunnel barrier and the electronic states of the Fe electrodes. By using this approach and by crystallizing MgO via post-process annealing TMR as high as 350% have been achieved [82]. High TMR of MTJs is important as it makes MTJs better matched to silicon-based electronics and thus enables better control of MTJ when used as a memory cell. In the context of oscillators, high TMR is desirable for a low resistance area product device to generate oscillations of a higher power. In Chapter 3.2.1, we discussed how spin currents in an MTJ applies a torque to the free layer ferromagnet to switch the magnet or to overcome damping in the magnet, thereby getting steady state precession based oscillations. Traditionally, the spin current is generated by passing a charge current through a ferromagnet in the MTJ stack called polarizer, which aligns the electron spin along the direction of its magnetization due to spin transfer torque. However, this method is inefficient and recently a new method that relies on spin Hall effect has been proposed for generating spin currents [83].

The spin Hall effect (SHE) was first predicted by Dyakonov and Perel [84, 85], where they predicted a charge current flow in the presence of spin-orbit coupling would generate a spin current in the direction orthogonal to charge current flow. A spin current is a flow of electrons with one orientation of spin in one direction and electrons with opposite orientation of spin in the opposite direction. Hirsch introduced the “spin Hall effect” term calling it similar to Hall effect [86], where charges are accumulated on the surface edge in a direction orthogonal to charge current flow in the presence of external magnetic field because of the Lorentz force. However, there is no requirement of a magnetic field to generate spin current in SHE. The spin current, unlike the charge current, is not conserved, so the value of spin polarization at the boundary of materials is limited by the spin relaxation and the area over which spin is

accumulated is dependent on spin diffusion length [87]. The origin of spin Hall effect, like the anomalous Hall effect, is due to the relativistic effect of spin-orbit coupling. Spin-orbit coupling can be considered as the Magnus effect equivalent for electrons, where an electron deviates from its straight path due to the direction of its spin.

Liu *et al.* successfully utilized the spin current generated by spin Hall effect in β-Ta for spin torque switching of the CoFeB ferromagnet coupled to it [16]. The switching of the CoFeB magnetization was then sensed by using TMR effect, where the CoFeB was the free layer of the MTJ (Figure 5.2). Thus, they demonstrated a new generation of three-terminal MTJ, where a charge current flow through the tantalum channel generates spin current in a transverse direction. The orientation of the electron spin impinging on a surface can be given by left-hand rule for a material with

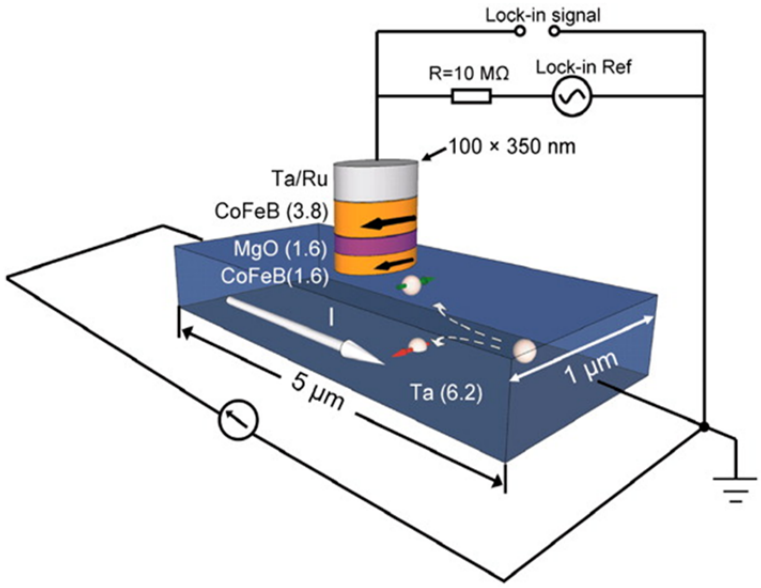

Figure 5.2: Schematic of three-terminal SHE-MTJ showing the direction of applied current and the corresponding spin current generated by SHE. The spin current generated by spin Hall effect is used to switching the magnetization of free layer magnet. Adopted from [16].

positive spin Hall angle. Spin Hall angle, θ_{SH}, is given by the equation:

$$\theta_{SH} = \frac{J_S}{J_e} \tag{5.3}$$

where, J_e is the charge current density, and $[\hbar/(2e)]J_s$ is the spin current density generated by the spin Hall effect, is a property of the material and its amplitude is dependent on the strength of spin-orbit coupling in the material. Here ħ is the reduced Planks constant and e is a charge of the electron. The spin Hall angle of material in effect gives its efficiency to generate spin current for a given applied charge current. The measured spin Hall angle for a material is also dependent on its thickness and the spin diffusion length in the material. Liu *et al.* proposed using SHE for applying spin current rather than the traditional way of electron spin polarization by sending current through a ferromagnet will be much more efficient with scaling of the SHE channel and hence will result in reducing the critical current (hence power) needed for switching the magnetization. The three-terminal MTJs they demonstrated also decoupled the impedance sensing and impedance switching process, thereby increasing their reliability compared to two terminal devices. Such a device is called SHE-MTJ.

In this chapter, we fabricate SHE-MTJs and study them in two different configurations. Firstly, we demonstrate SHE-MTJs as switches and memory element. Where we study the scaling of the SHE channel width for a fixed size of the MTJ pillar to observe increased efficiency of switching for a higher overlap between the long axis of the MTJ and the width of the SHE channel. We demonstrate a fully repeatable operation of SHE-MTJ as an MRAM bit cell with write pulses of duration as small as 100 ns. For studying the limits of switching speed for the fabricated device, we do switching probability measurements for write pulses of duration 250 ps to 10 ns.

In the second part of this chapter, we study the SHE-MTJ as an oscillator. We use the SHE to excite magnetization precession and read the precession output using the TMR of the nanopillar MTJ as voltage oscillation for an applied bias current. In doing this, we observe voltage control of magnetic anisotropy tuning of the oscillation frequency. We also use the SHE-MTJ as a traditional MTJ. Where, we excite magnetization precession from the spin transfer torque applied by the spin-polarized current from the fixed magnet of the MTJ nanopillar. We also demonstrate an open loop current-based magneto-acoustic oscillator in which, we use a laterally coupled HBAR to filter the SHE-MTJ oscillator.

5.2 ***SHE-MTJ devices for switches and memory***

Continued scaling of electronic devices has enabled unprecedented growth of computing performance in the past few decades. However, as the electronic device gate lengths approach 20 nm dimensions [88], further scaling of complementary metal oxide semiconductor (CMOS) field effect transistors (FET) require the realization of several complex material and device changes [89]. One of the methods for enabling further scaling in computing performance is by integration of spintronic devices for on-chip memory [90]. An efficient method of switching magnetic bits is a pre-requisite to enable such integration [91]. In this context, spin transfer torque (STT) switching of nanomagnets driven by CMOS transistors [92] has attracted significant effort. However, traditional MTJ based MRAM technology has the following fundamental drawbacks for compatibility with future scaled CMOS technologies: a) incompatibility of the high operating voltages and currents required for MTJ tunnel currents with scaled CMOS, b) large access transistor size required to meet the drive current requirement limits circuit density, and c) reliability issues created by the high

voltage (>0.8 V) and high current (>100 μA) damaging MTJ oxide. Hence it is of great interest to pursue MTJ switching methods alternative to STT, which would provide high spin polarization at low voltage and low current operation.

The spin Hall effect [16, 93, 94] in which large spin-polarized currents are generated transverse to the charge current direction in high spin-orbit coupling metals, may provide a solution to the voltage, current scaling and reliability problems of magnetic embedded memory. In particular, scaled SHE-MTJs can have a) better drive in scaled CMOS; b) fast switching time approaching 500 ps; c) decoupled read and write paths; d) improved trade-off of non-volatility vs. write time [95].

5.2.1 Fabrication process flow for SHE-MTJ

We fabricated a three-terminal MTJ device, under the guidance of Dr. Sriharsha Aradhya, which forms the basic cell for the MRAM. It has a spin-orbit torque induced write mechanism and TMR based read-out (Figure 5.3). The device material stack comprising of Ta (6 nm)/CoFeB (1.6 nm)/MgO (1.6 nm)/CoFeB (4 nm)/Ta (3 nm)/Ru (3 nm) is deposited using a 7 gun DC+RF magnetron sputtering tool at high vacuum of 10^{-8} Torr on a high resistivity silicon substrate having 400 nm of silicon oxide (Figure 5.3(a)). The CoFeB alloy used in the metal stack as the fixed and the free magnet has the composition $Co_{20}Fe_{60}B_{20}$. Silicon dioxide helps ensure the devices are electrically insulated from one another. The Ruthenium cap is used in the metal stack to protect the β-Ta layer from getting shorted during the fabrication process.

Device metal stack is then patterned using DUV lithography followed by ion milling to define the dimensions of the spin Hall effect channel (Figure 5.3(b)). The ion milling process used in the fabrication comprises of two steps. The first step is to define the device shape by etching at a high angle of incidence. The second step is to

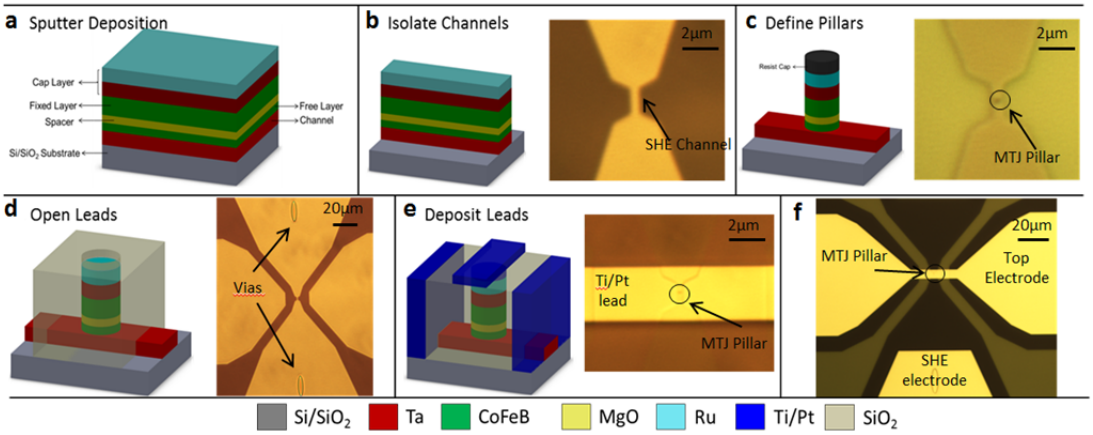

Figure 5.3: Fabrication process flow for SHE-MTJ with process steps: (a) sputter deposition, (b) isolate channel, (c) define pillar, (d) open leads and (e) deposit leads. (f) Image of the final device shows channel via to Ti/Pt top electrode.

remove the back sputtered material by doing a side wall clean at a low angle of incidence. During the ion milling, care is taken to ensure that the ion mill beam doesn't overheat the resist mask. After milling the devices, the resist mask is stripped using heated PG remover. It is a critical to ensure that no resist is left on the patterned channels as the MTJ pillars are fashioned out of the isolated channels of material stack. Resist remaining on the channel hinders the side wall cleaning step during the nanopillar fabrication and may result in shorting of MTJs.

E-beam lithography is used for patterning nanometer scale MTJs on the isolated channels. Step over step alignment is critical during this process step as the size of the isolated channels is comparable to the MTJs being fabricated out of them. The e-beam resist used for fabricating the MTJs is a tri-layer of omnicoat, PMMA, and HSQ (6%). Omnicoat is used as an anti-reflective coating, and the PMMA is the e-beam resist while HSQ is used to form a hard mask used in patterning the nanopillar by ion

milling (Figure 5.3(c)). Silicon dioxide is e-beam evaporated after ion milling to electrically

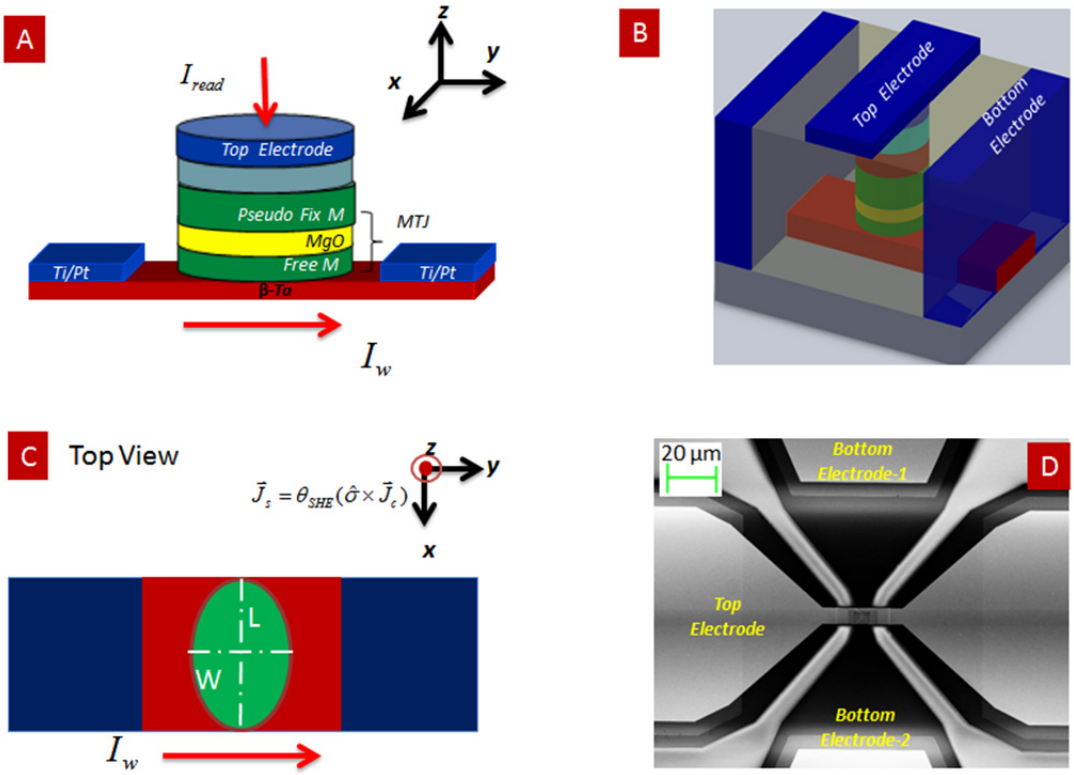

Figure 5.4: (a) A three-terminal memory device which uses the spin hall effect write electrode and MTJ based read out. (b) Isometric view of the device with different electrodes. (c) Top view of the device showing the orientation of the free layer magnet along the width of the SHE channel. (d) SEM of the device under test where bottom electrode-1 is used as ground.

isolate devices from each other. The deposited oxide is then patterned during the e-beam resist strip (Figure 5.3(d)). During the e-beam step, we also define vias for making contacts to the SHE channel made out of β-Tantalum. This is useful as it saves us an additional step of etching through the oxide. The innovation of this fabrication process lies in the multiple uses of the e-beam resist step, for defining MTJ nanopillar,

for making vias and for patterning evaporated oxide by liftoff. Contact leads made of for Ti(6 nm)/Pt(40 nm) are sputtered and patterned by resist liftoff using DUV lithography (Figure 5.3(e)). The fabricated device is then annealed at 300ºC to crystallize the CoFeB fixed and free magnet layers to increase the device TMR (Figure 5.3(f)).

The dimensions of the nanopillar are 270 nm × 68 nm, which are fabricated on different channels of width 400 nm, 500 nm, 600 nm and length 1600, 2000 and 2400 nm respectively. The length to width ratio of all the channels is kept constant to 4:1 to ensure they have equivalent resistance. The thickness of the free layer of 1.5 nm was selected to reduce the demagnetization field and hence the switching energy of the nanomagnet, but it is thick enough to keep the magnetization in the plane of the device. Isometric view of the SHE-MTJ shows the top electrode of Ti/Pt and the bottom electrode of β-Ta channel contacted via Ti/Pt electrodes (Figure 5.4(a)). The MTJ nanopillar is patterned such that the long axis of the magnet is oriented along the width of the SHE channel for appropriate spin injection (Figure 5.4(c)).

The top leads of the Ti/Pt bilayer were added on the Ta/Ru stack to make contacts to the MTJ. The magnetization state of the cell is written by applying a charge current via the SHE channel. The direction of the magnetic writing is set by the direction of the applied charge current. Positive currents (along $+y$ direction) produce a spin injection current with transport direction ($+z$) and spins polarized in ($+x$) direction. The injected spin current in its turn produces spin torque to align the nanomagnet in the ($-x$) direction (since the spin Hall angle for β-Ta is negative) (Figure 5.5). The transverse spin current ($\vec{I}_s = \vec{I}_\uparrow - \vec{I}_\downarrow$ with spin direction $\hat{\sigma}$) for a charge current ($\vec{I}_c$) in the write electrode is given by:

$$\vec{I}_s = P_{SHE}(w,t,\lambda_{sf},\theta_{SHE})\left(\hat{z}\times\vec{I}_c\right) \tag{5.4}$$

where, P_{SHE} is the spin Hall injection efficiency, which is the ratio of the magnitude of transverse spin current to lateral charge current. w is the width of the nanomagnet, t is the thickness of the SHE metal channel, λ_{sf} is the spin flip length in the SHE metal, and θ_{SHE} is the spin Hall angle (coefficient) for the SHE-metal to the free layer ferromagnet interface.

5.2.2 DC measurements

We measured the resistance of the SHE-MTJ as a function of external magnetic field, H_{Ext}, applied in-plane of the device along the easy axis of the magnet to measure the device coercivity and TMR, using a lock-in amplifier (Figure 5.5 (a)). The small signal resistance (dV/dI) is plotted as a function of applied magnetic field, showing a clear hysteresis window with a coercivity of 40 Oe with single domain switching of the free layer (Figure 5.5(b)). The major loop is shown in the inset. TMR of 40% was measured for the 270 nm × 68 nm device with a 400 nm channel width.

Bi-directional current induced switching was measured for the device using a lock -in setup where current is applied using Keithley 2400 sourcemeter to the SHE channel (Figure 5.6(a)). The current induced switching was done in the presence of an offset field of -102 Oe to center the hysteresis curve for the device. We verify the symmetry of the switching by using a negative offset field of 102 Oe (Figure 5.6 (b)). For positive offset field, the MTJ switches to AP/P when the current through SHE channel is positive/negative. When the offset field is reversed, the MTJ switches to P/AP when the current through SHE channel is negative/positive. In an integrated device with a synthetic antiferromagnet, the offset field will not be required, and the

relationship of the switching and current direction is purely given by the Equation (5.4).

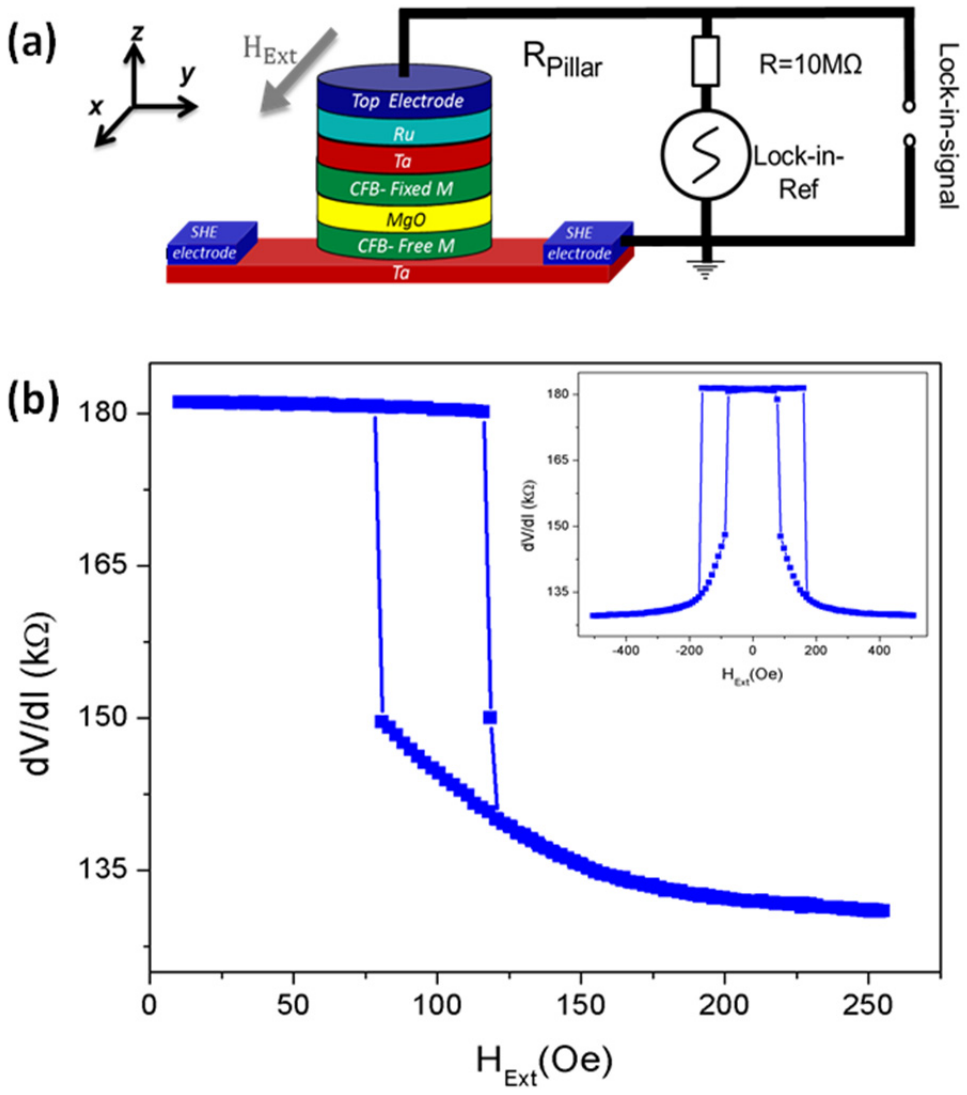

Figure 5.5: (a) Setup used for measuring the resistance of the device as the magnetic field is swept from 0 Oe to 250 Oe and back. (b) Right side minor loop of the SHE-MTJ shows TMR of 40%, with the major loop shown as in the inset.

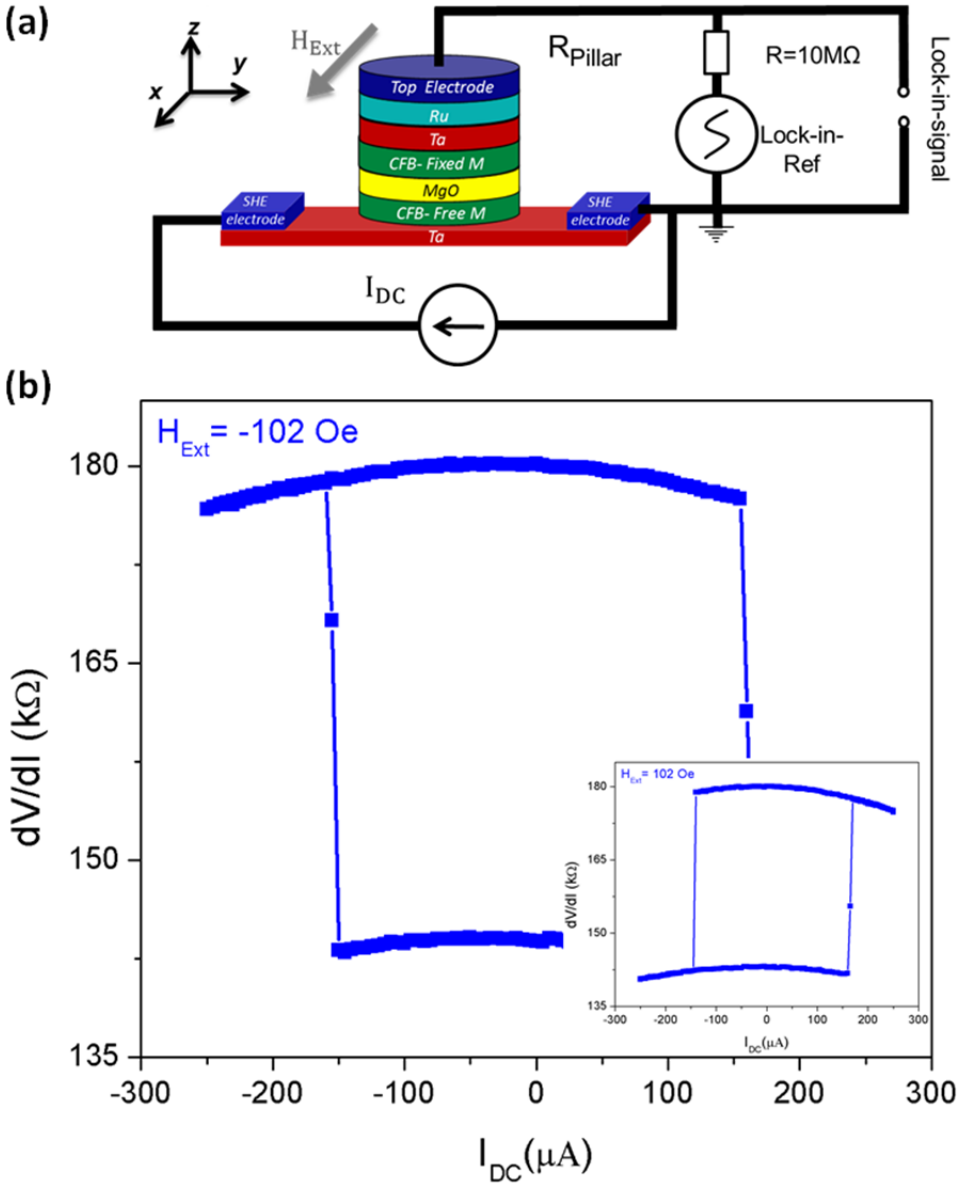

Figure 5.6: (a) Setup used for measuring the resistance of the MTJ as current is applied to SHE channel is swept. (b) The plot shows anti-parallel to parallel resistance state switching and back as the current is swept from -300 μA to 300 μA for an applied H_{Ext} of -102 Oe. Inset show the similar current switching for a H_{Ext} of 102 Oe where the resistance state switches from parallel to anti-parallel state as current is swept from -300 μA to 300 μA.

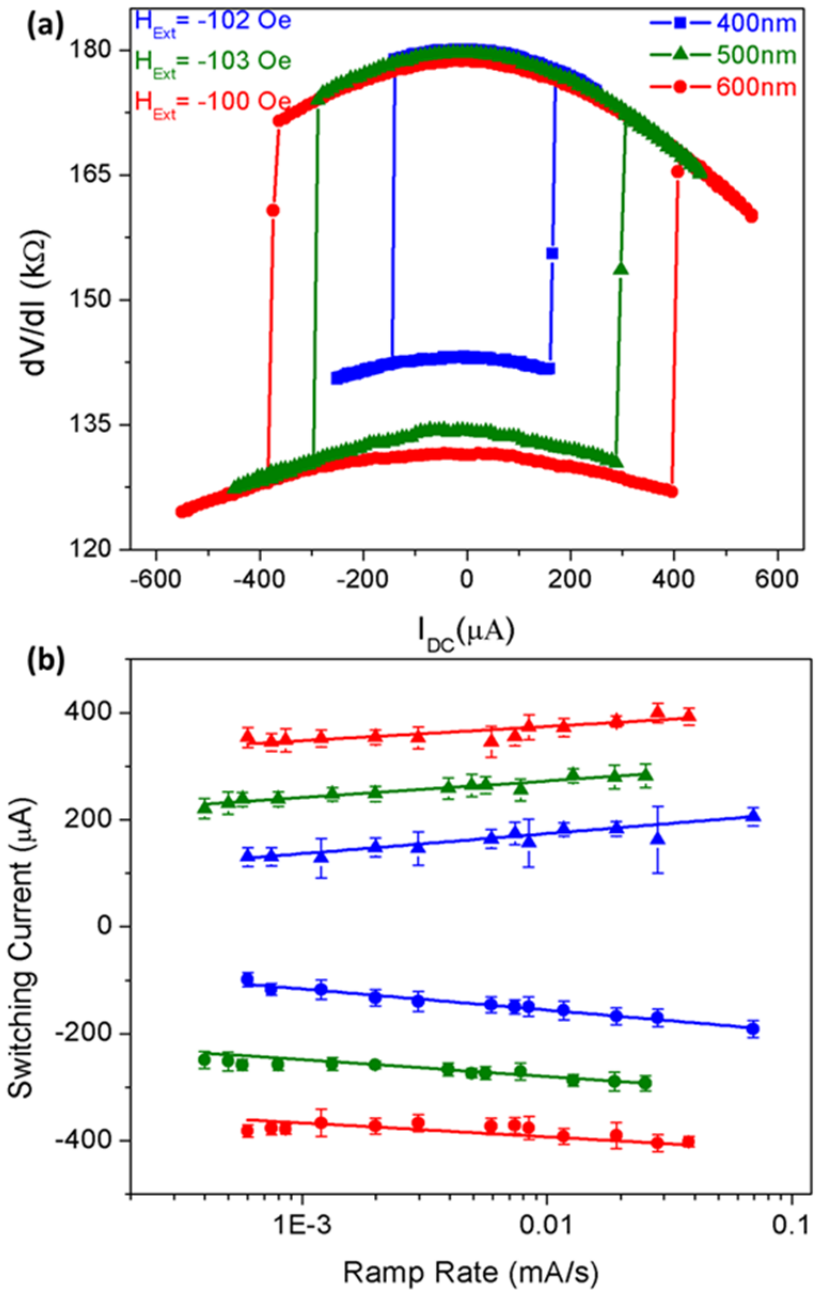

Figure 5.7: (a) Current-induced switching of SHE-MTJ of size 270 nm × 68 nm fabricated on channels of width 400 nm (blue), 500 nm (green) and 600 nm (red). (b) Switching currents as a function of ramp rate of the current for different channels. AP to P switching is shown using circles while P to AP switching is shown via triangles. Solid lines represent linear fits of switching current versus ramp rates.

5.2.3 Scaling of SHE channel

The effect of scaling the SHE channel on the switching of the SHE-MTJ was studied by comparing the DC switching properties for a 270 nm × 68 nm magnet, with SHE channel of various widths: 400 nm, 500 nm, and 600 nm. Bi-directional spin torque switching of the MTJs as a function of applied current in the SHE channel was measured for all the three channel widths (Figure 5.7(a)). The critical currents for P to AP switching and vice versa are comparable showing that symmetric bi-directional switching is feasible with spin Hall effect switching.

We extract the zero temperature critical currents and magnetic energy barriers for the devices using ramp rate measurements; where the switching current is measured for a given device as a function of the ramp rate of its current (Figure 5.7(b)). Using thermal activation model [96], this dependence of the critical current to the ramp rate is a linear fit to the function of the form:

$$I_c = I_{c0}\left[1 - \frac{k_B T}{E_b}\ln\left(\frac{k_B T}{E_b}\cdot\frac{I_{c0}/\tau_0}{\dot{I}_c}\right)\right] \tag{5.5}$$

where, the energy barrier E_b, the zero-temperature critical current I_{c0} are the fitting variables and $k_B T$ is the thermal energy. We assume that the temperature of the device was close to room temperature and the attempt time τ_0 is 1 ns. The extracted energy barrier and zero temperature critical current are shown in Table 5.1. The ratio of the calculated critical current at zero temperature and the energy barrier scales linearly with the channel width (Figure 5.8). This shows that the current density needed for switching the SHE-MTJ is constant (with a maximum error of 6%) for all the different widths of the channel.

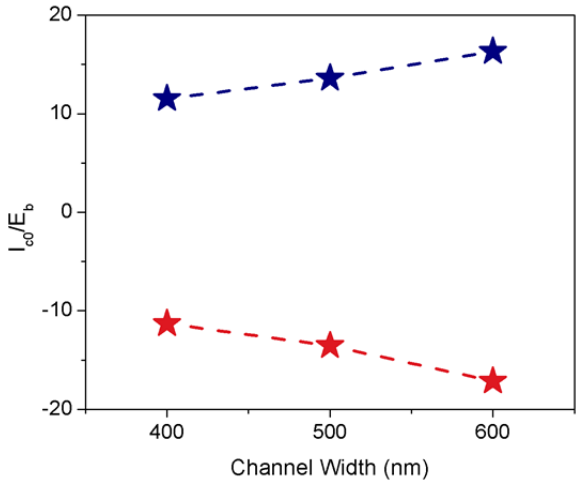

Figure 5.8: Zero temperature critical current normalized by energy barrier size scales linearly with SHE channel width for P to AP switching (blue) and AP to P switching (red).

We extract the 'effective spin Hall angle' (θ'_{SHE}) for the device by taking the ratio of the expected critical spin current density in spin transfer torque switching ($J_{s0\text{-}MTJ}$) to the charge current density (J_{c0-SHE}) derived from the critical current in spin Hall switching.

$$\theta'_{SHE} = \frac{J_{s0-MTJ}}{J_{c0-SHE}} = (W_{ch}t_{ch})\frac{J_{s0-MTJ}}{I_{c0-SHE}} = \frac{(W_{ch}t_{ch})}{I_{c0-SHE}}\left(\frac{2e}{\hbar}\mu_0 M_s t'_m \alpha\left(H_k + \frac{M_{eff}}{2}\right)\right) \tag{5.6}$$

The calculated effective spin Hall angles, which represent the efficiency of spin current generation, for the three devices, are 0.16 (W_{ch} = 400 nm), 0.18 (W_{ch} = 500 nm) and 0.20 (W_{ch} = 600 nm). Here the magnet thickness without the dead layer is t'_m, the saturation magnetization M_s, the effective demagnetization is M_{eff}, the material anisotropy effective field is H_k, and Gilbert damping α. We assumed a dead layer of 0.2 nm. This technique for effective spin Hall angle extraction is approximate due to

Table 5.1: Results of I_{c0} and E_b calculated from linear fits to Equation (5.6)

Channel Width (nm)	Switching AP to P		Switching P to AP	
	I_{c0}(μA)	$E_b(k_BT)$	I_{c0}(μA)	$E_b(k_BT)$
600	-629.36	55.46	614.62	53.30
500	-564.39	41.70	558.37	41.06
400	-519.88	30.36	520.44	31.87

the following factors: a) the approximate estimate of the dead layer thickness (t_m-t'_m); b) $I_{c0\text{-}SHE}$ is not exactly proportional to W_{ch}; c) ignoring the contribution of the field like torque arising due to interface Rashba effect. This effective spin Hall angle was calculated under the assumption that the spin torque is only due to Slonczewski spin torque. We calculated the effective spin injection efficiency to be in the range of 96% to 113% in the measured spin Hall effect device using equation given as:

$$P_{SHE} = \frac{I_{s0-MTJ}}{I_{c0-SHE}} = \frac{\pi abJ_{s0-MTJ}}{4I_{c0-SHE}} \approx 96-113\% \tag{5.7}$$

where, I_{s0-MTJ} is the current needed for MTJ switching assuming just Slonczewski torque. We compared the spin injection efficiencies of a traditional MTJ that uses spin polarization for generating the spin current to the SHE-MTJ of the same size using:

$$\frac{P_{SHE}}{P_{MTJ}} \sim 2 \tag{5.8}$$

where P_{MTJ} is the spin injection efficiency of a traditional MTJ was calculated using formulation by Manipatruni *et al.* [95]. We can thus confidently claim that SHE-MTJs

are much more energy efficient than traditional MTJs. We have also demonstrated that the critical current needed for the memory writing from AP to P and vice versa are symmetric, which greatly reduces the complexity of write circuits for the memory bit cells making SHE-MTJs ideal for CMOS integration for on-chip MRAM.

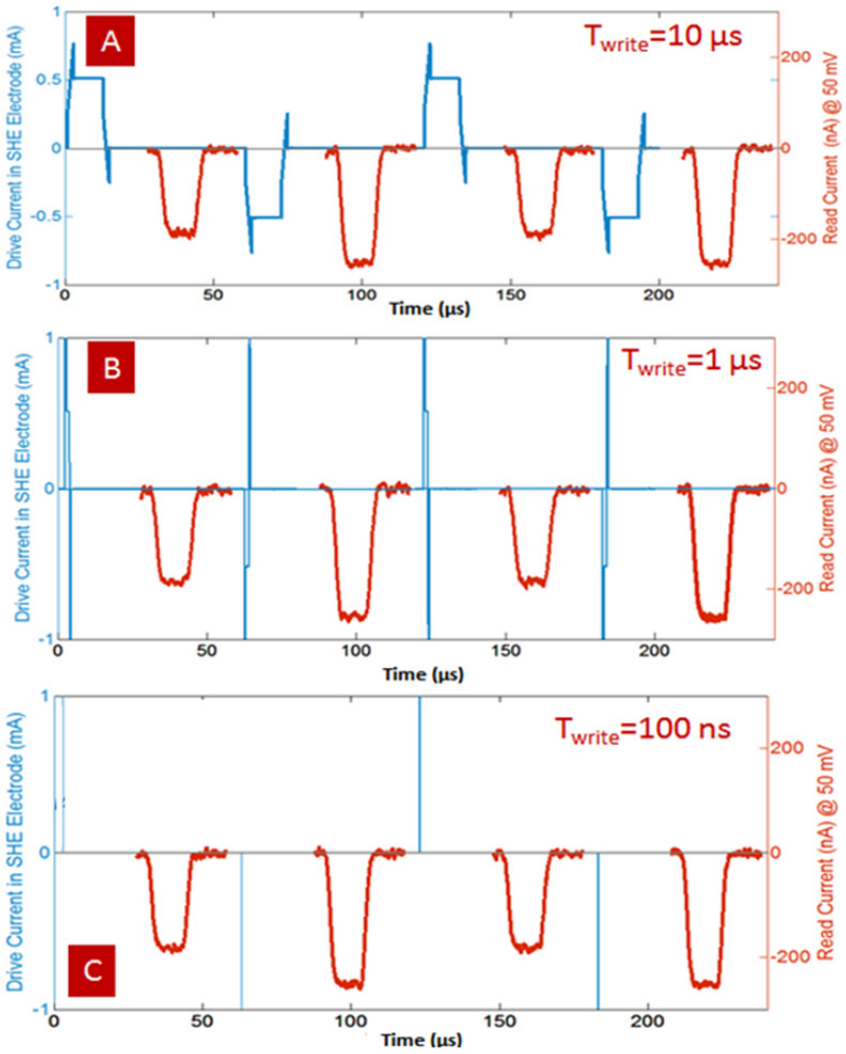

Figure 5.9: Transient write and read operation of SHE-MTJ with write pulses of width (a) 10 µs, (b) 1 µs and (c) 100 ns. Read is performed by using a 50 mV read voltage between the write operation shows the change in the device impedance reflected as current change.

5.2.4 SHE-MTJ as a MRAM element

We show the operation of the three-terminal SHE device as a memory element by performing consecutive write and read cycles. The write cycles are performed at 4 times the critical current followed by a read pulse of amplitude 50 mV applied to the terminal of the MTJ. Such high current biasing is not possible with tunnel junction based spin torque switching. The repeatable bi-directional transient switching current and voltage data were measured for the SHE-MTJ device. Applying 10 μs pulse width write pulses followed by a read pulse of 10 μs width with less than 100 nA of the read current (Figure 5.9(a)), we demonstrated complete current based read and writing of the SHE-MTJ. We further demonstrated the SHE-MTJ's memory operation with faster write pulses of 1 μs (Figure 5.9(b)) and 100 ns (Figure 5.9(c)).

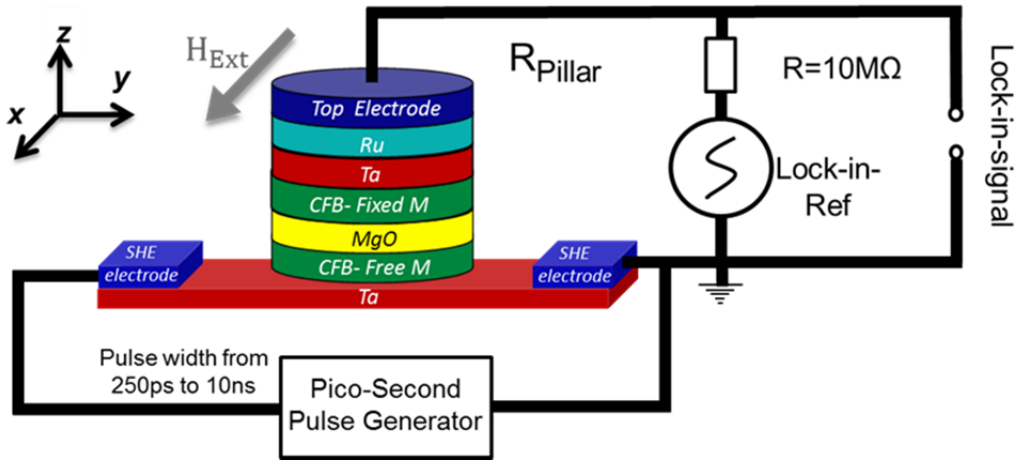

Figure 5.10: Setup for measuring switching probability as a function of pulse amplitude and pulse duration. Picosecond pulse generator PSPL 10100A is used to generate pulses of amplitudes 1.96 V to 3.147 V with pulse width varying from 250 ps to 10 ns.

To demonstrate that we are far from the limits of the switching speed, even with write pulse time of 100 ns, for the SHE- MTJ using a picosecond pulse generator PSPL 10100A, we applied voltage pulses to the SHE channel of varying amplitude while increasing the pulse duration from 250 ps to 10 ns. At each of the voltage and pulse width steps, 250 attempts were made to measure the switching probability with high accuracy. At each attempt, switching was verified by using a lock-in based resistance measurement (Figure 5.10). We measured 100% switching probability at a pulse width of 6.5 ns for switching from AP to P state for -3.147 V (Figure 5.11(a)). 100% switching probability was measured for a pulse width of 8 ns for switching from P to AP state for 3.147 V write pulse (Figure 5.11(b)). This discrepancy is due to the curvature in the magnetic states observed in the parallel state, which leads to different switching path in the presence of Oersted fields. These Oersted fields are generated by the SHE channel current flow affect the switching of the free layer. For negative spin Hall angle materials like β-Ta the Oersted field from spin Hall channel acts along the direction of the anisotropy field of the in-plane free layer magnet thus making it harder for the magnet to switch. Faster switching speeds can be reached by using Oersted field to assist switching which is possible with using SHE materials with positive SHE angle like platinum as demonstrated by Aradhya *et al.* [97]. Another way to reduce the effect of curvature in the magnetic state is by pinning the fixed layer magnet. This has shown to reduce the times taken by the edge states to respond to the switching current. SHE-MTJs we have demonstrated here definitely have a high potential for use as on-chip MRAM bit cells.

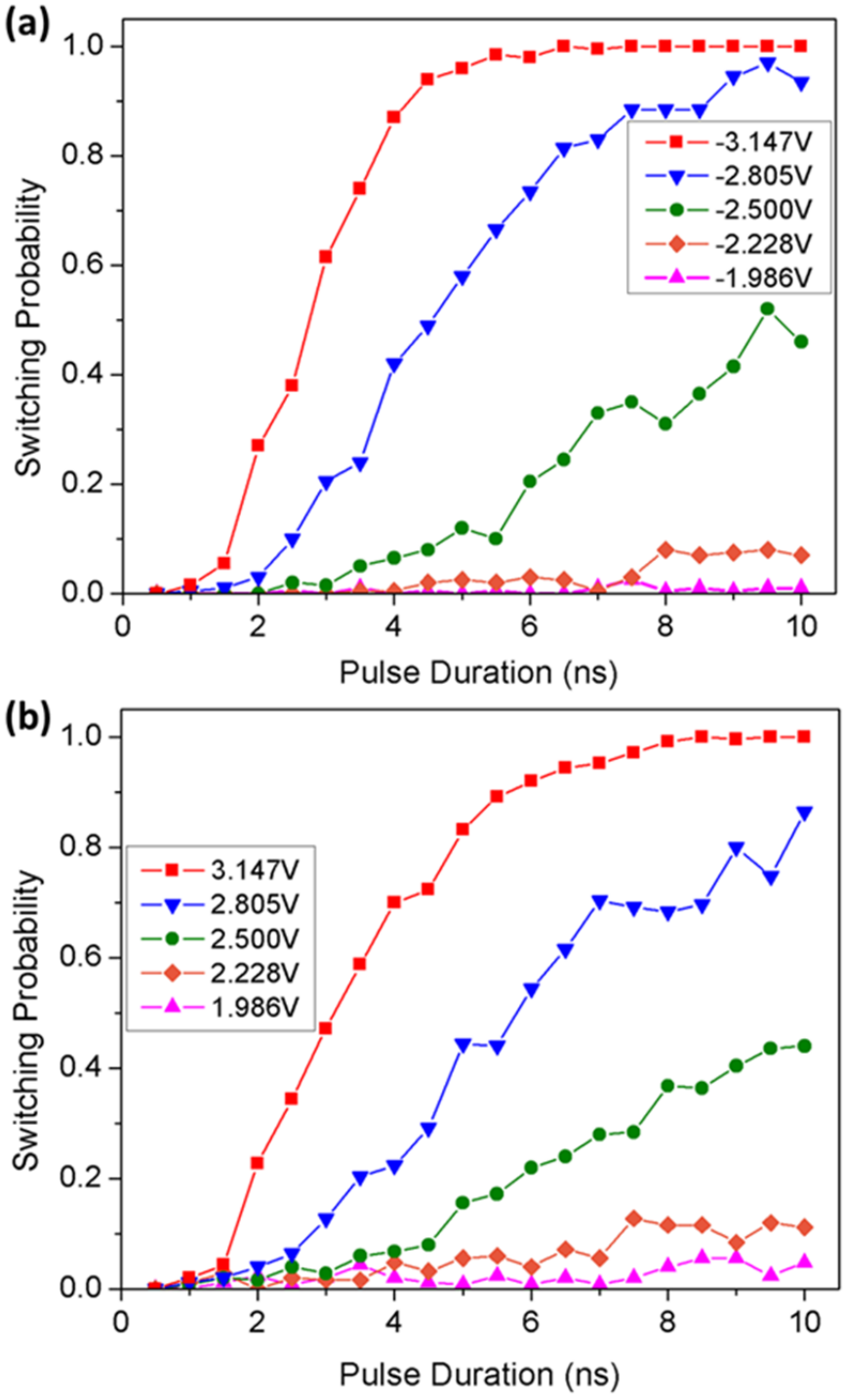

Figure 5.11: Switching probability as a function of write pulse voltage and write pulse duration for (a) AP to P switching (b) P to AP switching. Each point on the graph represents 250 switching attempts.

5.3 ***SHE-MTJ devices for oscillators***

SHE-MTJs discussed in the previous section showed great capability as a potential MRAM bit cell. In a different configuration of operation, these same devices can be utilized as high-frequency tunable oscillators. Liu *et al.* [15] demonstrated magnetization oscillation in a ferromagnet using spin current injected from the SHE channel. The magnetization precession of the ferromagnet is then measured as voltage oscillations using an MTJ where the ferromagnet is the free layer. This is similar to the SHE-MTJ used in switching where the resistance state is written using the spin current injected through the SHE channel and the resistance of the state is read using the spin torque effect in the MTJ. SHE-MTJ oscillators are advantageous as their oscillation frequency can be tuned with the SHE current as well as with the spin torque current applied to the MTJ. One additional advantage of the SHE-MTJ as an oscillator is that the constraint of having extremely low RA product (~10 $\Omega\mu m^2$) necessary for driving oscillations for a spin torque device are relaxed. This is because the oscillations are only measured using spin torque effect and driven via the spin Hall channel. Additionally, the SHE channel provides a new avenue for studying locking of MTJs by applying AC current through the channel.

We fabricated an SHE-MTJ device of 270 nm×110 nm size having a 600 nm wide channel. The material stack of the device is comprised of Ta (6 nm)/CoFeB (1.5 nm)/ MgO (1.2 nm)/CoFeB (4 nm)/Ta (3 nm)/Ru (3 nm) with Ti (6 nm)/Pt (50 nm) as the contact lead. Tantalum is the SHE channel that injects spin current into the adjacent CoFeB free layer, thereby overcoming the damping to get steady state precession of the magnetization. The fabrication process for the SHE-MTJ oscillator was similar to the SHE-MTJ switches (Figure 5.2). The MTJ nanopillar was oriented such that the easy axis of the magnet is along the width of the channel (Figure 5.4(c)). The main

difference between the two types of devices is the size of the tunneling oxide (MgO), which is 1.2 nm for the oscillator devices and 1.6 nm thick MgO for the switches. The thickness of the tunneling barrier was decreased to reduce the resistance of the device, necessary for efficient measurement of the spin dynamics coupled to a 50 Ω input impedance of the spectrum analyzer. The thickness of the free layer magnet is chosen to be 1.5 nm for reducing the effective demagnetization field to get steady state large angle oscillation for lower threshold current.

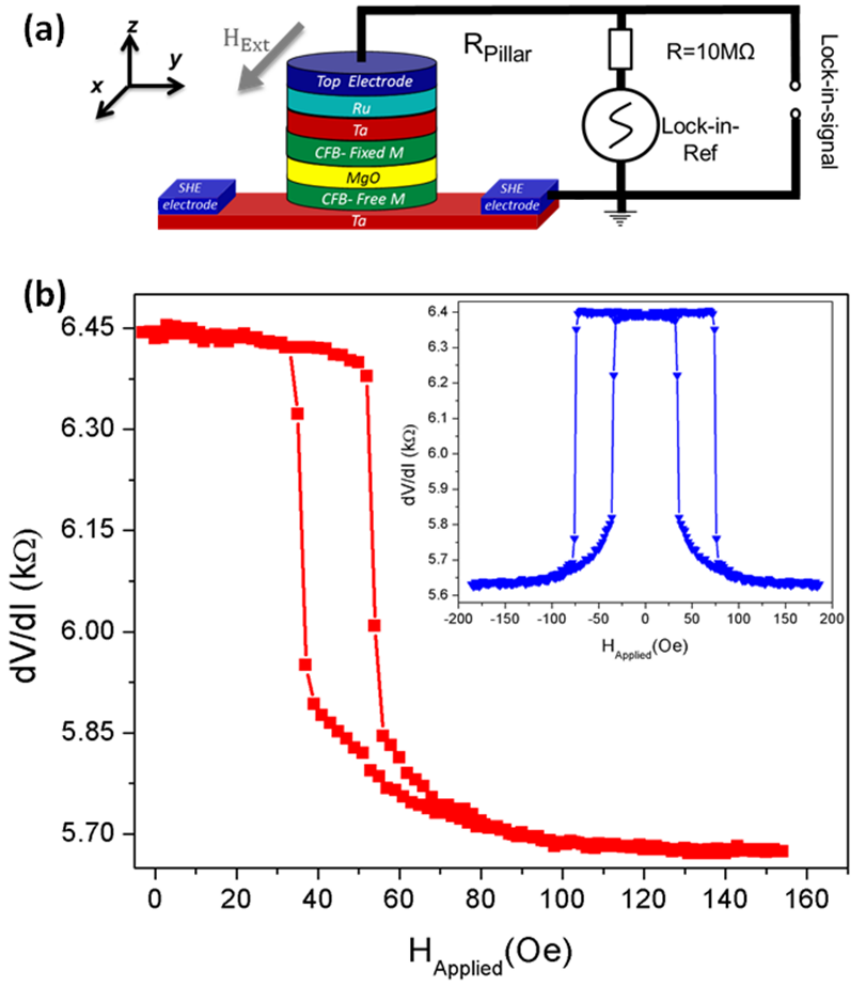

Figure 5.12: (a) Setup used for measuring the resistance of the device as the magnetic field is swept from 0 Oe to 250 Oe and back. (b) Right side minor loop of the SHE-MTJ shows TMR of 30%, with the major loop shown as in the inset.

5.3.1 DC measurements

The resistance of the SHE-MTJ device was measured as a function of external magnetic field ($H_{Applied}$) applied in-plane of the device along the easy axis of the magnet. We measured the device TMR using a lock-in amplifier setup (Figure 5.12(a)). The small signal resistance (dV/dI) is measured as a function of applied magnetic field, showing a clear hysteresis window with single domain switching of the free layer magnet free layer (Figure 5.12(b)). The major loop is shown in the inset. TMR of 30.6% was measured for the 270 nm × 110 nm device with a 600 nm channel width. The value of channel resistance, measured to be 6.5 kΩ was not included in calculating the device TMR even though it contributes to the resistance of the measured device.

Current-induced switching was also measured for the device using a lock-in amplifier setup where current is applied using Keithley 2400 sourcemeter to the SHE channel (Figure 5.13(a)). The current induced switching was done in the presence of an offset field of 49 Oe to center the hysteresis curve for the device. This external field is needed to cancel out the dipole field from the fixed layer of the device. We observe a clear hysteresis as the resistance of the devices changes from P to AP state when the current is swept from the negative to the positive value and from AP to P state when the current is swept back from the positive to the negative value (Figure 5.13(b)). The critical current needed for switching the device is very low, due to the low energy barrier of the device because of smaller shape anisotropy field. The current switching shows that spin Hall effect induced a spin current from the channel can apply enough torque to the free layer magnetization to switch its direction from P to AP and from AP to P for the positive and the negative value of the spin current. The resistance-area product of the device was measured to be 77 $\Omega\mu m^2$, which is high, due to the large size of the device.

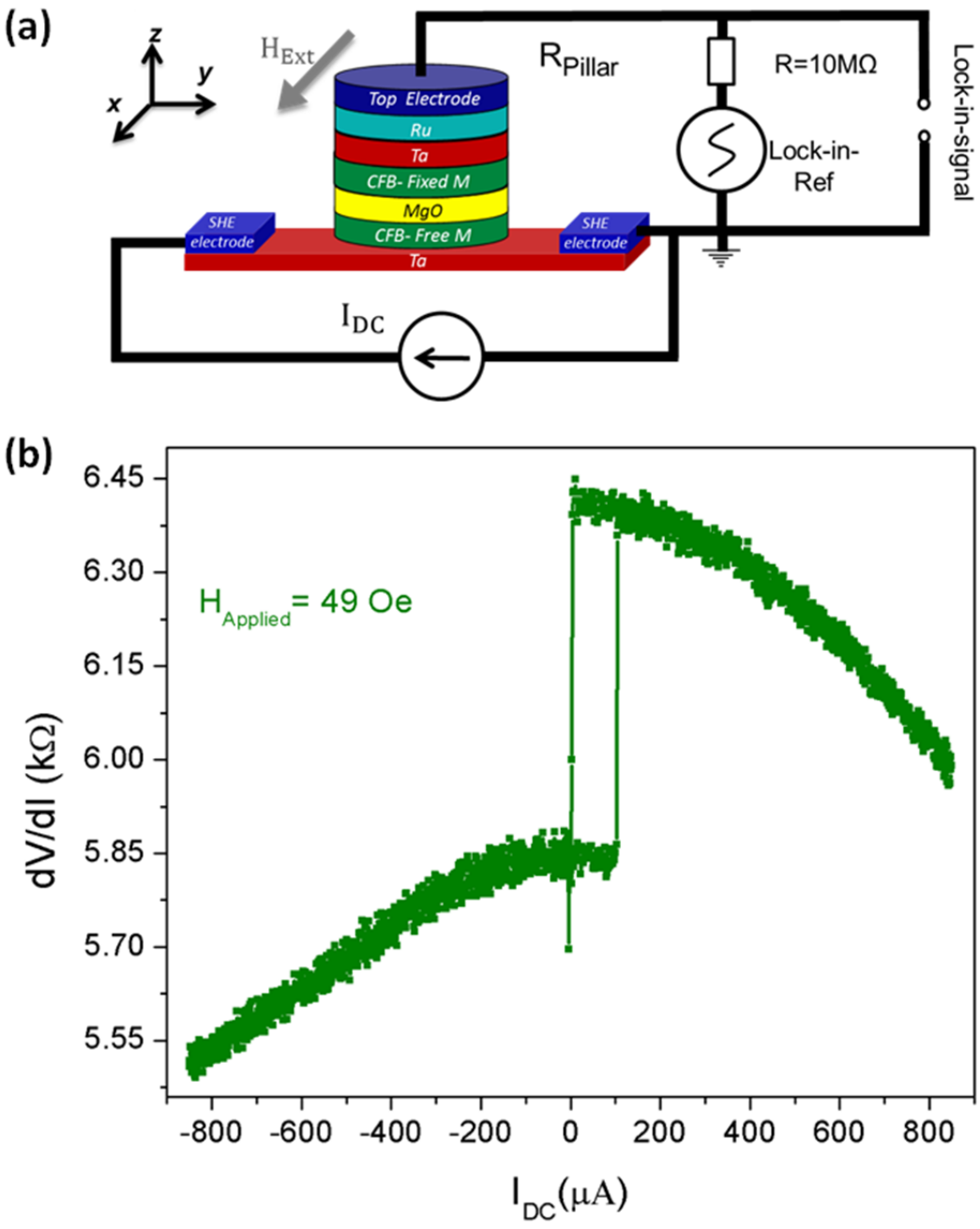

Figure 5.13: (a) Setup used for measuring the resistance of the MTJ as the current is applied to SHE channel is swept. (b) The plot shows parallel to anti-parallel resistance state switching and back as the current is swept from -800 μA to 800 μA for an applied $H_{Applied}$ of 49 Oe.

5.3.2 AC measurements

SHE devices were biased with a high magnetic field, $H_{Applied}$, of 135 Oe to align the magnetization of the free layer and the fixed layer parallel to each other. Using a bias tee and Keithley 2400 sourcemeter, a nominal current I_{MTJ} of -80 μA was applied to the top electrode of the MTJ pillar. The output of the capacitor (RF) end of the bias tee was connected to the spectrum analyzer (Figure 4.5(a)). The spectrum analyzer is set for a 5 MHz resolution bandwidth and 6 kHz video bandwidth selected to keep the noise floor as low as possible. A second Keithley 2400 sourcemeter was used to sweep current applied to the SHE channel from 0 to 600 μA (Figure 5.14(a)). The direction of the current applied to the SHE channel is to inject spins of orientation opposite to the magnetization of the free layer magnet. The injected spins apply a torque on the free layer magnet to switch the magnetization from P to AP state similar to the measurement of current induced switching (Figure 5.13(b)). When the amplitude of the spin current is increased from the 0 to 600 μA, the spin current compensates the damping of the free layer magnetization, thereby inducing steady state oscillation of the magnetization of the free layer. These magnetization precessions are measured as voltage oscillations across the MTJ for oscillating device resistance due to the TMR effect. As the I_{SHE} is slowly increased, we observe a very small decrease in oscillation frequency as the magnetization trajectory changes (Figure 5.14(b)). We measured the oscillation at 1.94 GHz (with 1.97 GHz for I_{SHE} of 100 μA) with a peak power of -93.2 dBm for an I_{MTJ} of -80 μA and I_{SHE} of 600 μA (Figure 5.15(a)). The linewidth of the fundamental mode is 400 MHz, and the $\Delta f_o/f_o$ ratio of the oscillation mode is 4.85. The oscillation measured here had total a power of 95.72 pW.

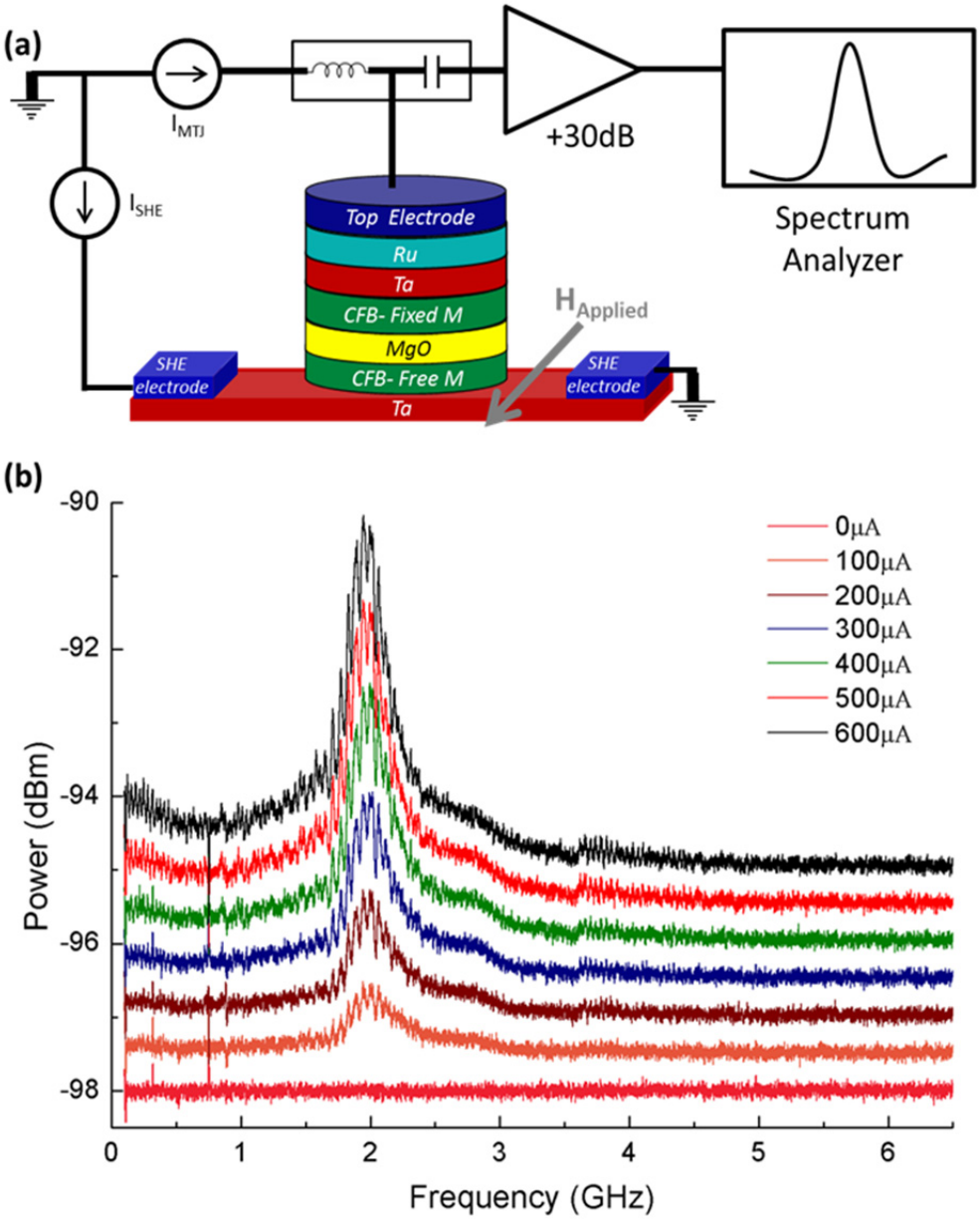

Figure 5.14: (a) Setup used for measuring oscillation in SHE-MTJ. The direction of $H_{Applied}$ represents the direction of the positive field; the direction of current represents the direction of positive currents. (b) SHE-MTJs oscillation measured on the spectrum analyzer as the I_{SHE} is scaled from 0 to 600 μA. The individual spectrums are shifted vertically for clarity of view. We see a lot of noise in the background compared to spin valve due to the high impedance of the SHE-MTJ.

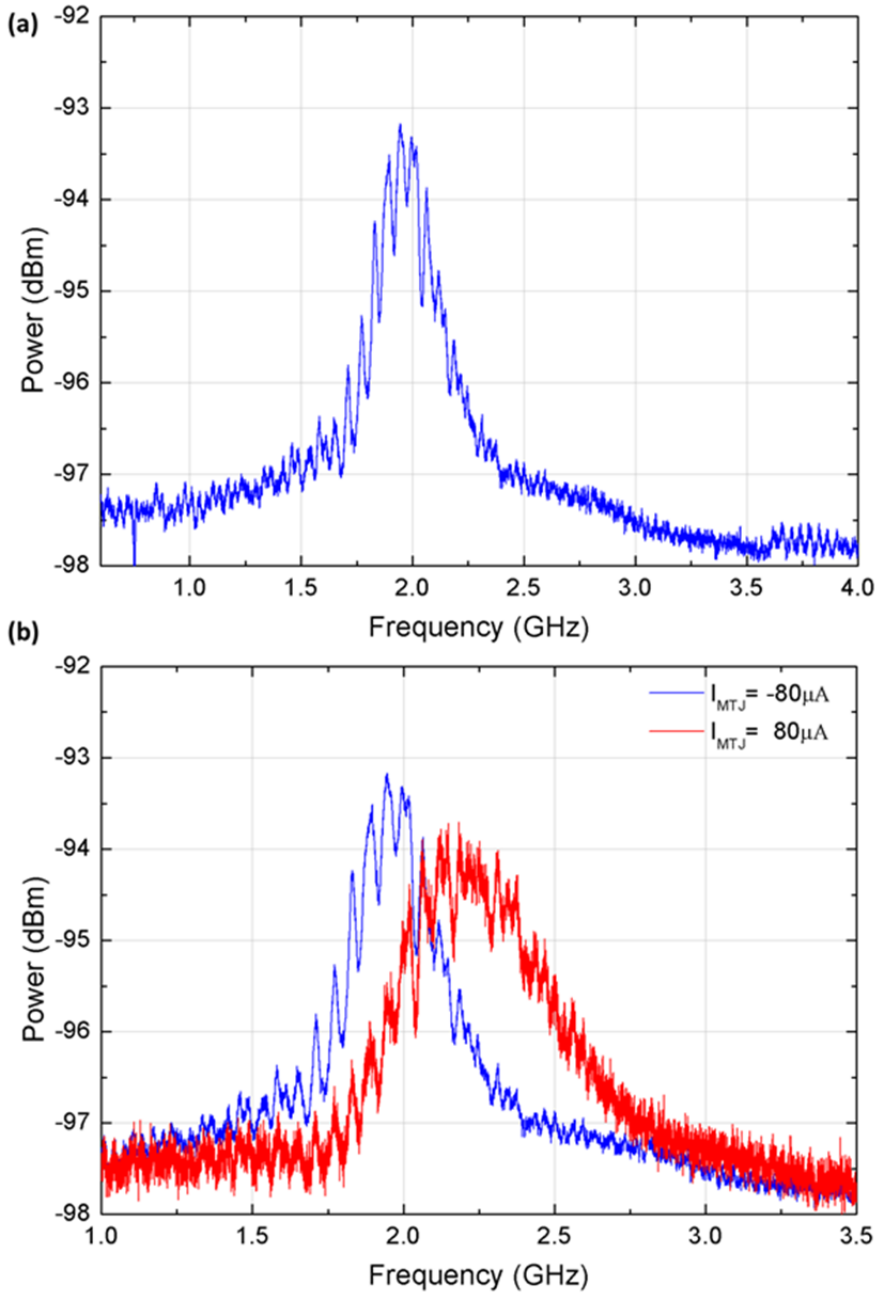

Figure 5.15: (a) Plot of the second harmonic at the frequency of 1.94 GHz with peak power of -93.2 dBm for 5 MHz of resolution bandwidth having a linewidth of 98 MHz. (b) Oscillation frequency changes from 1.94 GHz to 2.25 GHz by changing I_{MTJ} from -80 μA to 80 μA due to voltage control of magnetic anisotropy.

By changing the bias current to the MTJ, it has been shown that we can modulate the uniaxial anisotropy energy which depends on the electric field across the tunnel barrier. The anisotropy energy contribution to the effective demagnetization field of the free layer is given by the equation:

$$H_{demag}^{eff} = 4\pi M_s - \frac{2K_u}{M_s} \tag{5.9}$$

Where, M_s is the saturation magnetization of the free layer and K_u is the uniaxial anisotropy coefficient dependent of the electric field across the MTJ tunnel barrier. Liu *et al.* demonstrated that by changing the I_{MTJ} we can change the voltage across the tunneling barrier and thus change H_{demag}^{eff}, which changes the frequency of the oscillation given by Kittel formula shown in Equation (1.3). By changing the I_{MTJ} from -80 μA to 80 μA, we observed the frequency of oscillation increase from 1.94 GHz to 2.25 GHz (Figure 5.15(b)). The frequency tuning (0.745 GHz/V), we observe is comparable to the one observed by Liu *et al.* (~ 0.761 GHz/V) when normalize the frequency change to the overall voltage change across the MTJ [15]. Normalizing and comparing the voltages across the two devices is valid as the two devices have the same material stack with 1.2 nm thick MgO tunnel barrier. We observe a smaller change in frequency when comparing the current amplitudes as most of the voltage is dropped across the high resistance channel, so a higher current is needed to observe equivalent modulation of demagnetization field. The oscillation powers measured in the plots are for 50 Ω load resistance and are low due to impedance mismatch between the SHE-MTJ and the spectrum analyzer. The low power of the oscillation can also be attributed to the small amplitude of the read current I_{MTJ} applied to the device. Scaling I_{MTJ} to large values while keeping I_{SHE} high, we observed the noise floor of the spectrum analyzer increase over large bandwidth at

lower frequency range. We believe this happens due to noisy and chaotic magnetization precession of the SHE-MTJ in the presence of both the spin current from SHE channel and the spin-polarized current from I_{MTJ} [28].

5.3.3 Pillar current driven oscillations

Applying just I_{MTJ} to the device for zero amplitude of I_{SHE} in the same setup (Figure 5.14(a)), we were able to measure spin torque driven oscillations of the SHE-MTJ. The oscillations measured are due to the spin-polarized electrons from the fixed layer applying spin torque to the magnetization of the free layer and overcoming the damping in the free layer to get steady state precession. The oscillation power we observed increased when the magnetic field was applied at an angle of 35º to the easy axis of the magnet (Figure 5.16(a)). Changing the I_{MTJ} current, we were able to see frequency tuning of the device (Figure 5.16(b)). When we increased the I_{SHE} in the presence of large (180 μA or more) I_{MTJ}, we observed that the amplitude of oscillation decreased and as the linewidth increases and results in the previously observed increase in the noise floor of the measurements.

The peak power of -97 dBm was measured for I_{MTJ} current of -360 μA, with $H_{Applied}$ of 135 Oe at an angle of 35º from the easy axis of the magnet (Figure 5.16(a)) for oscillation of frequency 2.12 GHz measured for 1 MHz resolution bandwidth. The total power of this oscillation mode is 59.86 pW, and the linewidth of the oscillation is 300 MHz. The $\Delta f_o/f_o$ ratio for this oscillation mode is 7.066. The $\Delta f_o/f_o$ ratio of the spin torque oscillation of SHE-MTJ, though better than the SHE-MTJ oscillation, is still very poor compared to spin valve devices measured in Chapter 4. The large linewidths measured for SHE-MTJ arise from high surface roughness and non-uniformity of the fabricated device, observed in AFM characterization, leading to edge states that increase the linewidth of the oscillation.

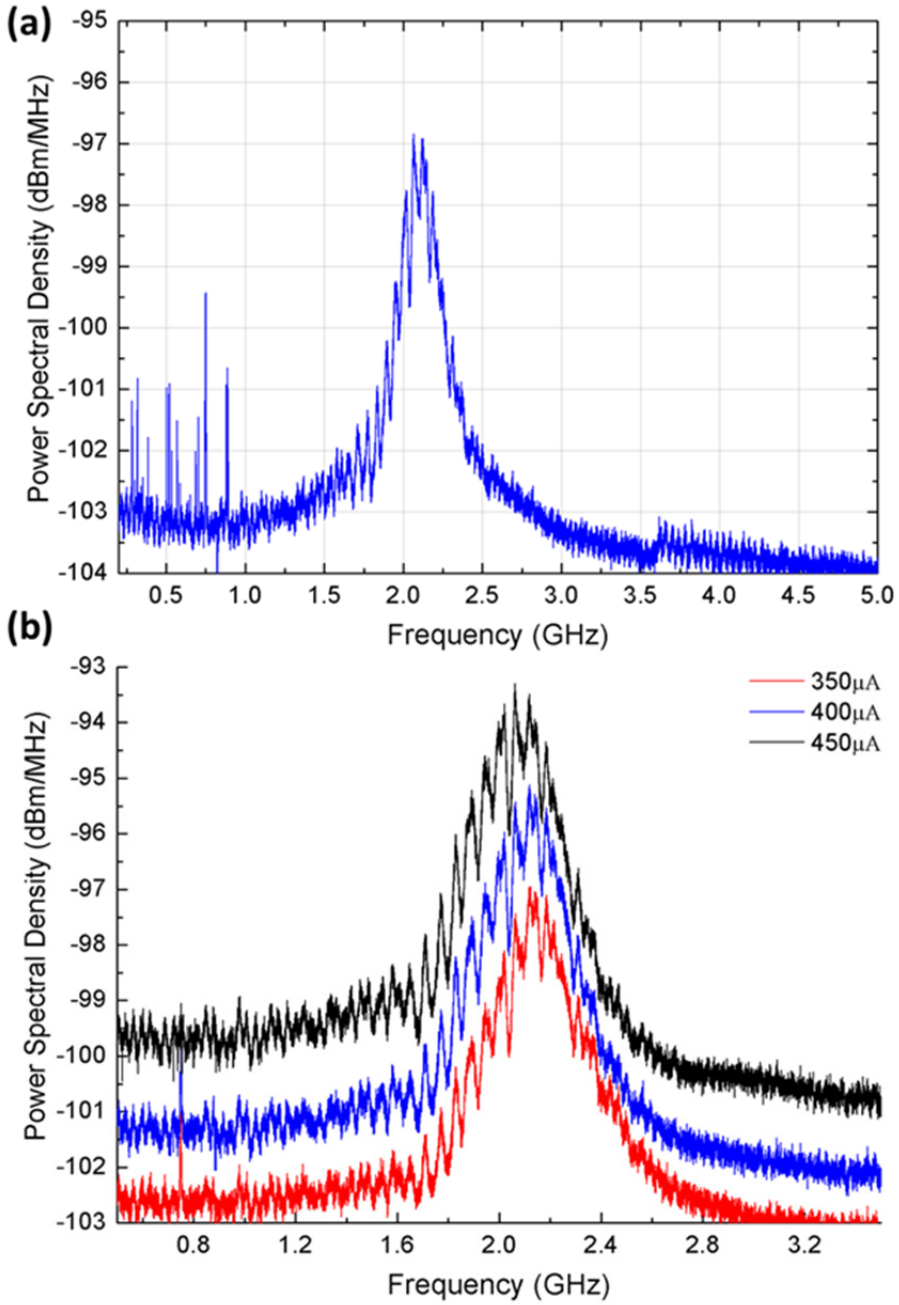

Figure 5.16: Frequency spectrum is showing oscillations of SHE-MTJ driven by spin torque current (I_{MTJ}) with 0 I_{SHE}, measured at $H_{Applied}$ of 135 Oe at an angle of 35º from the easy axis. (A) Oscillations measured for -360 μA of I_{MTJ}. (b) The frequency of oscillations changes from 2.12 - 2.1 GHz as the current is changed from -350 μA to -450 μA.

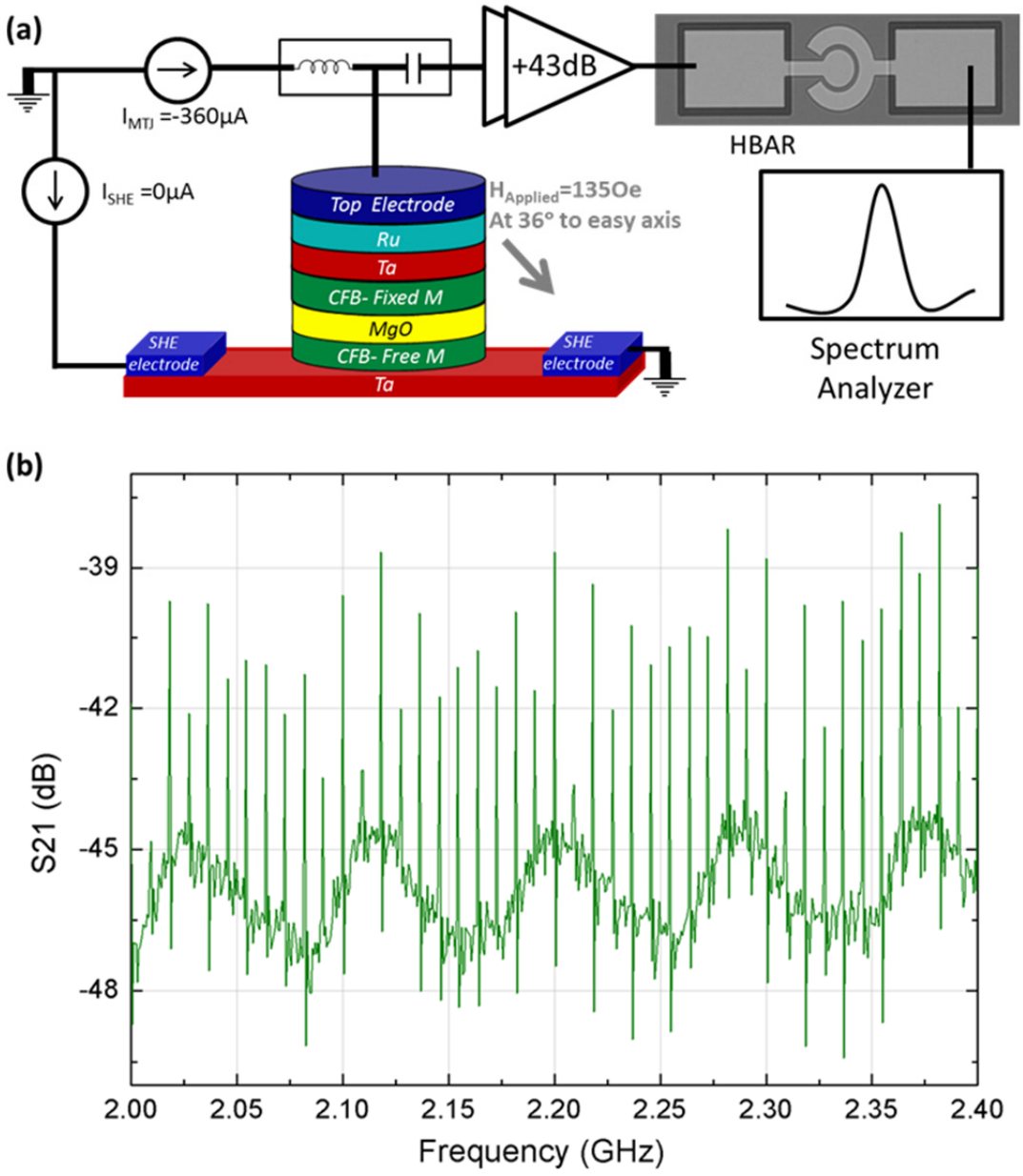

Figure 5.17: (a) Experimental setup for open loop measurements. The oscillation signal from SHE-MTJ is amplified and the filtered by HBAR and measured on the spectrum analyzer. (b) The plot shows transmission spectrum of the laterally coupled HBAR used for filtering the SHE-MTJ oscillator.

5.4 *Open loop current based magneto-acoustic oscillator using SHE-MTJ*

The standalone SHE-MTJ is driven by spin torque oscillation we measured in the previous section was then connected to a 2-port laterally coupled HBAR filter via a 43 dB broadband amplifier (2 amplifiers of gain 23 dB and 20 dB) (Figure 5.17(a)). The transmission response of the HBAR was measured for the bandwidth of interest using a network analyzer shows multiple resonances with insertion loss of around -39 dB (Figure 5.17(b)). The high insertion loss of the HBAR at 2 GHz frequency range is because the HBAR was designed for operation centered at a frequency of 4 GHz. At the low-frequency range, the AlN piezoelectric layer is not efficiently coupled to the acoustic modes of the HBAR, increasing the losses in the signal pickoff.

The output of the HBAR measured on the spectrum analyzer was plotted on top of the previously measured oscillation spectrum of the SHE-MTJ (Figure 5.18). We observe a sharp signal peak in the center of the spectrum that corresponds to the oscillation peak of the SHE-MTJ device. The linewidth of the filtered SHE-MTJ oscillation was measured to be 280 kHz, which corresponds to a $\Delta f_o/f_o$ ratio of 7560. This is the highest reported $\Delta f_o/f_o$ ratio for an open loop SHE-MTJ device or an MTJ oscillator device ever measured. The HBAR filtering increased the $\Delta f_o/f_o$ ratio of the SHE-MTJ oscillator by 1070 times. The measured linewidth of the oscillator with the filter in series depends on the quality factor of HBAR at the frequency of oscillation. We also see more peaks in the spectrum. These peaks correspond to the nearest HBAR (spaced by Δf = 9.1 MHz) resonances which fall within the large linewidth of the SHE-MTJ oscillator.

A closed loop system with the HBAR in feedback will further reduce the linewidth to get a record breaking $\Delta f_0/f_o$ ratio for SHE-MTJ oscillator while self-stabilizing its output. But due to the low output power of the SHE MTJ, we faced the same problems

caused by larger amplification and feedback in the presence of a low isolation circulator in the circuit implementation, as discussed in Chapter 4.4.3. The AC current feedback via the spin Hall effect channel was also attempted, but due to the high impedance of the SHE channel we were not able to observe current feedback based locking of the device with up to 90 dB of signal gain. With a higher power MTJ-based STO, a closed loop current-based magneto-acoustic oscillator can be implemented, which due to the HBAR filtering will have extremely narrow linewidth.

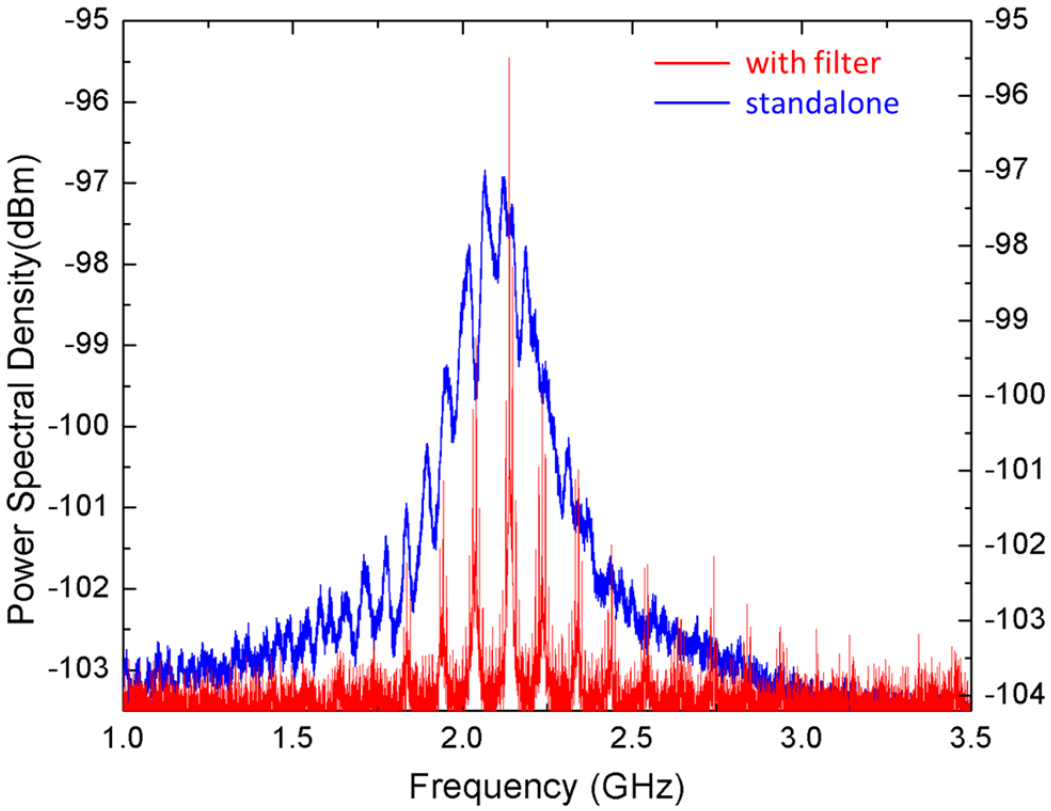

Figure 5.18: Plot shows the frequency spectrum of the SHE-MTJ oscillator measured after HBAR filtering shown in red and the frequency spectrum of the oscillator without HBAR filtering for comparison.

5.5 *Conclusion and future directions*

In this chapter, we introduced magnetic tunnel junctions and described how the spin-preserving tunneling in combination with different density of states at the Fermi level of the majority and the minority electrons lead to tunneling magnetoresistance. The TMR can be further enhanced by lattice matching (001) face of the ferromagnets to (001) texture of MgO tunnel barrier to match the evanescent states of the tunnel barrier to the electronic states in the ferromagnets. We introduced how spin Hall effect can be used to generate spin currents to apply spin transfer torque to the free layer magnet in MTJ. This three-terminal MTJ with separate read and write paths is called SHE-MTJ.

In this chapter, we demonstrated a novel fabrication process flow for making SHE-MTJs that allows for high yield and reduces process steps, making novel use of the e-beam resist as liftoff mask for oxide isolation step. In the fabricated SHE-MTJs with a TMR of 40%, we demonstrated bi-directional switching using current applied to SHE channel. Scaling of the SHE channel width for a fixed size of the MTJ pillar, we observed an increased efficiency of switching for a higher overlap between the long axis of MTJ and the SHE channel. We calculated that the critical current needed for switching in SHE-MTJ is half of the critical current needed for spin torque switching of MTJ due to it high spin injection efficiency. We demonstrated SHE-MTJ as the MRAM bit cell by applying read and write pulse to the devices and showed the repeatable operation for write pulses of duration as small as 100 ns. Switching probability of the SHE-MTJ as a function of write voltage amplitude and write pulse duration was measured to find switching from AP to P has 100% probability for -3.147 V at 6.5 ns. The P to AP switching was comparatively slower with 100% probability measured for 3.147 V at 8 ns pulse duration. We thus demonstrated SHE-

MTJs as potential MRAM bit cells, with sub 10 ns write times, having a decoupled read and write circuits that show symmetric switching characteristics for AP to P and P to AP state.

In the second part of this chapter, we studied the SHE-MTJ as an oscillator. Using spin injection from the SHE channel, we excited magnetization precession and measured the precession as voltage oscillations of the MTJ using the TMR effect. Applying to the SHE channel a current of 600 μA, a pillar current of -80 μA and a bias magnetic field of 135 Oe, we measured oscillations at 1.94 GHz having a peak power of -93.2 dBm for a 5 MHz resolution bandwidth. The linewidth of the oscillation was measured to be 400 MHz with a $\Delta f_o/f_o$ ratio of 4.85 having the total output power of 95.72 pW. We observed voltage controlled magnetic anisotropy based tuning of oscillation frequency having a tuning rate of 0.745 GHz/V, which is comparable to previously measured rate on a similar device.

Employing the SHE MTJ as a traditional MTJ, we excited magnetization precession in the SHE-MTJ for 0 μA spin Hall effect current drive, by applying -360 μA of current to the MTJ. We observed that the oscillation amplitude was higher when the bias magnetic field of 135 Oe was applied at an offset angle of 35º to the easy axis of the magnet. We measured the first harmonic of oscillation at 2.12 GHz having a peak power of -97 dBm measured for 1 MHz resolution bandwidth. The linewidth of the oscillation was 300 MHz with $\Delta f_o/f_o$ ratio of 7.066. We saw the frequency of oscillation decreases with the increased bias current. SHE-MTJ oscillator was then connected to a laterally coupled HBAR to form open loop current based magneto-acoustic oscillator, where HBAR behaves like an inline high quality factor filter. Frequency filtering from the HBAR reduced the linewidth of the oscillation from 300 MHz to 280 kHz and increased the $\Delta f_o/f_o$ ratio of the SHE-MTJ oscillator by 1070 times to 7560. This is the highest reported $\Delta f_o/f_o$ ratio an SHE-MTJ or an

MTJ in an open loop configuration without feedback. Attempts to measure the closed loop current based magneto-acoustic oscillator resulted in the formation of HBAR oscillator as observed in Chapter 4.4.3.

In the future, we would like to build SHE-MTJ with Pt-Hf SHE channel patterned to be just underneath the device for reducing the channel impedance while maintaining high spin Hall efficiency [98]. The fabricated device would have a thinner tunneling barrier of less than 0.8 nm thickness to reduce the RA product of the device. Such a device, with a high a TMR, can potentially generate oscillation power in the range of 100 nW to μW, which is needed for implementing the closed-loop current-based magneto-acoustic oscillator described in Chapter 3.3.1.

CHAPTER 6

SUMMARY AND FUTURE WORK

6.1 *Summary of work*

6.1.1 High-overtone bulk acoustic resonators

We demonstrated resonators, which are capable of coupling mechanical strain wave to spin torque oscillator or other physical systems, where AC strain can be used as a tool to manipulate the system behavior. 1-Port HBAR devices were fabricated and measured in silicon, diamond, and silicon carbide substrates. Our measurements showed that the silicon HBAR had high quality factors of 702 at 3 GHz resonance frequency measured at room temperature. On cooling the silicon HBAR down to 80 K, the quality factor increase to 5220. We developed a 1D analytical model for calculating the stress generated by HBAR and found good agreement in the calculated performance and simulated performance of the HBAR in Comsol. The diamond HBARs tested in the NV center systems have also shown good agreement to the simulated HBAR performance as a stress generator [52]. We further calculated that the silicon HBARs could generate 2.2 MPa of AC stress for 1 V drive amplitude at room temperature.

Laterally coupled HBAR were fabricated on sapphire substrates function as inline filters with the high quality factor from frequencies of 1.5 GHz all the way up to 8 GHz. Keeping the lateral spacing between the two ports of the HBARs small we got transmission loss as low as -25 dB over a wide range of frequencies. The loss is higher at frequencies below 2 GHz where the coupling from the piezoelectric is poor. We measured high quality factors for the device over the entire range of frequencies as

shown in Table 2.2. Due to the high quality factor, HBAR, when used as an inline filter in open-loop current-based magneto-acoustic oscillator, shows narrow linewidth in 10-185 kHz range. We measured the record-breaking f-Q product of 1.49×10^{14} Hz at 6 GHz, which shows that these HBARs when used as resonant components in oscillator loops, result in low phase noise oscillation performance.

6.1.2 SHE-MTJ

We fabricated SHE-MTJs with TMR of 40% and measured its bi-directional switching using the current drive through the SHE channel. Scaling the width of the SHE channel for a fixed size of the MTJ, we observed an increase in efficiency of switching for a higher overlap between the long axis of MTJ and the SHE channel. We calculated that the high spin injection efficiency of the SHE-MTJ results in 2 times lower amplitude of the critical current needed for switching when compared to a two terminal MTJ of the same size. We also demonstrated the operation of the SHE-MTJ as an MRAM bit cell by applying read pulses to the MTJ nanopillar and write pulse to the SHE channel. We showed repeatable MRAM operation for write pulses of duration as small as 100 ns. We further did switching probability measurements on the SHE-MTJ with β-Ta SHE channel and showed bi-directional switching of the SHE-MTJ at sub 10 ns (6.5 ns to AP to P and 8 ns for P to AP) for write voltages of amplitude 3.147 V with 100% probability.

We also studied the SHE-MTJ as an oscillator, where using the spin injection from the SHE channel, for a current of 600 μA, we measured oscillations at 1.94 GHz having a peak power of -93.2 dBm for a bias pillar current of -80 μA, and bias magnetic field of 135 Oe. The linewidth of the oscillation was measured to be 400 MHz with a $\Delta f_o/f_o$ ratio of 4.85 having a total output power of 95.72 pW when measured for a 50 Ω load. For a matched load, the peak power of the system is

27.76 pW which is 10 times the previously reported peak power for SHE-MTJ [15]. We observed voltage controlled magnetic anisotropy tuning of the oscillation frequency, having a tuning rate of 0.745 GHz/V which is comparable to previously measured rate on a similar device [15].

6.1.3 Open loop current based magneto-acoustic oscillator

Open loop current based magneto-acoustic oscillator was demonstrated, where the output from the spin valve or SHE-MTJ (or any magnetic oscillator) is filtered by the high quality factor laterally coupled HBAR devices shows an improvement in the linewidth. This system has shown to significantly enhance the linewidth of the spin valve oscillators from 35.4 MHz to 175 kHz with $\Delta f_o/f_o$ ratio as high as 23,657 measured for in-plane oscillation mode at 4.14 GHz for a spin valve device. This is the highest measured $\Delta f_o/f_o$ ratio for a spin valve oscillator in an open loop configuration. The $\Delta f_o/f_o$ ratio for the SHE-MTJ oscillators was enhanced by a factor of 1070 to reduce the linewidth if the oscillator from 300 MHz to 280 kHz.

The enhanced linewidth of the open loop magneto-acoustic oscillators corresponds to the bandwidth of the HBAR resonance filtering the oscillator. The small spacing of 9.1 MHz between the HBAR resonances results in sideband like spikes when the linewidth of the oscillator is bigger than 9.1 MHz. Reducing the electrode gap in HBAR, we can further decrease the transmission loss and thus reduce the amplification needed in magneto-acoustic oscillators [58]. The open loop system we demonstrated functions over a wide range of frequencies over the entire HBAR spectrum of 2 GHz to 6 GHz.

We implemented a self-locking closed loop current-based magneto-acoustic oscillator, but because of the low output power of the free running magnetic oscillator (SHE-MTJ and spin valves) it was necessary to amplify the signal by at least 90 dB to

get injection locking. The low isolation of the circulator used to feedback the filtered HBAR signal resulted in laterally couple HBAR devices being driven into oscillations. Such a system can be successfully implemented with circulators having modest -20 dB isolation using magnetic oscillators with 4 orders of magnitude higher output power in 10-100 nW range. The unintended feedback based HBAR oscillator formed was used to injection lock the spin valve oscillator, similar to an external signal source, resulting in the extremely narrow line width oscillation of the spin valve.

6.2 *Future work*

6.2.1 Closed loop microwave based magneto-acoustic oscillator

We have demonstrated in simulations, that closed loop (self-locked) magneto-acoustic oscillators, when successfully implemented, will stabilize the oscillation frequency of the STO. Just like the open loop current based magneto-acoustic oscillator the linewidth of a closed loop magneto-acoustic oscillator will be enhanced by the high quality factor of the HBAR frequency. Such a system will be ideal for RF applications due to its large tuning range at gigahertz frequencies. Further, the system can be used a magnetic field sensor of high accuracy because it can track small changes in the oscillation frequency due to its narrow linewidth. In this thesis, we proposed two different systems based upon different types of feedbacks- one where the feedback is through strain (Figure 3.8) and other where feedback is through current (Figure 3.10). The strain feedback-based oscillator, we envisioned needed high gain to lock the spin torque oscillator over a broad frequency range. The current feedback-based system requires about 39 dB lower gain for locking and hence, it was more efficient to implement compared to the strain-based locking system. The implementation of the current-based system is also simpler as it decouples the fabrication of HBARs from the STO, allowing for the use of exotic substrate materials

like sapphire which has lower transmission loss and higher quality factor [58]. The current-based feedback system has one major drawback that it needs exotic components like circulators for its implementation. Moreover, the performance of circulators concerning their isolation specification plays a crucial role in successful implementation of the system. With higher output power STO this constraint on the circulator performances relaxes but, their need still adds an additional challenge for future on-chip integrated implementation.

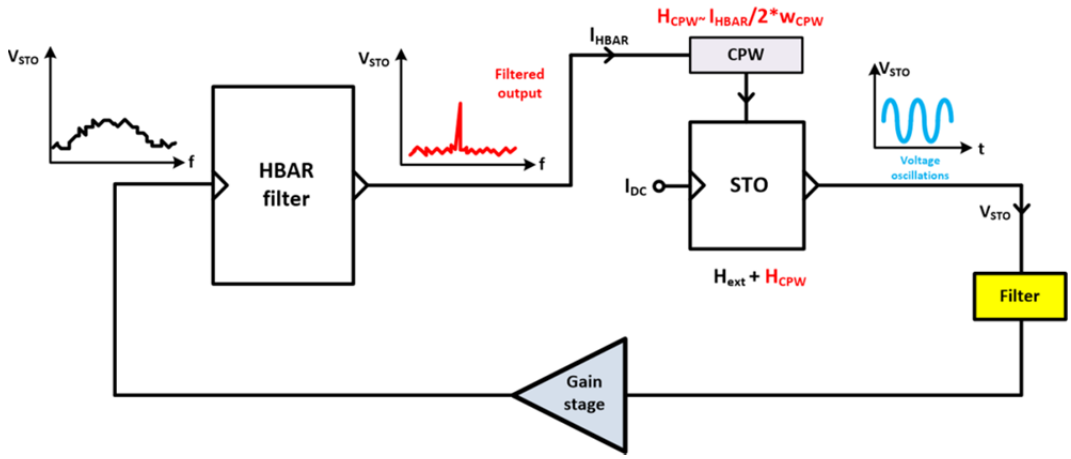

Figure 6.1: Microwave feedback based magneto-acoustic oscillator. The output from the STO is amplified, and feedback via HBAR as current I_{HBAR} which using a coplanar waveguide generates AC magnetic field used to injection lock the STO. The filter represents that only the fundamental mode is feedback.

The advantage of the strain-based system over the current-based system is in their ability to decouple the feedback path from the electrical domain and thus avoid the use of circulators. To take advantage of decoupling phenomenon, we propose a microwave generated magnetic field-based feedback system (Figure 6.1). In this system, the output from the STO is amplified and fed to the laterally coupled two-port HBAR. The HBAR filters the output of the STO, and due to its high quality factor gives out a

narrow linewidth signal similar to results observed in Chapter 4.4.2. The signal from the HBAR output port is fed back to the STO via a coplanar microwave waveguide fabricated on top the STO. The microwave current flowing in the waveguide will generate an AC magnetic field at the frequency of the current flow by Oersted's law. This magnetic field will interact with the magnetization of the spin torque oscillator as an external AC magnetic field injection locking the device [31, 37, 99]. This microwave based magneto-acoustic oscillator has many advantages over the other two feedback systems we discussed: a) like the strain-based system the microwave system decouples the electric feedback path and thus avoids use of circulators in the circuit; b) the microwave system is easier to fabricate, compared the strain-based system, by adding 2 extra mask layers to fabrication process for SHE-MTJ (Figure 5.3) for patterning SiO_2 insulator layer by liftoff and then a microwave waveguide by metal liftoff on top the pillar; c) the system will need less amplification compared to other feedback systems, as by scaling the width of the coplanar waveguide we get an amplification in the amplitude of field (h_{ac}) generated, this is given by:

$$h_{ac} = \frac{I_{ac}}{2w} \tag{6.1}$$

where I_{ac} is the amplitude of an AC current flowing through coplanar waveguide and w is the width of the waveguide.

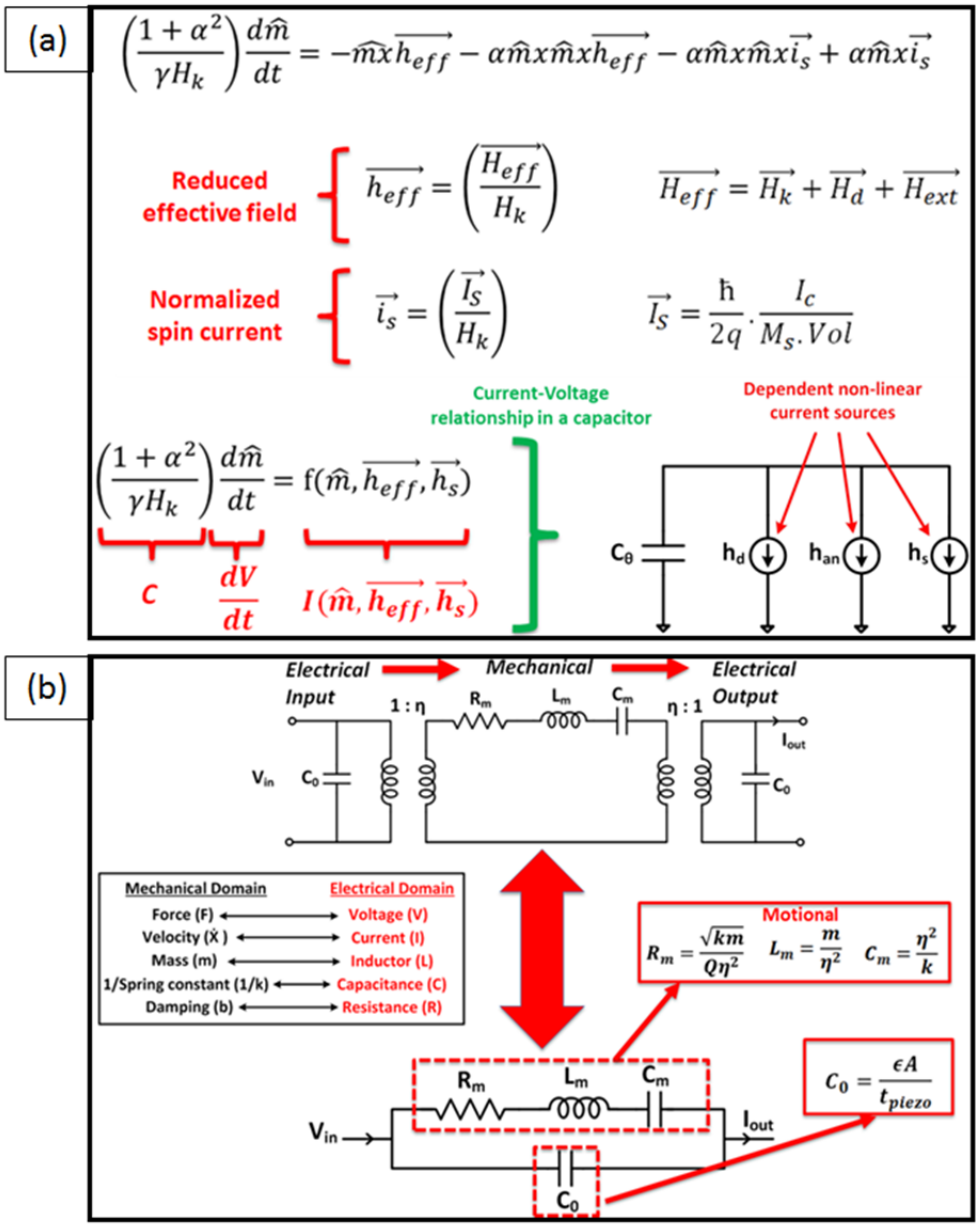

Figure 6.2: HSPICE simulation of the magneto-acoustic oscillator. (a) A modular approach to spintronics uses the capacitor-charging current system for implementing LLGS in HSPICE. (b) Butterworth Van-Dyke model used as an electrical equivalent circuit of HBAR in HSPICE.

Table 6.1 Simulation parameters used in HSPICE

Property	Value
Free layer size	$170\ nm\ \times\ 100\ nm\ \times\ 1.5\ nm$
M_s	$1100\ \text{erg}/cm^3$
H_{an}	$219\ Oe$
H_d	$13000\ Oe$
α	0.01
B_{eff}	$-7 \times 10^7\ \text{emu}/cm^3$
Rav	1 kΩ
H_{ap}	$300\ Oe$
Current	6.3 mA
TMR for low power	30% gives 40 pW output power
TMR for high power	100% for 25 nW output power
w(waveguide width)	0.5 μm
Quality factor	3000
Transmission loss	-20 dB
Size of resonator	100 μm × 60 μm
e33 (piezoelectric coeff.)	1.55 C/m^2

We simulated the microwave-based magneto-acoustic oscillator system in HSPICE, where LLGS equation is modeled using a linear capacitor whose voltage represents evolution the magnetization of the free layer. The capacitor is driven by non-linear current sources corresponding to the external magnetic field, shape anisotropy, demagnetization, and spin torque terms (Figure 6.2(a)) [100]. The effect of noise was also incorporated by adding noise current terms for the thermal noise and the uncertainty in the initial angle as additional inputs to the system. In HSPICE, we

also incorporated the effective model of HBAR using a Butterworth Van-Dyke circuit, where the values of inductor, capacitor and resistor and feedthrough capacitor are dependent on the mass, effective spring constant, resonant frequency, area, material properties, and the quality factor of the resonator (Figure 6.2(b)) [101]. We simulated a closed loop system including the amplifier modeled as a simple gain term, the parameters for which are given in Table 7.1.

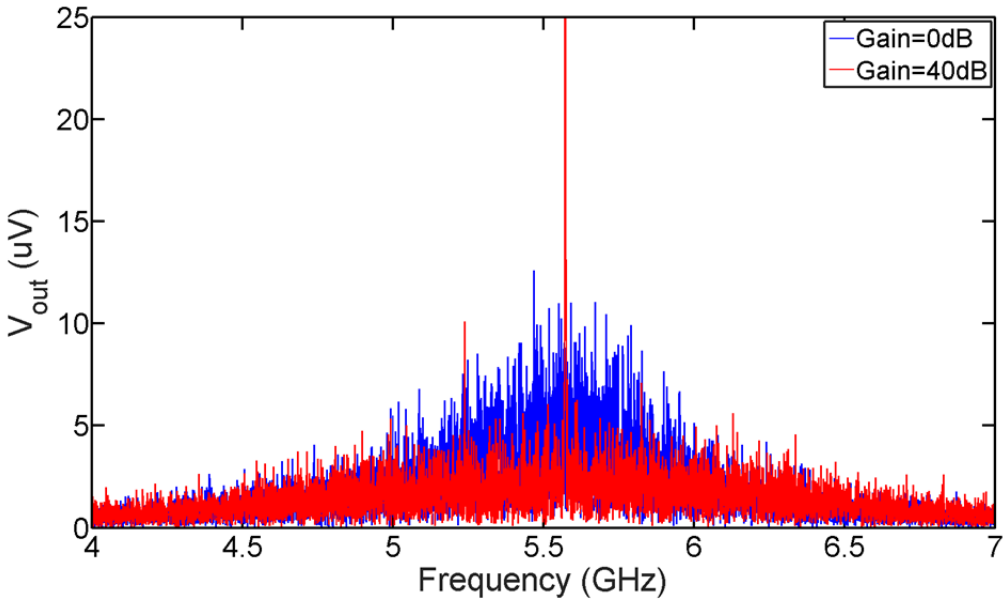

Figure 6.3: Frequency spectrum of the low power STO output simulated using HSPICE with microwave feedback (in red) from filtered HBAR output shows locking for a gain of 40 dB. System performance at 0 dB gain represents the performance of an unlocked low power STO (in blue).

The simulation of the closed loop microwave-based magneto-acoustic oscillator shows that the system locks for a gain of 40 dB for an out-of-plane mode of oscillation measured for I_{DC} of 6.3 mA. Out-of-plane mode of oscillation was chosen as it represents a best case scenario for the case of strain based locking [102], also out-of-plane mode has larger locking range and a lower threshold power for injection locking

[31]. The locked output of the simulated STO shows improved linewidth of higher power at the frequency of oscillation (Figure 6.3). To benchmark the performance of the microwave based magneto-acoustic oscillator and compare it to the strain and current feedback systems, we modeled and simulated all the three systems in HSPICE. We simulated the system for two different output peak powers of STO (40 pW and 25 nW), which could be changed by changing the polarization efficiency (and thus the TMR) of the STO.

Table 6.2 Results of HSPICE simulation of different magneto-acoustic oscillators

Feedback system	Gain needed for locking	
	Low power STO 40 pW	High power STO 25 nW
Acoustic	95 dB	70 dB
Current	75 dB	35 dB
Microwave	40 dB	20 dB

The microwave-based feedback system has the best efficiency as compared current and strain feedback as shown in Table 6.2. Microwave feedback needs 40 dB lesser gain than the strain-based system and 15-35 dB lesser gain than the current-based system. The amplitude of the gain needed in the microwave based magneto-acoustic oscillator can be further reduced by scaling the microwave coplanar waveguide from the modest 500 nm width to more aggressive 100 nm width. Another advantage of the microwave feedback system is that it can be scaled to provide feedback magnetic fields to multiple STOs on the same substrate. We believe such a system is a prime

candidate for demonstrating magneto-acoustic oscillator with narrow linewidth and high tunability.

6.2.2 Strain based locking of STOs using FBARs

Strain-based magneto-acoustic oscillator system is inefficient and hence will consume more power than the current and the microwave systems. In these simulations, we assumed the free layer magnet material is made of CoFeB, which has moderate to low magnetoelastic coefficient [103]. In Chapter 4.3, we demonstrated Terfenol-D can be used as free layer magnet in a spin valve device and performs comparably to CoFeGe/CoFe when employed as an oscillator. The value of magnetoelastic coefficient measured for Terfenol-D in literature is 20 times higher than that of CoFeB [77, 104]. Also, Terfenol-D has much lower M_s compared to CoFeB and hence the overall effect of the same amplitude of strain (which gets scaled by M_s) on the free layer is about 35 times more for Terfenol-D as given by Equation (3.8).

Further improvement in the system efficiency is possible with the use of a thin film FBAR based strain generator instead of an HBAR. FBAR with only a thin silicon substrate, matched to the thickness of the piezoelectric film, can produce 10 times higher strain than HBARs for the same amplitude of voltage drive. This system, though limited in the number of resonant frequencies, can utilize high strain generating bending and Lamb modes for straining the free layer magnet [105]. As this is a thin film structure, the entire structure stresses, and strains together and hence the challenge of positioning the stress maxima at the free layer of the STO is also resolved. Moreover, this system can also be used to test and implement strain based switching which has been proposed by Roy *et al*. to be a low power alternative

solution to challenges in memory scaling [74]. Higher amplitude of strain can be achieved with materials having high piezoelectric coefficients like $LiNbO_3$ and PZT.

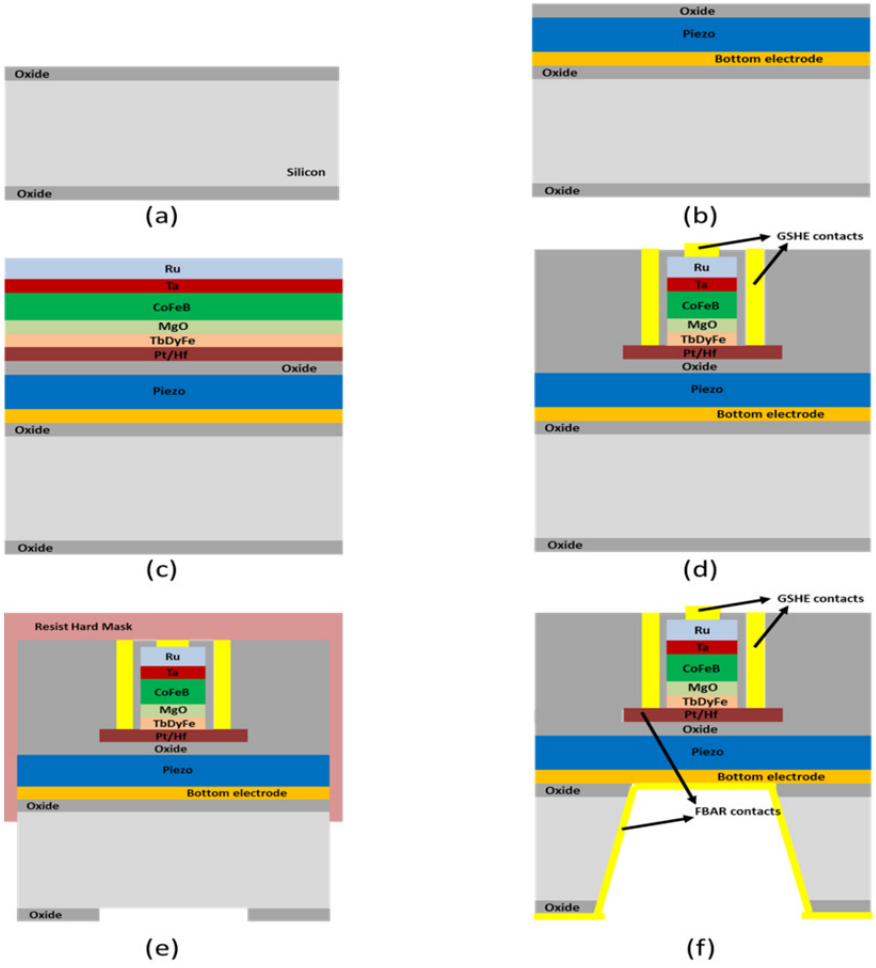

Figure 6.4: Process flow for fabricating SHE-MTJ with TbDyFe as the free layer on FBAR as the stress generator. (a) The thermal oxide is grown via LPCVD on a DSP silicon wafer. (b) Pt as bottom metal is sputtered and pattered by liftoff for reactive ion sputtering of AlN. (c) The SHE-MTJ material stack is deposited under high vacuum. (d) SHE-MTJ is fabricated via process shown in Chapter 5.2.1. (e) The oxide layer on the back is patterned by BOE etch acts as a hard mask for the KOH etch. (f) FBAR is released using a KOH etch of the silicon substrate.

An acoustic strain-based feedback system that uses Terfenol-D as free layer STO with an FBAR as a strain generator will thus perform 45 times better than a CoFeB free layer STO with an HBAR as a strain generator. This makes the system performance comparable to the microwave-based feedback system. We propose an innovative fabrication process flow for realizing the system (Figure 6.4). We start the process with thermal oxidation of silicon to passivate the surface (Figure 6.4(a)). The bottom electrode and the piezoelectric films are sputter deposited. PECVD oxide deposition is done on top of the piezoelectric film to form a passivation layer. This second passivation layer is used isolating the spin torque oscillator (Figure 6.4(b)). Magnetic film stack is then deposited contiguously in high vacuum to ensure clean interfaces. We use Pt with 0.7 nm Hf as channel material since it has been shown to reduce the damping (Figure 6.4(c)) [98]. We follow the process flow for SHE-MTJ as described in Chapter 5.2.1 to fabricate STO (Figure 6.4(d)). Patterning the backside thermal silicon dioxide using a resist mask and buffered oxide etch, we use it as a mask for KOH etching of the silicon substrate to form the released resonator (Figure 6.4(e)). The body of the resonator consists of piezoelectric film, and the SHE-MTJ fabricated on top of it. Aluminum is evaporated to draw out contacts from the bottom electrode for ease of wire bonding and testing (Figure 6.4(f)). Comsol simulations of this device structure show that positioning the SHE-MTJ near the anchor of the resonator (close to the edge of the release window) will further enhance the strain coupled into the free layer.

6.3 ***Conclusion***

In this chapter, we recapitulated some of the important results and achievements described in this thesis in the area: a) high-frequency HBAR resonator design and fabrication as a strain generator, and as an inline filter; b) fabrication, switching

characterization, and oscillator performance of spin Hall effect magnetic tunnel junction; c) linewidth enhancement and quality factor improvement of both spin valve and SHE-MTJ based magnetic oscillators using HBAR inline filters to implement open loop current-based magneto-acoustic oscillator.

We also presented two avenues for future work. First, we proposed a magnetic field-based magneto-acoustic oscillator. In this system, the output from the STO when filtered by the high quality factor HBAR is coupled via a microwave coplanar waveguide to the STO for injection locking the STO. We benchmarked the closed loop performance of this system versus the strain and current-based system by simulating the system in HSPICE. The results showed that microwave-based system requires 15 dB to 35 dB lower gain than the current-based system and has much higher efficiency when compared to strain base locking system.

Lastly, we proposed a new process flow for implementing acoustic strain-based locking. This process flow used an FBAR like thin film resonator as a stress transducer to a Terfenol-D free layer based SHE-MTJ. This configuration improves the efficiency of the acoustic strain-based locking and makes it a practical option to implement.

CHAPTER 7 APPENDIX

7.1 *Solutions for 1D analytical model of HBAR as a stress generator*

$$C1=$$

$$\left(\epsilon\, e_{33}\, V_{ext}\, \left(\text{Cos}[L_{si}\,\gamma_{si}]\,\text{Sin}[t_p\,\gamma_p]\,CC_{33}^{D}\,\gamma_p+\text{Sin}[L_{si}\,\gamma_{si}]\,EE_{si}\,\gamma_{si}\right)\right)\Big/$$
$$\left(\epsilon\,\text{Cos}[L_{si}\,\gamma_{si}]\,\text{Sin}[t_p\,\gamma_p]\,CC_{33}^{2\,D}\,t_p\,\gamma_p^2-\text{Sin}[t_p\,\gamma_p]\,\text{Sin}[L_{si}\,\gamma_{si}]\,e_{33}^2\,EE_{si}\,\gamma_{si}-\right.$$
$$\left.CC_{33}^{D}\,\gamma_p\left(4\,\text{Cos}[L_{si}\,\gamma_{si}]\,\text{Sin}\left[\frac{t_p\,\gamma_p}{2}\right]^2 e_{33}^2-\epsilon\,\text{Cos}[t_p\,\gamma_p]\,\text{Sin}[L_{si}\,\gamma_{si}]\,EE_{si}\,t_p\,\gamma_{si}\right)\right)$$

$$C2=$$

$$\left(2\,\epsilon\,\text{Cos}[L_{si}\,\gamma_{si}]\,\text{Sin}\left[\frac{t_p\,\gamma_p}{2}\right]^2 CC_{33}^{D}\,e_{33}\,V_{ext}\,\gamma_p\right)\Big/$$
$$\left(\epsilon\,\text{Cos}[L_{si}\,\gamma_{si}]\,\text{Sin}[t_p\,\gamma_p]\,CC_{33}^{2\,D}\,t_p\,\gamma_p^2-\text{Sin}[t_p\,\gamma_p]\,\text{Sin}[L_{si}\,\gamma_{si}]\,e_{33}^2\,EE_{si}\,\gamma_{si}+CC_{33}^{D}\right.$$
$$\left.\gamma_p\left(-4\,\text{Cos}[L_{si}\,\gamma_{si}]\,\text{Sin}\left[\frac{t_p\,\gamma_p}{2}\right]^2 e_{33}^2+\epsilon\,\text{Cos}[t_p\,\gamma_p]\,\text{Sin}[L_{si}\,\gamma_{si}]\,EE_{si}\,t_p\,\gamma_{si}\right)\right)$$

$$C3=$$

$$\left(2\,\epsilon\,\text{Sin}\left[\frac{t_p\,\gamma_p}{2}\right]^2\text{Sin}[L_{si}\,\gamma_{si}]\,CC_{33}^{D}\,e_{33}\,V_{ext}\,\gamma_p\right)\Big/$$
$$\left(\epsilon\,\text{Cos}[L_{si}\,\gamma_{si}]\,\text{Sin}[t_p\,\gamma_p]\,CC_{33}^{2\,D}\,t_p\,\gamma_p^2-\text{Sin}[t_p\,\gamma_p]\,\text{Sin}[L_{si}\,\gamma_{si}]\,e_{33}^2\,EE_{si}\,\gamma_{si}-\right.$$
$$\left.CC_{33}^{D}\,\gamma_p\left(4\,\text{Cos}[L_{si}\,\gamma_{si}]\,\text{Sin}\left[\frac{t_p\,\gamma_p}{2}\right]^2 e_{33}^2-\epsilon\,\text{Cos}[t_p\,\gamma_p]\,\text{Sin}[L_{si}\,\gamma_{si}]\,EE_{si}\,t_p\,\gamma_{si}\right)\right)$$

$$C4=$$

$$\left(2\,\epsilon\,\text{Cos}[L_{si}\,\gamma_{si}]\,\text{Sin}\left[\frac{t_p\,\gamma_p}{2}\right]^2 CC_{33}^{D}\,e_{33}\,V_{ext}\,\gamma_p\right)\Big/$$
$$\left(\epsilon\,\text{Cos}[L_{si}\,\gamma_{si}]\,\text{Sin}[t_p\,\gamma_p]\,CC_{33}^{2\,D}\,t_p\,\gamma_p^2-\text{Sin}[t_p\,\gamma_p]\,\text{Sin}[L_{si}\,\gamma_{si}]\,e_{33}^2\,EE_{si}\,\gamma_{si}-\right.$$
$$\left.CC_{33}^{D}\,\gamma_p\left(4\,\text{Cos}[L_{si}\,\gamma_{si}]\,\text{Sin}\left[\frac{t_p\,\gamma_p}{2}\right]^2 e_{33}^2-\epsilon\,\text{Cos}[t_p\,\gamma_p]\,\text{Sin}[L_{si}\,\gamma_{si}]\,EE_{si}\,t_p\,\gamma_{si}\right)\right)$$

$$A1=$$

$$-\left(\epsilon\,\text{Sec}[t_p\,\gamma_p]\,CC_{33}^{D}\,V_{ext}\,\gamma_p\,\left(-\text{Sin}[t_p\,\gamma_p]\,e_{33}^2+\epsilon\,\text{Cos}[t_p\,\gamma_p]\,CC_{33}^{D}\,t_p\,\gamma_p\right)\right.$$
$$\left.\left(\text{Cos}[L_{si}\,\gamma_{si}]\,\text{Sin}[t_p\,\gamma_p]\,CC_{33}^{D}\,\gamma_p+\text{Cos}[t_p\,\gamma_p]\,\text{Sin}[L_{si}\,\gamma_{si}]\,EE_{si}\,\gamma_{si}\right)\right)\Big/$$
$$\left(\left(\epsilon\,\text{Cos}[L_{si}\,\gamma_{si}]\,\text{Sin}[t_p\,\gamma_p]\,CC_{33}^{2\,D}\,t_p\,\gamma_p^2-\text{Sin}[t_p\,\gamma_p]\,\text{Sin}[L_{si}\,\gamma_{si}]\,e_{33}^2\,EE_{si}\,\gamma_{si}-\right.\right.$$
$$\left.CC_{33}^{D}\,\gamma_p\left(4\,\text{Cos}[L_{si}\,\gamma_{si}]\,\text{Sin}\left[\frac{t_p\,\gamma_p}{2}\right]^2 e_{33}^2-\epsilon\,\text{Cos}[t_p\,\gamma_p]\,\text{Sin}[L_{si}\,\gamma_{si}]\,EE_{si}\,t_p\,\gamma_{si}\right)\right)$$
$$\left.\left(\epsilon\,CC_{33}^{D}\,t_p\,\gamma_p-e_{33}^2\,\text{Tan}[t_p\,\gamma_p]\right)\right)$$

$$A2=$$

$$-\frac{C4\,e_{33}}{\epsilon}$$

Figure 7.1: Solutions to the analytic 1D model for calculating stress generated in HBAR shown in Chapter 2.2.3. Substrate properties are referred using subscript 'si', and piezoelectric material properties are referred using subscript 'p.'

7.2 *HBAR as an oscillator*

Closed loop current-based magneto-acoustic oscillator due to the low isolation provided by the circulator resulted in oscillations of the HBAR. One particular combination of amplifiers was used to measure the HBAR oscillations on the spectrum analyzer (Figure 4.20). Measured frequency spectrum showed the fundamental mode at 4.742 GHz with higher harmonics up to the 5th harmonic at 23.71 GHz (Figure 7.2). For every harmonic, including the fundamental mode, we see two sidebands separated by a frequency of 452 MHz from the central peak. These side bands correspond to a loop delay of 2.21 ns (Figure 7.4).

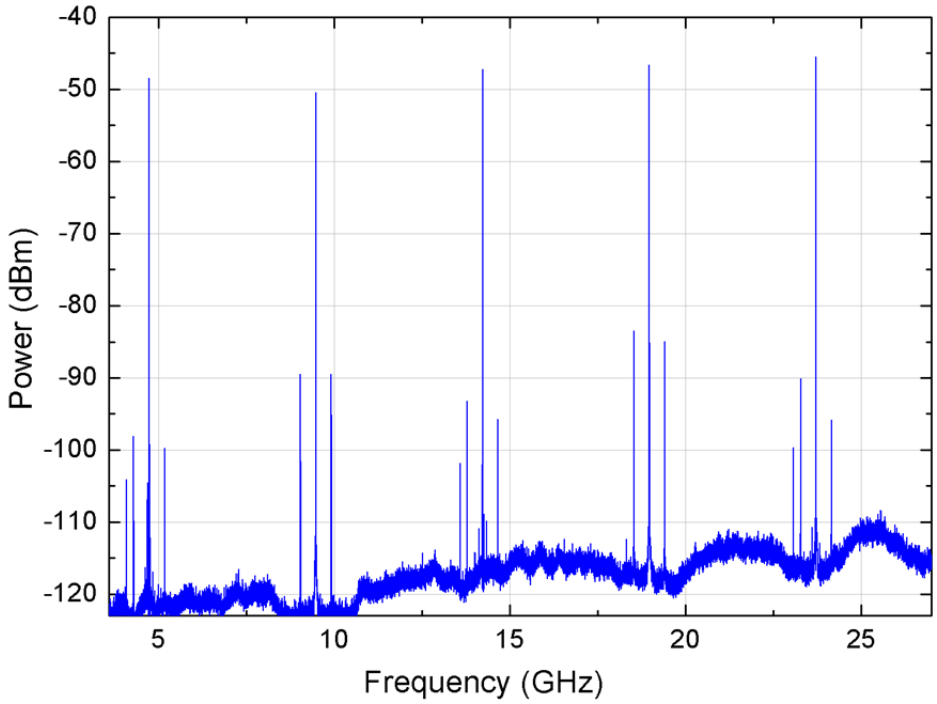

Figure 7.2: Frequency spectrum of the HBAR oscillator, measured for closed loop current-based magneto-acoustic oscillator setup, shows fundamental mode at 4.742 GHz and higher harmonics up to 23.7 GHz measured with a resolution bandwidth of 100 kHz.

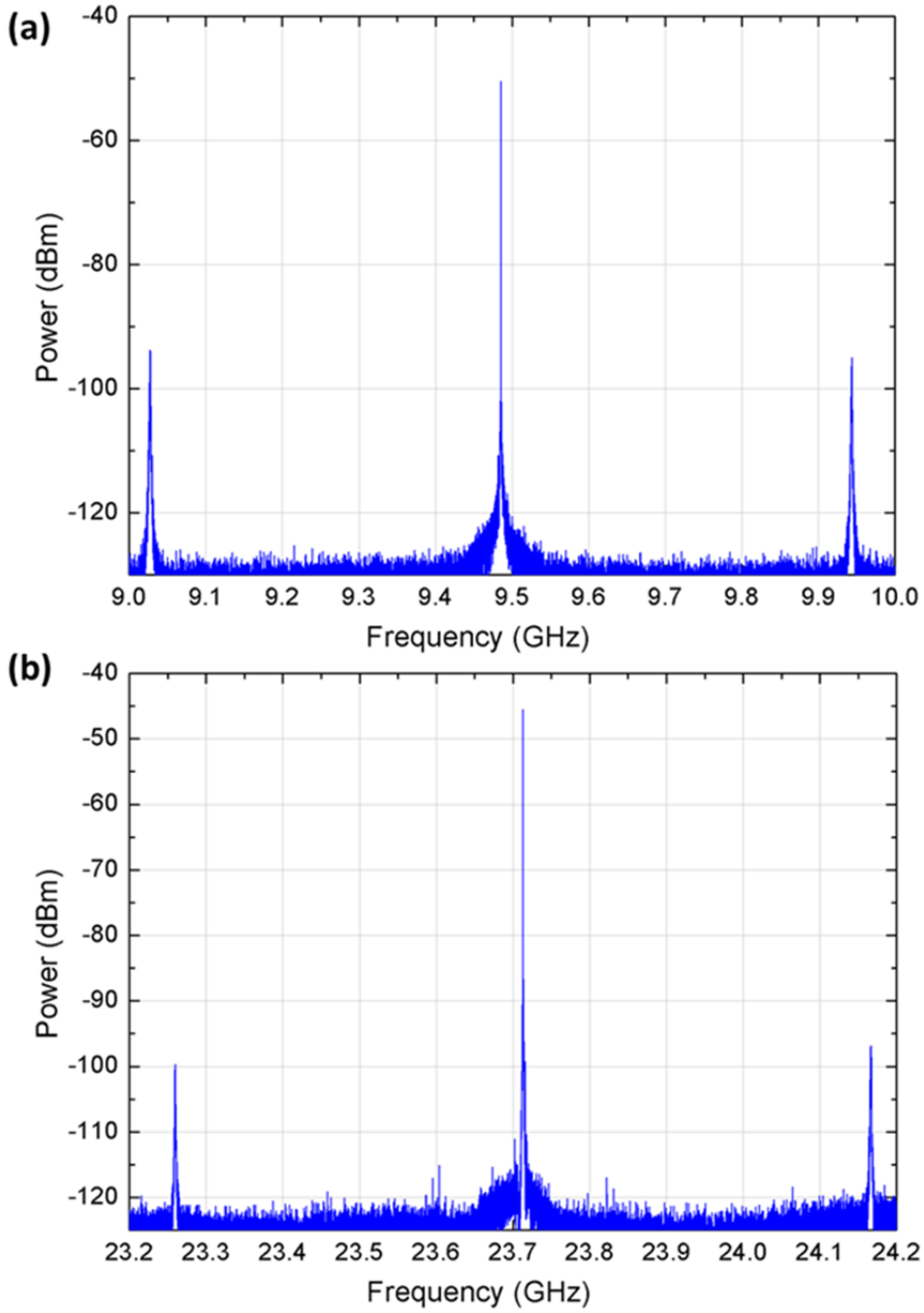

Figure 7.3: Frequency spectrum of HBAR oscillator shows harmonics and two side bands which are separated from the center frequency by 452 MHz. (a) The second harmonic of oscillation measured at 9.485 GHz. (b) The 5th harmonic of the fundamental oscillation frequency measured at 23.71 GHz.

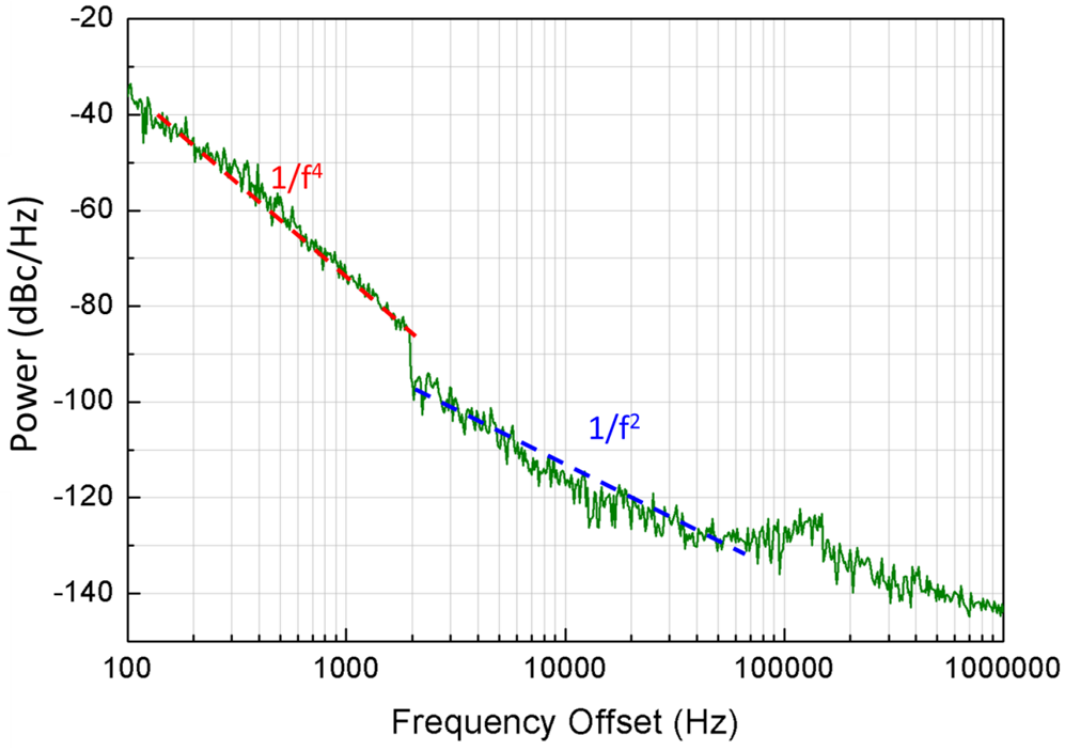

Figure 7.4: Phase noise spectrum, measured for the fundamental mode of oscillation at 4.72 GHz with power 7.3 dBm, shows $1/f^4$ trend up to 2 kHz offset and $1/f^2$ trend after 2 kHz offset.

The phase noise performance of the HBAR oscillator was measured for the fundamental mode had the output power of 7.3 dBm. The phase-noise shows a $1/f^2$ trend from 2 kHz offset, which is due to the amplitude noise in the oscillator system. This includes the amplitude noise of the resonator in the form of its resistance and the amplitude noise of all the amplifiers in the feedback loop. From offset frequency of 100 Hz to 2 kHz, we observe a $1/f^4$ trend in the measured phase-noise spectrum. Usually, in resonator based oscillator systems, $1/f^4$ noise in the phase noise spectrum comes from random walk noise in the frequency spectrum. This implies that the resonant frequency of the HBAR oscillator fluctuates randomly by 2 kHz around the

natural frequency. Other HBAR based oscillators fabricated on sapphire substrates do not show a $1/f^4$ trend at high offset frequencies like 2 kHz [106]. Another source of the $1/f^4$ might be from the circulator working with high flicker noise from the amplifiers in the feedback path. This seems a more likely source for the $1/f^4$ noise rather than the random walk of the HBAR resonance. Measured phase noise of the HBAR shows -117 dBc/Hz phase noise at 100 kHz offset. The noise performance of the HBAR oscillator presented here is comparable to state of the art HBAR oscillator with -130 dBc/Hz phase noise measured at 100 kHz offset frequency from the carrier [106].

BIBLIOGRAPHY

[1] J. C. Slonczewski, "Current-driven excitation of magnetic multilayers," *J. Magn. Magn. Mater.*, vol. 159, no. 1–2, pp. L1–L7, 1996.

[2] L. Berger, "Emission of spin waves by a magnetic multilayer traversed by a current," *Phys. Rev. B - Condens. Matter Mater. Phys.*, vol. 54, no. 13, pp. 9353–9358, 1996.

[3] S. I. Kiselev *et al.*, "Microwave oscillations of a nanomagnet driven by a spin-polarized current," *Nature*, vol. 425, no. 6956, pp. 380–383, 2003.

[4] D. C. Ralph and M. D. Stiles, "Spin transfer torques," *J. Magn. Magn. Mater.*, vol. 320, no. 7, pp. 1190–1216, 2008.

[5] D. Houssameddine *et al.*, "Spin transfer induced coherent microwave emission with large power from nanoscale MgO tunnel junctions," *Appl. Phys. Lett.*, vol. 93, no. 2, p. 022505, 2008.

[6] N. Amin and M. X. Tang, "Analysis of Electromagnetic Fields Generated by a Spin-Torque Oscillator," *IEEE Trans. Magn.*, vol. 45, no. 10, pp. 4183–4186, 2009.

[7] O. Prokopenko, E. Bankowski, T. Meitzler, V. Tiberkevich, and A. Slavin, "Spin-torque nano-oscillator as a microwave signal source," *IEEE Magn. Lett.*, vol. 2, p. 3000104, 2011.

[8] T. Chen *et al.*, "Spin-Torque and Spin-Hall Nano-Oscillators," *Proc. IEEE*, vol. 104, no. 10, pp. 1919–1945, 2016.

[9] W. H. Rippard *et al.*, "Spin-transfer dynamics in spin valves with out-of-plane magnetized CoNi free layers," *Phys. Rev. B - Condens. Matter Mater. Phys.*, vol. 81, no. 1, p. 014426, 2010.

[10] H. Maehara *et al.*, "Large emission power over 2 μW with high Q factor obtained from manocontact magnetic tunnel junction-based spin torque oscillator," *Appl. Phys. Express*, vol. 6, no. 11, p. 113005, 2013.

[11] W. H. Rippard, M. R. Pufall, and S. E. Russek, "Comparison of frequency, linewidth, and output power in measurements of spin-transfer nanocontact oscillators," *Phys. Rev. B - Condens. Matter Mater. Phys.*, vol. 74, no. 22, p. 224409, 2006.

[12] C. H. Sim, M. Moneck, T. Liew, and J. G. Zhu, "Frequency-tunable perpendicular spin torque oscillator," *J. Appl. Phys.*, vol. 111, no. 7, p. 07C914, 2012.

[13] D. Houssameddine *et al.*, "Spin-torque oscillator using a perpendicular polarizer and a planar free layer.," *Nat. Mater.*, vol. 6, no. 6, pp. 447–453, 2007.

[14] P. Villard *et al.*, "A GHz spintronic-based RF oscillator," *IEEE J. Solid-State Circuits*, vol. 45, no. 1, pp. 214–223, 2010.

[15] L. Liu, C. F. Pai, D. C. Ralph, and R. A. Buhrman, "Magnetic oscillations driven by the spin hall effect in 3-terminal magnetic tunnel junction devices," *Phys. Rev. Lett.*, vol. 109, no. 18, p. 186602, 2012.

[16] L. Liu, C.-F. Pai, Y. Li, H. W. Tseng, D. C. Ralph, and R. A. Buhrman, "Spin-Torque Switching with the Giant Spin Hall Effect of Tantalum," *Science (80-.).*, vol. 336, no. 6081, pp. 555–558, May 2012.

[17] A. A. Tulapurkar *et al.*, "Spin-torque diode effect in magnetic tunnel junctions.," *Nature*, vol. 438, no. 7066, pp. 339–342, 2005.

[18] S. Ishibashi *et al.*, "Large diode sensitivity of CoFeB/MgO/CoFeB magnetic tunnel junctions," *Appl. Phys. Express*, vol. 3, no. 7, p. 073001, 2010.

[19] S. Kaka, M. R. Pufall, W. H. Rippard, T. J. Silva, S. E. Russek, and J. A. Katine, "Mutual phase-locking of microwave spin torque nano-oscillators," *Nature*, vol. 437, no. 7057, pp. 389–392, 2006.

[20] N. Locatelli, V. Cros, and J. Grollier, "Spin-torque building blocks," *Nat. Mater.*, vol. 13, no. 1, pp. 11–20, 2013.

[21] K. Roy *et al.*, "Exploring spin transfer torque devices for unconventional computing," *IEEE J. Emerg. Sel. Top. Circuits Syst.*, vol. 5, no. 1, pp. 5–16, 2015.

[22] P. M. Braganca, B. A. Gurney, B. A. Wilson, J. A. Katine, S. Maat, and J. R. Childress, "Nanoscale magnetic field detection using a spin torque oscillator," *Nanotechnology*, vol. 21, no. 23, p. 235202, 2010.

[23] J.-G. Z. J.-G. Zhu, X. Z. X. Zhu, and Y. T. Y. Tang, "Microwave Assisted Magnetic Recording," *IEEE Trans. Magn.*, vol. 44, no. 1, pp. 125–131, 2008.

[24] J. Von Kim, V. Tiberkevich, and A. N. Slavin, "Generation linewidth of an auto-oscillator with a nonlinear frequency shift: Spin-torque nano-oscillator," *Phys. Rev. Lett.*, vol. 100, no. 1, p. 017207, 2008.

[25] S. E. Russek, W. H. Rippard, T. Cecil, and R. Heindl, "Spin-Transfer Nano-Oscillators," in *Handbook of Nanophysics: Functional Nanomaterials*, K. D. Sattler, Ed. Boca Raton, FL: CRC Press, 2010, pp. 38-1-38–24.

[26] A. Slavin and V. Tiberkevich, "Nonlinear auto-oscillator theory of microwave

generation by spin-polarized current," *IEEE Trans. Magn.*, vol. 45, no. 4, pp. 1875–1918, 2009.

[27] M. Quinsat *et al.*, "Amplitude and phase noise of magnetic tunnel junction oscillators," *Appl. Phys. Lett.*, vol. 97, no. 18, p. 182507, 2010.

[28] R. Sharma, P. Dürrenfeld, E. Iacocca, O. G. Heinonen, J. Åkerman, and P. K. Muduli, "Mode-hopping mechanism generating colored noise in a magnetic tunnel junction based spin torque oscillator," *Appl. Phys. Lett.*, vol. 105, no. 13, p. 132404, 2014.

[29] T. Yamamoto, T. Seki, T. Kubota, H. Yako, and K. Takanashi, "Zero-field spin torque oscillation in Co2(Fe, Mn)Si with a point contact geometry," *Appl. Phys. Lett.*, vol. 106, no. 9, p. 092406, 2015.

[30] W. H. Rippard, M. R. Pufall, S. Kaka, T. J. Silva, S. E. Russek, and J. A. Katine, "Injection locking and phase control of spin transfer nano-oscillators," *Phys. Rev. Lett.*, vol. 95, no. 6, p. 067203, 2005.

[31] S. Urazhdin, P. Tabor, V. Tiberkevich, and A. Slavin, "Fractional synchronization of spin-torque nano-oscillators," *Phys. Rev. Lett.*, vol. 105, no. 10, p. 104101, 2010.

[32] W. Rippard, M. Pufall, and A. Kos, "Time required to injection-lock spin torque nanoscale oscillators," *Appl. Phys. Lett.*, vol. 103, no. 18, p. 182403, 2013.

[33] A. Houshang, E. Iacocca, P. Dürrenfeld, S. R. Sani, J. Åkerman, and R. K. Dumas, "Spin-wave-beam driven synchronization of nanocontact spin-torque oscillators," *Nat. Nanotechnol.*, vol. 11, no. 3, pp. 280–286, 2015.

[34] V. S. Tiberkevich, R. S. Khymyn, H. X. Tang, and A. N. Slavin, "Sensitivity to external signals and synchronization properties of a non-isochronous auto-oscillator with delayed feedback.," *Sci. Rep.*, vol. 4, p. 3873, 2014.

[35] G. Khalsa, M. D. Stiles, and J. Grollier, "Critical current and linewidth reduction in spin-torque nano-oscillators by delayed self-injection," *Appl. Phys. Lett.*, vol. 106, no. 24, p. 242402, 2015.

[36] S. Tsunegi *et al.*, "Self-Injection Locking of a Vortex Spin Torque Oscillator by Delayed Feedback," *Sci. Rep.*, vol. 6, p. 26849, 2016.

[37] D. Kumar *et al.*, "Coherent microwave generation by spintronic feedback oscillator," *Sci. Rep.*, vol. 6, p. 30747, 2016.

[38] A. V Drozdovskii and A. B. Ustinov, "Phase noise management of spin-wave delay-line oscillators," *J. Phys. Conf. Ser.*, vol. 661, no. 1, p. 012062, 2015.

[39] J. Logan, R.T., L. Maleki, and M. Shadaram, "Stabilization of oscillator phase using a fiber-optic delay-line," in *Proceedings of the 45th Annual Symposium on Frequency Control 1991*, 1991, p. 508–512.

[40] A. Hajimiri, S. Limotyrakis, and T. H. Lee, "Jitter and phase noise in ring oscillators," *IEEE J. Solid-State Circuits*, vol. 34, no. 6, pp. 790–804, 1999.

[41] J. T. M. van Beek and R. Puers, "A review of MEMS oscillators for frequency reference and timing applications," *J. Micromechanics Microengineering*, vol. 22, no. 1, p. 013001, 2012.

[42] I. P. Prikhodko *et al.*, "In-run bias self-calibration for low-cost MEMS vibratory gyroscopes," in *2014 IEEE/ION Position, Location and Navigation Symposium - PLANS 2014*, 2014, pp. 515–518.

[43] B. E. Boser and R. T. Howe, "Surface micromachined accelerometers," *IEEE J. Solid-State Circuits*, vol. 31, no. 3, pp. 366–375, 1996.

[44] M. Lutz *et al.*, "MEMS oscillators for high volume commercial applications," in *TRANSDUCERS 2007 - 2007 International Solid-State Sensors, Actuators and Microsystems Conference*, 2007, vol. C, no. 408, pp. 49–52.

[45] R. Aigner, "SAW and BAW technologies for RF filter applications: A review of the relative strengths and weaknesses," in *2008 IEEE Ultrasonics Symposium*, 2008, pp. 582–589.

[46] R. Ruby *et al.*, "Positioning FBAR technology in the frequency and timing domain," *IEEE Trans. Ultrason. Ferroelectr. Freq. Control*, vol. 59, no. 3, pp. 334–345, 2012.

[47] R. Ruby, "Review and comparison of bulk acoustic wave FBAR, SMR technology," in *2007 IEEE Ultrasonics Symposium Proceedings*, 2007, pp. 1029–1040.

[48] S. Sridaran *et al.*, "Low jitter FBAR based chip scale precision oscillator," in *2014 IEEE International Ultrasonics Symposium*, 2014, pp. 85–88.

[49] K. M. Lakin *et al.*, "Thin film resonator technology," in *41st Annual Symposium on Frequency Control*, 1987, pp. 371–381.

[50] G. R. Kline, K. M. Lakin, and K. T. Mccarron, "Overmoded high Q resonators for microwave oscillators," in *1993 IEEE International Frequency Control Symposium*, 1993, pp. 718–721.

[51] E. R. Macquarrie, T. A. Gosavi, N. R. Jungwirth, S. A. Bhave, and G. D. Fuchs, "Mechanical spin control of nitrogen-vacancy centers in diamond," *Phys. Rev. Lett.*, vol. 111, no. 22, p. 227602, 2013.

[52] E. R. Macquarrie, T. A. Gosavi, S. A. Bhave, and G. D. Fuchs, “Coherent control of a nitrogen-vacancy center spin ensemble with a diamond mechanical resonator,” *Optica*, vol. 2, no. 3, pp. 233–238, 2015.

[53] D. A. Feld, R. Parker, R. Ruby, P. Bradley, and D. Shim, “After 60 years: A new formula for computing quality factor is warranted,” in *2008 IEEE Ultrasonics Symposium*, 2008, no. 6, pp. 431–436.

[54] R. Tabrizian and F. Ayazi, “Effect of phonon interactions on limiting the f.Q product of micromechanical resonators,” in *TRANSDUCERS 2009 - 2009 International Solid-State Sensors, Actuators and Microsystems Conference*, 2009, vol. 1, no. 3, pp. 2131–2134.

[55] K. F. Graff, *Wave Motion in Elastic Solids*. Dover Publications, 1975.

[56] S. Ardanuç and A. Lal, “Two-port electromechanical model for bulk-piezoelectric excitation of surface micromachined beam resonators,” *J. Microelectromechanical Syst.*, vol. 18, no. 3, pp. 626–640, 2009.

[57] D. Gachon *et al.*, “Laterally coupled narrow-band high overtone bulk wave filters using thinned single crystal lithium niobate layers,” in *2011 Joint Conference of the IEEE International Frequency Control and the European Frequency and Time Forum (FCS) Proceedings*, 2011, pp. 1–5.

[58] A. Reinhardt *et al.*, “Ultra-high Q.f product laterally-coupled AlN/silicon and AlN/sapphire High Overtone Bulk Acoustic wave Resonators,” in *2013 IEEE International Ultrasonics Symposium (IUS)*, 2013, pp. 1922–1925.

[59] S. Tamaru, H. Kubota, K. Yakushiji, S. Yuasa, and A. Fukushima, “Extremely Coherent Microwave Emission from Spin Torque Oscillator Stabilized by Phase Locked Loop,” *Sci. Rep.*, vol. 5, p. 18134, 2015.

[60] J. Persson, Y. Zhou, and J. Akerman, “Phase-locked spin torque oscillators: Impact of device variability and time delay,” *J. Appl. Phys.*, vol. 101, no. 9, p. 09A503, 2007.

[61] Y. Zhou, J. Persson, and J. Åkerman, “Intrinsic phase shift between a spin torque oscillator and an alternating current,” *J. Appl. Phys.*, vol. 101, no. 9, p. 09A510, 2007.

[62] R. C. O’Handley, O. S. Song, and C. A. Ballentine, “Determining thin-film magnetoelastic constants,” *J. Appl. Phys.*, vol. 74, no. 10, pp. 6302–6307, 1993.

[63] W. H. Rippard, M. R. Pufall, S. Kaka, S. E. Russek, T. J. Silva, and J. A. Katine, “Microwave Dynamics and Phase Locking in Spin Transfer Nanocontacts.” KITP Conference: Spintronics, University of California, Santa Barbara. 20 March 2006. Lecture.

[64] M. Beleggia, M. De Graef, Y. T. Millev, D. A. Goode, and G. Rowlands, “Demagnetization factors for elliptic cylinders,” *J. Phys. D. Appl. Phys.*, vol. 38, no. 18, pp. 3333–3342, 2005.

[65] W. F. B. Jr., “Thrmal Fluctuations of a Single-Domain Particle,” *Phys. Rev.*, vol. 130, no. 5, pp. 1677–1686, 1963.

[66] P. G. Gowtham, G. M. Stiehl, D. C. Ralph, and R. A. Buhrman, “Thickness-dependent magnetoelasticity and its effects on perpendicular magnetic anisotropy in Ta/CoFeB/MgO thin films,” *Phys. Rev. B - Condens. Matter Mater. Phys.*, vol. 93, no. 2, p. 024404, 2016.

[67] Z. Zeng *et al.*, “High-Power Coherent Microwave Emission from Magnetic Tunnel Junction Nano-oscillators with Perpendicular Anisotropy,” *ACS Nano*, vol. 6, no. 7, pp. 6115–6121, 2012.

[68] T. A. Gosavi, E. R. Macquarrie, G. D. Fuchs, and S. A. Bhave, “HBAR as a High Frequency High Stress Generator,” in *2015 IEEE International Ultrasonics Symposium (IUS)*, 2015, pp. 1–4.

[69] B. Dieny, V. S. Speriosu, S. S. P. Parkin, B. A. Gurney, D. R. Wilhoit, and D. Mauri, “Giant magnetoresistive in soft ferromagnetic multilayers,” *Phys. Rev. B*, vol. 43, no. 1, pp. 1297–1300, 1991.

[70] M. N. Baibich *et al.*, “Giant magnetoresistance of (001)Fe/(001)Cr magnetic superlattices,” *Phys. Rev. Lett.*, vol. 61, no. 21, pp. 2472–2475, 1988.

[71] J. Bass and W. P. P. Jr., “Current-perpendicular (CPP) magnetoresistance in magnetic metallic multilayers,” *J. Magn. Magn. Mater.*, vol. 200, no. 1–3, pp. 274–289, 1999.

[72] N. F. Mott, “The Electrical Conductivity of Transition Metals,” *Proc. R. Soc. London A Math. Phys. Eng. Sci.*, vol. 153, no. 880, pp. 699–717, 1936.

[73] E. Tsymbal and D. Pettifor, “Effects of band structure and spin-independent disorder on conductivity and giant magnetoresistance in Co/Cu and Fe/Cr multilayers,” *Phys. Rev. B*, vol. 54, no. 21, pp. 15314–15329, 1996.

[74] K. Roy, S. Bandyopadhyay, and J. Atulasimha, “Hybrid spintronics and straintronics: A magnetic technology for ultra low energy computing and signal processing,” *Appl. Phys. Lett.*, vol. 99, no. 6, p. 063108, 2011.

[75] K. Roy, S. Bandyopadhyay, and J. Atulasimha, “Energy dissipation and switching delay in stress-induced switching of multiferroic nanomagnets in the presence of thermal fluctuations,” *J. Appl. Phys.*, vol. 112, no. 2, p. 023914, 2012.

[76] S. Maat, M. J. Carey, and J. R. Childress, "Current perpendicular to the plane spin-valves with CoFeGe magnetic layers," *Appl. Phys. Lett.*, vol. 93, no. 14, p. 143505, 2008.

[77] P. I. Williams, D. G. Lord, and P. J. Grundy, "Magnetostriction in polycrystalline sputter-deposited TbDyFe films," *J. Appl. Phys.*, vol. 75, no. 10, pp. 5257–5261, 1994.

[78] Y. Ren, Y. L. Zuo, M. S. Si, Z. Z. Zhang, Q. Y. Jin, and S. M. Zhou, "Correlation between ultrafast demagnetization process and Gilbert damping in amorphous TbFeCo films," *IEEE Trans. Magn.*, vol. 49, no. 7, pp. 3159–3162, 2013.

[79] J.-G. (Jimmy) Zhu and C. Park, "Magnetic tunnel junctions," *Mater. Today*, vol. 9, no. 11, pp. 36–45, 2006.

[80] M. Julliere, "Tunneling between ferromagnetic films," *Phys. Lett. A*, vol. 54, no. 3, pp. 225–226, 1975.

[81] W. H. Butler, X.-G. Zhang, T. C. Schulthess, and J. M. MacLaren, "Spin-dependent tunneling conductance of Fe|MgO|Fe sandwiches," *Phys. Rev. B*, vol. 63, no. 5, p. 054416, 2001.

[82] S. Ikeda *et al.*, "Dependence of Tunnel Magnetoresistance in MgO Based Magnetic Tunnel Junctions on Ar Pressure during MgO Sputtering," *Jpn. J. Appl. Phys.*, vol. 44, no. 11L, p. L1442, 2005.

[83] S. O. Valenzuela and M. Tinkham, "Direct electronic measurement of the spin Hall effect.," *Nature*, vol. 442, no. 7099, pp. 176–179, 2006.

[84] M. I. Dyakonov and V. I. Perel, "Current-induced spin orientation of electrons in semiconductors," *Phys. Lett. A*, vol. 35, no. 6, pp. 459–460, 1971.

[85] M. I. D'yakonov and V. I. Perel', "Possibility of orienting electron spins with current," *JETP Lett.*, vol. 13, no. 11, pp. 467–469, 1971.

[86] J. E. Hirsch, "Spin Hall Effect," *Phys. Rev. Lett.*, vol. 83, no. 9, pp. 1834–1837, 1999.

[87] M. I. Dyakonov, "Spin Hall Effect," in *Future Trends in Microelectronics*, John Wiley & Sons, Inc., 2010, pp. 251–263.

[88] S. Natarajan *et al.*, "A 14nm logic technology featuring 2nd-generation FinFET, air-gapped interconnects, self-aligned double patterning and a 0.0588 μm^2 SRAM cell size," in *IEDM, IEEE Technical Digest - International Electron Devices Meeting*, 2014, p. 3.7.1-3.7.3.

[89] K. J. Kuhn *et al.*, "The ultimate CMOS device and beyond," in *Technical Digest - International Electron Devices Meeting, IEDM*, 2012, pp. 171–174.

[90] H.-S. P. Wong and S. Salahuddin, "Memory leads the way to better computing," *Nat. Nanotechnol.*, vol. 10, no. March, pp. 191–194, 2015.

[91] D. E. Nikonov and I. A. Young, "Overview of beyond-CMOS devices and a uniform methodology for their benchmarking," *Proc. IEEE*, vol. 101, no. 12, pp. 2498–2533, 2013.

[92] A. Brataas, A. D. Kent, and H. Ohno, "Current-induced torques in magnetic materials.," *Nat. Mater.*, vol. 11, no. 5, pp. 372–381, 2012.

[93] L. Liu, T. Moriyama, D. C. Ralph, and R. A. Buhrman, "Spin-torque ferromagnetic resonance induced by the spin Hall effect," *Phys. Rev. Lett.*, vol. 106, no. 3, p. 036601, 2011.

[94] C. F. Pai, L. Liu, Y. Li, H. W. Tseng, D. C. Ralph, and R. A. Buhrman, "Spin transfer torque devices utilizing the giant spin Hall effect of tungsten," *Appl. Phys. Lett.*, vol. 101, no. 12, p. 122404, 2012.

[95] S. Manipatruni, D. E. Nikonov, and I. A. Young, "Energy-delay performance of giant spin Hall effect switching for dense magnetic memory," *Appl. Phys. Express*, vol. 7, no. 10, p. 103001, 2014.

[96] E. B. Myers, F. J. Albert, J. C. Sankey, E. Bonet, R. a Buhrman, and D. C. Ralph, "Thermally activated magnetic reversal induced by a spin-polarized current.," *Phys. Rev. Lett.*, vol. 89, no. 19, p. 196801, 2002.

[97] S. V Aradhya, G. E. Rowlands, J. Oh, D. C. Ralph, and R. A. Buhrman, "Nanosecond-Timescale Low Energy Switching of In-Plane Magnetic Tunnel Junctions through Dynamic Oersted-Field-Assisted Spin Hall Effect," *Nano Lett.*, vol. 16, no. 10, pp. 5987–5992, 2016.

[98] M. H. Nguyen, C. F. Pai, K. X. Nguyen, D. A. Muller, D. C. Ralph, and R. A. Buhrman, "Enhancement of the anti-damping spin torque efficacy of platinum by interface modification," *Appl. Phys. Lett.*, vol. 106, no. 22, p. 222402, 2015.

[99] D. Dixit, K. Konishi, C. V. Tomy, Y. Suzuki, and A. A. Tulapurkar, "Spintronic oscillator based on magnetic field feedback," *Appl. Phys. Lett.*, vol. 101, no. 12, p. 122410, 2012.

[100] K. Y. Camsari, S. Ganguly, and S. Datta, "Modular Approach to Spintronics.," *Sci. Rep.*, vol. 5, p. 10571, 2015.

[101] J. D. Larson, P. D. Bradley, S. Wartenberg, and R. C. Ruby, "Modified Butterworth-Van Dyke circuit for FBAR resonators and automated

measurement system," in *Proceedings of the IEEE Ultrasonics Symposium*, 2000, pp. 863–868.

[102] T. A. Gosavi and S. A. Bhave, "Model for Acoustic Locking of Spin Torque Oscillator," in *2015 Joint Conference of the IEEE International Frequency Control Symposium & the European Frequency and Time Forum*, 2015, pp. 68–71.

[103] D. Wang, C. Nordman, Z. Qian, J. M. Daughton, and J. Myers, "Magnetostriction effect of amorphous CoFeB thin films and application in spin- dependent tunnel junctions Magnetostriction effect of amorphous CoFeB thin films and application in spin-dependent tunnel junctions," *J. Appl. Phys.*, vol. 97, no. 10, p. 10C906, 2005.

[104] Q. Su, J. Morillo, Y. Wen, and M. Wuttig, "Young's modulus of amorphous Terfenol-D thin films," *J. Appl. Phys.*, vol. 80, no. 6, pp. 3604–3606, 1996.

[105] R. Wang, S. A. Bhave, S. Zhgoon, K. Bhattacharjee, and W. Lafayette, "Multi-Frequency Linbo 3 Lamb Wave Resonators With < 3Ω Impedance," in *2016 IEEE 29th International Conference on Micro Electro Mechanical Systems (MEMS)*, 2016, no. January, pp. 679–682.

[106] T. Daugey, J. M. Friedt, G. Martin, and R. Boudot, "A high-overtone bulk acoustic wave resonator-oscillator-based 4.596 GHz frequency source: Application to a coherent population trapping Cs vapor cell atomic clock," *Rev. Sci. Instrum.*, vol. 86, no. 11, p. 114703, 2015.